EPR investigation of electronic excitations in rare gas solids (Review Article)

R. A. Zhitnikov and Yu. A. Dmitriev

A. F. Ioffe Physico-Technical Institute, 26 Politekhnicheskaya, St. Petersburg 194021, Russia[*)]

The methods are described for producing unstable paramagnetic excited states in rare gas cryocrystals Ne, Ar, Kr, and Xe through the trapping, in the cryocrystals growing from the gas phase, the products of the gas discharge taking place in the same or other rare gas. The paper presents a technique and results of an observation and investigation of excited states in rare gas cryocrystals with electron paramagnetic resonance (EPR). The discovered unstable paramagnetic centers are interpreted as being local metastable excited $np^5(n+1)s$ atomic-type states in rare gas cryocrystals which are subject to the action of the anisotropic electric field resulted from the crystal surroundings distorted by the center. An account is given of the mechanisms for formation of observed paramagnetic excited states in cryocrystals which arise owing to the excitation energy of the metastable $^3P_2$ atoms of Ne, Ar, Kr, Xe and He $2\,^3S_1$ and $2\,^1S_0$ atoms that form in the discharge in an appropriate gas and trap in the growing cryocrystal. © *1998 American Institute of Physics.* [S1063-777X(98)00110-8]

1. INTRODUCTION

The rare gas cryocrystals, Ne, Ar, Kr, and Xe, are the simplest solids in nature, being composed of closed-shell atoms that are bound to each other by weak Van-der-Waals forces and having, as a rule, the structure of tightly packed face-centered cubic lattice. At the same time, the electronic excitations in these crystals are distinguished by abundance of properties and complicated behavior.[1-6] Thus, the free excitons in these simple Van-der-Waals atomic crystals appear to be, contrary to expectations, not mere Frenkel-type excitons but of a more complicated intermediate type that, in many instances, is even closer to Wannier-type excitons. The self-trapping of these excitons, though, can bring into formation at once of even two types of point motionless excitons: molecular two-atom type, Rg_2^* (m-STE), and atomic type, Rg* (a-STE), with electron shells and energy levels close to excimer molecules and free excited atoms, respectively, in the corresponding rare gas. It is also remarkable that all three types of excitons—both free and self-trapped types (molecular and atomic)-are capable of existing in the same crystal simultaneously. This is due to the fact that there exist the activation barriers against the self-trapping of free excitons into both the molecular and atomic types of motionless excitons. The self-trapping processes involve the exciton-phonon interaction and local relaxation deformations of the crystal lattice, which causes in particular the formation of cavities (bubbles) containing excited atoms, Rg*.

These interesting phenomena have attracted considerable attention of many researchers worldwide who undertook extensive studies of electronic excitations in rare gas cryocrystals, in recent decades. The results are detailed in books[1-3] and extensive review articles alike, e.g.,[4-6].

It is worth noting that in all studies conducted the excited states in rare gas cryocrystals were obtained by exposure of a cryocrystal grown on a cold surface to ionizing radiation: electrons, ions, α-particles and hard enough electromagnetic radiation (VUV or x-rays), while the properties of these electronic excitations in the cryocrystals were examined with optical spectroscopy methods (luminescence, absorption, reflection, photoelectron emission).[1-6]

In recent years, researches[7-12] have been performed wherein an entirely new method was used for producing excited states in rare gas crystals. This consists in introducing and trapping the excited products from the rare gas discharge in the cryocrystal of either the same or other rare gas growing from the gas phase on a cold substrate, thereupon the excited states in cryocrystal arising under the action of the trapped particles are studied. In these papers,[7-12] as powerful a method as the electron paramagnetic resonance (EPR) is applied for the first time to the study of electronic excitations in rare gas cryocrystals. The present review is mainly devoted to the results of this work. The findings of investigations into electronic excitations in rare gas cryocrystals obtained by conventional methods, that is, with ionizing irradiation of rare gas cryocrystals along with the optical methods of their examination, are available from books and reviews, e.g.,[1-6].

2. EXPERIMENTAL PROCEDURE

The technique employed in[7-12] differs from the known ones as follows. The solid samples under study are obtained by gas condensation on a thin-walled bottom, used here as the substrate, of a quartz finger filled with liquid helium, this bottom being located at the center of the microwave cavity of an EPR spectrometer. Both the gas discharge and the matrix gas flow passing through a separate inlet tube avoiding the gas discharge, can be cooled down to the liquid nitrogen temperature. The products of the high-frequency gas discharge without intermediate feeding tubes are aimed in a vacuum directly onto the substrate, which prevents them
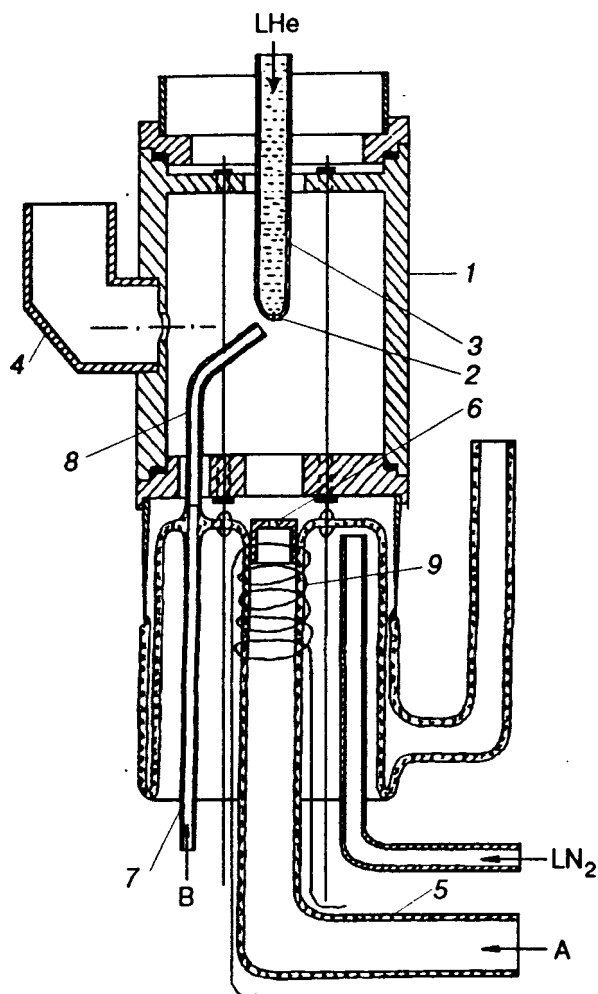
FIG. 1. The main part of the experimental set-up, including the microwave cavity of the EPR spectrometer, the gas discharge system, the gas inlet tube for matrix gas, and the quartz finger cooled by liquid helium (LHe) with the sample condensing on the bottom of the quartz finger as on a substrate (for notations see the text).

from decay on the walls of the tubes. Thus, the sample is obtained directly in the cavity of the EPR spectrometer, which makes it possible not only to carry out the EPR observation of the sample during the condensation but also to detect and study in the sample short-lived centers that are related to the gas discharge products.

The experimental set-up consists of a 3-cm EPR spectrometer with a microwave cavity cooled by liquid nitrogen vapors, a gas filling and purification system, a high-frequency oscillator for exciting an electrodeless gas discharge, measuring instruments, and pumping facilities.[7–12]

Figure 1 shows the main part of the experimental set-up: the microwave cavity of the 3-cm EPR spectrometer, a low-temperature gas discharge device and the substrate cooled by liquid helium, on which the sample is condensed.

Here 1 is the cylindrical H_{011} mode microwave cavity of the X-band EPR spectrometer, 2 is the bottom of the quartz finger 3, filled with liquid helium, and 4 is a waveguide. The bottom 2 of the quartz finger is a low-temperature substrate for the gases being condensed. An electrodeless high-frequency gas discharge is excited in the glass tube 5 with an

outlet 6 of 0.2–0.6 mm diameter. The matrix gas could be supplied to the substrate 2 by a glass tube 7 and further by a quartz tube 8 inserted into the cavity (channel B). The end of the quartz tube 8 is located close (3 mm) to the bottom 2 of the quartz finger, which facilitates effective freezing out of the matrix gas.

The whole device presented in Fig. 1 is cooled externally with liquid nitrogen vapor (LN_2) and its temperature can be varied from 77 to 300 K.

A high-frequency (14-MHz) oscillator is used to maintain the discharge. The high-frequency power is fed through a coaxial cable to the coil 9 wound over the gas discharge tube 5.

The experimental procedure is as follows. Pure rare gas (Ne, Ar, Kr, Xe, He) in channel A was passed through the liquid-nitrogen-vapor-cooled gas discharge tube 5, in which an electrodeless high-frequency discharge was excited. Ground-state rare gas atoms together with gas discharge products passed through the outlet 6 of the discharge tube 5 into the evacuated cavity and reached the bottom 2 of the quartz finger 3 filled with liquid helium at 1.2–4.2 K. The pure additional matrix gas, also cooled by liquid nitrogen vapors (LN_2), was passed through the tubes 7 and 8 (channel B), avoiding the gas discharge, onto the substrate. The EPR spectra of the sample were recorded continuously during its condensation, i.e., growth of the rare gas cryocrystal with gas-discharge products trapped in the sample. The short-lived centers were separated from the stable centers by switching off the discharge, i.e., switching off the voltage on the coil 9 during recording the EPR spectrum. High-purity rare gases were used with the following impurity contents: 0.004% Ne, 0.007% Ar, 0.0009% Kr, 0.0003% Xe, and 0.01% He.

3. EXPERIMENTAL RESULTS AND INTERPRETATION

3.1. Pure rare gases Ne, Ar, Kr, and Xe. Experimental results

In all experiments described in Sec. 3.1, a rare gas (Ne, Ar, Kr, Xe) supplied to the substrate 2 was passed only through the tube 5 (channel A) with the gas discharge running, while the second channel, B, (the tubes 7 and 8, Fig. 1) was free from a gas, i.e., closed, and no excess matrix gas was fed through it in the runs of Sec. 3.1.

Figures 2–6 show the EPR spectra of unstable paramagnetic centers which form in a cryocrystal of a pure rare-gas (Ne, Ar, Kr, Xe) being passed through the gas discharge zone, i.e., through the tube 5 only (Fig. 1) that is cooled in these experiments to the liquid-nitrogen temperature, 77 K. These spectra (Figs. 2–6) were observed only during a continuous flow of a rare gas from the tube 5 onto the cold ($T = 1.2$–4.2 K) substrate 2 along with the products of the gas discharge taking place in this tube. The EPR signal disappeared at the instant when the gas discharge was turned off, i.e., the EPR spectrum record was cut off immediately. Thus, the paramagnetic centers responsible for these spectra have short lifetimes. According to estimates based on the time constant of the recording system of the EPR spectrometer, the lifetime of these centers is no more than 0.1 s.
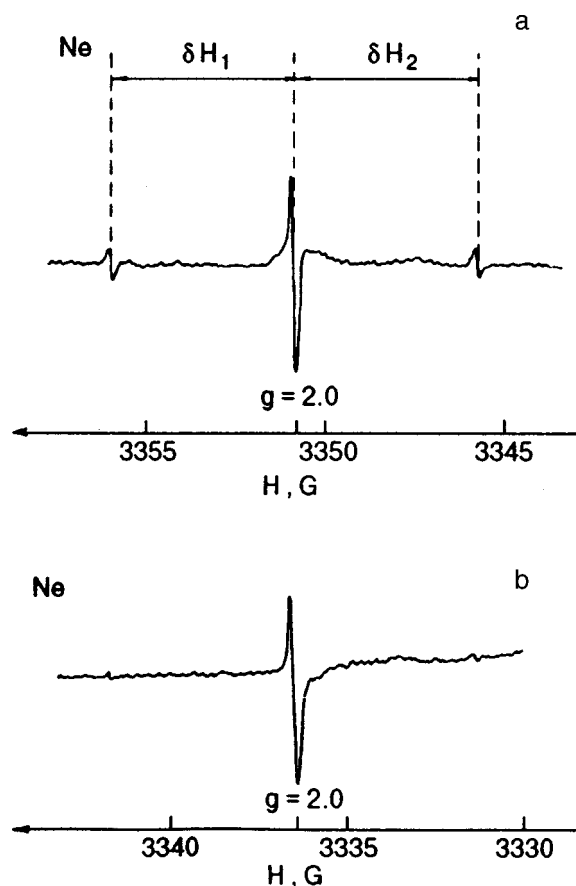
FIG. 2. EPR spectrum of unstable paramagnetic centers in a neon cryocrystal. The gas is let only through the gas discharge tube *5* (Fig. 1). The gas flow rate to the substrate *2* is $Q=0.3$ mmole/h; magnetic resonance frequency $f_{res}=9379.31$ MHz (a), $f_{res}=9339.00$ MHz (b). The side-line intensity, in Fig. 2b reduces as compared to Fig. 2a.
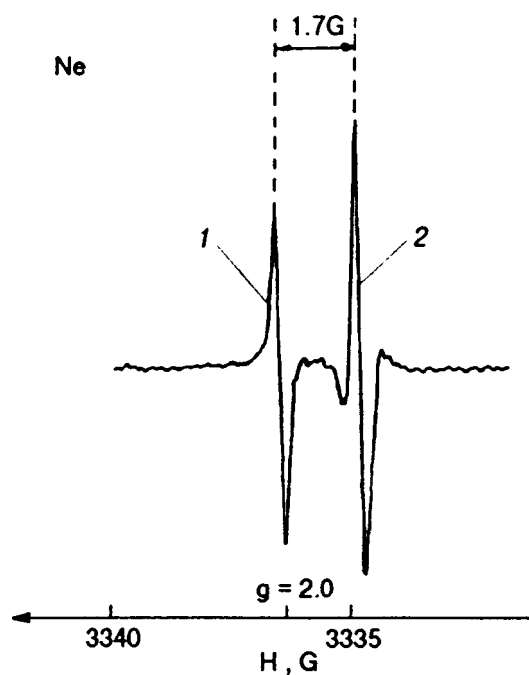

FIG. 3. EPR spectrum of unstable paramagnetic centers in a neon cryocrystal with increased gas flow to the substrate $Q=0.7$ mmole/h; $T=4.2$ K, $f_{res}=9338.94$ MHz.

It was found that these paramagnetic centers are localized in a frozen rare gas. Thus, when the discharge is turned on in the tube *5* and in the presence of a rare gas flow from this tube into the cavity, but in the absence of liquid helium in the quartz finger *3*, i.e., when no cryocrystals are formed, the EPR signals indicated above are completely absent. This testifies that the observed short-lived paramagnetic centers are located in the cryocrystals, not in the gas phase. This is also confirmed by an examination of the properties of these centers, which are discussed below.

The EPR spectra, obtained at comparatively low gas flow rate through the gas discharge (no more than 0.5 mmole/h), were found, for the cryocrystals of pure neon and argon, to be completely identical both in appearance (i.e., as in Fig. 2) and in all quantitative characteristics (also see Ref. 8). Nor were any differences observed between the spectra obtained at the substrate temperatures $T=1.2$ and 4.2 K. The parameters of these spectra coincide completely within the measurement error for neon and argon cryocrystals and are given in Table 1. The *g*-factor quoted there refers to the middle (brightest) line in Fig. 2. The other designations are clear from this figure.

The relative strengths of the center and satellite lines in the spectra shown in Fig. 2 change from run to run both in neon and argon, from the maximum strength of the satellite lines to the point they are completely unobservable. The variability of the central line to side line intensity ratio indicates that the side doublet and the center line belong to different paramagnetic centers.

As the gas flow through the discharge tube increases, and when the flow to the substrate *2* exceeds 0.7 mmole/h, new lines appear in the spectra of the short-lived centers in the neon and argon cryocrystals, and in the process the lines shown in Fig. 2 are preserved. Figure 3 gives the middle

TABLE I. The parameters of EPR spectra of unstable paramagnetic centers in rare gas cryocrystals at low gas flow rate to the substrate ($T=4.2$ K).

Rare gas	No. of runs	*g*-factor	δH_1	δH_2	ΔH_1^a	ΔH_2^b
					Gauss	
Ne	7	1.99987(12)	5.19(8)	5.24(8)	0.1–0.2	0.1–0.2
Ar	4	1.99986(12)	5.21(8)	5.18(8)	0.1–0.2	0.1–0.2
Kr	5	1.99986(12)	-	-	0.15–0.25	-
Xe	4	1.99983(12)	-	-	0.2–0.3	-

Note: a—here ΔH_1 is the width of the central line; *b*—here ΔH_1 is the widths of the side lines.
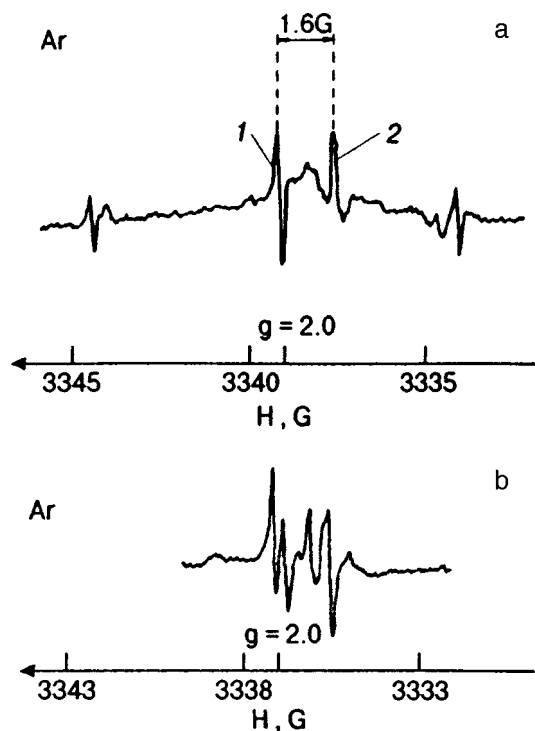
FIG. 4. EPR spectrum of unstable paramagnetic centers in an argon cryocrystal with increased gas flow to the substrate at $T = 4.2$ K and $Q = 2.2$ mmole/h, $f_{res} = 9346.60$ MHz (a); $f_{res} = 9340.93$ MHz (b).

FIG. 5. EPR spectrum of unstable paramagnetic centers in a krypton cryocrystal at $T = 4.2$ K, $Q = 0.2$ mmole/h; $f_{res} = 9382.04$ MHz (a); $Q = 0.5$ mmole/h, $f_{res} = 9368.63$ MHz (b).

region of the EPR spectrum for neon for an increased gas flow rate. Two closely spaced lines are seen, with line 1 coinciding with the center line in Fig. 2 and having a g-factor equal to that given in Table. The spacing between these lines amounts to 1.7 G. Figure 4a shows the EPR spectrum for Ar also for an increased gas flow rate. Here line *1* coincides with the center line in Fig. 2, and the new line is separated from it by 1.6 G. Thus, as the gas flow grows, the same changes may occur in the EPR spectra of short-lived centers for neon and argon, as follows from the similarity of the spectra in Figs. 3 and 4a. In some experiments, however, for the same gas flow rate as in Fig. 4a two more lines appeared between the two center lines shown in this figure, and all four lines had comparable strengths (see Fig. 4b).

The EPR spectra of Kr and Xe cryocrystals obtained at the same conditions as for the spectrum in Fig. 2, i.e., when a rare-gas flow rate is low, consist each of one line (see Figs. 5a and 6a), which lines, as indicated by Table, are identical in g-factor, within the accuracy of the experiment, to one another and to the middle lines in the spectra of Ne and Ar. These lines are also close in linewidths for all the four rare gases. One can, thus, believe that the principal unstable paramagnetic center is of a common nature to all the four rare-gas cryocrystals produced under similar conditions, i.e., at modest flow rate through the gas discharge.

In EPR spectra of Kr and Xe cryocrystals no side lines provided by the other unstable center were observed, as it was in Ne and Ar (Figs. 2 and 4a). As indicated above, sometimes these side lines could not be observed in Ne and Ar also. At present one cannot be sure whether the centers that give side lines are absent in Kr and Xe cryocrystals or
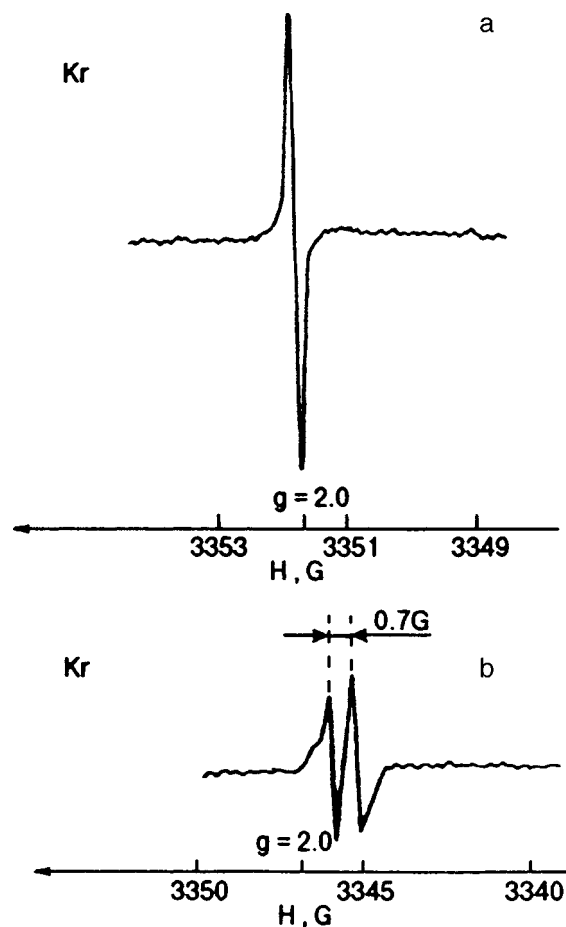
whether these centers in the experiments were too scarce to be spectroscopically observable.

Shown in Figs. 5b and 6b, are the experimental results for Kr and Xe obtained with the gas discharge in tube 5 at room temperature, i.e., without liquid-nitrogen cooling the tube. These spectra differ from those in Figs. 5a and 6a, although they are equally short-lived, i.e., disappear immediately when the discharge is turned off. In the spectrum of Xe, the number, location and intensity of lines changed from one experiment to the next. But they were close to one another within the confines of the spectrum of Fig. 6b were located around $g = 2.0$, and the entire spectrum disappeared immediately once the discharge was turned off.

It should be noted that the excess lines arising with the increased gas flow rate vary in their characteristics (g-factors, location, linewidths) with the kind of the rare gas used (Figs. 3, 4a, 4b, 5b, and 6b), and reveal no such a similarity they do in the spectra of the rare gases with the low gas flow rate, presented in Figs. 2, 5a, 6a, and Table I.

All the excess lines occurring with an increased gas flow rate onto the substrate are unstable just as the lines presented in Fig. 2 and Table are, and disappear along with the principal lines when the discharge is turned off.

Using the EPR line microwave saturation method, the lower boundary for the lifetime τ of the unstable para-
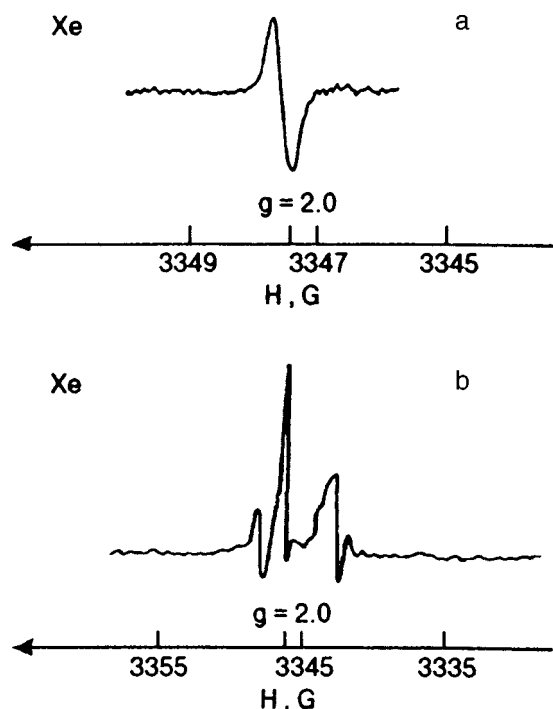
FIG. 6. EPR spectrum of unstable paramagnetic centers in a xenon cryo-crystal at $T = 4.2$ K, $Q = 0.04$ mmole/h, $f_{res} = 9370.15$ MHz (a); $Q = 0.6$ mmole/h, $f_{res} = 9366.92$ MHz (b).

magnetic centers was determined in all cryocrystals, Ne, Ar, Kr, and Xe.[8] These lifetime values are found to be in the interval 10^{-1} s $\geqslant \tau \geqslant 10^{-4}$ s for certain of these centers, and in the interval 10^{-1} s $\geqslant \tau \geqslant 10^{-2}$ s for others.[8]

3.2. Interpretation of the experimental results for pure Ne, Ar, Kr, and Xe

To elucidate the nature of the observed short-lived paramagnetic centers, it is necessary to consider the products of the discharge in a rare gas that may enter the cryocrystal of this gas being condensed, as well as the possible action of the gas discharge on the cryocrystal already frozen onto the substrate, and to compare the results of this examination with the properties and characteristics of the EPR spectra shown in Figs. 2–6 and in Table I.

In order to reach the cold substrate 2 on which the sample is condensed, the gas-discharge products must travel a distance ~3 cm through vacuum. If they are rare-gas atoms their thermal velocities are of order 10^4 cm/s, i.e., only particles with a lifetime $\geqslant 10^{-4}$ s can reach the substrate. The only neutral products of the discharge in the rare gas which satisfy this condition are excited metastable atoms of this gas in the lower $^3P_2$ and $^3P_0$ states (for free $^3P_2^0$ atoms, the lifetimes have the values[13] $\tau(\text{Ne}) = 20$ s, $\tau(\text{Ar}) = 60$ s, $\tau(\text{Kr}) = 85$ s, $\tau(\text{Xe}) = 150$ s, and for $^3P_0^0$ atoms, the lifetimes range from 400 s for neon to 0.08 s for xenon). The entry of charged particles, i.e., electrons and ions, from the gas discharge into a growing cryocrystal of rare gas, as well as bombardment by these particles of the cryocrystal already formed, is impossible, since observation of the EPR spectra of short-lived centers is carried out as the cryocrystal

condenses. Therefore, the strong magnetic field of the EPR spectrometer, $H_0 = 3300$ G, is turned on all the time; it is transverse to the flow of these charged particles, deflects them to the side, and prevents them from reaching the substrate 2, i.e., the sample. Thus, for 1-keV electrons in a 3300-Gauss magnetic field, the orbit radius is 0.32 mm, and still considerably less for thermal-energy ions ($r_i < 0.1$ mm), i.e., all charged particles from the gas discharge (both electrons and ions) are locked up firmly with magnetic field in the gas discharge zone 9, and cannot reach the substrate 2.

Finally, the solid cryocrystal of a rare gas already formed on the substrate, as well as the gas being condensed, can be both subjected to irradiation by light from the gas discharge, including VUV. The action of the light from the discharge in a rare gas on the cryocrystal of this gas or gas at the instant of condensation can produce only the short-lived $^3P_1$ and $^1P_1$ atoms. These excited atoms cannot cause the formation of the observed EPR spectra, since the radiative lifetimes of the $^3P_1$ and $^1P_1$ atoms are too short: for all rare gases, they are of order $10^{-8} - 10^{-9}$ s. Such lifetimes should result in the EPR linewidths no less than 5–50 G, whereas the observed spectra have linewidths of the order of 0.1 G (see Table I and Fig. 2); this requires a lifetime of the paramagnetic center of the order of $5 \cdot 10^{-7}$ s. At the same time, it is known that the lifetime, for example, of the $^3P_2$ atoms of neon in a cryocrystal of this gas is no less than 6×10^{-4} s.[14] As indicated above, the lifetimes of the unstable centers observed in the present study $\tau \geqslant 10^{-4} - 10^{-2}$ s. Therefore, the paramagnetic centers based on the $^3P_2$ rare gas atoms trapped in cryocrystals should satisfy the requirement of a fairly small EPR linewidth, consistent with that observed experimentally. However, these $^3P_2$ atoms, like $^3P_0$ atoms, cannot be practically formed under action of radiation from the gas discharge since the radiation transitions $^1S_0 \rightarrow {}^3P_2$, $^3P_0$ to these metastable states from the ground state $^1S_0$ are forbidden. Hence, the radiation from the gas discharge cannot be responsible for the formation of the paramagnetic centers producing the observed EPR spectra.

Thus, the observed centers (Figs. 2–6) can only be due to the entry into the rare gas cryocrystal of atoms of this gas in the $^3P_2$ state directly from the gas discharge. Atoms in the $^3P_0$ state, which can also reach the crystal from the discharge, should be excluded from the consideration, since they are diamagnetic and cannot form paramagnetic centers in the cryocrystal.

Hence, it must be taken as proved that the cause of the formation of the observed short-lived paramagnetic centers is the trapping, in a growing rare-gas cryocrystal, of excited atoms of this gas in the metastable $^3P_2$ state. This atom is paramagnetic and, as was noted above, can have a sufficiently long lifetime in the cryocrystal to provide the experimentally observed small EPR linewidths, $\Delta H_{1,2} \sim 10^{-1}$ G.

However, a significant difficulty arises here. This is because all the lines in the observed EPR spectra have g-factors that are very close to $g = 2.0$ (Table I), whereas the $^3P_2$ state has the g-factor of 1.5, and its lines should be at entirely different magnetic fields (i.e., for $g = 1.5$, $H_{res} = 4400$ G, and for $g = 2.0$, $H_{res} = 3300$ G, as is the case experimentally). It was found experimentally that the EPR spectra are
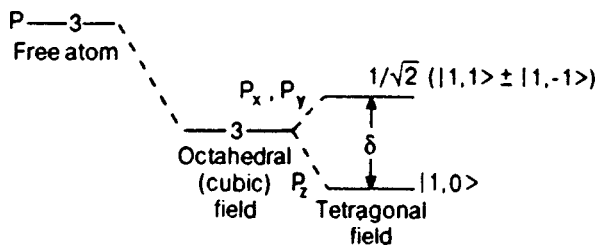
FIG. 7. Shift of the energy levels of the P-state atom in the octahedral crystal field followed by the splitting in the tetragonal field.

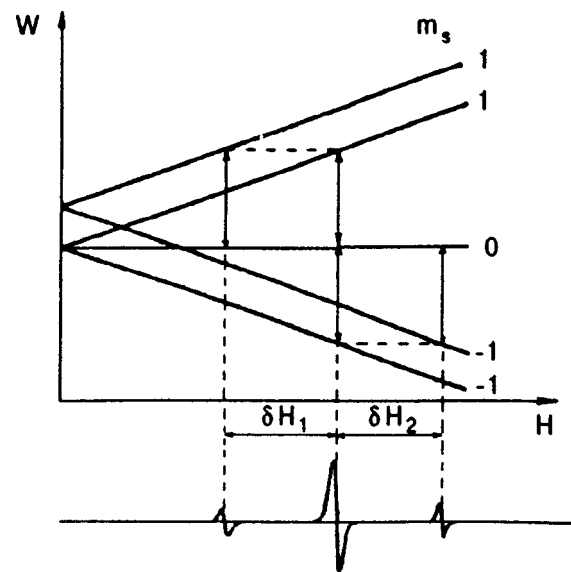

FIG. 8. Splitting of the levels of an atom with spin $S = 1$ in an axial electric crystal field and appearance of side lines in the EPR spectrum.

completely absent in magnetic fields close to 4400 G. To explain this discrepancy the following was suggested.[7–12] Presumably, the trapped $^3P_2$ rare gas atom is stabilized in the cryocrystal of the same gas in such a manner that the effective crystal electric field acting on it is anisotropic and of low enough symmetry. The action of the crystal electric field of the tetragonal symmetry on the energy levels of the P-state atom is shown in Fig. 7 (see Ref. 15, § 11.5, Fig. 11.2). It is seen from the figure that a crystal field of low enough symmetry lifts the degeneracy of the P-state energy levels and causes, in the case of the tetragonal symmetry field, for example, the splitting δ between $P_z(m_L = 0)$ and $P_x, P_y(m_L = \pm 1)$ states. If the splitting δ is sufficiently large, then at liquid helium temperature (1.2 to 4.2 K) almost only the lower $m_L = 0$ level will be populated, which has the g-factor defined, in the tetragonal field, as (see Ref. 15, § 11.6) $g_{zz} = g_\parallel = g_e$, $g_{xx} = g_\perp = g_e - 2\lambda/\delta$. Here g_e is the spin g-factor of the free electron, the exact value being $g_e = 2.00232$, λ is the fine structure constant for the free ^3P atom of the rare gas at hand, which appears in the spin-orbit interaction hamiltonian, $\hat{H} = \lambda \hat{\mathbf{L}} \cdot \hat{\mathbf{S}}$. The constant λ therewith is evaluated from the equation $\lambda = \Delta_{so}/S(L+1) = \Delta_{so}/3$, here Δ_{so} is the total splitting of the fine structure for the ^3P atom considered, L and S are correspondingly its total orbital and spin moments; for the ^3P-state, $L = S = 1$. This treatment is strictly correct for the atom in a state with the normal, i.e., $[L,S]$-coupling. However, it is known that the rare gas atoms in the state with $np^5(n+1)s$ electron configuration show the departure from the $[L,S]$-coupling, this actually being intermediate between $[L,S]$ and $[j,j]$, that is $[J',j]$-coupling. The Ne $2p^53s$ ^3P-atom therewith still follows the interval rule and definitely shows $[L,S]$-coupling. Because of this, the calculation of λ is quite justified for Ne with the formula $\lambda = \Delta_{so}/3$. Based on the total spin-orbit splitting for the Ne $2p^53s$ ^3P-atom, $\Delta_{so} = 0.097$ eV,[13] one gets $\lambda(\text{Ne}) = 0.032$ eV. Starting with Ar, the considerable departure from the $[L,S]$-coupling for the $np^5(n+1)s$ rare-gas atom is beginning to emerge, which rises for Kr and Xe as the atomic mass increases. However, this expression, $\lambda = \Delta_{so}/3$, can likely be used in estimating expected g-factors for these atoms in a crystalline field; here, taken from Ref. 13, Δ_{so} is also the total splitting for three lower levels of the $np^5(n+1)s$ configuration of the free rare-gas atoms. In that event $\lambda(\text{Ar}) = 0.06$ eV, $\lambda(\text{Kr}) = 0.24$ eV, $\lambda(\text{Xe}) = 0.42$ eV. If the splitting caused by an anisotropic crystal field is large, so that $\delta \gg 2\lambda$ for all the cryocrystals (i.e., Ne, Ar, Kr, and Xe), then it follows from the above expressions that $g_\parallel = g_\perp = g_e$

$= 2.0$, i.e., the g-factors of the $np^5(n+1)s$ $^3P_2$-atoms trapped in the corresponding cryocrystals turn isotropic, equal to 2.0 and are close in magnitude (i.e., $g = g_{\text{isotr}} = 2.0$), which agrees with and explains the result of the experiments (see Fig. 2 and Table I).

The spectrum consisting of two side lines in Figs. 2 and 4a can be explained as follows. If an atom in the $^3P_2$ state is localized in the position in the crystal where the effective electric crystal field has axial symmetry, the state with $m_L = 0$ in Fig. 7 splits in a zero magnetic field into two spin sub-levels with $m_s = \pm 1$ and 0 (see Ref. 15, § 10.3). For this case, the levels of the atom in the magnetic field and the EPR transitions are shown in Fig. 8. Thus, the transitions $m_s = 0 \leftrightarrow m_s = +1$ and $m_s = 0 \leftrightarrow m_s = -1$ will move apart along the magnetic field to give rise to two noncoincident EPR lines symmetric relative to 2.0, i.e., the side lines observed in the experiment. From this figure, taking the values for $\delta H_1 = \delta H_2 = \delta H_{1,2} = 5.2$ G from Table I, one can determine the splitting $(3/2)D$ of the levels $m_s = \pm 1$ and 0 for Ne and Ar in a zero magnetic field: $(3/2)D = \delta H_{1,2} g \beta / h = 2.8 \times 10^6 \cdot \delta H_{1,2}$ Hz $= 14.6$ MHz. The fraction of $^3P_2$ atoms trapped at the sites with the crystal field of that kind is apparently small and can vary from run to run, which accounts for the variability of the side lines in Fig. 2.

One may suppose that most of the $^3P_2$ rare gas atoms are trapped in the substitutional position of the face centered cubic (FCC) crystal of the rare gas and give rise to the intensive central line in the EPR spectra in Fig. 2, and a lesser part of the $^3P_2$ atoms are trapped into octahedral interstitial sites of this crystal to give the side lines. The fraction of the latter atoms is likely to vary from experiment to experiment depending on hard-to-control variations in experimental conditions.

Note that, in an undistorted FCC crystal, these trapping sites have a crystal electric field of very high (cubic) symmetry, so that splitting of the P-state cannot result, as evident from Fig. 7. A low-symmetry (anisotropic) crystal field

providing the observed EPR spectra of trapped atoms with $g = 2.0$ appears presumably due to crystal lattice distortions caused by the outer s shell of this $np^5(n+1)s\ ^3P_2$ atom. Distortion of a rare gas FCC crystal lattice by a rare gas P atom trapped therein as well as local rearrangement of this lattice were considered in Refs. 3, 16, and 17. In the above works, it is shown that the origin of the anisotropic crystal field which act on the trapped $np^5(n+1)s$ P-atom and, hence, is able to provide a splitting δ, Fig. 7, is as follows. The $np^5(n+1)s$ Rydberg state of a rare gas atom has a radius much greater than the ground np^6-state of a lattice atom has, thus the $(n+1)s$-electron of the trapped atom gives rise to outward displacement of the surrounding lattice atoms, resulting in a considerable rearranging of the nearest surroundings of the Rydberg excited atom. Such a rearranging of this surroundings breaks the cubic symmetry and produces a local electric field of low symmetry acting on the $np^5(n+1)s$ P-atom. This moving apart of the closed-shell np^6 atoms of the crystal lattice that surround the trapped excited $np^5(n+1)s$ atom is triggered by the repulsion forces that are due to the requirement, according to Pauli's principle, for the s-electron wave function of the trapped excited atom be orthogonal to the wave functions of the surrounding lattice atoms. Such a shift of the lattice atoms results in the formation of a cavity around the trapped excited atom, putting it in a so-called bubble.[1–3] A thorough theoretical study of this issue have been undertaken and the estimation of the bubble radius of 4 Å for the $2p^5 3s$ excitation in Ne cryocrystal was obtained. In Ref. 17, a theoretical treatment is given of formation around the $2p^5 3s$ excitation in the Ne crystal of, first, bubbles with symmetric elastic moving apart the surrounding Ne atoms of the lattice, second, bubbles that has induced the plastic distortion of the surroundings consisting in the production in the nearest lattice surroundings of defects in the Frenkel pair form, that is, vacancies and interstitial atoms. It is stated in the paper, that the bubbles with plastic distortion have lower energy than the pure elastic bubbles. In the Ne cryocrystal, the bubbles with two vacancies in the first coordination sphere and interstitial Ne atoms in the next more distant spheres are deduced[17] to have the lowest energy. Regular bubbles with only elastic distortion around the $np^5(n+1)s$ state are of cubic symmetry.[17] Though the plastic deformations with vacancies arising in the first coordination sphere around the $np^5(n+1)s$ excitation, cause a lower symmetry distortion of the surroundings,[17] thus creating an anisotropic electric crystal field acting on the trapped excited atom. It is worth noting that this local electric field acting on the $np^5(n+1)s$-atom should be not only quite anisotropic but strong as well. The latter quality is due to the fact that it is not the mere Van-der-Waals interaction that contributes to the local electric field (this interaction therewith should be much greater for the excited $np^5(n+1)s$ P-state, resulting from its large polarizability, than that one which is characteristic of two rare gas atoms, np^6 ground-state of the crystal lattice including), but, for Rydberg atoms, the much stronger chemical bonding between a trapped $np^5(n+1)s$ excited atom and a np^6 lattice atom should also appear. This is precisely the strong chemical bonding that gives rise, under proper conditions, to

diatomic excimer molecules of rare gases: $Rg(^1S_0) + Rg(^3P_2) \rightarrow Rg_2^*(^3\Sigma_u^+)$. This chemical bonding, of course, should contribute in some measure to the interaction between the $np^5(n+1)s$-atom trapped in rare gas crystal and its anisotropic crystal surroundings. This may provide, for the atom, a great enough splitting δ to meet the condition $\delta \gg 2\lambda$. In so doing, not only does the magnitude of λ increases, as is evident from the foregoing, with increasing mass of the rare-gas atom in the range between Ne and Xe, but the interaction energy between the trapped $np^5(n+1)s$ atom and crystal surroundings also increases including both Van-der-Waals (because the polarizability of the ground-state and metastable $^3P_2$ atoms alike enhances) interaction and chemical bonding. This, probably, provides the condition $\delta \gg 2\lambda$ for the atoms of all rare gases, resulting in $g = 2.0$ and closing together of g-factors of Ne, Ar, Kr and Xe with low gas flow rates to the substrate (see Table I).

The process of distortion of the lattice by the P-atom may proceed through metastable intermediate variants of the configuration of the neighborhood with certain delays in these configurations. Each of these configurations of the immediate neighborhood should be associated with a different symmetry of the crystal electric field acting on the $^3P_2$ atom. This probably accounts for the appearance, as the experimental conditions change (increasing the gas flow rate onto the substrate 2 or the enhancement of discharge temperature), of new lines in the EPR spectra for Ne, Ar, Kr, and Xe (Figs. 3–6), because of variation in δ and consequently g-factors of the EPR lines. Indeed, an increase in the flow rate of a rare gas or in its temperature may result in heating of the sample, growth of the size of its crystallites, and appearance of trapped $^3P_2$ atoms for which the process of distortion of the surroundings now takes place far from the surface of the sample, in the interior of the crystals and at a higher temperature. This may cause a change in the conditions of local rearrangement of the lattice around certain groups of $^3P_2$ atoms and may give rise to the additional lines in the spectra of Figs. 3–6.

It is possible that a contribution to the destruction of the cubic crystal environment of the $^3P_2$ atoms trapped in rare gas crystal in the described experiments comes also from the dynamic Jahn–Teller effect.[18]

It is noteworthy that the large lifetimes $\tau \geq 10^{-2} - 10^{-4}$ s found in this work (see Sec. 3.1) eliminate the possibility of explaining the observed EPR spectra as being due to rare gas excimer molecules, $Rg_2^*(^3\Sigma_u^+)$, trapped in cryocrystals. Indeed, the lifetimes, $\tau[Rg_2^*(^3\Sigma_u^+)]$, of these molecules in the rare gas cryocrystals are shown[6] to be $\tau(Ne_2^*) = 5 \times 10^{-6}$ s, $\tau(Ar_2^*) = 1.2 \times 10^{-6}$ s, $\tau(Kr_2^*) = 3.2 \times 10^{-6}$ s, $\tau(Xe_2^*) = 9 \times 10^{-6}$ s, respectively, i.e., much shorter than the lifetimes τ found in this work for paramagnetic centers for which $\tau \geq 10^{-2} - 10^{-4}$ s.

Thus, it was demonstrated that the unstable paramagnetic centers observed are due to the rare gas $np^5(n+1)s\ ^3P_2$ atoms which, once trapped from the gas discharge in a growing cryocrystal, become localized in it, deform and rearrange their surroundings and are subject to the action of an anisotropic electric field of this distorted surroundings. As
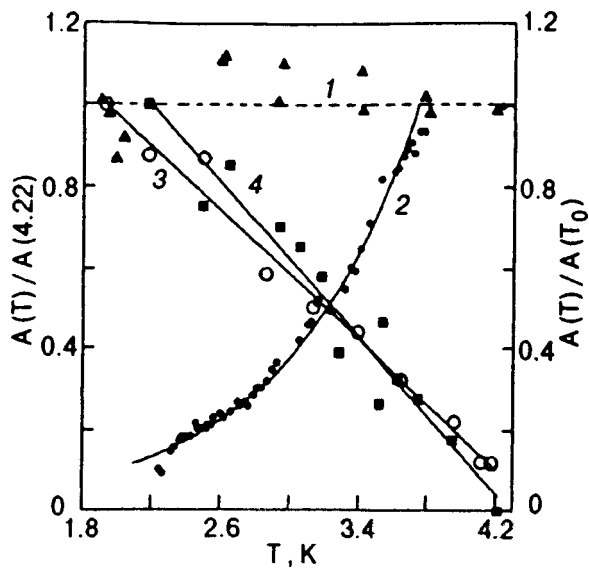
FIG. 9. Temperature dependences of the EPR signal amplitude, $A(T)$, for the unstable centers which form in growing pure Ne cryocrystal as it traps Ne gas discharge products (line *1*, triangles), and for the centers which form in growing Ne (line *2*, filled circles), Ar (line *3*, open circles) and Kr (line *4*, squares) cryocrystals as they trap He gas discharge products.
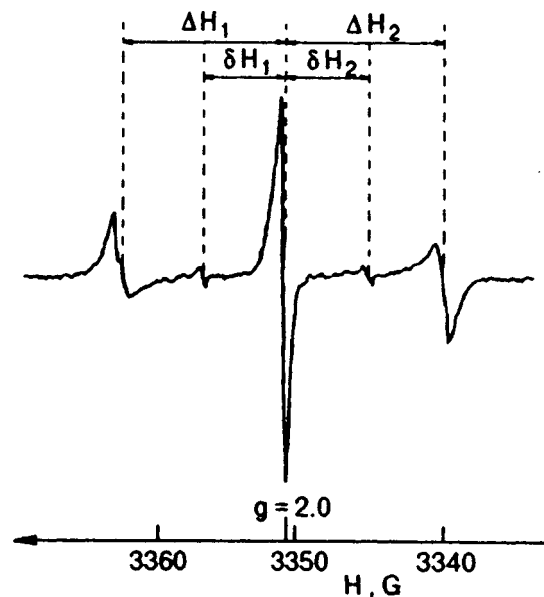

FIG. 10. EPR spectrum of unstable paramagnetic centers in a neon cryocrystal, which arise as a result of a He gas discharge product trapped in the growing Ne cryocrystal; $f_{res} = 9381$ MHz.

a result, the local paramagnetic metastable $np^5(n+1)s$ atomic-type excited states observed by EPR and described above arise in the cryocrystals.

It should be noted that the self-trapped excitons of $np^5(n+1)s$ atomic type are known to form efficiently under the action of ionizing radiation in Ne cryocrystals and with somewhat lesser efficiency in Ar cryocrystal. In irradiated cryocrystals of the heavy rare gases, Kr and Xe, though, only self-trapped excitons of molecular type, m-STE Rg_2^*, are observed, while self-trapped excitons of atomic type, a-STE, are not found. The explanation is as follows:[1-6] in Kr and Xe cryocrystals, the activation barriers against self-trapping into a-STE are very high, while with self-trapping into m-STE these are significantly lower. With Ne and Ar, the a-STE self-trapping barriers are well below these barriers in Kr and Xe, which makes possible the self-trapping into a-STE in Ne and Ar. A possibility for the local excited $np^5(n+1)s$ atomic-type states to form in Kr and Xe cryocrystals in the experiments described above is likely to be due to the method of producing the excited atomic-type states which differs fundamentally from the free exciton self-trapping in these cryocrystals. The point is that, in experiments described above, the excited $np^5(n+1)s$ $^3P_2$ rare gas atoms are inserted directly into a rare gas cryocrystal growing from the gas phase and trapped in the cryocrystal. This process does not involve an overcoming the self-trapping activation barrier and in this regard the localization of the $np^5(n+1)s$ atomic-type centers should proceed in Kr and Xe cryocrystals as unhindered as it does in Ne and Ar.

Figure 9, line *1*, shows the temperature dependence of the signal amplitude obtained for the central line of the spectrum for Ne in Fig. 2. It can be seen, that the number of observed unstable centers that form in the cryocrystal is independent of the temperature, i.e., the equilibrium number of these centers is invariant to the temperature with the gas flow

rate and discharge condition remaining constant. Precisely the same independence from temperature was observed for the side lines of the spectrum for Ne in Fig. 2, and for all lines of the spectra presented in Figs. 3–6. It must be added to the above, that the experiments show the lifetimes τ of all unstable paramagnetic centers investigated in the present work to be independent of temperature. Thus, with both the lifetimes of the paramagnetic centers and the flow rate of $np^5(n+1)s$ $^3P_2$ atoms from the gas discharge, the independence from temperature of the equilibrium number of these centers (Fig. 9, line *1*) agrees well with the mechanism proposed: the observed unstable centers are formed through the trapping and localizing in a growing cryocrystal the rare-gas $^3P_2$ atoms from the gas discharge.

3.3. Excitation energy transfer from the trapped metastable excited He 2^3S_1 atom to the Ne cryocrystal

In this study, investigations have been carried out where pure. He was passed through the gas discharge (channel A in Fig. 1) while pure Ne was fed to the substrate through a separate inlet tube (channel B) avoiding the gas discharge active part. A new effect has been found: the formation in a neon cryocrystal of local metastable excited states arising as helium gas discharge products are trapped in the growing cryocrystal.[9,10]

The EPR spectrum of the neon cryocrystal trapping He gas discharge products are shown in Fig. 10. These spectra were observed during the neon condensation and disappeared at the instant when the discharge was turned off. For simplicity the term ''edge-side lines'' shall be used to denote the outer broad side lines in Fig. 10, and the term ''side lines'' to refer to the inner narrow side lines.

There is absolute coincidence between both line positions and linewidths of the three middle lines in the He–Ne spectrum (Fig. 10) and the corresponding pure Ne lines

shown in Fig. 2. Indeed, the g-factor and linewidth of the central line of the He–Ne spectrum recorded here appear to be 1.99986(12) and 0.15(3) G, respectively, and exactly the same as those for the pure Ne cryocrystal, 1.99987(12) and 0.10(3) G. The side-line linewidths as well as separations between central and side lines are also the same; for the pure Ne these are summarized in Table I. However, there is a significant difference between the spectra of the Ne cryocrystal obtained by condensation of the pure Ne passed through the discharge active part, and the spectra of solid Ne trapping He gas discharge products. The latter contains a pair of additional strong edge-side lines of unstable centers, located around central line and separated from it by ΔH_1 and ΔH_2, for the high-field and low-field lines, respectively. The separation in magnetic field between each edge-side line and the central line is a factor of about 2 above the distances between each of the two weaker inner side lines and central line.

The fact that three middle lines of the He–Ne spectrum recorded here (Fig. 10) are clearly those of the pure Ne spectrum means that these spectra are due to centers of the same type and permits an explanation of the nature of the He–Ne spectrum in the same way as have been done in Sec. 3.2 for pure Ne. Thus, the centers being discussed in the present section can be interpreted also as being atomic-type excited $2p^5 3s$ states which become localized in the FCC Ne crystal lattice, shift the nearest matrix atoms outwards, rearrange their surroundings and are subjected to the action of the anisotropic electric field of this environment which, being rearranged, is no longer of cubic symmetry.

The nature of the strong edge-side lines, which occur only when a neon cryocrystal is trapping the He gas discharge products, will be discussed below. It is believed that these are also related to the $2p^5 3s$ centers, but with the surroundings distorted in a different way.

While the nature of the neon cryocrystal excited states recorded here is believed to be clear, the mechanism of their production is to be determined. Indeed, in the experiments on pure rare gases (Sec. 3.1), the excited Ne $^3P_2$ atoms (as well as Ar, Kr and Xe atoms), which are trapped in the growing cryocrystal of the same kind and rearrange the nearby crystal lattice, form directly in the gas discharge, whereas in the present study the gas flows aimed onto the substrate contain no excited Ne atoms at all, including $^3P_2$ atoms. Apart from ground-state He atoms, the only incoming He gas discharge products at the growing Ne cryocrystal are the metastable He 2^3S_1 and He 2^1S_0 atoms. Other excited helium atoms have too short life times to reach the substrate from the gas discharge. Charged particles from the discharge can also be excluded from consideration, since they are deflected from the substrate by the strong magnetic field of the EPR spectrometer (see Sec. 3.2).

Thus, the unstable paramagnetic centers observed here, which are probably the atomic-type $2p^5 3s$ excited states of the neon cryocrystal, originate from the excitation energy of incoming metastable He atoms from the gas discharge.

Figure 9, line 2, shows a plot of $A(T)/A(T_1)$ as a function of T, where $A(T)$ is the EPR signal intensity of the central line of the He–Ne spectrum (see Fig. 10) and T_1

=4.22 K. In these experiments, the substrate temperature or, correspondingly, the temperature of the sample growing on the substrate 2 (Fig. 1) is lowered by the pumping of liquid helium vapor. The sample temperature is detected by measuring the gas pressure in the liquid helium bath.

It can be seen from Fig. 9, line 2, that the experimental dependence $A(T)/A(T_1)$ can be fairly well approximated by $A(T)/A(T_1) = \exp(-E/kT)$ with the "activation energy" $E = 12$ K = 0.001 eV. Using either increasing or decreasing sample temperature, many such experimental dependences in the temperature range 2.2–4.2 K were recorded. Taking into account the statistical scattering of the experimental data, the "activation energy" can be estimated as $E = 12(6)$ K = 0.0010(5) eV.

The lifetime τ of the $2p^5 3s\, ^3P_2$-state in the neon cryocrystal was found to be independent of temperature.

Our explanation of the effect found in the present section is as follows.[9,10]

The energy level of the He 2^3S_1 atom appears to be located in the X-excitation energy band of the Ne cryocrystal, near the top of this band. This permits one to suppose that there exists an effective energy transfer from the metastable He 2^3S_1 atom to the neon cryocrystal X-exciton band. It is believed that the most probable way of producing $2p^5 3s$ atomic-type states in neon cryocrystal is the quasi-resonance excitation energy transfer from the metastable He 2^3S_1 atom to the neon cryocrystal X-exciton band followed by the self-trapping of the X-exciton into the $2p^5 3p$ ten-level state which then decays to the lower $2p^5 3s$ four-level excited state whose lowest $^3P_2$ level is just that observed in the experiment. It is well known from the optical investigations that the self-trapped X-exciton is actually the $2p^5 3p$ atomic-type state decaying to the $2p^5 3s$ state with luminescence in the visible region.[9,10]

The excitation energy (19.82 eV) transfer from the He 2^3S_1 atom to the neon cryocrystal X-exciton band should be a quasi-resonance process, since the center of the band is at 19.2 eV while the band half-width is about 0.6 eV. Thus, the energy transfer from the He 2^3S_1 atom is not of a completely resonant nature. The fact that the "activation energy", i.e., the "defect of resonance" (or energy misfit), of the energy-transfer process is so small ($E = 0.001$ eV) can be explained as being due to the broad wings of the X-exciton band. Temperature dependence of the probability of such an energy transfer seems likely to be determined by the neon cryocrystal phonon spectrum and the shape of the high-energy wing of the band in the region close to 19.8 eV.[10]

The above mechanism of production of the Ne $2p^5 3s$ centers, which explains their existence as being the result of trapping the metastable He 2^3S_1 atoms in the growing neon cryocrystal, enables an explanation of the additional edge-side lines separated by ΔH_1 and ΔH_2 from the central line in the EPR spectrum of the $2p^5 3s$ centers shown in Fig. 10. The origin of these lines is presumably similar to that of the weak side lines centered around the central line at the distances δH_1 and δH_2, which has already been discussed in Sec. 3.2. Each of these pairs of lines possibly results from the action of an axially symmetric anisotropic crystalline electric field on the $2p^5 3s$ atomic-type center, which is due

to the outward shift, the distortion and the rearrangement of the $2p^5 3s$-center nearest surroundings in the neon cryocrystal. When a $^3P_2$ neon atom is trapped in the neon cryocrystal directly from the neon discharge, as it has a large radius, it causes the neighboring matrix atoms to shift outwards, thus producing a rearrangement of its nearest surroundings. This is the reason why the axial field occurs, which gives rise to the weak side lines displaced from the central line by δH_1 and δH_2. On the other hand, when metastable He atoms are trapped in the neon cryocrystal there may be additional deformation of the Ne lattice in the vicinity of the $2p^5 3s$ atomic-type state which are produced according to the mechanism described earlier in this section. This deformation can be provided by the energy produced during the X-exciton self-trapping and by the fact that the radius of the $2p^5 3p$-state, which is intermediate in the process of $2p^5 3s$-state formation in neon cryocrystal, is even larger than that of the $^3P_2$ Ne atom. This additional lattice deformation occurring around some of the local excitations formed gives rise to new paramagnetic $2p^5 3s$-centers yielding the strong edge-side lines centered around the central line at the distances ΔH_1 and ΔH_2 from this (Fig. 10).

3.4. Internal ionization of Ar and Kr rare-gas cryocrystals by the excitation energy of trapped metastable excited He atoms

All energy levels of Ar and Kr atoms lie far below the lowest excited He level. Therefore, the excitation energy cannot be transferred from the trapped metastable excited He atom to the exciton bands of Ar and Kr cryocrystals through either resonance or quasi-resonance processes which is the case for the Ne cryocrystal, as described in the previous section.

In the present section, detection and investigation are reported of a new phenomenon: internal ionization of the rare-gas cryocrystals (Ar and Kr) by He gas discharge excited products (the metastable 2^3S_1 and 2^1S_0 He atoms) trapped in the growing cryocrystals followed by the formation in these cryocrystals of the local metastable excited $np^5(n+1)s$ atomic-type states.

The experimental set-up used here is shown in Fig. 1. The matrix gas (Ar, Kr) flow passes through a separate inlet tube *7–8* (channel B) avoiding the gas discharge and is cooled to liquid-nitrogen temperature. The high-frequency (14 MHz) strong continuous He gas discharge in channel A is used.

Figures 11 and 12 show the EPR spectra of the growing argon and krypton cryocrystals trapping He gas discharge products. These spectra were observed only during the Ar or Kr gas condensation and disappeared at the instant when the He discharge was turned off. On the other hand, no EPR spectra were observed in experiments where He flow was passed through the tube *5* with the radio-frequency discharge running but with no Ar or Kr gas being fed onto the substrate through the inlet tube. It was found that the He gas discharge used cannot provide any EPR spectra before the Ar (Kr) condensation as well as after the Ar (Kr) flow is turned off despite a solid Ar (Kr) layer condensed on the substrate *2* in

FIG. 11. EPR signals of unstable paramagnetic centers, which arise as the He gas-discharge products are trapped in a growing Ar cryocrystal. The spectrometer gains for the low- and high-temperature signals are the same. Both lines have g-factors of 1.99986(12).

a long time run. This is also true of the experiments with He gas discharge and Ne cryocrystals which are described in Sec. 3.3. These results are strong demonstration that the unstable centers observed in Refs. 7–12 cannot be due to the action of the light from the gas discharge on the rare gas cryocrystals.

The fact that the lines of the spectra recorded here are clearly those of the pure Ar and Kr spectra (Figs. 5a and 6a) means that the present spectra and the pure-gas spectra are due to centers of the same type and permits one to give an explanation of the nature of the present centers in the same way as has been done previously (Sec. 3.2). Namely, the centers observed here can be interpreted as being metastable excited $np^5(n+1)s$ atomic-type states which become localized in a face-centered cubic Ar (Kr) crystal lattice, shift the nearest matrix atoms outwards, rearrange their surroundings and are subject to the action of the anisotropic electric field of this environment which, being rearranged, is no longer of cubic symmetry.
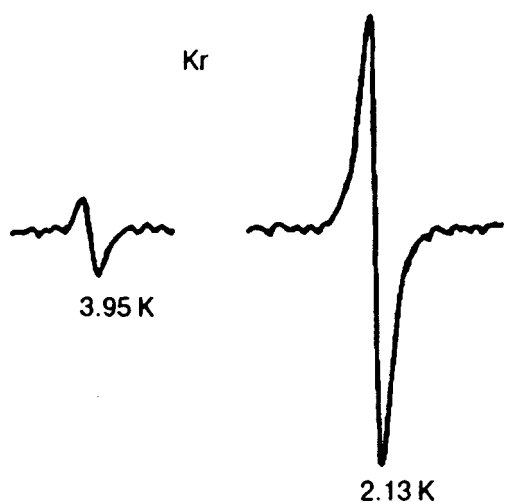
FIG. 12. EPR signals of unstable paramagnetic centers, which arise as the He gas-discharge products are trapped in a growing Kr cryocrystal. The spectrometer gains for the low- and high-temperature signals are the same. Both lines have g-factors of 1.99986(12).

After the discovery in Ar and Kr cryocrystals of the EPR spectra presented in Figs. 11 and 12 which appear as He gas discharge products are trapped in the growing cryocrystals, the dependence of the production probability of the local excited $np^5(n+1)s$ atomic-type state in the cryocrystals on the sample-temperature has been studied. Toward this goal, the signal intensity of the above spectra was measured as a function of the substrate temperature.

Shown in Fig. 9 are the temperature dependences of the EPR line intensities that are typical of Ar (line *3*) and Kr (line *4*) cryocrystals. The EPR lines are like that depicted in Figs. 11 and 12. The EPR signal intensities are measured in $A(T)/A(T_0)$ units, where, for the Ar and Kr cryocrystals, T_0 is the lowest temperature point at which the sample is still sufficiently stable. This gives the measure of the lowest possible temperature T_0 which somewhat changes from run to run.[11,12]

It is evident from Fig. 9 that the temperature dependence of the EPR signal intensity, i.e., the temperature dependence of the production probability of the atomic-type $np^5(n+1)s$ excitations in Ar and Kr cryocrystals, can be well fitted by a linear function $A(T)/A(T_0) = -a(T-T_0)+b$. The experiments carried out show the line slope, or the magnitude of a, to vary within narrow limits comparable, presumably, to those of experimental error. A set of six experiments with Ar yields $a(Ar)$ changing from 0.33 to 0.44, an average quantity being $a(Ar) = 0.39$, while three Kr runs give $a = 0.31-0.57$ and $a(Kr) = 0.46$. In these experiments, b ranges between 1.66–1.93, for Ar ($b(Ar) = 1.78$), and between 1.82–2.38, for Kr ($b(Kr) = 2.11$). If one considers the trapping of metastable He 2^3S_1 atoms in neon cryocrystals (see Sec. 3), the temperature dependence has been shown to be exponential ("Arrhenius-like") $A(T)/A(T_1) = \exp \times[-(E/k)(1/T - 1/T_1)]$, where $E = 12(6)$ K $= 0.0010(5)$ eV.

Thus, the temperature dependences of the $np^5(n+1)s$ center production probability are closely related for the Ar

and Kr cryocrystals while quite distinct from that of the Ne cryocrystal both in the trend and shape.

Examining experimental results outlined, the following mechanism of formation of the metastable $np^5(n+1)s$ states in the growing Ar and Kr cryocrystals subjected to the action of He discharge products can be proposed.

There is no question the metastable He 2^3S_1 and 2^1S_0 atoms, in the present study, are trapped in great numbers in the growing Ar and Kr cryocrystals, for the trapping process goes on in these cryocrystals as it evidently does in Ne (Sec. 3.3). Excitation energies of the metastable He atoms $E(2^3S_1) = 19.82$ eV and $E(2^1S_0) = 20.62$ eV are considerably larger than the energy gaps of the Ar and Kr cryocrystals: $E_g(Ar) = 14.16$ eV and $E_g(Kr) = 11.61$ eV (Ref. 1, p. 27). Therefore, the trapped metastable He 2^3S_1 and 2^1S_0 atoms transfer their excitation energies to the Ar or Kr cryocrystal to produce an internal ionization of this cryocrystal when a hole, i.e., Ar^+ or Kr^+ ion, arises in the valence band while a free electron e appears in the conduction band. It is known[1] that in the rare gas cryocrystals the holes become self-trapped in a very short time ($10^{-12}-10^{-13}$ s) after their production to give rise to the molecular ions: $Rg^+ + Rg \rightarrow Rg_2^+$. Occupying first a vibrationally excited level, the molecular ion relaxes to the lowest vibrational levels transferring its energy to the phonon spectrum of the cryocrystal. At some time a free electron in the conduction band encounters a hole to recombine with it and produce an excited Rg_2^{**} molecule which may, on occasion, dissociate, yielding an excited atom: $Rg_2^+ + e \rightarrow Rg_2^{**} \rightarrow Rg^* + Rg$. The process is known to occur both in the rare gases and in their cryocrystals.[1] This reaction of dissociative recombination may be one way to produce ultimately the metastable excited $^3P_2$ atomic-type states in Ar and Kr cryocrystals observed in the present study.[11,12]

A plausible mechanism of production, in Ar and Kr cryocrystals, of the excited $np^5(n+1)s$ states observed is discussed below in greater detail.

The process of formation of the $3p^54s$ states in Ar cryocrystals, having trapped the metastable He 2^3S_1 and 2^1S_0 atoms from the helium gas discharge, can be conceived of as follows.[11,12]

The trapped He 2^3S_1 and 2^1S_0 atoms transfer their excitation energies to the Ar cryocrystal, with the above-mentioned internal ionization of the cryocrystal, as a consequence, this results in the formation of a free electron in the conduction band and a hole Ar^+ in the valence band; the hole becomes rapidly self-trapped (in a time of $10^{-12}-10^{-13}$ s), i.e., turns to the vibrationally excited molecular Ar_2^+ ion. Provided that, after a short time, a free electron moving in the conduction band encounters and recombines with an Ar_2^+ hole that has had no time to relax vibrationally, the reaction of dissociative recombination is possible: $Ar_2^+ + e \rightarrow Ar_2^{**} \rightarrow Ar + Ar^*(3p^54p)$. The reaction is followed by the excited atom decay $Ar^*(3p^54p) \rightarrow Ar^*(3p^54s)$ to form the $3p^54s$ $^3P_2$ state observed by EPR. This is likely to be a mechanism of formation, in Ar cryocrystals, of the metastable excited $3p^54s$ atomic-type states as the excitation energy is being transferred from the metastable He atoms to the cryocrystal.

Suppose that the time a free electron moving in the conduction band takes to approach an Ar_2^+ molecular ion is sufficiently long that the ion has relaxed to the lowest vibrational state. Then the energy released during the $Ar_2^+ + e$ recombination is allowed to transfer to the exciton band with $n = 1$.[11,12] This exciton then can either decay to the ground state or become self-trapped to the two-center excimer state, Ar_2^*, which also decays to two ground-state Ar atoms. These processes cannot lead to the formation of the atomic-type $3p^5 4s$ state. That is why the process of production of the atomic-type $3p^5 4s$ state through the recombination of the vibrationally relaxed Ar_2^+ molecular ion should be far less probable than the dissociative recombination of the vibrationally excited Ar_2^+ ion. Which of the two processes occurs in a particular experiment depends on the growing cryocrystal temperature. With increasing sample temperature the vibrational relaxation rate of the Ar_2^+ molecular ion rises, whereas the mobility of electrons in the conduction band grows smaller leading to an increase with sample temperature in the time separation between the Ar_2^+ ion production and its recombination with an electron. All these reasons have the effect of reducing the probability of the dissociative recombination and consequently the yield of $3p^5 4s$ centers, which underlies the temperature dependence found for Ar (Fig. 9). The probability of the excitation energy transfer to the exciton band with $n = 1$ followed by decay to two ground-state Ar atoms increases with increasing sample temperature.

In the Kr cryocrystal, the processes must be somewhat different from those described above for Ar.[11,12] Metastable He atoms trapped in the growing Kr cryocrystal will also perform the internal ionization of the cryocrystal to produce in a short time ($10^{-12} - 10^{-13}$ s) a vibrationally excited self-trapped hole, Kr_2^+, and a free electron in the conduction band. At low temperatures when a molecular ion Kr_2^+ recombining with an electron should be vibrationally excited, the most likely mechanism of the energy loss is that through the excitation energy transfer to the exciton band with $n = 1$, $\Gamma(1/2)$ followed by the self-trapping to the $4p^5 5s$ state and production of the excited $^3P_2$ state detected in the experiment by EPR. The energy gap between $\Gamma(1/2)$ and $\Gamma(3/2)$ subbands of the exciton with $n = 1$ must hamper nonradiative transitions from the first subband to second in the process.[11,12] It seems possible that the dissociative recombination, $Kr_2^+ + e \rightarrow Kr_2^{**} \rightarrow Kr + Kr^*(4p^5 5s)$, can also contribute to the observed signal, giving metastable $4p^5 5s$ state. As the sample temperature increases, the vibrational relaxation of the Kr_2^+ molecular ion speeds up while the movement of electrons in the conduction band slows down. This brings about the recombination, $Kr_2^+ + e$, in which case the excitation energy is likely to be transferred to the exciton band with $n = 1$, $\Gamma(3/2)$ with subsequent decay to the ground state either immediately from the subband with $n = 1$, $\Gamma(3/2)$ or through the self-trapped excimer Kr_2^+ state. This will lead to a decrease in the yield of the metastable excited $^3P_2$ states as the cryocrystal temperature increases. The processes discussed above are responsible for the fall in the $4p^5 5s$ center yield in the Kr cryocrystal with increasing temperature. It is of interest that the temperature dependences of the

probability of the $np^5(n+1)s$ center formation for Ar and Kr cryocrystals are similar in appearance (Fig. 9), notwithstanding certain distinctions between mechanisms of production of these metastable atomic-type centers.

Thus, the metastable excited He atoms, He $(2^3 S_1)$ and He $(2^1 S_0)$, from the He gas discharge become trapped in the growing Ar or Kr cryocrystals and transfer their excitation energy to the cryocrystal to form, in the process of internal ionization, a Rg^+ ion and a free electron in the conduction band, whereupon the fast (of 10^{-12} s) self-trapping reaction of a hole follows: $Rg^+ + Rg \rightarrow Rg_2^+$. Thereafter either the dissociative recombination reaction $Rg_2^+ + e \rightarrow Rg_2^{**} \rightarrow Rg + Rg[np^5(n+1)s]$ or recombination $Rg_2^+ + e \rightarrow Rg + Rg$ to produce ground-state atoms could take place. The former is likely at lower temperatures while the latter—at higher temperatures when the vibrational relaxation rate of the Rg^+ molecular ion increases and the mobility of free electrons in the conduction band decreases. This is the reason for the observed temperature dependence.[11,12]

3.5. Additional check experiments

This section considers the possibility that the unstable centers in rare gas cryocrystals observed and discussed in Refs. 7–12 can be due to any atomic or molecular paramagnetic impurity ions matrix isolated in the cryocrystals. Uncharged impurity atoms and molecules should be excluded at once from consideration, since they are known to give only stable paramagnetic centers in the matrices of solid rare gases, as was shown in many works (for example, on H, D and N atoms[19,20]). At the same time, matrix-isolated ions may in principle give rise to unstable paramagnetic centers with limited lifetime τ, since the ions may be suggested to recombine, after a time lapse of τ, with free electrons existing in the matrix to form uncharged diamagnetic particles. However, both ions and electrons were demonstrated above to be unable, in the described experiments, to travel from the gas discharge onto the growing cryocrystal, because they are locked in the discharge zone with the magnetic field of the EPR spectrometer $H = 3300$ G forcing them to follow small-radius trajectories (thus, for O^+ ion the orbit radius is under 0.1 mm).

At the same time, uncharged atoms and molecules presented as natural impurities in the rare gas discharge can reach the substrate and trap within the growing cryocrystal. Thus, the processes may be imagined to occur as follows: uncharged impurity atoms or molecules passing onto the growing cryocrystal are subject to ionization, near the surface or in the near-surface layer, by VUV radiation from the gas discharge, whereupon these ions, along with electrons, are trapped in the cryocrystal to give rise to the observed EPR spectra following which the recombination, after a time lapse of τ, of the ions with trapped electrons takes place with the result that uncharged diamagnetic particles appear; this might provide a nonstability of the observed EPR spectra. The present section is concerned with experiments examining if the above mechanism might be responsible for the EPR unstable signals observed in the rare gas cryocrystals.

It should be noted first that, if the matrix-isolated para-

magnetic ions which after a certain time become uncharged and diamagnetic through recombination with electrons make the unstable centers observed, then the EPR signals they yield cannot disappear completely once the discharge is turned off but at least a portion of the signal must remain and be stable. The reason is that a rare gas cryocrystal being condensed contains enough abundance of electron traps like impurity molecules and atoms, and lattice defects. These traps bind electrons to inhibit them from recombining with ions, so the later become stable matrix-isolated paramagnetic particles in the cryocrystal and yield stable EPR spectra. However, in all experiments, all lines of unstable paramagnetic EPR spectra under study disappear completely after the discharge is turned off. This testifies against the hypotheses about the impurity paramagnetic ions.

As a final check on the suggestion that unstable EPR spectra observed are due to impurity paramagnetic ions specialized experiments were run. In these experiments, the growing rare gas cryocrystal which trapped gas discharge products was added with great deal of effective electron traps which were to result in large numbers of completely stable ions, thereby stabilizing the observed signals which had been quite unstable until then. As an acceptor to create effective electron traps, the oxygen was chosen because of the great electron affinity of both the molecule and the atom: $E_a(O_2) = 0.440(8)$ eV, $E_a(O) = 1.465$ eV.[21] A deposited cryocrystal of a rare gas has been demonstrated[22] to contain practically always a sufficient number of electron traps, the natural O_2 impurity (in small amounts) among them, to stabilize completely a variety of matrix-isolated ions. However, in certain cases[23] an amount of Cl_2 with the electron affinity of $E_a(Cl_2) = 2.38$ eV was added to the matrix as an electron acceptor to enhance the number of stabilized ions in the rare gas cryocrystals. In the first stage of the check study being discussed in the present section, gaseous O_2 was added to the pure Ne or Ar passed through the channel A (channel B was shut). The EPR unstable signals such as those depicted in Fig. 2, which are characteristic for the pure Ne and Ar, were detected; these signals disappeared completely once the gas discharge was turned off, i.e., no evidence of stable EPR spectra was observed. The addition of oxygen in the gas discharge resulted only in decreased signal amplitude. Based on the interpretation discussed in Sec. 3.3, this could be explained by the de-excitation of the rare gas $^3P_2$ atoms at collisions with O_2 molecules in the gas discharge, which would tend to the Penning ionization of the molecules. It should be noted that O^+ ions are particularly promising when trying to provide an explanation for the observed unstable signals as being matrix-isolated paramagnetic ions which subsequently recombine with electrons. First, O atoms, like the stable matrix-isolated N atoms which are characteristically easy to observe in the EPR spectra, are undoubtedly present in the gas discharge and, to be sure, are also trapped and matrix-isolated in the cryocrystal (though the observation of their EPR spectra have not been successful). Yet, only the Ne gas discharge provides VUV photons with the energy high enough (16.8 eV) to ionize oxygen atoms ($E_i = 13.6$ eV) near the cryocrystal surface while, in the case of Ar, Kr and Xe, the gas discharge produces
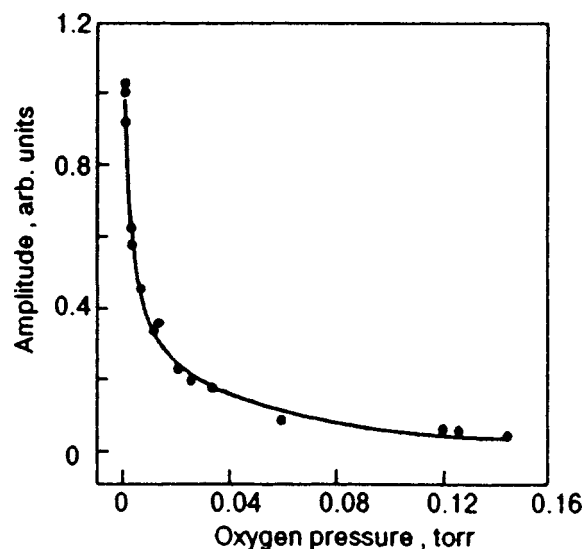

FIG. 13. EPR signal amplitude of the unstable paramagnetic centers in a neon cryocrystal as a function of the oxygen pressure in the channel B (Fig. 1) through which the additional O_2 flow is fed to the substrate *2*.

photons of too low energy (11.7 eV, 10.6 eV and 9.6 eV, respectively) to do this. Second, O^+ ion is promising again in this consideration because of its $2s^2 2p^3\ ^4S_{3/2}$ state, as is the case for the nitrogen atom also, which provides $g = 2.0$ for the free O^+ ion even without the action of the crystal field. However, in the considered experiments, the addition of O_2 to the gas discharge did not resulted in both stabilization and rise of the observed spectra in Ne and Kr.

In subsequent experiments, the gaseous O_2 was added through the channel B (Fig. 1) so that it had no action on the gas discharge, whereas only pure rare gas (Ne or Ar) was passed through the channel A and gas discharge. Shown in Fig. 13 is the amplitude of the pure Ne central line (Fig. 2) plotted against the O_2 pressure in the channel B (Fig. 1). From this figure it is noticed that here, too, the unstable signals show no increase in amplitude on addition of oxygen into the growing Ne cryocrystal, by passing the gas discharge, as might be hoped for, but a rapid decline. This influence of O_2 is fully reversible—as the oxygen flow rate through the channel B decreases, the EPR signal grows in amplitude, following the same curve as in Fig. 13, and, thus, regains its initial value completely as the oxygen flow comes to an end.

Figure 14, spectrum a, shows the central signal (see Fig. 2), the oxygen flow being cut off, recorded after a four-hours run in which the oxygen has been introduced into the growing neon cryocrystal through the channel B and dependences like that depicted in Fig. 13 have been taken. As this took place, the maximum O_2 flow rate onto the substrate *2* through the channel *B* was something of an order of magnitude greater than the flow rate onto the substrate of the rare gas through the channel A. The signal amplitude in Fig. 14, spectrum a, returned to that of the pure Ne at the onset of experiment, before O_2 was let in. Also seen in Fig. 14, spectrum a, are three lines of the $N(^4S_{3/2})$ spectrum which are due to uncontrollable small amounts of nitrogen in the gas discharge. Such spectra of the N-atoms matrix-isolated in a
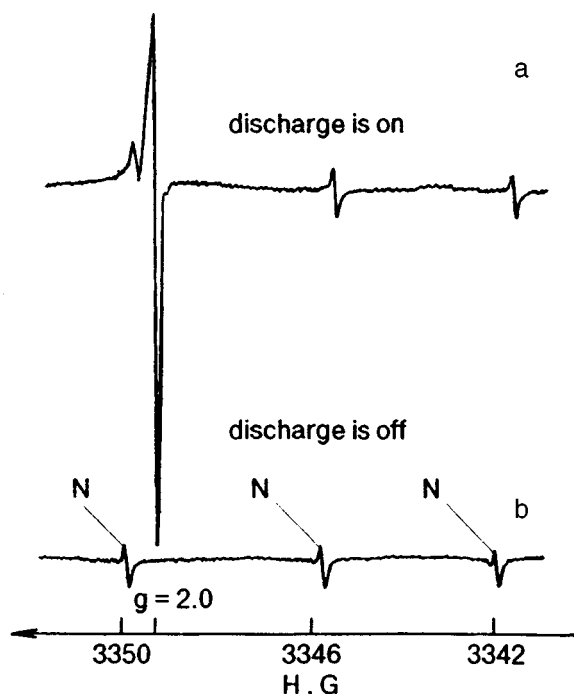
FIG. 14. EPR spectra of a neon cryocrystal recorded after a four-hours run in which the gaseous neon was passed through the gas discharge, channel A (Fig. 1), while the additional oxygen was fed through the channel B with the flow rate changing during the run. Record a—EPR spectrum taken as the neon discharge in the channel A runs and the oxygen flow in the channel B is cut off; record b—EPR spectrum recorded just after the spectrum a was taken and the discharge in channel A turned off. The unstable signal with $g = 2.0$ disappears completely, while the week signals of N-atoms trapped in the neon cryocrystal remain unchanged, which relates to the well known stability of the spectrum of nitrogen atoms matrix-isolated in Ne.

neon cryocrystal have been observed earlier.[20] The spectrum b in Fig. 14 was taken just after the discharge was turned off. It is evident from the figure that the signal like that depicted in Fig. 2 disappears completely after the discharge is turned off, i.e., remains fully unstable after such a prolonged experiment, in spite of great quantity of effective electron traps such as O_2 molecules in the cryocrystal. This permits one to rule out totally the suggestion that the unstable paramagnetic centers which were observed in rare gas cryocrystals present matrix-isolated ions, whatever they may be. In Fig. 14, spectrum b, the lines of the matrix-isolated N atoms which are kept constant testifies to reliability of this inference.

Mention may be made that, in the present study, the possibility of the observed spectra owing to matrix-isolated positive ions (cations) is investigated. With negative ions (anions), they should, once matrix-isolated, yield stable EPR signals much as uncharged paramagnetic particles do, since these fixed negative ions cannot recombine in a low temperature matrix.

4. CONCLUSION

Thus, the arguments of Sec. 3.2, the addition check experiments wherein an electron acceptor O_2 was admitted, and the temperature investigations (Fig. 9) essentially exclude all sorts of alternative explanations of the unstable paramagnetic centers observed in the rare gas cryocrystals Ne, Ar, Kr, and

Xe that are subject to action of the products of gas discharge in either these gases or He trapped in the growing cryocrystal. Consequently, it is proved that the unstable paramagnetic centers observed by EPR present the metastable excited $np^5(n+1)s$ atomic-type states which are localized in the cryocrystal, deform and rearrange their nearest surroundings, and are subject to the action of the anisotropic electric field caused by these deformed surroundings.

Figure 9 (lines *1* and *2*), shows a surprising phenomenon: completely dissimilar temperature dependences for the equilibrium concentration of the same centers in the same substance. The only explanation is that the unstable centers of the same nature and in the same substance are in fact formed in various ways. The reasonable and compatible explanation for this complicated effect which is given above (Secs. 3.2, 3.3, and 3.4) is a weighty argument in support of correctness of this explanation. Distinction between temperature dependences for the same centers allows one to exclude also the possibility that they are some radiation-induced paramagnetic centers formed in the quartz substrate under the action of the gas discharge radiation. In that case, one could not explain the observed distinction between temperature dependences. The fact that the centers disappear once the Ne, Ar or Kr flow through the channel B is cut off (see Secs. 3.3 and 3.4), whereas the substrate is still exposed to the He gas discharge radiation, is also a strong evidence against this suggestion.

Special experiments were also carried out, using the set-up depicted in Fig. 1, to try to discover unstable EPR spectra close to $g = 2$ (like that described above) in pure H_2 and N_2 cryocrystals trapping products of the gas discharge in the same gases, H_2 or N_2. No unstable EPR spectra close to $g = 2$ were detected in these pure cryocrystals in the runs. This is a further evidence for the above interpretation of the nature of the unstable paramagnetic centers in the rare gas cryocrystals which were observed.

*)E-mail: zhitnikv@mares.ioffe.rssi.ru

[1] N. Schwentner, E. E. Koch, and J. Jortner, *Electronic Excitations in Condensed Rare Gases*, Springer-Verlag, Berlin-Heidelberg (1985).
[2] M. Ueta, H. Kanzaki, K. Kobayashi, Y. Toyozawa, and E. Hanamura, *Excitonic Processes in Solids*, Springer-Verlag, Berlin-Heidelberg (1986).
[3] K. S. Song and R. T. Williams, *Self-Trapped Excitons*, Springer-Verlag, Berlin-Heidelberg (1996).
[4] E. I. Rashba, in *Excitons*, E. I. Rashba and M. D. Struge (Eds.), North-Holland, Amsterdam (1982), p. 543.
[5] E. V. Savchenko and I. Ya. Fugol', in *Cryocrystals*, B. I. Verkin and A. F. Prihot'ko (Eds.), Naukova Dumka, Kiev (1983) (in Russian), p. 360.
[6] G. Zimmerer, in *Excited State Spectroscopy in Solids*, U. M. Grassano and N. Terzi (Eds.), North-Holland, Amsterdam (1987), p. 37.
[7] R. A. Zhitnikov, Yu. A. Dmitriev, and M. E. Kaimakov, Sov. Phys. JETP **22**, 1009 (1991).
[8] R. A. Zhitnikov, Yu. A. Dmitriev, and M. E. Kaimakov, Fiz. Nizk. Temp **18**, 751 (1992) [Sov. J. Low Temp. Phys. **18**, 532 (1992)].
[9] R. A. Zhitnikov and Yu. A. Dmitriev, Fiz. Nizk. Temp. **19**, 612 (1993) [Low Temp. Phys. **19**, 437 (1993)].
[10] R. A. Zhitnikov and Yu. A. Dmitriev, J. Phys.: Condens. Matter **6**, 2727 (1994).
[11] R. A. Zhitnikov and Yu. A. Dmitriev, J. Phys.: Condens. Matter **7**, 2819 (1995).
[12] R. A. Zhitnikov and Yu. A. Dmitriev, Appl. Magn. Reson. **8**, 457 (1995).

[13] A. A. Radtsig and B. M. Smirnov, *Reference Data on Atoms, Molecules, and Ions*, Springer-Verlag, Berlin, 1985.

[14] T. Suemoto and H. Kanzaki, J. Phys. Soc. Jpn. **46**, 1554 (1979).

[15] J. E. Wertz and J. R. Bolton, *Electron Spin Resonance. Elementary Theory and Practical Applications*, McGraw-Hill, New York (1972).

[16] F. V. Kusmartsev and E. I. Rashba, Czech. J. Phys. **B32**, 54 (1982).

[17] Chun-rang Fu and K. S. Song, J. Phys.: Condens. Matter **9**, 9785 (1997).

[18] F. V. Kusmartsev and E. I. Rashba, Zh. Éksp. Teor. Fiz. **86**, 1142 (1984) [Sov. Phys. JETP **59**, 668 (1984)].

[19] R. A. Zhitnikov and Yu. A. Dmitriev, Zh. Éksp. Teor. Fiz. **92**, 1913 (1987) [Sov. Phys. JETP **65**, 1075 (1987)].

[20] Yu. A. Dmitriev and R. A. Zhitnikov, Zh. Tekhn. Fiz. **57**, 1811 (1987) [Sov. Phys. Tech. Phys. **32**, 1082 (1987)].

[21] A. A. Radtsig and B. M. Smirnov, *Reference Data on Atoms, Molecules, and Ions*, Springer, Berlin, 1985.

[22] L. B. Knight, Jr. and J. Steadman, J. Chem. Phys. **77**, 1750 (1982).

[23] L. B. Knight, Jr. and J. Steadman, J. Chem. Phys. **78**, 5940 (1983).

QUANTUM LIQUIDS AND QUANTUM CRYSTALS

Kinetics of diffusion mode in a phonon–impuriton system of ^{3}He–^{4}He mixtures of quantum liquids

K. È. Nemchenko

*Kharkov State University, 310077 Kharkov, Ukraine**
(Submitted May 29, 1998)
Fiz. Nizk. Temp. **24**, 941–945 (October 1998)

Relaxation processes in a phonon–impuriton systems of superfluid ^{3}He–^{4}He mixtures are studied on the basis of the system of kinetic equations. The obtained general energy–momentum relations are valid for any ratio of the times of phonon–impuriton interaction to the times of equilibrium stabilization in the phonon and impuriton subsystems. In the hydrodynamic and kinetic modes of phonon rates, the effective diffusion coefficient for the dissipative mode as well as the velocity and attenuation of sound in the acoustic mode are calculated. © *1998 American Institute of Physics.* [S1063-777X(98)00210-2]

Fundamentals of the kinetic theory of superfluid ^{3}He–^{4}He mixtures were formulated by Khalatnikov and Zharkov.[1] Subsequent investigations[2–7] formed the basis for a comprehensive theory of propagation of first and second sounds and dissipative processes in the entire temperature range in which a quasiparticle description of these quantum solutions is valid. However, superfluid ^{3}He–^{4}He mixtures display a dissipative (diffusion) mode along with acoustic mechanisms of relaxation of hydrodynamic parameters.[8,9] This mode mainly describes relaxation of temperature and ^{3}He concentration and is a unique mode of quantum mixtures of helium isotopes. This mode was studied in Refs. 8 and 9 under hydrodynamic conditions at relatively high temperatures by using hydrodynamic equations for superfluid mixtures.[10] In our earlier publication,[11] we analyzed the dissipative mode on the basis of the kinetic equation for a gas of impuriton in the hydrodynamic approximation at ultralow temperatures, when the contribution from thermal excitations can be neglected.

In the present communication, we shall analyze the diffusion mode in superfluid ^{3}He–^{4}He mixtures by taking into account impurity quasiparticles and thermal excitations of HeII in a wide temperature range, in which the kinetic mode can be observed in the system of thermal excitations along with the hydrodynamic mode.

An analysis of dissipative processes in the system of quasiparticles in superfluid ^{3}He–^{4}He mixtures will be carried out on the basis of kinetic equations for the quasiparticle distribution function f_α ($\alpha = 3,4$):

$$\frac{\partial f_3}{\partial t} + (\mathbf{v}_3 \cdot \nabla) f_3 = J_{33}(f_3) + J_{34}(f_3, f_4),$$

$$\frac{\partial f_4}{\partial t} + (\mathbf{v}_4 \cdot \nabla) f_4 = J_{44}(f_4) + J_{43}(f_4, f_3). \tag{1}$$

Here f_3 and f_4 are the distribution functions of quasiparticles in ^{3}He and thermal excitations in HeII, respectively,

$\mathbf{v}_3 = \partial \varepsilon_3 / \partial \mathbf{p}_3$, $\mathbf{v}_4 = \partial \varepsilon_4 / \partial \mathbf{p}_4$ the corresponding velocities, and $J_{\alpha\beta}$ ($\alpha, \beta = 3,4$) the collision integrals. The ratio of the total density $\rho_n = \rho_{3n} + \rho_{4n}$ of the normal component to the density ρ_4 of ^{4}He in the mixture is assumed to be small in Eqs. (1), so that the superfluid background can be treated as in equilibrium. We linearize Eqs. (1) in the small deviation δf_α of distribution functions from the equilibrium state, i.e.,

$$f_\alpha = f_{0\alpha} + \delta f_\alpha, \quad \alpha = 3.4 \tag{2}$$

and seek the solution for δf_α in the form

$$\delta f_\alpha = -f'_{0\alpha} g_\alpha, \tag{3}$$

where $f'_{0\alpha}$ is the derivative of the function $f_{0\alpha}$ with respect to energy. As a result, we obtain from Eq. (1) the following system of equations for the Fourier components of the functions g_α:

$$(\omega - \mathbf{k} \cdot \mathbf{v}_3 - iI_{33} - iI_{34}) g_3 - iI_{34} g_4 = 0,$$

$$(\omega - \mathbf{k} \cdot \mathbf{v}_4 - iI_{44} - iI_{43}) g_4 - iI_{43} g_3 = 0, \tag{4}$$

where $I_{\alpha\beta}$ are integral collision operators. Proceeding from this system of equations, we calculate the parameters of the diffusion mode as well as the velocity and attenuation of second sound in the superfluid solutions in the hydrodynamic approximation in the rates of impuriton interactions $\omega \tau_{33} \ll 1$ and of the rapid longitudinal relaxation $\omega \tau_{44} \ll 1$ in the phonon subsystem. In this case, we assume that the times τ and τ_ζ of the phonon–impuriton interaction, which describe the momentum and energy relaxation respectively, are arbitrary. Equations (4) lead to

$$(\omega - \mathbf{k} \cdot \mathbf{v}_3 - iI_{33} - iI_{34} + I_{34} R_4 I_{43}) g_3 = 0, \tag{5}$$

$$R_4 = (\omega - \mathbf{k} \cdot \mathbf{v}_4 - iI_{44} - iI_{34})^{-1}. \tag{6}$$

The problem of determining the energy–momentum relations $\omega = \omega(k)$ satisfying Eq. (5) is equivalent to determining the poles of its resolvent

$$R_3 = \omega - \mathbf{k} \cdot \mathbf{v}_3 - iI_{33} - iI_{34} + I_{34}R_4I_{43}. \tag{7}$$

In the hydrodynamic approximation for the impuriton system, we must project (7) onto the subspace of invariants of the collision operator I_{33} and find the poles of the expression

$$P_c R_3 P_c = P_c(\omega - P_c\Omega P_c)^{-1}P_c, \tag{8}$$

$$\Omega = \mathbf{k} \cdot \mathbf{v}_3 + iI_{34} + I_{34}R_4I_{43} - i\mathbf{k} \cdot \mathbf{v}_3 P_n\mathbf{k} \cdot \mathbf{v}_3\tau_{33}. \tag{9}$$

Here we have introduced the projector operators onto the subspace of invariants of impuriton collisions, i.e.,

$$P_c = |J_N\rangle\langle J_N| + |J_{pz}\rangle\langle J_{pz}| + |J_E\rangle\langle J_E| \tag{10}$$

and onto the subspace orthogonal to it:

$$P_n = 1 - P_c. \tag{11}$$

The basis vectors $|J\rangle$ are defined as

$$|J_N\rangle = \frac{|1\rangle}{\langle 1|1\rangle^{1/2}}, \quad |J_{pz}\rangle = \frac{|p_{3z}\rangle}{\langle p_{3z}|p_{3z}\rangle^{1/2}}, \quad |J_E\rangle = \frac{|\bar{e}_3\rangle}{\langle \bar{e}_3|\bar{e}_3\rangle^{1/2}}, \tag{12}$$

where $\bar{e}_3 = e_3 - \langle e_3|1\rangle/\langle 1|1\rangle$. The vectors $|J_{px}\rangle$ and $|J_{py}\rangle$ are disregarded since the z-axis is chosen along the vector $\mathbf{k}$. The scalar product is introduced as follows:

$$\langle \Phi_3|\Psi_3\rangle = -\int \Phi_3^*(\mathbf{p}_3)\Psi_3(\mathbf{p}_3)f'_{03}d\Gamma_3. \tag{13}$$

While deriving Eq. (9), we used the correct τ-approximation[6]

$$I_{33} = -\frac{P_n}{\tau_{33}} \tag{14}$$

and assumed that the parameters $\beta = v_3^2/v_4^2, \omega\tau_{33}, \rho_{4n}/\rho_{3n}$ are small. We find the matrix of the operator R_3 in the basis $|J\rangle$. The equality of the determinant of the matrix to zero leads to the dispersion equation defining $\omega(k)$ in the form

$$\left(\frac{\omega}{k}\right)^2 = \frac{u_{2N}^2}{1+b_{11}} + \frac{u_{2E}^2(1+b_{01})^2}{(1+b_{11})(1+b_{00})}, \tag{15}$$

where

$$u_{2N}^2 = \frac{n_3}{\rho_n}\left(\frac{\partial P_f}{\partial n_3}\right)_{T,n_4}, \quad u_{2E}^2 = \frac{\bar{S}^2 T}{C_V\rho_n}, \tag{16}$$

$$b_{00} = i\frac{k^2\kappa_3}{\omega C_V} - \frac{1}{\omega C_V T}R_{11}, \tag{17}$$

$$b_{11} = i\frac{k^2\eta_3}{\omega\rho_n}\frac{4}{3} - \frac{1}{\omega\rho_n}R_{22}, \tag{18}$$

$$b_{01} = \frac{1}{k\bar{S}T}R_{12}. \tag{19}$$

Here $C_V = C_3 + C_4$, $\bar{S} = S_4 + S_3 = S_4 + (2/3)C_3$, n_α and C_α are the number of atoms of the species α per unit volume and the heat capacity of the α component of the mixture, respectively, S_4 is the entropy of thermal excitations, P_f the pressure of the impuriton gas, κ_3 and η_3 are the thermal

conductivity and first viscosity of the impuriton gas,[11] and the matrix elements of R are complex functions of thermodynamic parameters and interaction rates.

The matrix elements of R appearing in (17) are calculated according to the algorithm worked out in Ref. 6. As a result of relatively simple but cumbersome calculations, we obtain

$$R_{11} = \omega^2 C_4 T[A_{00} - 2\xi A_{01} + \xi^2 A_{11}],$$

$$R_{12} = \omega^2\sqrt{3\rho_{4n}C_4 T}[A_{01} - \xi(A_{02}+A_{11}) + \xi^2 A_{12}],$$

$$R_{22} = \omega^2 3\rho_{4n}[A_{11} - 2\xi A_{12} + \xi^2 A_{22}], \tag{20}$$

where

$$A_{0k} = Q_k\frac{i\tau}{ikv_4\tau + (1-\beta)Q_0}, \quad k = 0,1,2,$$

$$A_{11} = Q_1 X, \quad A_{12} = Q_2 X - \frac{1}{3v_4 k}, \quad A_{22} = q_0 A_{12},$$

$$A_{13} = Q_3 X,$$

$$X = \frac{i\tau q_0 + (1-\beta)/kv_4}{i\tau kv_4 + (1-\beta)Q_0},$$

the variables $\xi = kv_4/\omega$ and $q_0 = (\omega + i/\tau)/kv_4$, and the functions of angular variables are defined as

$$Q_0 = \frac{1}{2}\ln\frac{q_0+1}{q_0-1}, \quad Q_1 = q_0 Q_0, \quad Q_2 = q_0 Q_1,$$

$$Q_3 = q_0^2 Q_2 - 1/3, \quad Q_4 = q_0 Q_3.$$

Relations (15)–(20) make it possible to solve the problem of determining the energy–momentum relations for the diffusion mode as well as the second sound. In an analysis of the acoustic mode, it is sufficient to put $\omega \propto k$ in the general relations (15)–(20). The obtained equations coincide in this case with the results obtained in Ref. 6 for the propagation of second sound in the hydrodynamic, transient, and kinetic modes in the phonon–impuriton system.

In order to analyze the diffusion mode, we must introduce into expressions (15)–(20) the relations between ω and k typical of dissipative modes:[12]

$$\omega \propto -ik^2. \tag{21}$$

In the case of a purely impuriton system ($\rho_{4n} = 0$, $C_4 = 0$), relations (15)–(20) lead to the results obtained in Ref. 11:

$$\omega = -ik^2 D_3, \tag{22}$$

where

$$D_3 = \frac{\kappa_3}{C_3}\frac{u_{3N}^2}{u_3^2}, \tag{23}$$

$$u_3^2 = u_{3N}^2 + u_{3E}^2, \quad u_{3N}^2 = \frac{n_3}{\rho_{3n}}\left(\frac{\partial P_f}{\partial n_3}\right)_{T,n_4},$$

$$u_{3E}^2 = \frac{\bar{S}_3^2 T}{C_3\rho_{3n}}. \tag{24}$$

In this limit, the obtained mode corresponds to a thermal wave in normal liquids, which describes dissipative relaxation of temperature and density of particles to equilibrium.

In the opposite limiting case of complete equilibrium in a phonon–impuriton system, the general relations (15)–(20) lead to

$$\omega = -ik^2 D_{\text{eff}}. \tag{25}$$

Here

$$D_{\text{eff}} = \frac{\kappa}{C_V} \frac{u_{2N}^2}{u_2^2} + D \frac{u_{2E}^2}{u_2^2} \left(1 - \frac{k_T}{k_T^*} \right)^2, \tag{26}$$

where $\kappa = \kappa_3 + \kappa_4$ is the total thermal conductivity of the gas of quasiparticles, D the diffusion coefficient of the mixture, $k_T^* = n_3 / c\bar{S}$, and k_T is the thermal-diffusion ratio for the mixture. Relations (25) and (26) are valid in the entire temperature range to which the quasiparticle description is applicable, and correspond to the results obtained in Refs. 8, 9 from an analysis of the complete phenomenological system of hydrodynamic equations. It should be noted that D_{eff} also defines the effective thermal conductivity of mixtures in non-equilibrium steady states, i.e.,

$$\kappa_{\text{eff}} = \kappa + D \frac{u_{2E}^2}{u_{2N}^2} C_V \left(1 - \frac{k_T}{k_T^*} \right)^2 \tag{27}$$

and coincides with the expression presented in Ref. 10.

The general expressions (15)–(20) derived above also make it possible to study the kinetic mode in a system of quasiparticles, which is intermediate between the limits (22) and (25). In this case, we assume that the phonon rates satisfy the relations $\omega\tau \gg 1$, $\omega\tau_\zeta \gg 1$, $\rho_{3n} \gg \rho_{4n}$. and relations (15)–(20) give

$$\omega = -ik^2 D_3 - i \frac{1}{\tau_k}, \tag{28}$$

where

$$\frac{1}{\tau_k} = \frac{C_4}{C_3} \frac{u_{3N}^2}{u_3^2} \frac{2}{\tau_\zeta}. \tag{29}$$

The last term in (28) does not depend on the wave vector and is inversely proportional to the time of relaxation of phonon–impuriton collisions. This corresponds to relaxation in the system due to direct absorption of phonons by the impuriton system and is similar to the mechanism described by Adamenko and Tsyganok[4] for a phonon–roton system. If the phonon mean free path is much larger than the characteristic sizes of the problem, the relaxation in the dissipative mode is determined only by the impuriton subsystem, and relation (28) is transformed into (22).

In order to study relaxation processes in the kinetic mode, we consider the relaxation of the initial δ-shaped deviation of any hydrodynamic parameter $\varphi = \varphi(z,t)$ (this can

be either the temperature or the concentration of ^{3}He) associated with the mode (28):

$$\varphi(z,t) = \frac{1}{\sqrt{4\pi D_3 t}} \exp\left(-\frac{z^2}{4D_3 t} \right) \exp\left(-\frac{t}{\tau_k} \right)$$

$$\equiv \varphi_D(z,t) \exp\left(-\frac{t}{\tau_k} \right), \tag{30}$$

where the function $\varphi_D(z,t)$ describes hydrodynamic diffusion relaxation. In the case of purely diffusive motion,[13] the total deviation of the relaxing quantity from its equilibrium value in the entire volume is independent of time:

$$S_D(t) = \int_{-\infty}^{+\infty} \varphi_D(z,t) dz = 1. \tag{31}$$

Processes of direct absorption lead to an additional and probably stronger relaxation, and the quantity $S_D(t)$ is not conserved in this case. Thus, these processes can play a significant role in the relaxation of temperature and concentration in superfluid ^{3}He–^{4}He mixtures with small inhomogeneities of the system.

Such a situation arises during stratification of metastable supersaturated ^{3}He-^{4}He mixtures when small nuclei of a new phase are formed at the initial stages of separation.[14] The growth of a nucleus should be described by using formulas (28) and (29) for the kinetic mode as well as the general expressions (15)–(20) which are valid for an arbitrary relation between the phonon mean free path and the characteristic sizes of inhomogeneities in superfluid ^{3}He–^{4}He mixtures. Among other things, calculations based on formula (28) proved that at $T = 0.2$ K, phonons determine the growth of only large drops having a size larger than 600 μm. However, the contribution of phonons must be taken into account even at $T = 0.3$ K in the description of the growth of much smaller nuclei of diameter 80 μm.

Thus, we have obtained general energy–momentum relations (15)–(20) which are valid for arbitrary ratios of the times τ, τ_ζ of phonon–impuriton interaction to the times of equilibrium stabilization in the phonon and impuriton subsystems. The effective diffusion coefficient of the dissipative mode is calculated in the hydrodynamic, transient, and kinetic modes relative to phonon rates [relations (26), (28), and (22), respectively], and the velocity and attenuation of sound in the acoustic mode are determined.

*E-mail: nemchenko@rocketmail.com

[1] I. M. Khalatnikov and V. N. Zharkov, Zh. Éksp. Teor. Fiz. **32**, 1108 (1957) [Sov. Phys. JETP **5**, 905 (1957)].

[2] G. Baym and C. Ebner, Phys. Rev. **164**, 235 (1967).

[3] I. N. Adamenko, È. Ya. Rudavskiĭ, V. I. Tsyganok, and V. K. Chagovets, Pis'ma Zh. Éksp. Teor. Fiz. **39**, 404 (1984) [JETP Lett. **33**, 487 (1984)].

[4] I. N. Adamenko and V. I. Tsyganok, Zh. Éksp. Teor. Fiz. **87**, 865 (1984) [Sov. Phys. JETP **60**, 491 (1984)].

[5] I. N. Adamenko and V. I. Tsyganok, Zh. Éksp. Teor. Fiz. **88**, 1641 (1985) [Sov. Phys. JETP **61**, 978 (1985)].

[6] I. N. Adamenko, K. É. Nemchenko, and V. I. Tsyganok, Zh. Éksp. Teor. Fiz. **91**, 731 (1989) [*sic*].

[7] I. N. Adamenko, K. E. Nemchenko, and V. I. Tsyganok, J. Low Temp. Phys. **88**, 15 (1992).

[8] L. V. Gor'kov and L. P. Pitaevskii, Zh. Éksp. Teor. Fiz. **33**, 634 (1957) [Sov. Phys. JETP **6**, 486 (1958)].

[9] A. Griffin, Can. J. Phys. **47**, 426 (1969).

[10] I. M. Khalatnikov, *The Theory of Superfluidity* [in Russian], Nauka, Moscow (1971).

[11] K. É. Nemchenko, Fiz. Nizk. Temp. **23**, 799 (1997) [Low Temp. Phys. **23**, 599 (1997).

[12] J. Ferziger and H. Kaper, *Mathematical Theory of Transport Processes in Gases*, North-Holland, Amsterdam (1972).

[13] E. M. Lifshitz and L. P. Pitaevskiĭ, *Physical Kinetics,* Pergamon, Oxford, 1979.

[14] I. N. Adamenko, V. K. Chagovets, A. I. Chervanyov *et al.*, J. Low Temp. Phys. **96**, 294 (1994).

Translated by R. S. Wadhwa

SUPERCONDUCTIVITY, HIGH-TEMPERATURE SUPERCONDUCTIVITY

Study of stimulated dynamics and pinning of Abrikosov vortex lattice in type II superconductors in an a.c. magnetic field

J. G. Chigvinadze and G. I. Mamniashvili

*Institute of Physics, Georgian Academy of Sciences, 380077 Tbilisi, Georgia**

A dynamic mechanical method using a weak low-frequency magnetic field is proposed for investigation of stimulated dynamics and pinning in the Abrikosov vortex lattice in type II superconductors. It is shown that the application of a weak a.c. field facilitates depinning of Abrikosov vortices and additional dissipation of energy by liberated vortices. As the frequency of the field increases, a mode in which the vortices virtually do not oscillate is attained, i.e., dissipation ceases, while pinning is extremely effective. The observed effects can be successfully explained on the basis of the Gor'kov–Kopnin theory. © *1998 American Institute of Physics.* [S1063-777X(98)00310-7]

INTRODUCTION

The studies of dynamics of the vortex state in type II superconductors were always considered to be significant both from theoretical and practical points of view, and became even more important after the discovery of HTSC.

The Abrikosov vortex lattice (AVL) is a special type of elastic continuum possessing interesting vibrational properties. In view of high superconducting transition temperatures and their layered structure, HTSC exhibit much higher mobility of the vortex lattice (as compared with type II superconductors), which is hampered by pinning associated with various structural defects. This leads to specific phase transitions (such as two- and three-dimensional melting) in the B, T plane (B is the magnetic induction and T the temperature) in the vortex lattice, which are determined by the relation between the anisotropic amplitude of oscillations and the amplitude of thermal depinning.

In this case, the study of AVL dynamics is especially important since the high mobility of vortices complicates the practical application of HTSC materials. A large number of investigations involving resistive and magnetic method of measurements on macroscopic scale provided valuable information on AVL dynamics.[1,2]

Among macroscopic methods, the static mechanical method of magnetic moment measurement providing the first macroscopic proof of the possibility of $d_{x^2-y^2}$-symmetry of the order parameter and the measurement of intrinsic pinning anisotropy associated with it are worth mentioning.[3] It should be noted that pinning anisotropy of Abrikosov vortices due to dislocations was observed by the static mechanical method in TaNb alloy.[4] The experimental pattern is similar to that observed by Ishida *et al.*[3] The direct dynamic mechanical method of investigation of losses, which provides information on interaction of vortices in type II superconductors, is even more sensitive method of investigation of

losses.[5] Mechanical methods were used to study relaxation processes accompanying the formation and decay of AVL in traditional type II superconductors as well as HTSC. It was established that above a certain transition temperature near T_c, which is associated with possible melting of AVL,[6,7] the logarithmic nature of characteristic relaxation dependence changes to a power dependence with exponent 2/3.

A comparison of the results of macro- and microscopic investigations like NMR provides valuable information about the structure and dynamics AVL. The efficiency of NMR technique as a tool for studying complex vortex structures in condensed media can be illustrated by considering as an example the unique properties of the vortex state in rotating superfluid ^{3}He.[8] Considerable progress has been reported in recent years in NMR studies of the AVL dynamics. At very low temperatures $T \ll T_c$, the NMR spectrum reflects the local magnetic field distribution associated with the existence of a stable AVL, while the vortex lattice dynamics is manifested as a narrowing of the NMR lines and in the processes of relaxation of nuclei. The temperature dependence of the spin–spin and spin–lattice relaxation rates of nuclei makes it possible to determine the characteristic correlation times of AVL as well as its melting point.

An interesting method based on dephasing of the nuclear spin echo[9] was proposed recently for studying the AVL dynamics stimulated by an external low-frequency (lf) and pulsed magnetic fields. This method has been used for a long time for studying the dynamics of domain walls in magnets, and makes it possible to study of the effects associated with the hyperfine field anisotropy and to obtain quantitative estimates of local inhomogeneities and mobility of domain walls besides providing valuable information about the identification of the NMR spectrum.[10] The DW dynamics stimulated by the applied lf and pulsed fields was also studied intensely by macroscopic methods.[11]

DISCUSSION OF EXPERIMENTAL RESULTS

In this communication, we propose an original technique for studying the stimulated dynamics and pinning of AVL in a weak ac magnetic field. As the first application of this technique, we present the results of direct measurement of losses in an ac magnetic field. The measuring technique can be described as follows. The superconducting cylindrical sample is suspended on a thin elastic thread in a constant magnetic field $H_0 > H_{c1}$ at right angles to the cylinder axis producing Abrikosov vortices. The changes in the attenuation and frequency of vibrations caused by Abrikosov vortices are measured.[5] In fields $H_0 < H_{c1}$, the frequency ω and the logarithmic damping decrement are independent of the vibration amplitude φ. However, as soon as the field H_0 exceeds the value H_{c1} and Abrikosov vortices (pinned at the lattice defects) are formed in the bulk of the superconductor, vortex pinning leads to the formation of an additional moment which makes the frequency and damping of the suspended system dependent on the vibration amplitude. In particular, the amplitude dependence of the frequency and attenuation acquires a critical amplitude beyond which the vibrational frequency begins to decrease and the attenuation begins to increase. Measurement of these dependences provides information about the pinning force as well as the dissipative processes accompanying the AVL movement. It was shown by Galaiko[12] that the interaction between free and pinned vortices plays a significant role in this case. As the vibrational amplitude of the suspended system increases, the concentration of free and pinned vortices changes, thus leading to an amplitude dependence of dissipative processes in the mixed state. In the measuring technique adopted by us, a weak ac field ($h \approx 1.5$ Oe) is applied parallel to the main field H_0 generating Abrikosov vortices. This leads to an additional dissipation of the vibrational energy of the suspended mechanical system.

The sample, made of a thermodynamically reversible TaNb single crystal, had the form of a cylinder of diameter 2.5 mm and length $l = 5$ mm and was attached to the vibrational system having a moment of inertia $J = 84.85$ g·cm^2, eigenfrequency $\omega = 0.49$ s^{-1}, and lower critical field $H_{c1} = 65$ Oe. The external field in which the effect of a weak ac field on the critical state of a type II superconductor was measured amounted to $H_0 = 80$ Oe and exceeded (though not significantly) the lower critical field. It was mentioned above that the ac field h is just a small correction ~ 1.5 Oe to H_0.

It can be seen from Fig. 1 that more significant variations of dissipation are observed for lower frequencies of the applied field h. In the absence of a field h, the attenuation and vibrational frequency depend on the vibrational amplitude of the suspended system. These dependences are analogous to those described by us earlier[5] and are associated with the existence of Abrikosov vortices, thus pointing towards a detachment of vortices from pinning centers for vibrational amplitudes φ exceeding a certain critical value φ_c.

It follows from Fig. 1a that, for comparatively high frequencies 180 kHz $\leqslant f \leqslant 240$ kHz, the logarithmic damping decrement δ of the suspended system is independent of the frequency f and has the same magnitude as in the absence of
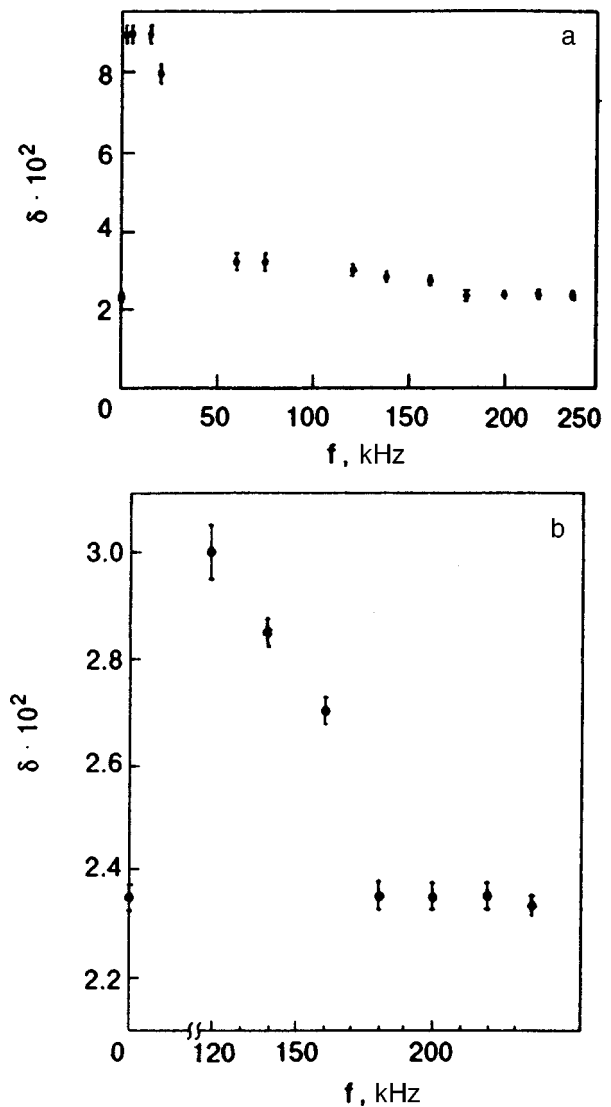

FIG. 1. Logarithmic damping decrement δ of the vibrations of a suspended system as a function of the ac magnetic field frequency f (a). The same dependence on a magnified scale in the frequency range 120–240 kHz (b).

an ac field ($\delta = \delta_0$). The value of δ begins to increase upon a further decrease in frequency, and is four times larger than δ_0 in fields ~ 10 kHz.

The application of a weak ac magnetic field h of frequency f leads to a variation of the amplitude effects of frequency ω and attenuation δ observed for $f = 0$. The amplitude dependence of ω or, to be more precise, the frequency variation $\Delta\omega$ depends on the frequency f of the ac field in a manner analogous to the variation of the vibrational damping δ shown in Fig. 1. The dependence of $\Delta\omega$ on the ac field frequency f is shown in Fig. 2 ($\Delta\omega$ is the difference between the cyclic vibrational frequency of the cylinder for an amplitude $\varphi = 0.02$ rad and its value for $\varphi = 0.1$ rad). It can be seen that the change $\Delta\omega$ is observed for the value of frequency f of the ac field below 180 kHz. In this respect, it differs from the dynamics of damping increment δ which remains unchanged in the interval from 240 to 170 kHz and starts increasing only for $f = 160$ kHz (see Fig. 1b showing
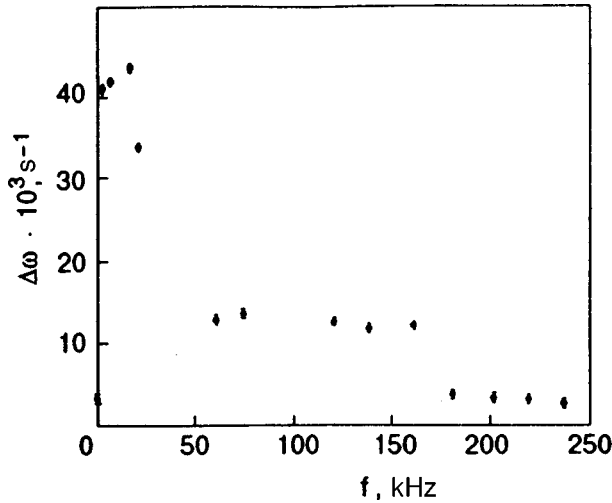
FIG. 2. The dependence of $\Delta\omega$ on the ac field frequency f ($\Delta\omega$ is the difference in the cyclic frequencies of the vibrations of a suspended system for amplitudes $\varphi = 0.02$ and 0.1 rad).

FIG. 4. The dependence of logarithmic damping decrement δ of the vibrations on the vibrational amplitude φ in an ac field $h \approx 1.4$ Oe.

the results of more meticulous measurements in the range 120–240 kHz).

Thus, our experiments show that the application of a weak ac field facilitates depinning of Abrikosov vortices and additional dissipation of energy by liberated vortices. These considerations are confirmed by an analysis of amplitude effects in the presence of a weak ac field. It was found that the critical amplitude φ_c at which vortices are detached from pinning centers in vibrational experiments decreases abruptly with the ac field frequency (Fig. 3; cf. Fig. 4). The curve in Fig. 3 shows that the value of φ_c decreases sharply below the lower observability limit of our experiments (2×10^{-2} rad) at low frequencies (approximately to $f \approx 50$ kHz). As the frequency f of the ac field becomes higher, the angle φ_c increases and attains the value of the critical amplitude observed in zero ac field at frequencies $f = 220$–240 kHz. Figure 4 shows for comparison the amplitude dependence of damping (at $f = 180.2$ kHz) at which the value of φ_c is so large that it is approximately equal to the critical amplitude in zero ac field.
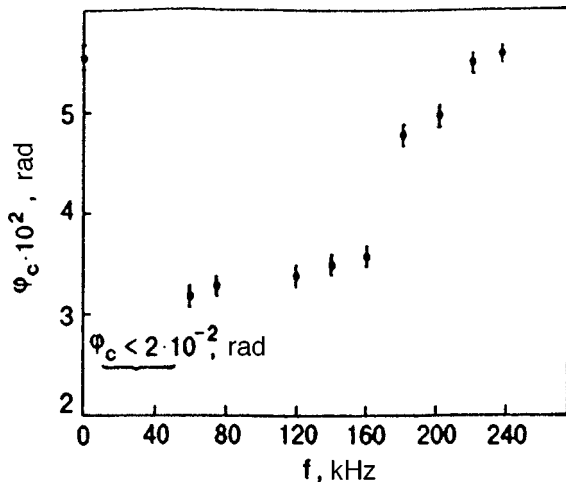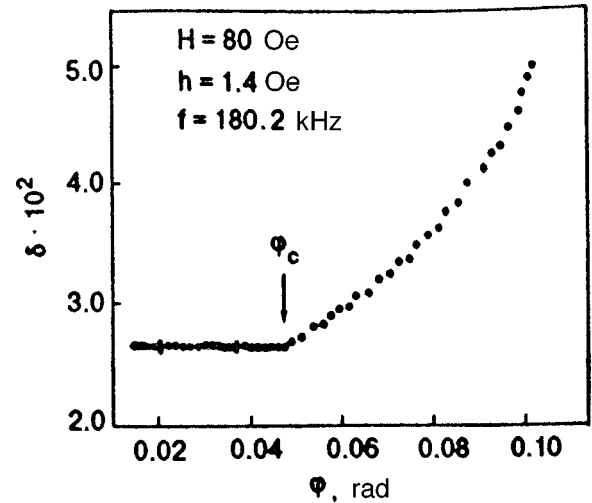
We shall use the Gor'kov–Kopnin theory[13] for interpreting the obtained results. We are speaking of the experiment with a cylinder vibrating in a dc magnetic field on which a weak ac field is superimposed. We shall consider the case when the frequency ω of the ac field is quite high: $\omega > \omega_p$ (ω_p is the limiting frequency at which flux lines are detached from pinning centers). We shall also assume that the displacement **u** of vortices is smaller than the separation between pinning centers. In this case, vortices perform reciprocating motion about pinning centers. As long as vortices are free, they can drift slowly as a result of vibrations of the cylinder and hence dissipate the energy of its vibrations.

The average energy dissipation is independent of the ac field frequency ω at low frequencies, when the displacement **u** is independent of ω. As the value of ω increases, however, the situation changes. Since the drag force acting on vortices is proportional to the velocity (and hence the frequency), the amplitude of displacement of a vortex from the pinning center starts decreasing starting from a certain frequency. The size of pinning centers is quite large (of the order of and larger than $\xi = 4.5 \times 10^{-6}$ cm; see the electron micrograph presented in Fig. 5 for a thermodynamically reentrant $Ta_{70}Nb_{30}$ single crystal used in these experiments). For this reason, the displacement of vortices soon becomes of the order of or smaller than the size of a pinning center, and the vortex remains pinned all the time. Naturally, energy dissipation decreases abruptly in this case.

In order to estimate the frequency at which the dependence of displacement on ω starts being manifested, we write the Gor'kov–Kopnin equation (equation of motion of vortex lattice in an ac field[13,14]):

$$\sigma_f \frac{B^2}{c^2}\left[\mathbf{n}_z \times \frac{\partial \mathbf{u}}{\partial t}\right] = (c_{11} - c_{66})[\mathbf{n}_z \times \nabla \ \mathrm{div} \ \mathbf{u}] + c_{66}[\mathbf{n}_z$$

$$\times \nabla^2 \mathbf{u}] + c_{44}\left[\mathbf{n}_z \times \frac{\partial^2 \mathbf{u}}{\partial z^2}\right], \qquad (1)$$

where **u** is the displacement of vortices, $\mathbf{n}_z$ the unit vector in the direction of the magnetic field (z-axis) in Fig. 6, σ_f the

FIG. 3. The dependence of the critical angle φ_c on the ac field frequency f.
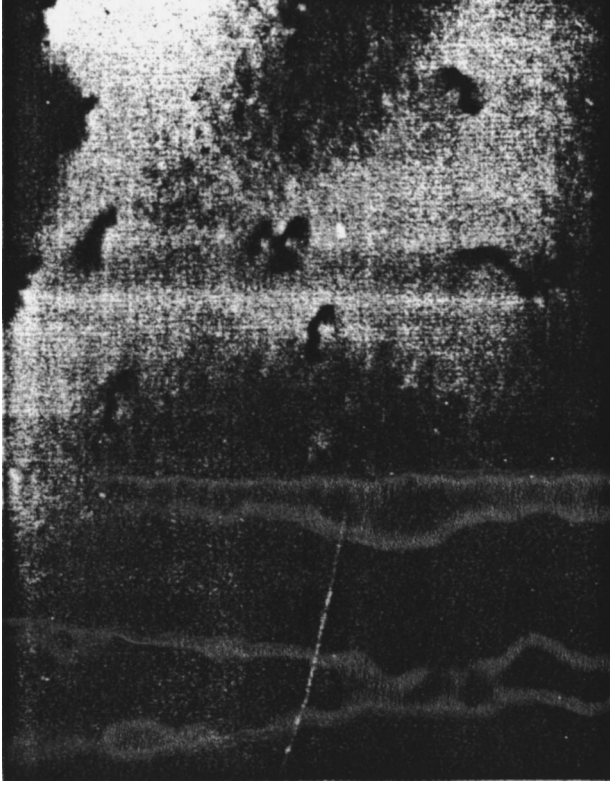
FIG. 5. Electron micrograph of a thermodynamically reentrant $Ta_{70}Nb_{30}$ single crystal (magnification 98 000).

conductivity of the superconductor in the mixed state during the motion of vortices, H the constant field, B the magnetic induction, and $c_{\alpha\beta}$ are elastic moduli of the vortex lattice:

$$c_{11}=\frac{B^2}{4\pi}\frac{\partial H}{\partial B}+\frac{1}{8\pi}\int_0^B B'^2\frac{\partial^2 H}{\partial B'^2}\,dB',$$

$$c_{44}=\frac{BH}{4\pi},\quad c_{66}=\frac{1}{8\pi}\int_0^B B'^2\frac{\partial^2 H}{\partial B'^2}\,dB'. \qquad (2)$$

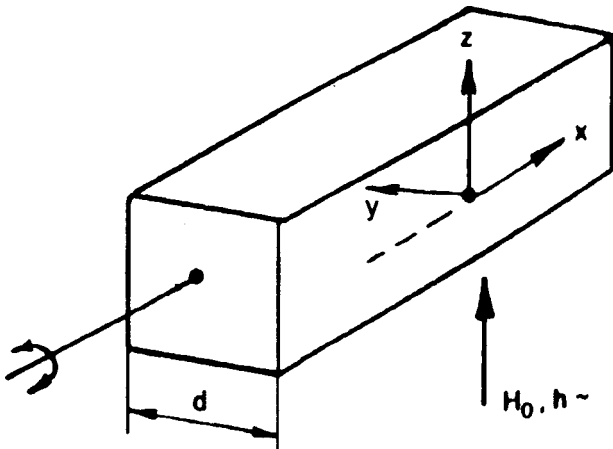It was shown by Gor'kov and Kopnin[13] that together with the boundary condition at the sample surface in the form

FIG. 6. Experimental setup for estimating the dependence of vortex displacement **u** on the ac field frequency f.

$$v_k(c_{11}-c_{66})\,\mathrm{div}\,\mathbf{u}+c_{66}v_i\frac{\partial u_k}{\partial x_i}+c_{44}\frac{\partial u_k}{\partial z}$$

$$=v_z\frac{B_0H_k}{4\pi}-v_k\frac{B_0(H_z-H_0)}{4\pi}, \qquad (3)$$

where $v(v_i,v_z)$ is the vector normal to the sample surface, Eq. (1) leads to an equation for the distribution of the ac field in the sample in the form of Maxwell's equations with modified values of σ and μ. The displacement **u** of vortices occurs along the y-axis and depends only on y. From Eq. (1), we obtain

$$\sigma_f\frac{B^2}{c^2}\frac{\partial u_y}{\partial t}=c_{11}\frac{\partial^2 u_y}{\partial y^2}. \qquad (4)$$

For $y=0$ (component along the y-axis), we obtain from the boundary condition (3)

$$c_{11}\frac{\partial u_y}{\partial y}=\frac{B_0H_-}{4\pi}. \qquad (5)$$

Presenting u_y in the form $u_y=\mathrm{Re}(e^{-i\omega t}u_y)$, we obtain from (4)

$$\frac{\partial^2 u(y)}{\partial y^2}+\frac{i\omega\sigma_f B^2}{c^2 c_{11}}u(y)=0.$$

This leads to the following expression for $u(y)$:

$$u(y)=Ae^{-(1+i)y/\delta_{ik}},$$

where

$$\delta=\left(\frac{2c_{11}c^2}{B^2\omega\sigma_f}\right)^{1/2}=\frac{c}{\sqrt{2\pi\mu_\parallel\omega\sigma_f}};$$

and $\mu_\parallel=B_0^2/4\pi c_{11}$ is the effective permeability of the vortex system. From Eq. (5), we obtain

$$A=-\frac{B^2}{4\pi c_{11}}\delta_{ik}\frac{1-i}{2}\frac{H_-}{B_0}=-\mu_\parallel\delta_{ik}\frac{1-i}{2}\frac{H_\sim}{B_0}.$$

Hence

$$u(y)=-\mu_\parallel\delta_{ik}\frac{1-i}{2}\frac{H_\sim}{B_0}e^{-(1+i)y/\delta_{ik}}.$$

For the estimate of the frequency ω at which $d\sim\delta_{ik}(\omega)$, we obtain

$$f_0=\frac{\omega_0}{2\pi}=\frac{c_{11}c^2}{\pi d^2\sigma_f B^2}\simeq\frac{1}{\pi}\frac{c_{11}}{B^2}\rho_f\frac{c^2}{d^2}.$$

Using the experimental results and Eq. (2), we find that the quantity c_{11}/B^2 is of the order of unity in fields of the order of 250–300 Oe ($H\approx 2H_{c1}$). This gives

$$f_0=\frac{1}{\pi}\frac{\rho_f 10^9[\Omega\cdot\mathrm{cm}]}{d^2[\mathrm{cm}]}\ [\mathrm{s}^{-1}].$$

In the present case, $\rho_f\approx 4\times10^{-7}\ \Omega\cdot\mathrm{cm}$ for $H_0=80$ Oe, and $d=2.5$ mm. Hence

$$f_0\approx 10\ \mathrm{kHz},$$

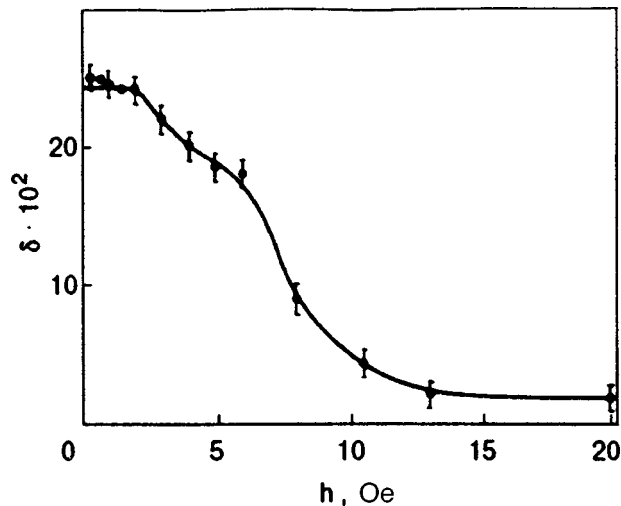which is in good agreement with the frequency at which energy dissipation starts to decrease.

FIG. 7. The dependence of logarithmic damping decrement δ of the vibrations on the ac field h.

Hence it can be assumed that the decrease in energy dissipation is associated with the increase in drag obstructing the displacement of vortices in an ac field. As the separation between vortices and pinning centers decreases, their effective trapping at pinning centers becomes stronger, which, in turn, leads to a decrease in energy dissipation to its value at zero frequency.

We also studied the dependence of damping on the ac field h for various frequencies f and $\omega_0 = 2.05 \text{ s}^{-1}$ (Fig. 7). It was found that upon an increase in the amplitude of the ac field, the dissipation remains nearly constant for small h, and then decreases sharply upon an increase in h.

In order to explain this result, we again turn to the Gor'kov–Kopnin theory.[13,14] The displacement of vortices increases with the ac magnetic field. In a quite strong ac field, the displacement of vortices becomes of the order of the sample size. Since the amplitude of the ac field does not exceed $0.01H_0$, we assume that the vortices are displaced towards the sample surface and leave it after overcoming the Bean–Livingston barrier.[15] It can naturally be assumed that the vortices remain pressed against the sample wall for most of the time upon a further increase in the field strength, and are not displaced during vibrations of the cylinder. Hence the damping will naturally decrease (by the way, the exit of vortices from the sample would also decrease the damping). An estimate similar to that given above for the ac field strength for which the vortex displacement becomes of the order of the cylinder diameter shows that the dissipation decreases for values of h of the order of tens of oersteds, which is in good agreement with the experimental results.

CONCLUSION

In this paper, we have proposed a new dynamic approach for studying the stimulated dynamics and pinning of the Abrikosov vortex lattice with the help of a weak low-frequency field.

It is shown that the application of a weak ac field facilitates the depinning of Abrikosov vortices and an additional

dissipation of the energy by the liberated vortices. This is confirmed by an analysis of the amplitude effects.

The effects observed by us can be explained satisfactorily by the Gor'kov–Kopnin theory.

Like the investigations of the stimulated vortex lattice dynamics by dephasing of the nuclear spin echo, the dynamic mechanical approach used by us also allows direct observation of the relaxation processes in the Abrikosov vortex lattice. Moreover, this technique supplements the NMR investigations since it is convenient for studying B, T phase diagrams over a wide range of parameters,[6] slow relaxation processes with characteristic times of the order of 1 s and more,[7] pinning potentials,[16] etc. Apparently, the NMR technique is more convenient for studying rapid relaxation processes with characteristic times of the order of 10^{-1} s and below.[17,18] It should also be noted that the values of pinning potential obtained by using mechanical[16] and NMR methods[9,17] are close (of the order of 0.2 and 0.1 eV, respectively).

It would be interesting to study the damping under a stimulating low-frequency force in the same samples. This would considerably improve the reliability and accuracy of the results.

*E-mail: jaba@physics.iberiapac.ge

[1] A. Campbell and J. Evetts, *Critical Currents in Superconductors*, Taylor and Francis, London (1972).
[2] V. V. Shmidt, *Introduction to Superconductor Physics*, Nauka, Moscow (1982).
[3] T. Ishida, K. Okuda, H. Asaoka *et al.*, in *Proceedings of the 21st Int. Conf. Low Temp. Phys.*, Prague (1996), **B**1217.
[4] J. G. Chigvinadze, Fiz. Nizk. Temp. **10**, 151 (1984) [Sov. J. Low Temp. Phys. **10**, 77 (1984)].
[5] J. G. Chigvinadze, Zh. Éksp. Teor. Fiz. **63**, 2144 (1972) [Sov. Phys. JETP **36**, 1132 (1972)].
[6] A. A. Iashvili, T. V. Machaidze, L. T. Paniashvili, and J. G. Chigvinadze, Sverkhprovodimost: Fiz., Khim., Tekh. **7**, 297 (1994).
[7] V. N. Bakradze, A. A. Iashvili, T. V. Machaidze *et al.*, Sverkhprovodimost: Fiz., Khim., Tekh. **7**, 301 (1994).
[8] Yu. M. Bun'kov, G. E. Gurgenishvili, M. Kruzius, and G. A. Kharadze, Usp. Phys. Nauk **144**, 141 (1984) [Sov. Phys. Usp. **27**, 731 (1984)].
[9] F. Borsa, P. Carretta, F. Cintolesi *et al.*, Appl. Magn. Reson. **9**, 149 (1995).
[10] E. Machowska and S. Nadolski, Solid State Commun. **68**, 215 (1988).
[11] G. H. J. Wantenaar, G. V. H. Wilson, D. H. Chaplin, and S. J. Campbell, J. Magn. Magn. Mater. **89**, 13 (1990).
[12] V. P. Galaĭko, Pis'ma Zh. Éksp. Teor. Phys. **3**, 121 (1966) [JETP Lett. **3**, 76 (1966)].
[13] L. P. Gor'kov and N. B. Kopnin, Usp. Phys. Nauk **116**, 413 (1975) [Sov. Phys. Usp. **18**, 496 (1975)].
[14] N. B. Kopnin and J. G. Chigvinadze, Preprint FNT-2, Tbilisi (1990).
[15] C. P. Bean and J. D. Livingston, Phys. Rev. Lett. **12**, 14 (1964).
[16] V. N. Bakradze, A. A. Iashvili, T. V. Machaidze *et al.*, Zh. Éksp. Teor. Phys. **104**, 2519 (1993) [JETP **77**, 138 (1993)].
[17] C. H. Recchia, J. A. Martindale, C. H. Pennington *et al.*, Phys. Rev. Lett. **78**, 3543 (1997).
[18] M. Corti, B. J. Suh, F. Tabak *et al.*, Phys. Rev. B **54**, 9469 (1996).

Translated by R. S. Wadhwa

HF energy losses at the minima of magnetic field dependences of absorption in HTSC

G. V. Golubnichaya, A. Ya. Kirichenko, I. G. Maksimchuk, and N. T. Cherpak

*A. Ya. Usikov Institute Of Radiophysics and Electronics, National Academy of Sciences of the Ukraine,
310085 Kharkov, Ukraine**)

Peculiarities of the electromagnetic power absorption are investigated at extreme points of
magnetic field dependences in high-T_c superconductors. A linear dependence of absorption on the
magnetizing field at the points of minima on the curves is established. It is shown that the
main contribution to absorption at these points comes from hf losses directly in grains. The relative
value of losses at the minima on magnetic field curves can be used for estimating the grain
quality. © *1998 American Institute of Physics.* [S1063-777X(98)00410-1]

1. INTRODUCTION

Hysteresis effects in magnetic field dependences of critical current,[1–5] magnetic susceptibility,[3,6] and electromagnetic energy losses in microwave[7] and rf fields[8] has attracted the attention of researchers even from first steps of investigation of physical features of high-T_c superconductors (HTSC) of the $YBa_2Cu_3O_{7-x}$ type. An analysis of these dependences confirmed the strong influence of the granular structure of HTSC on their transport and magnetic properties. It was found that intergranular medium is mainly responsible for the value of transport current and electromagnetic losses, while the magnetic flux trapping in the sample is mainly determined by superconducting grains.

Many authors paid special attention to an analysis of the extreme point on the magnetic field dependence in a decreasing magnetic field (the peak of critical current or the minimum of the imaginary component of magnetic susceptibility as well as electromagnetic losses). It was found that these experimental points on the critical current and magnetic susceptibility curves[3] (or electromagnetic absorption on the scale of external dc magnetic field) coincide. The influence of the magnetizing field (i.e., the maximum values H_m of magnetic field attained before its decrease) and the working temperature[1–8] as well as the temperature and magnetic past history of the sample in a given experiment[2,4,5] on the position of the extremum has been determined. The results of these experiments led to the conclusion that the existence of an extremum in a decreasing field is determined by the maximum possible compensation of the applied field in the intergrain medium by the opposite field created by field lines of the magnetic flux trapped by superconducting grains. In this case, the action of the applied magnetic field on weak intergrain links is strongly suppressed. However, the critical field or electromagnetic absorption being measured at the extremum never attains its initial value (prior to the application of the magnetic field). Besides, the point corresponding to the zero value of sample magnetization does not coincide with the position of absorption minimum in a decreasing magnetic field, although these two special points are close.[9]

The authors of the publications mentioned above at-tribute the lack of complete compensation of local fields in the intergrain space at the peak of the critical current curve or at the minimum of the electromagnetic field absorption curve on magnetic field dependences in a decreasing magnetic field either to the spread in the geometrical size and orientations of individual grains in the sample,[10] or to the variation of the magnitude and direction of local magnetic fields in the intergrain space over a wide range.[2,11] The effect of magnetic flux trapped by the grains on their critical current or electromagnetic field absorption in grains was completely disregarded. This research aims at the evaluation of the effect of magnetic flux trapped by grains on the absorption of high-frequency (rf) electromagnetic field directly in grains and the estimation of the effect of the dissipative field of the trapped flux on the losses in the intergrain space at absorption minima on magnetic field dependences.

2. EXPERIMENTAL TECHNIQUE

The absorption power P of the rf field (the tangent of the loss angle $\tan\delta = P = 1/Q$ in the sample) was measured by the inductive technique. The experimental setup made it possible to measure the change in losses P as a result of the introduction of a superconducting sample into the field of the coil. Measurements were made at a frequency of 2.525 MHz at liquid nitrogen temperature ($T = 77$ K) during sample cooling in zero magnetic field (ZFC mode).

A dc magnetic field up to 165 Oe was created by Helmholtz coils. The direction of the ac component of the rf magnetic field created by the measuring inductive coil in all the experiments was collinear to the applied dc magnetic field. The ac magnetic field strength did not exceed 0.01 Oe.

We recorded three types of magnetic field dependences of absorption P in the sample: upon an increase in the applied magnetic field H to H_m, during its subsequent decrease, and also the losses in the sample with a trapped magnetic flux in zero magnetic field $H = 0$. We could reverse the direction of the applied field; the direction of the field in which initial measurements were made was assumed to be positive (H), while the opposite direction was regarded as negative ($-H$).
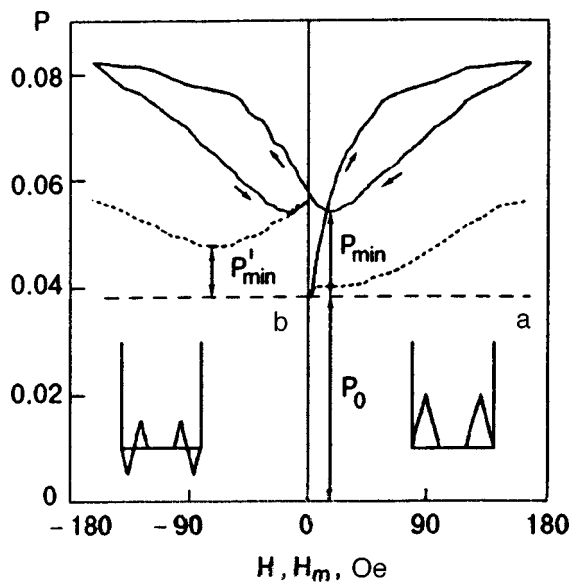
FIG. 1. Typical shape of magnetic field dependence of absorption in YBa$_2$Cu$_3$O$_{7-x}$ ceramic samples. The insets show schematically the magnetic flux distribution in a grain at the absorption minima in a decreasing magnetic field (a) and in a sample with a trapped magnetic flux during magnetization reversal (b).

The field dependences $P(H_m)$ of absorption in a sample with a trapped magnetic flux were measured after switching off the magnetic field which was initially varied smoothly from zero to a certain value H_m. The value of the magnetizing field H_m was increased in each next measuring cycle $0 \rightarrow H_m \rightarrow 0$. When the direction of the magnetic field was reversed to $-H_m$ (magnetization reversal), the maximum attained value of the positive magnetizing field ($H_m = 165$ Oe) was preserved, and only the value of reverse magnetization field ($-H_m$) was varied.

Special attention was paid to the minimum values of losses in a decreasing magnetic field H as well as in samples with a trapped magnetic flux during magnetization reversal ($-H_m$).

The experiments were made on YBa$_2$Cu$_3$O$_{7-x}$ ceramic samples prepared at the Institute of Single Crystals, National Academy of Sciences of the Ukraine, according to the standard technique of solid synthesis under various conditions of preparation.

3. DISCUSSION OF EXPERIMENTAL RESULTS

The solid curve in Fig. 1 shows a typical hysteresis loop of rf losses in an HTSC ceramic sample, which was obtained in a magnetic field first increasing from zero to 165 Oe, and then decreasing to zero and in the region of "negative" values of H. After the value of -165 Oe was attained, the field was again returned to zero value. The direction of field variation in this cycle is shown by arrows.

The dashed curves show magnetic field dependences of losses in the sample with a trapped magnetic flux during its magnetization to 165 Oe in the forward direction and upon magnetization reversal to -165 Oe.

A typical feature of the magnetic field dependence of absorption in a decreasing magnetic field is the presence of a

minimum. It was found in numerous investigations[1–10] that the minimum on this curve is due to mutual compensation of local fields in the intergrain space (i.e., on the surface of grains), which are induced by the applied magnetic field and by the total dissipative field of Abrikosov vortices trapped by grains, which has the opposite direction. Using the model developed by Evetts and Glowacki[2] on the basis of the Bean's concept on the critical state, we find that the magnetic flux trapped by a grain at the minimum of the curve has a spatial distribution shown schematically in the inset a (Fig. 1) below the minimum under investigation. The local magnetic field at the surface of grains is equal to zero in this case. Figure 1a corresponds to the case when only a part of a granule goes over to the critical state, i.e., the magnetic field has not yet penetrated to the center of the granule.

The absorption of the rf field at the minimum is the sum of the absorption P_0 in the superconductor in zero magnetic field (see Fig. 1) and the component P_{min} due to the effect of the trapped magnetic flux.

Blinov et al.[12] were the first (to our knowledge) to obtain the magnetic field dependence of absorption in a sample with a trapped magnetic flux during magnetization reversal. These authors paid attention to a strong difference between this dependence and a similar curve obtained during magnetization in the forward direction. The presence of a minimum on this dependence was interpreted from the point of view of the spatial distribution of the local magnetic field in the magnetized sample. The fields induced by magnetic fluxes trapped during forward (H_m) and reverse ($-H_m$) magnetization of the sample in this case are compensated at the surface of grains. The distribution of the magnetic flux trapped in a grain at the point of absorption minimum in the range of negative values of H_m is shown in the inset b to Fig. 1. The total local field at the boundaries of grains is naturally assumed to be zero in this case, while the magnitude of losses at this minimum is determined by the total losses P_0 and P'_{min}.

As the maximum attained value H_m of the magnetic field increases, the position of the rf absorption minimum H_{min} in a decreasing magnetic field as well as the position of the minimum H'_{min} in a sample with a trapped magnetic flux during magnetization reversal are displaced towards higher values of magnetic field (Fig. 2a). The displacement of the positions of the minimum H_{min} (solid curve) coincides with the dependences obtained in Refs. 1, 7–9, and 11, but the fields used in the experiments do not attain saturation. The minimum H'_{min} (dashed curve) is characterized by higher values and is displaced more rapidly. Figure 2b shows the increase of losses at both minima P_{min} (solid curve) and P'_{min} (dashed curve), i.e., in a decreasing field and in the trapped field during magnetization reversal, respectively, as a function of the magnetizing field H_m. The dependence $H_{min}(H_m)$ as well as the $P_{min}(H_m)$ dependence do not attain quasi-stationary level in the magnetization field range under investigation, which suggests (see Refs. 7, 9, and 11) that the external field does not penetrate to the center of grains under these conditions.

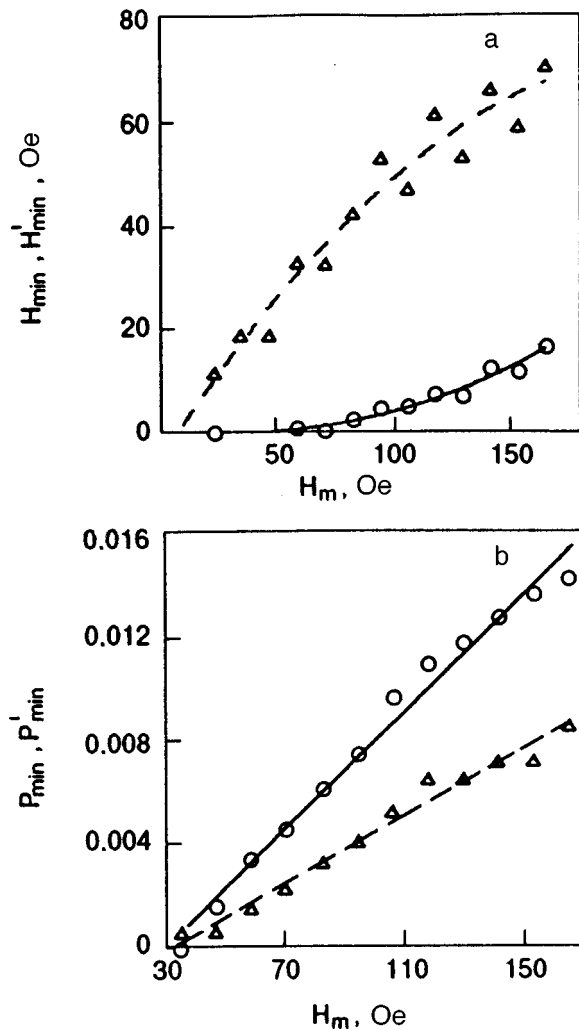It can be seen from Fig. 2b that the dependences $P_{min}(H_m)$ and $P'_{min}(H_m)$ are almost linear. The values of

FIG. 2. Positions of the minima ($H_{\min}, H'_{\min}$) (a) and the magnitude of losses ($P_{\min}, P'_{\min}$) (b) at these points as functions of the maximum attained magnetization field: in a decreasing field ($\bigcirc$) and in a sample with a trapped magnetic flux during magnetization reversal ($\triangle$).

FIG. 3. Dependence of absorption $P_{\min}$ at the minimum in a decreasing field on the double losses $2P'_{\min}$ at the minimum in a sample with a trapped magnetic flux during magnetization reversal (see text).

losses at the minimum of the curve recorded in a decreasing magnetic field are approximately twice as large as rf losses at the minimum of the absorption curve recorded on a sample with a trapped magnetic flux during magnetization reversal, i.e., $P_{\min} \approx 2P'_{\min}$ in the entire range of magnetization fields.

In order to verify the validity of the relation $P_{\min} \approx 2P'_{\min}$, we analyzed the dependence $P_{\min}(2P'_{\min})$ for a large number of HTSC samples for a fixed value of magnetizing field $H_m = 165$ Oe (Fig. 3). During sample synthesis, we varied the technological processes of sample preparation (such as the temperature and duration of annealing, pressure and temperature of compression), and introduced impurities of silver, Y_2BaCuO_5, etc. For this reason, the samples were characterized by different values of rf losses before and after the application of the magnetic field and different forms of magnetic field dependences of absorption.

Figure 3 shows the values of $2P'_{\min}$ and $P_{\min}$ for more than 200 HTSC ceramic samples. The dashed straight line with a slope of 45° is drawn from the origin, while the theoretical (solid) regression line is plotted by using the least square method.
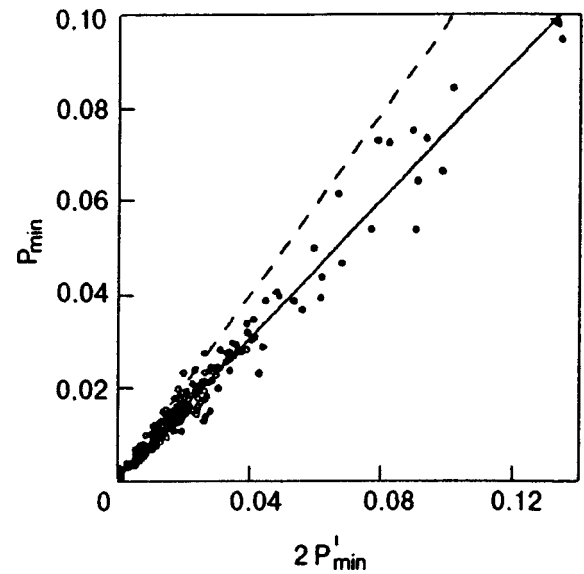
The high coefficient of correlation ($r = 0.98$) suggests that rf losses at the minima under investigation are connected through a stringent relation, while random variations of the grain size and orientation, which determine the spread in the local intergrain field, play the role of an auxiliary correction to the main absorption. It is worth noting that, according to geometrical concepts of regions with trapped magnetic flux according to Bean, the density of the magnetic flux trapped in a granule at the minimum of the absorption curve in a decreasing magnetic field $H_{\min}$ (see the inset a to Fig. 1) is twice as high as the density of trapped flux at the minimum $H'_{\min}$ (see inset b to Fig. 1). Thus, using the Kim–Anderson model concerning the dependence of critical current on magnetic induction and taking into account the fact that losses are inversely proportional to the critical current density,[13] we can easily assume that losses in gains depend linearly on the density of magnetic flux trapped in the sample.

This naturally leads to the conclusion that losses at the minima of magnetic field dependences is mainly due to absorption directly in grains, and hence characterizes, in fact, the quality of grains in a HTSC ceramic sample. At these points of magnetic field dependences, rf losses in the intergrain medium are minimized and can be regarded as a small correction to losses in grains, which is responsible for a deviation from the equality $P_{\min} = 2P'_{\min}$. It can be naturally assumed that the magnitude of this correction to main losses in grains is determined by technological conditions of sample preparation. We can estimate the nature of its variation by analyzing, for example, the behavior of the losses under investigation in samples with different densities ρ. For this purpose, the ratio $P_{\min}/2P'_{\min}$ in Fig. 4 is shown as a function of density ρ for more than 50 samples. Approximation of the obtained experimental values by a second-degree polynomial indicates the existence of a peak for the density $\rho \sim 4.5$ g/cm^3. Consequently, the samples having such a density are probably distinguished by the best quality grains, i.e.,
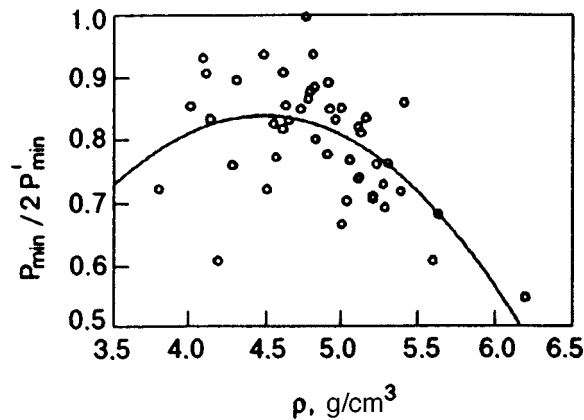
FIG. 4. Dependence of the ratio $P_{min}/2P'_{min}$ of losses at the minimum in a decreasing field to the double losses at the minimum in a sample with a trapped magnetic flux during magnetization reversal on the sample density ρ.

by the lowest probability for the existence of twinning planes, cracks, and other crystal lattice defects.

4. CONCLUSIONS

An analysis of peculiarities of rf losses of electromagnetic energy at the minima of magnetic field dependences of absorption in a decreasing magnetic field and a comparison of these losses with those at the minima in samples with a trapped magnetic flux during magnetization reversal indicate the dominating effect of losses directly in grains at these points of the curves. The influence of statistical spread in local magnetic fields in magnitude and direction in the intergrain space on rf absorption at the minima under investigation is slightly exaggerated in existing publications.

In spite of the generally accepted opinion that rf energy losses in HTSC ceramic samples in magnetic fields are mainly associated with losses in the intergrain medium, the absorption takes place predominantly in grains for certain values of magnetic fields on magnetic field curves. The magnitude of these losses at points H_{min} and H'_{min} can be used to estimate the quality of grains.

The analysis of the behavior of rf losses in samples with a trapped magnetic flux during magnetization reversal indicates that Bean's model is applicable for the case of magnetization reversal in ceramic samples also.

*)E-mail: cherpak@ire.kharkov.ua

[1] L. S. Kokhanchik, V. A. Marchenko, T. V. Nikiforov, and A. V. Nikulov, Fiz. Nizk. Temp. **14**, 872 (1988) [Sov. J. Low Temp. Phys. **14**, 479 (1988)].

[2] J. E. Evetts and B. A. Glowacki, Cryogenics **28**, 641 (1988).

[3] A. M. Dolgin and S. N. Smirnov, Sverkhprovodimost': Sverkhprovodimost: Fiz., Khim., Tekh. **2**, 100 (1989).

[4] E. Altshuler, S. Garsia, and A. Aguilar, Phys. Status Solidi **2446**, K169 (1990).

[5] Y. Yang, C. Beduz, and S. P. Ashworth, Cryogenics **30**, 618 (1990).

[6] Y. Yang, C. Beduz, Z. Yi, and R. G. Scurlok, Physica C **C201**, 325 (1992).

[7] E. I. Pakulis and T. Osada, Phys. Rev. B **37**, 5940 (1988).

[8] I. E. Aronov, A. Ya. Kirichenko, A. A. Krokhin, and N. T. Cherpak, *Problems in High-Temperature Superconductivity* [in Russian], Kiev (1989).

[9] R. Laikho, E. Supponen, Yu. P. Stepanov *et al.*, Fiz. Tverd. Tela **31**, 268 (1989) [Sov. Phys. Solid State **31**, 701 (1989)].

[10] K. Kwasnitza and Ch. Widmer, Cryogenics **29**, 1035 (1989).

[11] S. Zanella, L. Martini, V. Ottoboni *et al.*, Phys. and Mater. Scien. of High Temp. Supercond., 252 (1989).

[12] E. V. Blinov, M. G. Semenchenko, V. G. Fleisher *et al.*, JETP Lett. **48**, 159 (1988)].

[13] A. V. Gurevich, R. G. Mints, and A. L. Rakhmanov, *Physics of Composite Superconductors* [in Russian], Nauka, Moscow (1987).

Translated by R. S. Wadhwa

LOW-TEMPERATURE MAGNETISM

Description of ordering, temperature dependence of susceptibility, and magnetostriction of a one-sublattice spin system with $S=1$ and strong biquadratic exchange

V. M. Kalita and A. F. Lozenko

Institute of Physics, National Academy of Sciences of the Ukraine, 252650 Kiev, Ukraine[*)]

The magnetic ordering model is considered for a single-lattice spin subsystem with $S=1$ and a large biquadratic exchange whose energy has the same order of magnitude as the bilinear exchange interaction energy. The expression for free energy is obtained in the microscopic approximation, and the phase states are defined and analyzed. The Landau potential is represented as a power expansion in the model microscopic free energy. This expression is used to describe the peculiarities of the temperature dependences of the magnetic susceptibility and magnetoelastic deformation. © *1998 American Institute of Physics.*
[S1063-777X(98)00510-6]

Conventional Heisenberg exchange interaction bilinear in spins can be supplemented in many systems by a stronger interaction, e.g., biquadratic (in spins) exchange (BE) interaction. In some cases (see, for example, Ref. 1), the intensity of BE is not small according to some indications, but comparable with and even higher than that of bilinear exchange. Exchange interaction biquadratic in spins can change qualitatively the properties of magnets. The main property of a system with a strong BE is the possibility of the existence of the so-called quadrupole phase (QP),[2] which is described by a (rank two) tensor order parameter and has zero magnetization. Other manifestations of BE are described in Ref. 3.

Thermodynamic properties of a one-sublattice isotropic magnet with ferromagnetic bilinear exchange and BE have been described by many authors (see, for example, Refs. 3–7). A more general case, when three- and four-spin exchange interactions were also taken into account, is considered in Ref. 8. However, the problem has not been solved completely. For example, various possible configurations of quadrupole spin states at $T=0$ analyzed in Ref. 8 were erroneously called domains. The calculations made by Chen and Levy[4,7] are valid for equilibrium states and cannot be used for calculating nonequilibrium free energy defined in the form of a function of order parameters. Appropriate procedure of computation of the nonequilibrium free energy and Landau potential is described in Refs. 9–11 and in Refs. 6 and 8 as applied to the problem under investigation, but some of the solutions analyzed in these publications are unstable. This can easily be verified by introducing a small perturbation containing, for example, the zz-component of the spin quadrupole moment operator. Such an instability is not a feature of the system itself, but appears due to the approximations used. The mean-field approach for a spin system with BE presumes the presence of a vector magnetic field as well as a tensor quadrupole mean field. Since the system is isotropic,

and the phase transition between ferromagnetic, and quadrupole states occurs as a first-order transition, it appears that the directions of fields, and hence the orientation of order parameters for these states, can be arbitrary. However, the mutual relation between the directions of spontaneous lowering of the symmetry for different states deserves special attention.

Indeed, Andreev and Grishchuk[2] proved that a QP possesses a magnetic susceptibility, i.e., the magnetic field applied in the quadrupole state induces a magnetization whose direction is determined by the field. But the same field also determines a definite orientation for the quadrupole order parameter which was initially orientationally degenerate since the average magnetization now determines the quantization axis, and the directions of principal axes of the quadrupole moment are no longer invariant relative to this axis, although they are not determined completely by this axis alone. Thus, if we require that the magnetization of the quadrupole phase in the external field and the spontaneous magnetization of the ferromagnetic phase (FP) have the same direction, i.e., are oriented by the same applied field specifying quasi-mean values for the FP, we find that the orientation of the quadrupole moment in the QP and the orientation of the magnetic moment in the FP are interrelated.

The mean tensor field taken into account during the formation of the QP does not contain a vector field, can be presented in terms of the components of the quadrupole order parameter, and hence cannot determine the magnetization in the FP completely. It will be shown below that correct interpretation of the interrelation between these fields leads to a complete description of the problem. These considerations will be important for our analysis since we shall study the possibilities for the existence in the system of QP and FP (which are transformed into each other) under various conditions.

We shall consider a simple one-sublattice spin system with $S=1$ with isotropic bilinear and biquadratic exchange interactions. A thermodynamic analysis of possible types (including QP and FP) of spin ordering will be carried out, and temperature dependences of magnetic susceptibility and lattice deformations will be analyzed. Since the application of a magnetic field is required and the mean-field approximation is used for calculating the magnetic susceptibility and magnetostriction, we shall use an approach that makes it possible to take, into account correctly the mutual orientation of the order parameters in the QP and FP in an applied magnetic field.

HAMILTONIAN

We consider a spin system with the Hamiltonian

$$H = J \sum_{\mathbf{fg}} \mathbf{S_f} \cdot \mathbf{S_g} + B \sum_{\mathbf{fg}} (\mathbf{S_f} \cdot \mathbf{S_g})^2, \qquad (1)$$

where $\mathbf{S_f}$ and $\mathbf{S_g}$ are spin operators, $\mathbf{f}$ and $\mathbf{g}$ are the vectors specifying positions of spins with $S=1$, and J and B are the bilinear and BE constants such that $J<0$ and $B<0$. The negative values of the constants J and B ensure the stability of the one-sublattice magnetic structure.

Denoting the components of the quadrupole moment operator $Q_{\alpha\beta} = (1/2)(S_\alpha S_\beta + S_\beta S_\alpha)$, by $Q_{\alpha\beta}$, we can write Hamiltonian (1) in the form

$$H = [J-(1/2)B] \sum_{\mathbf{f,g}} (\mathbf{S_f} \cdot \mathbf{S_g}) + \sum_{\alpha,\beta} B_{\alpha\beta} \sum_{\mathbf{f,g}} Q_{\mathbf{f}\alpha\beta} Q_{\mathbf{g}\alpha\beta}, \qquad (2)$$

where $\alpha, \beta = x, y, z$, and the coefficients $B_{\alpha\beta}$ are defined as follows: $B_{\alpha\beta} = 2B$ if $\alpha \neq \beta$, and $B_{\alpha\beta} = B$ if $\alpha = \beta$.

Loktev and Ostrovskii[12,13] described spin systems with $S=1$ by introducing for spin an intrinsic system of coordinates, in which

$$\langle \psi_{\mathbf{f}} S_{x\mathbf{f}} \psi_{\mathbf{f}} \rangle = \langle \psi_{\mathbf{f}} S_{y\mathbf{f}} \psi_{\mathbf{f}} \rangle = \langle \psi_{\mathbf{f}} Q_{\mathbf{f}xy} \psi_{\mathbf{f}} \rangle = 0, \qquad (3)$$

where $|\psi_{\mathbf{f}}\rangle$ denotes the function of the ground state of the **f**th spin, and x, y, z are the axes in the intrinsic system of coordinates. In the magnetized state in which the mean values $\bar{S}_z = \langle \psi_{\mathbf{f}} S_{z\mathbf{f}} \psi_{\mathbf{f}} \rangle$ differ from zero, the function $|\psi_{\mathbf{f}}\rangle$ of the ground state is defined unambiguously and has the form[12,13]

$$|\psi_{\mathbf{f}}\rangle = \cos \text{fi} |1\rangle + \sin \varphi |-1\rangle, \qquad (4)$$

where $|1\rangle$ and $|-1\rangle$ are the eigenfunctions of the operator S_z. Such a form of the function allows us to describe ferromagnetic as well as quadrupole states considered in Introduction. In an external magnetic field $h\|z$, the ferromagnetic state corresponds to the function (4) with $\varphi = 0$, for which $\bar{S}_z = 1$. The magnetization of the quadrupole state in the field is given by

$$\bar{S}_z = \frac{h}{2(J-B)}. \qquad (5)$$

For $h \to 0$, the quadrupole state corresponds to function (4) with $\varphi = \pi/4$.

The susceptibility of the quadrupole state differs from zero and can be written in the form

$$\chi^{-1} = 2(J-B). \qquad (6)$$

The behavior of magnetization and susceptibility in the quadrupole spin state is the same as for an isotropic antiferromagnet.[2]

FREE ENERGY

We shall describe the system corresponding to Hamiltonian (1) at finite temperatures by using the system of coordinates defined by relations (3).

It should be borne in mind, however, that statistical calculations of nonequilibrium free energy in terms of the Gibbs partition function, which were made in Refs. 3, 4, and 7, are based on the theorem on the extremum of approximate equilibrium free energy,[14] which is a function of extrinsic parameters. The replacement of the extrinsic parameters, say, of the external magnetic field by the exchange field carried out by these authors is not substantiated since the exchange field is a function of an intrinsic parameter. For this reason, the Landau potential used in such calculations contains fourth-order invariants of the external magnetic field,[15,16] which contradicts the thermodynamic theory of phase transitions.[17] Consequently, following Refs. 6 and 8, we shall calculate free energy in accordance with the thermodynamic definition of free energy $F = E - T\sigma$, where E and σ are the energy and entropy, which are functions of order parameters. This approach to the calculation of nonequilibrium free energy is substantiated sufficiently well in Refs. 9–11 and its application in Refs. 6 and 8 is justified.

Wave eigenfunctions of spin in the mean field method applied to system (1), which satisfy relations (3), can be written in the form[8,12,13]

$$|\psi_1\rangle = \cos \varphi |1\rangle + \sin \varphi |-1\rangle, \quad |\psi_2\rangle = |0\rangle,$$

$$|\psi_3\rangle = -\sin \varphi |1\rangle + \cos \varphi |-1\rangle. \qquad (7)$$

In the basis of these functions, only the z-components of spin differ from zero, and the quadrupole moment has a diagonal form. Consequently, free energy is a function of the thermodynamic parameters

$$M = \frac{1}{N} \sum_{\mathbf{f}} \bar{S}_{z\mathbf{f}}; \quad d_{zz} = \frac{1}{N} \sum_{\mathbf{f}} \bar{Q}_{\mathbf{f}zz};$$

$$d_{yy} = \frac{1}{N} \sum_{\mathbf{f}} \bar{Q}_{\mathbf{f}yy}; \quad d_{xx} = \frac{1}{N} \sum_{\mathbf{f}} \bar{Q}_{\mathbf{f}xx}, \qquad (8)$$

where N is the number of spins.

The energy of interaction for system (1) as a function of thermodynamic mean values (8) has the form

$$\tilde{E} = \frac{E}{N} = [J-(1/2)B]M^2 + B(d_{xx}^2 + d_{yy}^2 + d_{zz}^2). \qquad (9)$$

Denoting by P_1, P_2, and P_3 the probabilities of the spin states $|\psi_1\rangle$, $|\psi_2\rangle$, and $|\psi_3\rangle$ which can be defined in terms of the ratio of number of particles in each of these states to the total number of particles, we can write the conventional expression for entropy per particle:

$$\sigma = -\sum_{i=1}^{3} P_i \ln P_i. \tag{10}$$

Calculating $\bar{S}_z, \bar{Q}_{zz}, \bar{Q}_{yy}, \bar{Q}_{xx}$ in basis (7), we find that parameters (8) can be expressed in terms of φ, P_1, P_2, and P_3:

$$M = (P_1 - P_2)\cos(2\varphi);$$

$$d_{xx} = 1 - \frac{1}{2}(P_1 + P_3) + \frac{1}{2}(P_1 - P_3)\sin(2\varphi),$$

$$d_{zz} = P_1 + P_3; \tag{11}$$

$$d_{yy} = 1 - \frac{1}{2}(P_1 + P_3) - \frac{1}{2}(P_1 - P_3)\sin(2\varphi).$$

Using formulas (11) we can write the expression for entropy in the form of a functions of M, d_{zz}, d_{xx}, and d_{yy}. Consequently, the free energy of system (1) can be written in the form

$$\tilde{F} = \frac{1}{N} F = \tilde{E} - T\sigma = \left(J - \frac{1}{2}B \right)M^2 + B\left[d_{zz}^2 + 2\left(1 - \frac{1}{2}d_{zz}\right)^2 \right.$$

$$+ \frac{1}{2}(d_{xx} - d_{yy})^2 \right] + T\left[\frac{1}{2}\left(d_{zz} + \sqrt{M^2 + (d_{xx} - d_{yy})^2} \right) \right.$$

$$\times \ln\left(\frac{1}{2}\left(d_{zz} + \sqrt{M^2 + (d_{xx} - d_{yy})^2}\right) \right) + \frac{1}{2}(d_{zz}$$

$$- \sqrt{M^2 + (d_{xx} - d_{yy})^2})\ln\left(\frac{1}{2}\left(d_{zz} - \sqrt{M^2 + (d_{xx} - d_{yy})^2}\right) \right)$$

$$+ (1 - d_{zz})\ln(1 - d_{zz}). \tag{12}$$

For the free energy (12), we can obtain the following solutions of the equations of state, determined from the minimum value of $\tilde{F}$ in M, d_{zz}, d_{xx}, and d_{yy}: (1) the solution with $M \neq 0$, $d_{zz} \neq d_{yy} = d_{xx}$ corresponding to the ferromagnetic phase; (2) quadrupole solutions with $M = 0$ and (a) $d_{xx} = d_{yy} \neq d_{zz}$, (b) $d_{zz} = d_{yy} \neq d_{xx}$, and (c) $d_{zz} = d_{xx} \neq d_{yy}$, corresponding to the quadrupole phase, and (3) the solution with $M = 0$, $d_{zz} = d_{xx} = d_{yy} = 2/3$, corresponding to the paramagnetic phase (PP). An analysis carried out by us as well as the results obtained in Refs. 4–7 shows that for $|B| \ll |J|$, only solutions (3) and (1) exist for $T > T_c$ and $T < T_c$, respectively, the transition between them being of the second order. As the value of $|B|$ increases but still remains smaller than $|J|$, this transition becomes of the first order. For $|B| > |J|$, the phase transition from state (3) to (1) occurring upon a decrease in T is replaced by a first-order transition from (3) to (2c) at $T = T_Q$. The magnetic field oriented along the z-axis alone is insufficient for the selection of solution (2c) from the three solutions (2) since in order to determine uniquely the orientation of the quadrupole moment, we must exclude degeneracy in the plane perpendicular to the field. Using this theory, we can consider a hypothetical system of states at $T < T_c$, $T < T_Q$, emerging upon the variation of B for a constant J. In this case, a transition between the FP and QP occurs for $B = J$ and is of the first order. Naturally, the discussion has a sense only for theoretical analysis of the

results without any comparison with experimental data. Since we are dealing with a first-order transition, the applicability of the system of coordinates for M to quadrupole moment is only of illustrative interest. It is important, however, that the tensor of quadrupole moment in the QP corresponds to an oblate ellipsoid, while the same tensor of quadrupole moment in the FP corresponds to a prolate ellipsoid. If a magnetic field is applied to the QP, the quadrupole moment is oriented so that the magnetic field lies in the plane of the oblate ellipsoid, and the tensor of quadrupole moment of the QP in the magnetic field becomes biaxial. If a magnetic field is applied to the FP, the direction of M, and hence the extended axis of the ellipsoid, will be oriented along the field, and the tensor will remain uniaxial.

Taking into account what has been said above, it is convenient to describe the behavior of these phases in a unified system of coordinates by considering an auxiliary Hamiltonian stabilizing the spatial degeneracy of system (1) and having the form

$$H = \sum_{\mathbf{f}} [(-hS_{z\mathbf{f}} + \tilde{A}(S_{z\mathbf{f}})^2 + \tilde{B}(S_{x\mathbf{f}})^2 + \tilde{C}(S_{y\mathbf{f}})^2)], \tag{13}$$

where the field h and the parameters $\tilde{A}$, $\tilde{B}$, $\tilde{C} < 0$, $|\tilde{A}| > |\tilde{B}| > |\tilde{C}|$; $h \to 0$ and $\tilde{A}$, $\tilde{B}$, $\tilde{C} \to 0$ define quasi-mean values (Bogoliubov's method) for M along the z-axis and the principal values for quadrupole moment so that the normal to the plane of the oblate ellipsoid in QP lies along the y-axis.

LANDAU POTENTIAL

Using the equality $d_{zz} + d_{xx} + d_{yy} = 2$ following from $S_z^2 + S_x^2 + S_y^2 = 2$, we expand the energy (12) into a series in M, $\Delta_{zz} = d_{zz} - 2/3$ and $\Delta_{xx} = d_{xx} - 2/3$, confining our analysis to the fourth power in small parameters M, Δ_{zz}, and Δ_{xx}:

$$\Phi = \left(J - \frac{1}{2}B + \frac{3}{2^2}T \right)M^2 + \frac{3^2}{2^5}TM^4 + (2B + 3T)(\Delta_{zz}^2$$

$$+ \Delta_{xx}^2) + \frac{3^2}{2}T(\Delta_{zz}^4 + \Delta_{xx}^4) + (2B + 3T)\Delta_{zz}\Delta_{xx}$$

$$- \frac{3^2}{2}T(\Delta_{zz}^2\Delta_{xx} + \Delta_{xx}^2\Delta_{zz}) + 3^2T(\Delta_{zz}^3\Delta_{xx} + \Delta_{xx}^3\Delta_{zz})$$

$$+ \frac{3^3}{2}T\Delta_{zz}^2\Delta_{xx}^2 + \frac{3^2}{2^2}TM^2(\Delta_{xx}^2 + \Delta_{zz}^2) + \frac{3^2}{2}TM^2\Delta_{zz}\Delta_{xx}$$

$$- \frac{3^2}{2^3}TM^2\Delta_{zz}. \tag{14}$$

Thus, the Landau potential of system (1) is a function of the vector order parameter and two components of the tensor order parameter.

If the value of B is comparable with J in the order of magnitude, the thermodynamic model (14) for the state with $M \neq 0$, $\Delta_{zz} \neq 0$, $\Delta_{xx} \neq 0$ is strongly nonlinear.[18] This means that the Landau potential for the FP, which can be presented as a function of M alone, contains, in contrast to (14), higher powers in M since if $B \sim J$, we cannot use the approximation of direct proportionality of the quadrupole order parameter to

the square of M. The terms describing an interaction of the quadrupole origin are symmetric to the transposition $\Delta_{zz} \rightarrow \Delta_{xx}$, which permits the solution with $\Delta_{zz} = \Delta_{xx}$ for $M = 0$. For $M \neq 0$, the last term in (14) implies that $\Delta_{zz} \neq \Delta_{xx}$ and $\Delta_{zz} > \Delta_{xx}$.

The coefficients of the Landau potential (14) have singularities which are manifested in the reversal of signs of the coefficients of second-degree invariants of T, which take place for

$$T_c = -\frac{2^2}{3}[J - (1/2)B], \quad T_Q = -\frac{2}{3}B.$$

For $T = 0$ and $J = B$, the energy of the quadrupole state is equal to the energy of the ferromagnetic state, and hence one state is transformed into the other when this equality holds and at $T = 0$. However, the equality $T_c = T_Q$ holds for $J = B$. Consequently (see above), only one of the phases is realized in model (1) for any values of the parameters J and B and for $J \neq B$: either the FP for $|J| > |B|$, or the QP for $|J| < |B|$.[7] This peculiarity of the model does not depend on the number of terms in the expansion of free energy and will probably disappear when fluctuations are taken into account. It is still interesting to consider the cases when the QP and FP exist in a crystal with $J \neq B$ in different temperature intervals and replace each other. For example, a possible way to eliminate the above-mentioned peculiarity is to take into account in (1) isotropic three-particle interactions of the type

$$D\sum_{\mathbf{f,g,l}}(\mathbf{S_f \cdot S_g})(\mathbf{S_g \cdot S_l}). \tag{15}$$

As a result, potential (14) will contain the terms $(2/3)DM^2$ and $DM^2\Delta_{zz}$, and hence the coefficients of the invariants M^2 and $M^2\Delta_{zz}$ will be renormalized. In this case, the phase transition at $T = 0$ occurs if $J = B - D$. For these values of exchange parameters, $T_Q \neq T_c$, and $T_Q > T_c$ for $D < 0$. This means that for certain values of D and B, there exists an interval of values of J in which an increase in temperature leads first to a first-order phase transition from the FP to the QP, followed by a first-order phase transition from the QP to the PP.

MAGNETIC SUSCEPTIBILITY AND MAGNETOSTRICTION

Following Ref. 1, we take into account magnetoelastic interactions in potential (14) as well as the Zeeman term

$$\Phi_2 = a_1 M^2 + a_2 M^4 + b_1(\Delta_{zz}^2 + \Delta_{xx}^2) + b_2(\Delta_{zz}^4 + \Delta_{xx}^4)$$
$$+ b_3\Delta_{zz}\Delta_{xx} + b_4(\Delta_{zz}^2\Delta_{xx} + \Delta_{xx}^2\Delta_{zz}) + b_5(\Delta_{zz}^3\Delta_{xx}$$
$$+ \Delta_{zz}\Delta_{xx}^3) + b_6\Delta_{zz}^2\Delta_{xx}^2 + f_1M^2(\Delta_{zz}^2 + \Delta_{xx}^2)$$
$$+ f_2M^2\Delta_{zz}\Delta_{xx} + f_3M^2\Delta_{zz} + \gamma M^2(U_{zz} + U_{xx}) + \eta(U_{zz}$$
$$+ U_{xx})(\Delta_{zz} + \Delta_{xx}) + c(U_{zz}^2 + U_{xx}^2) - hM, \tag{16}$$

where the coefficients a, b, and f correspond to the coefficients of the relevant terms in expression (14) taking into account possible three-spin interactions. In the general case, these coefficients can be regarded as arbitrary since they were obtained in (14) in the mean field approximation. Such

a form of the Landau potential allows us to simplify considerably the expressions obtained as a result of calculations. It would be expedient to carry out a thermodynamic analysis of model (16) in the most general form.

Magnetoelastic interactions of the spin–spin type are denoted by constant γ, while constant η is of the one-particle origin.[19] Minimizing potential (16) in U_{zz} and U_{xx}, we find that magnetostriction in (16) is directly proportional to M^2, Δ_{zz}, and Δ_{xx}. The lattice is deformed in the (z,x) plane, so that the following equality holds:

$$U_{zz} = U_{xx} = -\frac{\gamma M^2 + \eta(\Delta_{zz} + \Delta_{xx})}{2c}. \tag{17}$$

In order to simplify the problem, we neglect in the potential (16) the magnetoelastic interactions associated with the orientation of magnetization relative to the crystallographic axes. It follows from (17) that in view of one-particle magnetoelastic interactions in QP in which $M = 0$, while $\Delta_{zz} = \Delta_{xx} \neq 0$, lattice deformation differs from that in magnets with a strong one-ion anisotropy[19] since the former are associated with the emergence of a quadrupole order and exhibit an anomalous dependence on temperature.[1] Depending on the relation between the constants γ and η, such a magnetostriction can be stronger than lattice deformations in the FP.

In addition, the application of a magnetic field to such a system gives rise to strains which are proportional to h^2 as in the case of anisotropic magnets. Such a magnetostriction was described in Refs. 15, 16, and 20 with the help of generalized susceptibilities of the Landau potential. In view of the quadratic dependence of strain on the field, however, it is expedient to calculate the derivatives $(\partial^2 U_{zz})/\partial h^2$ and $(\partial^2 U_{xx})/\partial h^2$. Taking into account relation (17) and differentiating twice the equations of state for potential (16) with respect to the field,

$$\frac{\partial\Phi_2}{\partial M} = 0, \quad \frac{\partial\Phi_2}{\partial\Delta_{zz}} = 0, \quad \frac{\partial\Phi_2}{\partial\Delta_{xx}} = 0, \tag{18}$$

we obtain the following limiting equations in h (for $h \to 0$):

$$\left.\frac{\partial^2 U_{zz}}{\partial h^2}\right|_{h\to0} = \left.\frac{\partial^2 U_{xx}}{\partial h^2}\right|_{h\to0} = -\frac{\gamma}{c}\chi^2 - \frac{\eta}{2c}\left(\left.\frac{\partial^2\Delta_{zz}}{\partial h^2}\right|_{h\to0}\right.$$
$$\left. + \left.\frac{\partial^2\Delta_{xx}}{\partial h^2}\right|_{h\to0}\right). \tag{19}$$

Here χ is the magnetic susceptibility for $h \to 0$:

$$\chi = \frac{1}{2[a_1 + f_3\Delta + (2f_1 + f_2)\Delta^2]}; \tag{20}$$

$$\left.\frac{\partial^2\Delta_{zz}}{\partial h^2}\right|_{h\to0} + \left.\frac{\partial^2\Delta_{xx}}{\partial h^2}\right|_{h\to0}$$
$$= -\frac{2f_3 + 4(f_2 + 2f_1)\Delta}{2b_1 + b_3 + 6b_4\Delta + 6(2b_2 + 2b_5 + b_6)\Delta^2}\chi^2. \tag{21}$$

In formulas (20) and (21), Δ stands for $\Delta = \Delta_{xx} = \Delta_{zz}$, which is valid for a state with $M = 0$ since $h \to 0$.

It follows from (20) that the reciprocal susceptibility in the PP for which $M=0$ and $\Delta_{zz}=\Delta_{xx}=0$ is proportional to T ($\chi^{-1}\cong a_1$), i.e., obeys the Curie–Weiss law.

If the QP precedes the FP, $\Delta\neq 0$, and the dependence $\chi^{-1}(T)$ is nonlinear. The contribution to the denominator in the expression for χ can strongly depend on Δ since the parameters f_1, f_2, and f_3 are not small and have different signs. Substituting (20) into (21) and (19), we obtain

$$\frac{\partial^2 U_{zz}}{\partial h^2}\bigg|_{h\to 0}=\frac{\partial^2 U_{xx}}{\partial h^2}\bigg|_{h\to 0}$$

$$=\left[-\frac{\gamma}{c}+\frac{\eta}{c}\frac{f_3+2(f_2+2f_1)\Delta}{2b_1+b_3+6b_4\Delta+6(2b_2+2b_5+b_6)\Delta^2}\right]\chi^2.$$

$$(22)$$

In the paramagnetic state for which $\Delta=0$, this expression can be written in the form

$$\frac{\partial^2 U_{zz}}{\partial h^2}\bigg|_{h\to 0}=\frac{\partial^2 U_{xx}}{\partial h^2}\bigg|_{h\to 0}=\left[-\frac{\gamma}{c}+\frac{\eta}{c}\frac{f_3}{(2b_1+b_3)}\right]\chi^2.$$

$$(23)$$

Thus, the temperature dependence of the second derivatives of strain with respect to the field has two singularities. The first singularity is associated with the vanishing of the reciprocal susceptibility χ^{-1} at $T=T_c$ for $a_1=0$, while the second is the vanishing of the denominator in the parentheses in (23) $(2b_1+b_3=0)$ at $T=T_Q$. It should be emphasized that the second singularity is realized for a strong BE and in the presence of quadrupole-elastic interactions.

The phase transition from the PP to the QP occurs as a first-order transition. The transition temperature is higher than T_Q, and hence the equality $\Delta=0$ does not hold at $T=T_Q$. However, numerical calculations made in Refs. 6 show that the difference between T_Q and the phase-transition temperature amounts to only a few percent. For this reason, the singularity on the temperature dependence of the second derivatives of deformations with respect to the field is not only asymptotic; the values of the second derivatives with respect to the field increase considerably in this temperature interval in view of the small difference between T_Q and the phase- transition temperature.

CONCLUSION

Completing the thermodynamic analysis of the magnetic ordering in the one-sublattice spin system with $S=1$ and a strong BE, we can single out several important peculiarities distinguishing such systems from Heisenberg magnets with bilinear exchange. The first peculiarity is associated with a strong nonlinearity of the Landau thermodynamic potential, which can lead to a nontypical temperature dependence of magnetization. The second peculiarity is the deviation from the Curie–Weiss law for magnetic susceptibility, which is due to the emergence of quadrupole order. The third peculiarity concerns the anomalies in the temperature dependence of lattice deformations for temperatures higher than the magnetic ordering temperature, which are also associated with the emergence of the quadrupole order. The fourth peculiarity is the existence of a singularity on the temperature dependence of the second derivatives of deformations with respect to the field, which is possible with one-particle mechanism of magnetoelastic interactions in the case of quadrupole ordering.

*)E-mail: ryabch@labmag.ip.kiev.ua

[1] V. M. Kalita, A. F. Lozenko, and P. A. Trotsenko, Fiz. Nizk. Temp. **21**, 671 (1995) [Low Temp. Phys. **21**, 525 (1995)].

[2] A. F. Andreev and I. A. Grishchuk, Zh. Éksp. Teor. Fiz. **87**, 467 (1984) [Sov. Phys. JETP **60**, 267 (1984)].

[3] E. L. Nagaev, *Magnets with Complex Exchange Interaction* [in Russian], Nauka, Moscow (1988).

[4] H. H. Chen and P. M, Levy, Phys. Rev. Lett. **27**, 1383 (1971).

[5] V. M. Matveev, Zh. Éksp. Teor. Fiz. **65**, 1626 (1973) [Sov. Phys. JETP **38**, 813 (1973)].

[6] N. Nauciel-Bloch, G. Sarma, and A. Castets, Phys. Rev. B **5**, 4603 (1972).

[7] H. H. Chen and P. M. Levy, Phys. Rev. B **7**, 4267 (1973).

[8] V. M. Kalita, Fiz. Tverd. Tela **33**, 1940 (1991) [Sov. Phys. Solid State **33**, 1092 (1991)].

[9] M. A. Leontovich, Sov. Phys. JETP **8**, 844 (1938).

[10] V. G. Bar'yakhtar, I. M. Vitebskii, and D. A. Yablonskii, Fiz. Tverd. Tela **19**, 2135 (1977) [Sov. Phys. Solid State **19**, 1249 (1977)].

[11] V. M. Kalita and V. M. Loktev, Ukr. Fiz. Zh. **40**, 235 (1995).

[12] V. M. Loktev and V. S. Ostrovskii, Ukr. Fiz. Zh. **23**, 1708 (1978).

[13] V. M. Loktev and V. S. Ostrovskii, Fiz. Nizk. Temp. **20**, 983 (1994) [Low Temp. Phys. **20**, 775 (1994)].

[14] S. V. Tyablikov, *Methods in Quantum Theory of Magnetism*, Plenom Press, NY, 1967.

[15] P. Morin, D. Schmitt, and Tr. Lacheisserie, Phys. Rev. B **21**, 1742 (1980).

[16] P. Morin and D. Schmitt, Phys. Rev. B **27**, 4412 (1983).

[17] L. D. Landau and E. M. Lifshitz, *Statistical Physics* [in Russian], Nauka, Moscow (1976).

[18] Yu. M. Gufan, *Structural Phase Transitions* [in Russian], Nauka, Moscow (1982).

[19] A. K. Zvezdin, V. M. Matveev, A. A. Mukhin, and A. I. Popov, *Rare-Earth Ions in Magnetically Ordered Crystals* [in Russian], Nauka, Moscow (1985).

[20] P. Morin and D. Schmitt, Phys. Rev. B **26**, 3891 (1982).

Translated by R. S. Wadhwa

Optical absorption edge in $\alpha-\mathrm{Fe_2O_3}$: The exciton−magnon structure

A. I. Galuza, A. B. Beznosov, and V. V. Eremenko

*B. Verkin Institute for Low Temperature Physics and Engineering, National Academy of Sciences
of the Ukraine, 310164 Kharkov, Ukraine*[*)]

Transmission spectra of synthetic and natural hematite (α-$\mathrm{Fe_2O_3}$) crystals are measured at temperatures 10, 25, and 300 K in the wavelength range 500–1100 nm, and the absorption spectra are computed. Pure exciton and exciton−magnon $d-d$ transition bands are revealed, the corresponding wavelengths at 10 K being $\lambda_0 = 1020$ nm and $\lambda_1 = 965$ nm respectively. The half-widths and oscillator forces are $g_0 = 84$ cm^{-1}, $f_0 = 4 \times 10^{-9}$, $g_1 = 60$ cm^{-1}, $f_1 = 1.4 \times 10^{-7}$ for 10 K, $g_0 = 85$ cm^{-1}, $f_0 = 5 \times 10^{-9}$, $g_1 = 110$ cm^{-1}, $f_1 = 2.1 \times 10^{-7}$ for 25 K. The mechanisms of band formation for weakly allowed $d-d$ transitions in hematite are analyzed. © *1998 American Institute of Physics.* [S1063-777X(98)00610-0]

The interest towards low-temperature properties of the oxides of $3d$-elements, which has been stimulated in recent years by the advances made in the physics of oxide superconductors, has spread to a considerable extent towards the temperature dependence of the optical characteristics of magnetically concentrated crystals, including iron oxides.

An iron ion in oxides can be in different charge states separated by relatively small energy intervals. This is manifested in the existence of iron compounds with different degrees of oxidation and different levels of stability, i.e., FeO, $\mathrm{Fe_2O_3}$, and $\mathrm{Fe_3O_4}$. Moreover, different electron configurations separated by even narrower energy intervals may also exist in the same charge state of iron ion in iron–oxygen atomic groups. This leads to a variety of phases (crystalline, magnetic, ferroelectric, etc.) with much lower energy differences within the same chemical compound, as well as to noticeable interconfigurational fluctuations which may be thermally activated or of quantum-mechanical origin.[1,2] These peculiarities of the electron structure of iron oxides determine their low-temperature properties to a considerable extent.

Direct information about the electron energy spectrum of iron–oxygen atomic groups can be obtained from optical measurements. It should be interesting to carry out investigations of hematite (α-$\mathrm{Fe_2O_3}$) as a standard and most stable insulating oxide of iron.[3]

Optical absorption of hematite begins in the near infrared spectral region and is formed by $d-d$ transition bands between energy levels for the electron configuration d^5 of the $\mathrm{Fe^{3+}}$ ion, which are split by the intrinsic crystal field.[4,5] The main spectral structure is associated with electron transitions involving magnons, phonons, or with simultaneous excitation of two magnetic cations, since double forbiddenness (in parity and spin) considerably weakens pure exciton one-particle $d-d$ transitions. Bands of such a pure exciton absorption corresponding to the transition $^6A_{1g}(^6S) \rightarrow {}^4T_{1g}(^4G)$ have been observed in the transmission spectra of $\mathrm{Y_3Fe_5O_{12}}$,[6] $\mathrm{FeBO_3}$,[7] and $\mathrm{Fe_3BO_6}$.[8] In this work, we shall endeavor to reveal pure exciton $d-d$ transition bands in hematite and to study the temperature dependence of its optical absorption edge.

SAMPLES AND EXPERIMENTAL TECHNIQUE

Samples of α-$\mathrm{Fe_2O_3}$ crystals in the form of thin plates cut from natural mineral hematite (plate thickness $t = 6$ μm), as well as synthetic single crystals (cuts parallel to the (111) plane with a surface density of defects of the order of 10^2–10^3 cm^{-2}, plate thickness 23 and 170 μm) were investigated.

Transmission spectra $\tau(\lambda)$ were measured experimentally at helium ($T = 10$ K), hydrogen ($T = 25$ K), and room temperatures in the wavelength range $500 \leq \lambda \leq 1100$ nm. Measurements were made by the double beam method[9] using a double prism monochromator DMR-4, a standard helium cryostat with fused quartz windows and a halogen incandescent lamp KIM-12-100 as the source of light. Photomultipliers FEU-79 and FEU-83 cooled by liquid nitrogen were used as radiation detectors. The photocathodes of the amplifiers were located quite far from the sample surface to prevent distortion of the transmission spectrum being recorded by the possible luminescence in d-compounds.

Because of the brittleness of hematite, the sample of thickness 6 μm was not detached during measurements from the glass substrate to which it was glued for mechanical processing. The distortions caused by the presence of the substrate and glue were weakened by introducing into the comparison channel a compensating couple made of TF-4 glass plates with a high refractive index $n \approx 1.72$ (the latter were joined by using the same glue with which the sample was fastened to the substrate).

RESULTS AND DISCUSSION OF SPECTRA

The spectral dependences of the absorption coefficient $\alpha(\lambda)$ of hematite shown in Fig. 1 were calculated from the data on transmittance of thin samples $t = 6$ and 23 μm taking into account the reflection coefficient R:[10]
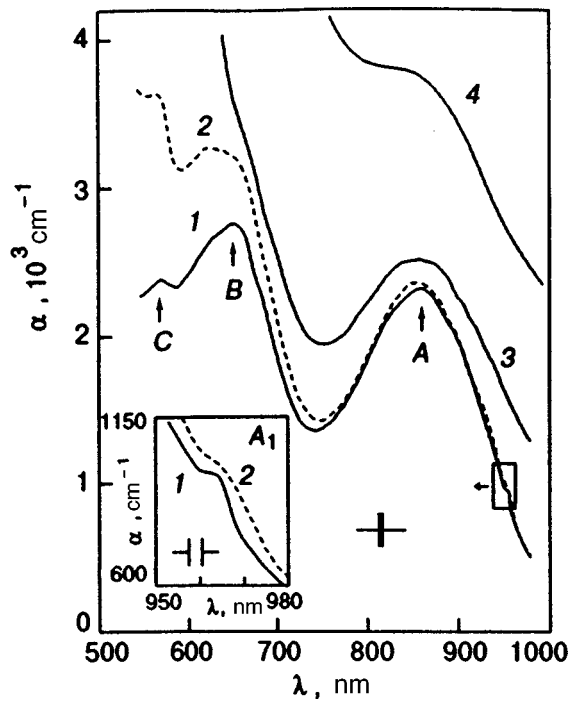
FIG. 1. Absorption spectra of α-Fe$_2$O$_3$ crystals at temperatures 10 K (curve *1*), 25 K (curve *2*), and 300 K (curve *3, 4*). Curves *1–3* correspond to a synthetic single crystal of thickness 23 μm, and curve *4* to a natural hematite mineral of thickness 6 μm. *A*, *B*, and *C* are many-particle transition bands. Curves *1* and *2* in the inset are in the region of the exciton–magnon band A_1.

$$\alpha = \frac{2 \ln(1-R) - \ln \tau}{t}.$$

The spectra recorded in the region of bands *A* and *B* (transitions $^6A_{1g}$ to $^4T_{1g}$ and $^4T_{2g}$, wavelengths $\lambda = 860$ and 640 nm, respectively) are in accord with the results obtained in Refs. 11–13.

If by the absorption edge we mean the spectral region in which the relation $\alpha t \sim 1$ is still satisfied for quite bulky samples ($t = 10$ μm), i.e., the transmittance $\tau \sim 0.3$ and the absorption coefficient $\alpha \sim 1000$ cm^{-1}, the absorption edge in hematite corresponds to the wavelength $\lambda \sim 1$ μm. Note that the effect of temperature variation on the absorption edge in α-Fe$_2$O$_3$ is much weaker than that due to the presence of impurities: the absorption of the natural sample (the mineral contained Ti, V, Si, Al, Mn, Ca, Mg, Cr, Ni, P and S impurities in descending order of concentration) is about 1.5 times (curve *4*) stronger than in a synthetic single crystal (curves *1–3*). In this case, a comparison of absorption in samples with thickness 23 μm (Fig. 1) and 170 μm (Fig. 2) shows that the influence of lattice defects is apparently comparable with the temperature effect. The absorption in a thin sample is slightly higher in accordance with an increase in the relative contribution from the defect-enriched surface layers.

The effect of interference on the shape of the transmission spectrum was negligible, since the value of τ did not exceed 0.2 in the entire range of measurements.

It can be seen from Fig. 1 that the weakly manifested structure of the *A*-band includes the low-temperature singularity A_1 in the form of a small ''hump'' on the long-wave
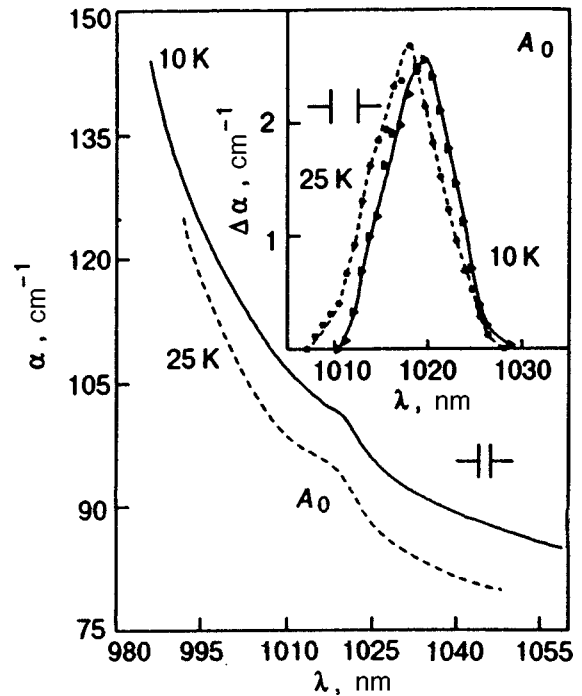

FIG. 2. Absorption spectra of a α-Fe$_2$O$_3$ single crystal of thickness 170 μm at temperatures 10 and 25 K. The inset shows the pure exciton band A_0.

slope in curves *1* and *2*, which can be seen clearly in the inset to Fig. 1. By disregarding the background (right slope of the *A*-band), we were able to determine the spectral position of the band A_1 (its peak at $T = 10$ K corresponds to $\lambda \approx 965$ nm), as well as the number of dispersed electrons corresponding to it:[14]

$$N_e = \frac{mc}{2\pi^2 e^2} \int_0^\infty n(\omega)\alpha(\omega)d\omega,$$

where *m* and *e* are the electron mass and charge, *c* and ω the velocity and frequency of light, and *n* is the refractive index of the material. In the approximation of the Lorentz oscillator force *f*, the quantity N_e must be equal to Nf, where *N* is the total number of electrons that can participate in the formation of the A_1-band. Assuming that five such electrons correspond to each Fe atom, we obtain the value $f = 1.4 \times 10^{-7}$ at 10 K and $f = 2.1 \times 10^{-7}$ at 25 K. The maximum absorption in the band is equal to 93 cm^{-1} at 10 K and 77 cm^{-1} at 25 K. The corresponding half-widths are 60 cm^{-1} and 110 cm^{-1}. The error in determining the oscillator parameters is estimated at $\sim 20\%$.

Such a value of *f* could be associated with a pure exciton transition. However, such an interpretation is not quite in accord with the nature of the absorption spectrum as a whole in the vicinity of the A_1-band, and necessitates the quest for an alternative interpretation. Assuming that the frequencies of $d-d$ transitions in oxide compounds of Fe^{3+} with octahedral symmetry (α-Fe$_2$O$_3$ also possesses this symmetry) differ only on account of the difference in the component of cubic symmetry in the crystal field (parameter Dq),[3,4] which is determined by the separation between Fe^{3+} and O^{2-}, we analyzed the available data on *r* and frequency ω of the pure exciton transition $^6A_{ig} \rightarrow {}^4T_{ig}$ in corundum (crystalline ana-

log of hematite[3]) with iron impurity ($r = 1.92$ Å,[15] and $\omega = 9450$ cm^{-1})[16] and in $Y_3Fe_5O_{12}$ ($r = 2.02$ Å,[17] $\omega = 9807$ cm^{-1}).[6] It was found that in the linear approximation for the function $\omega(r)$ for hematite (the value of r averaged over oxygen surroundings is equal to 2.025 Å),[18] we can expect the value $\omega = 9825$ cm^{-1} ($\lambda = 1018$ nm).

The transmittance range was extended to 1100 nm by investigating samples of large thickness (Fig. 2), and the weak band A_0 shown in the inset was detected after elimination of the background. The spectral position of A_0 was determined as (1018 ± 3) nm at 25 K and (1020 ± 3) nm at 10 K. Within the limits of the error (associated mainly with the procedure of background elimination), these results coincide with the above estimate so that we can identify the A_0 band as a consequence of a pure exciton transition $^6A_{1g}(^6S) \rightarrow {}^4T_{1g}(^4G)$. Calculations of the oscillator force for the band A_0 also lead to the values characteristic of such transitions: 4×10^{-9} and 5×10^{-9} at temperatures 10 and 25 K, respectively. The maximum absorption in the band is equal to 2.6 cm^{-1} at 10 K and 2.7 cm^{-1} at 25 K. The corresponding values of half-width are 84 and 85 cm^{-1}. Identical methods are used for eliminating the background and determining the oscillator parameters for the bands A_0 and A_1.

The doublet structure with a separation of about 5 nm between the components, which is manifested in the asymmetric form of the band A_0, is close to that observed in $Y_3Fe_5O_{12}$[6] and may be a result of splitting of the excited level T_{1g} of this transition, in particular under the effect of the trigonal component of the crystal field.[19]

The identification of the original line A_0 allows us to make certain assumptions about the origin of the other components of the band A also (Fig. 1). Thus, the low-temperature singularity A_1, which has a higher intensity than A_0 and is separated from it by 693 cm^{-1}, is probably associated with the simultaneous excitation of an exciton and a magnon: the frequency position of A_1, with respect to A_0 is in good agreement with the energy of the two-magnon band in the Raman spectrum of α-Fe$_2$O$_3$ according to the data obtained by Hart *et al.*[20] (the half-value of this energy, i.e., the magnon frequency at the edge of the band, is 690 cm^{-1}), and an increase in the oscillator force by an order of magnitude is associated with the removal of spin forbiddenness in transitions of this type.[5,21]

A further increase in the frequency leads to the participation of the crystal lattice vibrations in absorption (three optical phonons with frequencies 305, 435, and 525 cm^{-1} have been detected in infrared spectra[22]), as a result of which the parity forbiddenness is relaxed and the absorption increases, attaining a peak near 860 nm. The structure of the band A, which is determined by combinations of magnons and phonons participating in the absorption process, is not resolved easily even at 10 K, although the singularity at 925 nm can be attributed to the participation of two phonons, at 895 nm to two magnons, at 865 nm to a magnon and three phonons, and so on. The band width depends on the maximum number of quasiparticles participating in the given optical transition. For the observed half-width of 2400 cm^{-1} this number may be six or more. The large value of the oscillator force for the entire band A ($\sim 1.5 \times 10^{-4}$ according

to our estimates), which exceeds the value of f for a pure exciton transition by more than four orders of magnitude, points towards a strong exciton–phonon interaction in hematite.

Broadening of the crystal field transition due to stresses emerging in the crystal during mechanical polishing of the samples may also make a certain contribution to the width of the observed bands.[23] The mechanism of such a broadening in hematite may be the surface amorphization with the formation of a thin layer having its own phonon spectrum. This assumption is confirmed by the IR spectra of amorphous α-Fe$_2$O$_3$[22] containing only two phonon bands with frequencies 410 and 950 cm^{-1}, which differ considerably from the frequencies for crystalline hematite.

The B-band, which is observed only at low temperatures (starting from nitrogen temperatures[24]) and is close to the A-band in width and intensity, is associated with $d-d$ transitions from the ground state $^6A_{1g}(^6S)$ to the excited level $^4T_{2g}(^4G)$ next to $^4T_{1g}(^4G)$ involving both phonons and magnons (Fig. 1). We were not able to detect the pure exciton band corresponding to this transition (as in other oxides of d^5 elements[6–8,13,25,26]) probably due to a high background absorption level ($\alpha \sim 1000$ cm^{-1} in hematite). In the B-band, we can find a doublet with splitting close to the magnon frequency,[20] the intensity being redistributed towards the low-frequency component upon a decrease in temperature.

The degenerate level ^4E_g, $^4A_{1g}(^4G)$ is the next on the energy scale for the electron configuration d^5, but a transition to this level in oxides is expected at wavelengths shorter than 500 nm[6,7,27] and with the same oscillator force as in the first two transitions.[27] Hence the weak peak C ($\lambda \approx 560$ nm) cannot be associated with this transition. Apparently, this peak is a part of the B-band structure, and its observed frequency shift relative to the B-band can be presented in principle as a set of phonon and magnon frequencies.

In the interval $\lambda > 700$ nm, the absorption coefficient of hematite decreases slightly only in the interval between room and nitrogen temperatures,[12] which correlates with the process of freezing out of phonons, while the decrease in α for $\lambda < 700$ nm continues even during cooling from 25 to 10 K, which may be attributed to the effect of high-intensity temperature-dependent absorption bands at shorter wavelengths. Such a band with a strong temperature dependence is located in the vicinity of 400 nm. It is observed in the spectra of transmission, reflection and magneto-optical effects, and was attributed to transitions of $3d$ electrons to the $4p$ shell,[12] charge transport from the $2p$ shell of oxygen to the $3d$ shell of iron,[12,13,28] or to the two-exciton $d-d$ transition in Fe^{3+}.[10,26] For the excitation of both excitons in the same sublattice, a 1.5–2 orders of magnitude increase in absorption is envisaged in the latter mechanism upon an increase in temperature from 10 to 100 K (as it was observed by Fujiwara *et al.*[29] during investigations of the crystals MnF$_2$ and RbMnF$_3$). For a considerable bandwidth, this may lead to the temperature dependence of the absorption edge observed in hematite.

Thus, it can be concluded from the above analysis of the absorption edge of α-Fe$_2$O$_3$ that the weak A_0 line observed

at low temperatures is associated with pure exciton $d-d$ transitions and is the original line for the bands connected with the $^6A_{1g}(^6S) \rightarrow {}^4T_{1g}(^4G)$ transition, the exciton–magnon band (it is assumed to be the low-temperature band A_1), and the strong absorption band A formed as a result of many-particle transitions involving excitons, phonons and magnons.

*)E-mail: galuza@ilt.kharkov.ua

[1] K. Kato, S. Iida, Yanai, and Mizushima, J. Magn. Magn. Mater. **31-34**, 783 (1983).

[2] C. Boekema, K-C. Chan, R. L. Lichti *et al.*, J. Magn. Magn. Mater. **54-57**, 353 (1986).

[3] W. Bragg and G. Claringbull, *Crystal Structure of Minerals*, New York (1965).

[4] C. Ballhausen, *Introduction to Ligand Field Theory*, New York (1962).

[5] V. V. Eremenko, N. F. Kharchenko, Yu. G. Litvinenko, and V. M. Naumenko, *Magnetooptics and Spectroscopy of Antiferromagnets*, Springer-Verlag, New York (1992).

[6] W. Wettling, B. Andlauer, P. Koidl *et al.*, Phys. Stat. Sol. **59**, 63 (1973).

[7] B. Andlauer, O. F. Schirmer, and J. Schneider, Solid State Commun. **10**, 1655 (1973).

[8] B. Andlauer, R. Diehl, and M. S. Skolnick, J. Appl. Phys. **49**, 2200 (1978).

[9] A. I. Galuza and Yu. N. Yurkovskii, Otkrytiya i Izobreteniya **No. 6**, 192 (1988).

[10] A. I. Galuza, V. V. Eremenko, and A. I. Kirichenko, Fiz. Tverd. Tela (Leningrad) **21**, 1125 (1979) [Sov. Phys. Solid State **21**, 654 (1979)].

[11] F. J. Morin, Phys. Rev. **93**, 1195 (1954).

[12] P. C. Bailey, J. Appl. Phys. **31S**, 39S (1960).

[13] L. A. Marusak, R. Messier, and W. B. White, J. Phys. Chem. Solids **41**, 981 (1980).

[14] L. D. Landau and E. M. Lifshitz, *Electrodynamics of Continuous Media*, Pergamon Press, Oxford, 1960.

[15] K. Moorjani and N. McAvoy, Phys. Rev. **132**, 504 (1963).

[16] G. Lehmann, Z. Phys. Chem., Neue Folge **72**, 279 (1970).

[17] F. Euler and J. A. Bruce, Acta Crystallogr. **19**, 971 (1965).

[18] R. F. Newnham and Y. M. de Haan, Z. Kristallogr. **117**, 234 (1962).

[19] T. F. Veremeichik, B. N. Grechushnikov, I. N. Kalinkina, and D. T. Sviridov, Opt. Spectrosc. **36**, 1125 (1974).

[20] T. R. Hart, H. Temkin, and S. B. Adams, in *Proceedings of the 3rd Int. Conf. Light Scattering*, Brasil (1975).

[21] J. J. Krebs and W. G. Maisch, Phys. Rev. B **4**, 757 (1971).

[22] S. I. Popova, T. S. Tolstykh, and A. S. Ivlev, Opt. Spectrosc. **35**, 954 (1973).

[23] M. L. Jones, D. W. Shortt, and A. L. Schawlow, Phys. Rev. B **42**, 132 (1990).

[24] R. F. G. Gardner, F. Sweett, and D. M. Tanner, J. Phys. Chem. Solids **24**, 1175 (1963).

[25] K. W. Blazey, J. Appl. Phys. **45**, 2273 (1974).

[26] G. S. Krinchik, A. P. Khrebtov, A. A. Askochenskii *et al.*, Zh. Éksp. Teor. Fiz. **72**, 699 (1977) [Sov. Phys. JETP **45**, 366 (1977)].

[27] G. B. Scott, D. E. Lacklison, and J. L. Page, Phys. Rev. B **10**, 971 (1974).

[28] C. T. Chen and B. D. Cahan, J. Opt. Soc. Am. **71**, 932 (1981).

[29] T. Fujiwara, W. Gebhardt, K. Petanides, and Y. Tanabe, J. Phys. Soc. Jpn. **33**, 39 (1972).

ELECTRONIC PROPERTIES OF METALS AND ALLOYS

Influence of the shape of the electrodes on the tunnel current

R. J. P. Keijsers and J. Voets

Research Institute for Materials, University of Nijmegen, Toernooiveld 1, 6525 ED Nijmegen,
The Netherlands

O. I. Shklyarevskii

Research Institute for Materials, University of Nijmegen, Toernooiveld 1, 6595 ED Nijmegen,
The Netherlands and B. I. Verkin Institute for Low Temperature Physics and Engineering,
National Academy of Sciences of Ukraine, 47 Lenin ave., 310164 Kharkov, Ukraine*

H. van Kempen

Research Institute for Materials, University of Nijmegen, Toernooiveld 1, 6525 ED Nijmegen,
The Netherlands**

The tunnel resistance of highly stable, mechanically controlled break junctions of Al, Au, Cu, Pb, Ni, Pt, and Pt–Ir, have been recorded as a function of the electrode spacing over 6–7 decades. Clear deviations from the expected exponential behavior have been observed. Comparison with previous experimental and theoretical studies indicate that the discussed deviations in some cases are most probably due to the shape of, rather than to interactions between, the two electrodes. © *1998 American Institute of Physics.* [S1063-777X(98)00710-5]

1. INTRODUCTION

Over the last decade, the scanning tunneling microscope (STM) has developed into one of the most generally used instruments for the study of surfaces and small structures.[1–5] The atomic resolution in topographical measurements is a consequence of the strong dependence of the tunnel current on the distance between the tip and sample. The simplest and crudest approximation describing the tunnel current is a planar model of the barrier, leading to an exponential decrease of the tunnel current as a function of increasing electrode spacing. If the interaction between the tunneling electron and the opposing electrode, at which a charge builds up, is incorporated as a first order correction (image potential), the barrier height and width are found to reduce, but the general result stays the same for low bias voltages.[6]

Some experimental investigations of the tunnel current as a function of distance between tip and sample have been presented in the past. Gimzewski and Möller[7] have studied the transition from tunneling regime to point contact for a clean Ir tip and polycrystalline Ag surface. They observed the onset of a plateau in the tunnel resistance at small tip-sample distances ($\leqslant$2.5–3 Å before a jump to contact), which was subsequently explained theoretically by Lang.[8] He modeled the system by two flat jellium electrodes with a single tip atom present at one of the surfaces, and found that the tunnel current as a function of electrode separation leveled out at a conductance value of $\eta 2e^2/h$ (η being of order unity) as the situation came close to a one-atom size contact. A tight-binding calculation by Ferrer, Martín-Rodero, and

Flores[9] produced comparable results. Düring, Züger, and Pohl[10] studied the approach of an Ir tip to an Ir sample, and found only a weak onset for a plateau at small separations. Ciraci and Tekman[11] showed theoretically that, depending on material and tip-specific features, the tunnel resistance may saturate at very small distances, but can also increase almost linearly up to contact when plotted on a logarithmic scale. On the other hand, Krans *et al.*[12] observed *faster* than exponential behavior at a Pt mechanically controllable break junction, which they explained from attractive forces between the front atoms of the two tips. However, in all these experimental and theoretical investigations of tip-sample approach, deviations from exponential tunneling behavior were observed over at most two decades of the tunnel resistance, just before the jump to contact.

In a recent theoretical article, Laloyaux *et al.*[13] calculated the tunnel current for different $3D$ geometries of the two electrodes (tip and sample) by solving the exact Schrödinger equation numerically for the electron tunneling problem in such a multidimensional configuration. They studied the tunnel current as a function of tip-sample distance for sharp (hemispherical) and blunt (cylindrical) tips above a flat surface, and also studied the influence of the presence of a Gaussian boss or dip at the sample surface. Their results showed that certain tip-sample geometries can lead to significant deviations from the exponential relation between tunnel current and tip-sample distance over more than four orders of magnitude of the tunnel current, whereas the above described electron-mediated tip-sample interactions, which

arise because the potential barrier between the electrodes allows the wave functions to overlap at very small separations,[14] have never been predicted nor observed to cause deviations for more than two orders of magnitude.

In this work we shall present experimental observations of deviations from exponential tunneling behavior over a wide range of tunnel resistances between 10–20 kΩ and 1–5 GΩ, which can be attributed to a dependence of the tunnel current vs. distance relation on the $3D$ junction geometry. The results will be compared to the theoretical results of Laloyaux *et al.*[13] To ensure that the tip in our experiments had a well-defined apex, we discarded all measurements which did not show a well-defined jump to a one-atom point contact at relatively small distances. We also observed current-distance curves which showed characteristics attributable to strong mutual interactions between the electrodes. These last results are discussed in detail elsewhere.[15]

2. EXPERIMENTAL

The observation of possible deviations from exponential tunneling behavior requires a highly stable tunnel junction with an adjustable tip-sample (or tip-tip) distance. Therefore, we used the mechanically controllable break (MCB) junction technique[16] for our experiments. MCB junctions have already proven their high stability and adjustability in a study of the transition from weak link to superconducting tunnel junction[16] and in one-atom point contact experiments.[12] The stability of our setup is illustrated by the fact that we found it possible to reproduce current-distance characteristics several times over periods of more than 60 min. A drawback of the MCB-technique is that it is difficult to calibrate the tip-sample displacement, because it depends on the specific sample arrangement and on the way the sample breaks.

The setup we have used is drawn in a somewhat simplified way in Fig. 1. The sample (a 50 μm metallic filament) is glued onto a phosphor-bronze bending beam covered with a thin insulating layer of kapton foil, using two small drops of Stycast 2850 FT epoxy. The sample is then cut for about 90% of its diameter at the midpoint between the two drops of epoxy. After that, the sample is mounted in the setup (Fig. 1), and is cooled to 4.2 K in high vacuum surroundings. The sample is then broken by turning the spindle, thus creating two clean electrodes. The tunnel distance (or contact size) can be adjusted using a differential screw connected to the spindle. Both spindle and differential screw are driven by using fork-blade mechanisms, enabling us to decouple the setup from the outside world if desired. Fine adjustment and scanning of the distance is done by means of the piezo driver. Mounting of a backspring (see Fig. 1) turned out to increase the stability of our setup strongly. External vibrations were suppressed by suspending the cryostat from the ceiling using elastic cords (''bungy cords'').

In order to be able to observe deviations from exponential behavior of the tunnel resistance R_T as a function of the tip distance z, we must ascertain that z is proportional to the vertical displacement y of the center of the beam when it is bent. Therefore, the relation between z and y will be discussed in considerable detail here.
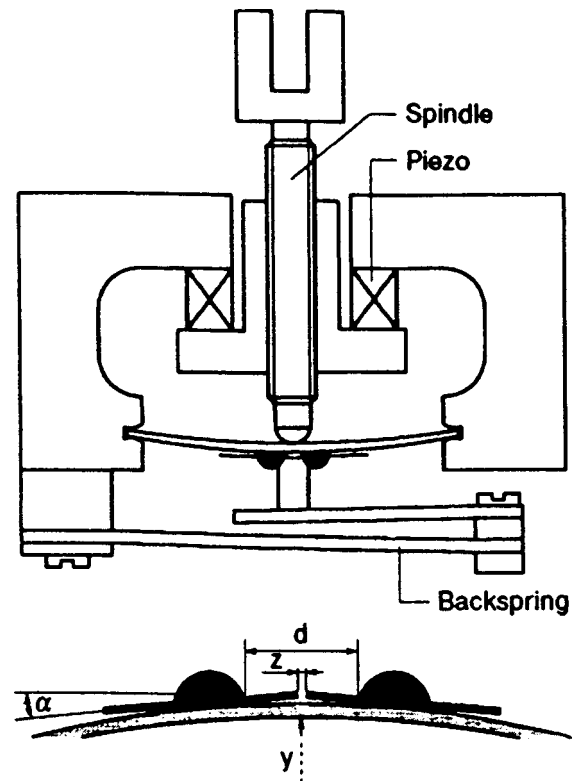

FIG. 1. Schematic drawing of the MCB-setup. The sample consists of a thin (50 μm) metallic wire, which is glued with two drops of Stycast 2850 FT on top of a phosphorbronze bending beam that is covered with an insulating layer. The wire is cut to more than 80% of its diameter, and can be broken in vacuum at low temperatures by turning the spindle. A differential screw mechanism that is also attached to this spindle can be used to bring the junction into the tunnel regime, or to establish a small contact. Very small tip-tip displacements can then be realized in a controlled way by applying a voltage over the piezo ring. The backspring can be used to obtain ''negative'' bending angles, but was also found to increase the stability of the setup strongly.

When the beam is bent, the surface of the beam beneath the filament will be stretched, leading to an increase in the distance between the two fixation points, and thus to an increase of z. Assuming that the tips just touch when there is no vertical displacement, the increase Δ_s due to surface stretching can be expressed as[17]

$$\Delta_s = \frac{Fh}{16EI}(2ld - d^2), \quad I = \frac{wh^3}{12}. \tag{1}$$

Here, d is the distance between the two anchoring points (see Fig. 1), F is the vertical force exerted on the bending beam, E is the modulus of elasticity of the beam, and h, l, and w are its thickness, length and width. Using an expression for the vertical displacement from Ref. 17, Δ_s can be re-written as

$$y = \frac{Fl^3}{48EI} \Rightarrow \Delta_s = 3y\,\frac{hd}{l^2}\left(2 - \frac{d}{l}\right). \tag{2}$$

The beams we use have dimensions $l \times w \times h = 28 \times 10 \times 0.4$ mm, and the distance d is about 0.5 mm.

Bending of the beam also leads to a non-zero slope α at the fixation points (Fig. 1). This causes an additional contribution Δ_z, to the distance between the tips, as well as a vertical displacement Δ_y

$$\Delta_z = d(1 - \cos \alpha) + 2p \sin \alpha, \quad \Delta_y = 2\varepsilon \sin \alpha, \qquad (3)$$

where ε stands for the distance between the point where the wire has been broken and the middle of the section of the wire between the two anchoring points, and p is the vertical distance of the wire at the anchoring points to the plane of flexure. For the case of a wire lying on top of a bending beam, this distance will be half the beam thickness h. The slope α is given by[17]

$$\alpha = \frac{3yd}{l^2} \left(2 - \frac{d}{l} \right) \qquad (4)$$

and has a small value in all experiments ($\alpha = 0.008$ rad for $y = 2$ mm). Therefore, $\Delta_z \approx (1/2) d\alpha^2 + 2p\alpha$. For $p = h/2$, the second term equals Δ_s. The term $(1/2) d\alpha^2$ is proportional to y^2, which in principle leads to a nonlinear relation between the separation $z = \Delta_s + \Delta_z$, of the two tips, and y. However, in our setup, this term is two orders of magnitude smaller than both the other term in (3) and Δ_s. In an experiment, y is typically varied over less than 1 μm around a value of 2 mm, and the change in slope $\partial z / \partial y$ over this range is less than 1.5×10^{-4} %. Neglecting the nonlinear term, a value of 330 for the ratio y/z is found, which is the estimated attenuation of the applied vertical displacement to the induced tip-tip distance.

The vertical displacement Δ_y is zero when the wire is cut exactly in the middle ($\varepsilon = 0$), but can be quite large when the wire breaks close to one of the fixation points ($\varepsilon = d/2$),

$$\Delta_y \approx 2\varepsilon \alpha = 3y \frac{d^2}{l^2} \left(2 - \frac{d}{l} \right), \qquad (5)$$

which is of the same order of magnitude as z. Because $\Delta_y \propto y$, the distance between the two tips will nevertheless be proportional to y, albeit the tips do not approach horizontally. However, when preparing the samples, extreme care was taken to ensure that the notch was as close as possible to the midpoint between the two gluing points, leading to no or just a small vertical displacement of the electrodes with respect to each other.

3. RESULTS AND DISCUSSIONS

In the above it has been shown that bending of the beam leads to $z \propto y$. There are however other effects that may affect the shape of measured current-distance characteristics. First of all, the experimentally measured $R_T(z)$ curve may deviate from its real shape due to thermal drift. However, we found that this effect was only significant in our experiments during the first hour after filling our cryostat with liquid helium.

Furthermore, we found that material flow (''backward,'' i.e., the tunnel distance increases while the piezo voltage is kept constant) was a rather large effect shortly after breaking the sample. It was found to depend strongly on the notch depth, and turned out to be larger for ''soft'' materials like Au, Al and Pb, than for Ni, Pt or a Pt-Ir(3%) alloy. Figure 2a shows the drift of the tunnel resistance R_T for an Al-sample which was previously cut for about 80% of its diameter. The
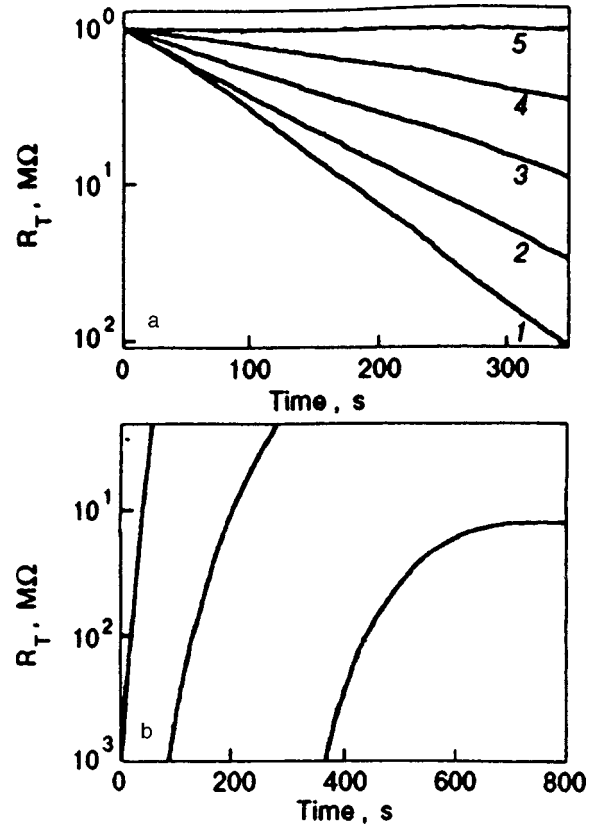

FIG. 2. (a) Drift of the tunnel resistance R_T of an Al-sample directly after break ($T = 4.2$ K). Each curve represents a period of about 6 min. starting 10 (*1*), 20 (*2*), 30 (*3*), 60 (*4*) and 180 (*5*) min after breaking. After three hours, the change in R_T has become less than 5% over a period of 6 min. (b) Drift of the tunnel resistance R_T of a Pb-sample, measured directly after the electrodes have been pressed together for a short time ($T = 4.2$ K). The drift decreases quickly and is negligible after 12 min.

change in R_T was as large as two orders of magnitude over 5–6 min (which is the typical measuring time) shortly after the break, but dropped to an acceptable level of a linear change of $R_T(t)$ of 2–5% in 6 min after waiting for 3 h, and became negligible after a period of 10 h. The total ''backflow'' of sample material can be estimated to be $\approx 100 – 1000$ Å, starting from the moment of break. The amount of wire elongation shortly before the break is approximately 5–10 μm.

Another material-flow effect can be observed when one is changing the tip shapes by making a deep excursion of the electrodes into each other, creating a point contact with a diameter of 100–300 Å for a short time. The deformation is at least partially elastic, and after separating the electrodes R_T tends to decrease (see Fig. 2b). However, this effect is much smaller than the one described above, and R_T saturates after 10–15 min for ''soft'' materials, and after 3–5 min for Pt and the Pt–Ir(3%) alloy.

A flow of the bending beam material may also be involved in the effects observed, but its contribution must be very small due to the fact that the cross-sectional area of the bending beam is about four orders of magnitude larger than the one of the notched filament, and almost all of the bending takes place within the elastic deformation limits of the beam.

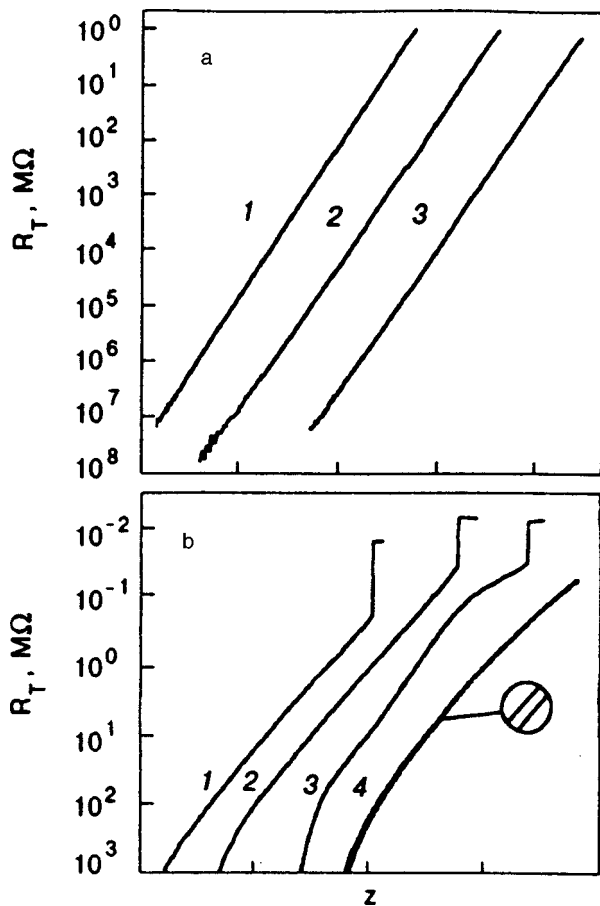After a jump to a one-atom contact, the electrodes can

FIG. 3. (a) Logarithmic plot of the tunnel resistance as a function of *z*-piezo voltage for MCB-junctions of Pt (*1*), Au (*2*), and Cu (*3*), at *T* = 4.2 K. Curves *1–3* show almost perfect exponential behavior over at least seven orders of magnitude; (b) Logarithmic plot of the tunnel resistance as a function of *z*-piezo voltage for MCB-junctions of Al (*1*), Pt (*2*), Pt–Ir (*3%*) (*3*) and Pb (*4*). at *T* = 4.2 K. Curves *1, 2, 4* display a slow bending (decrease of the slope) over the same range. Curve *3* shows on some parts an increase, and on some parts a decrease of the slope. All these types of behavior were predicted theoretically by Laloyaux *et al.*[13] The curves were recorded starting from a large distance (high R_T), decreasing the electrode spacing until a jump to contact took place. For curve *4*, the scans were reversed shortly before the jump, showing the small piezo-hysteresis in our setup. A small part of curve *4* has been enlarged by a factor ten. The achieved displacement is estimated to be ≈1 Å per decade change in R_T. Because the electrode separation to piezo voltage ratio depends on specific sample parameters (see text), the horizontal axis had to be rescaled for some curves for clarity.

also suffer an irreversible change in atomic configuration. In that case, however, a new equilibrium situation is reached within seconds.

All the effects described above can influence the shape of the measured current-distance characteristics. However, by waiting long enough for electrode material to relax into an equilibrium configuration, it was possible to diminish these effects to a negligibly small magnitude.

It was shown above that, theoretically, the transfer from vertical displacement to tip-tip displacement should not deviate noticeably from linear behavior. In Fig. 3a the tunnel resistance R_T of Pt, Au and Cu MCB-junctions is plotted on a logarithmic scale as a function of the applied piezo voltage, which in turn is proportional to the vertical displacement *y*. All curves are displayed "as recorded", demonstrating the

high stability of the MCB setup; the curves were always reproduced 2–4 times to check their validity. All three curves of Fig. 3a display a perfect exponential behavior of the tunnel resistance over about seven orders of magnitude, at bias voltages of 1 mV below, and 100 mV above, $R_T = 10^{10} \, \Omega$. The fact in itself that it is possible to record perfect exponential behavior strongly supports the assumption of a linear $z(y)$ dependence, because it is very unlikely that some nonlinear relation between *y* and the tip-tip distance can be compensated so perfectly by effects of the shape of, or interactions between, the two electrodes. An exponential $R_T(z)$ dependence can be the result of a tunnel geometry of a sharp tip above a flat surface, for it was shown that a geometry of a hemispherical tip above a flat surface does not lead to notable deviations from exponential behavior,[13] and furthermore, attractive Van der Walls forces are negligible for sharp conical tips.[14] The applied bias voltages are sufficiently low to avoid effects of power dissipation[7] and electrostatic forces.[10] We also recorded $R_T(z)$-curves at bias voltages up to 300 mV, and found no significant changes compared to the measurements at lower biases.

When all precautions are taken, the $R_T(z)$-curves measured when scanning *z* from a large distance almost up to the jump-to-contact point, and then scanning back, practically coincide. The very small deviation between the "upwards" and "downwards" recorded curves, which is due to the hysteresis of the piezo driver, is hardly visible. (The loops could be reproduced several times, so the deviations cannot be due to material flow.)

As stated before, it is not possible to calibrate the electrode separation as a function of applied piezo voltage for an MCB-junction, because the $z(y)$ depends on certain sample parameters [e.g., the distance *d* between the gluing points, see formula (2)]. Indeed we found that the slope of $\log(R_T(z))$ as a function of piezo voltage may differ by a factor of two for different samples. However, using known values for the work functions φ of specific materials for clean electrodes, and a simple formula for the tunnel current as a function of tip-sample separation,[1] it can be estimated that a one-decade change in the value of the tunnel current (tunnel resistance) corresponds roughly to a displacement of about 1 Å for the materials discussed here (and also for a number of other materials). This enables us to get a reasonable estimation of the experimentally obtained electrode displacements. The value is comparable to the ones that can be found from experiments with an Ir tip approaching a Ag surface[7] (1.7 Å per decade), an Ir tip moving towards an Ir surface[10] (1.0 Å/decade), and experiments using a Pt MCB junction[12] (0.6–1.1 Å/decade).

The curves in Fig. 3b display features which, to our opinion, must be attributed to effects of tip-sample geometries. They show clear deviations from an exponential dependence over the whole range that was scanned (more than four orders of magnitude in R_T, starting at 1 GΩ and ending at ≈100–50 kΩ, where a jump to a one atom point contact occurs). This suggests that it is unlikely that we are dealing with effects stemming from tip-sample interactions, because these have been shown to extend over a much smaller range close to contact, both theoretically (over one[8,9] or two[11]

decades) and experimentally (up to only 20–30 kΩ[7,10] or 500 kΩ[12]). The observed deviations from an exponential dependence were present in about five percent of all recorded curves. The curves displayed in Fig. 3b have been selected to demonstrate clearly the observed deviations.

Curves *1*, *2* and *4* in Fig. 3b display a gradual, continuous change of the slope over the whole range of displacement, starting at least 4–5 Å before the jump to contact. This kind of behavior was predicted by Laloyaux *et al.*[13] for a geometry of a cylindrical tip facing a flat sample, where they found a slow bending of log $(I_T(z))$ over four orders of magnitude of the tunnel current for a tip-sample displacement from 1 to 5 Å. Curve *3* of Fig. 3b displays another type of $R_T(z)$-dependence that we have observed. It is characterized by an alternately increasing and decreasing slope of log $(R_T(z))$, and was observed for Al and Pt also. This type of curve was predicted by Laloyaux *et al.*[13] for configurations of a hemispherical tip (modeling a sharp tip) opposing a gaussian dip or boss in or on a flat surface. Their calculated log $[I_T(z)]$ showed approximately the same, though somewhat weaker, effects in the tip against dip geometry compared to the one of a tip facing a boss. Also, the tunnel current decreased more slowly for the first geometry when compared to the latter (three or four, respectively, orders of magnitude at a displacement from 1 to 5 Å). We indeed did observe that for the same sample mounting (so the same $y(z)$-relation), the change in piezo voltage required to change R_T from 1 GΩ to 100 kΩ could occasionally be up to 50% larger than usual for that specific mounting.

Qualitatively, the experimental results seem to support the theoretical work of Laloyaux *et al.*[13] However, the actual shapes of the electrodes were not known in these experiments.

For many tunneling experiments, and certainly for experiments which intend to study effects of the electrode geometry, it is useful to have at least some knowledge of the electrode surface topography. We therefore also performed experiments where small pieces ($5 \times 3 \times 1$ mm) of piezo material were placed underneath the two anchoring points. Using one piece that changes its thickness as a voltage is applied, and one piece that gives a horizontal displacement of its surfaces with respect to each other (shear piezo), it was possible to move the electrodes with respect to each other laterally. The variation of the tunnel current can then be measured as the electrodes are moved around. The obtained lateral displacement at 4.2 K is estimated to be about 0.6 Å/V.

The breaking process is likely to result in at least one electrode being sharp, and using this electrode as a tip, a three dimentional scan of the other (more blunt) electrode can be obtained. A typical example is given in Fig. 4 (see also Ref. 15). It show features that can be interpreted as atomically resolved images and demonstrates that the surface of the (Au-) electrodes is rather rough, which can be expected for electrodes created in a breaking process.

The shear-piezo option was used to record log($R_T(z)$) curves for several different Pt samples at selected sites such as the ones indicated in Fig. 5. Assuming that a shear-piezo scan like Fig. 5 represents a profile of the "blunt" electrode, while the other electrode acts as a sharp tip, the log $[R_T(z)]$
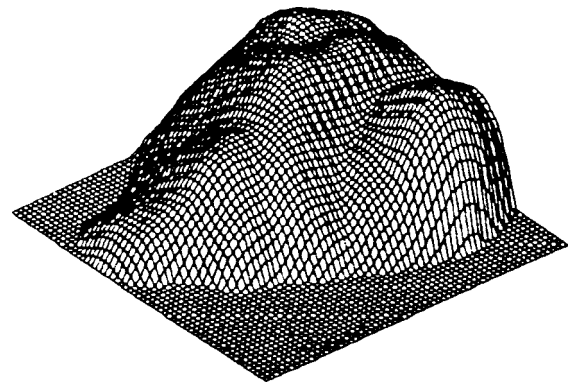

FIG. 4. Three-dimensional image of the foremost part of the surface of the bluntest Au electrode. All data below a certain value have been cut, and a horizontal plane has been introduced in the figure at this value. The figure displays an area of about 15×15 Å.

curves recorded at the selected sites are expected to correspond to the theoretical situations[13] of a tip opposing a boss (Fig. 5, locations *A* and *B*), a dip (*E*), or a rather flat part of the surface (*C* and *D*). Figure 6 shows six log $(R_T(z))$ curves representing the behavior that was generally observed when these curves were recorded at selected locations that are similar to the sites $A-F$ indicated in Fig. 5. Bended log$[R_T(z)]$ curves were mostly only found for locations like *E* and *F* in Fig. 5, the bending being stronger for *F*, where the "tip" is approaching a very steep part of the "sample", and several tip atoms may contribute to the electron tunneling process. At locations like *A*, *B*, *C*, and *D*, mainly straight log$[R_T(z)]$ curves were obtained, the curves at *D*-type locations often being less steep than for $A-C$. Still bended curves were sometimes observed for locations *B*, *C* and *D*, but for very sharp locations like *A*, the log$[R_T(z)]$ curves were almost always straight lines. These experimental results do not correspond to the ones that were expected from the work of Laloyaux *et al.*[13] The experiment was repeated using Al and Pt–Ir MCB junctions. In general, the same
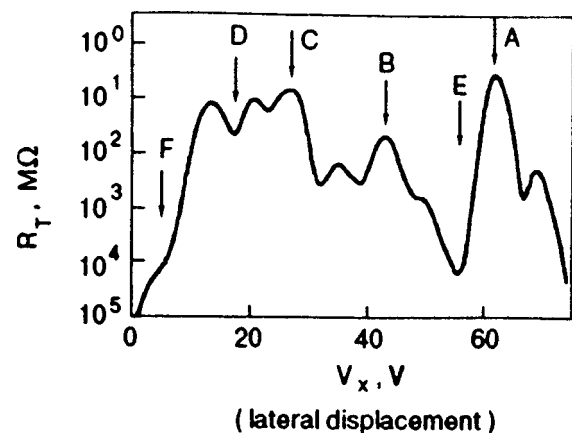

FIG. 5. Logarithmic plot of the tunnel resistance of a Pt MCB junction as a function of the shear-piezo voltage ($T=4.2$ K, $V_{bias}=50$ mV). The displacement is estimated to be 0.5–1.0 Å/V. Assuming one of the electrodes to be atomically sharp, the curve can be interpreted as a line profile of the other electrode, demonstrating that the surface is rather rough. The arrows indicate different types of selected locations at which log($R_T(z)$) were recorded (see text).
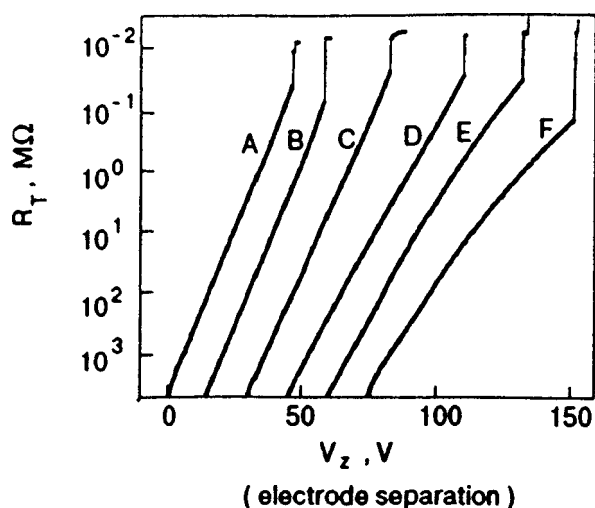
FIG. 6. Logarithmic plot of the tunnel resistance of Pt MCB junctions as a function of z-piezo voltage ($T = 4.2$ K, $V_{bias} = 5$ mV). Curves $A-F$ are examples of the $\log(R_T(z))$ behavior that was mostly observed for different samples at selected locations comparable to the locations $A-F$ indicated in Fig. 5.

discrepancy between theoretical predictions and experimental results was found. Since the experimental situation is far more complicated than the theoretical one, where planar surfaces with cylindrically symmetric protrusions and indentations of a certain shape were considered, the model geometries may be too simple to describe adequately the tunneling between the rather rough electrode surfaces of an MCB junction. Also, the information on the surface topography that we have is limited to only a single line; what seems to be a flat part in our line scan, might turn out to be not flat at all if the perpendicular direction would be scanned also. Additionally, one should bear in mind that the line scan of Fig. 5 cannot be an exact image of the surface topography, because the slope of the curves differs for different locations, and because the $\log[R_T(z)]$ curves are sometimes bended. Nevertheless, since it is not likely that the shape and slope of the $\log[R_T(z)]$ curve changes abruptly somewhere along the scanned line, and because these changes are much smaller than the ones displayed in Fig. 5, the recorded line scan will still provide a reasonable image of the surface topography in one direction. The measurements at selected locations therefore show that at locations with different surface topographies, different $\log(R_T(z))$ relations may be found.

We also studied the jump to contact at locations like $A-F$ of Fig. 5. The behavior of one-atom contacts has been studied extensively by Krans *et al.*[12] In experiments where the contact size of MCB junctions, was slowly decreased, they found that Al and Cu tend to jump to tunneling from a conductance value close to $2e^2/h$, the conductance quantum for a single conductance channel. Pt junctions, however, were found to jump mostly from a 1.4–1.8 times larger value, indicating that more than one conductance channel was present shortly before the jump. This was explained in terms of s- and d-like wave functions, constituting separate conductance channels for Pt.

The line scan was used to do a site-selected investigation

of the jump to contact for Pt MCB junctions. At locations comparable to E and F in Fig. 5, jumps to what seemed to be multi-atom contacts usually occurred. At locations like B and C, there were mostly immediate jumps to a conductance value of 1.5–2.0 conductance quanta (so comparable to the results of Ref. 12), while at D, there were jumps to a much broader range of resistance values, corresponding to 1.5 or more conductance quanta. The most remarkable result was found at very sharp locations like A in Fig. 5. At such locations, a jump to a resistance value close to $h/2e^2$ (so only one conductance channel present), quickly followed by a jump to about half the resistance value (two conductance channels), was observed for about 60% of all cases. An example of this type of behavior is the jump to contact of curve A in Fig. 6. These results demonstrate that the specific electrode geometry also influences the way in which the first conductance channels are formed when the electrodes are slowly brought into contact.

4. CONCLUSION

In the above it has been shown experimentally that the tunnel resistance as a function of the electrode spacing can deviate strongly from the expected exponential behavior over the whole experimental range of more than four orders of magnitude of the tunnel resistance. From comparison with previous theoretical studies can be concluded that these deviations are not likely to be due to interactions between the electrodes, but can be attributed to effects of the tip-sample geometry on the dependence of the tunnel current on the distance between the two electrodes. Qualitatively, the results correspond to the calculations of Laloyaux *et al.*; however, tunneling at selected locations using a line profile of one of the electrodes indicates that the rough surfaces of an MCB junction cannot be completely described by the rather straightforward theoretical model.

*E-mail: olegs@sci.kun.nl.
 shklyarevskii@ilt.kharkov.ua
**E-mail: hvk@sci.kun.nl

[1] L. L. Soethout, H. van Kempen, and G. F. A. van de Walle, Adv. Electron Electron Phys. **79**, 155 (1990).
[2] L. E. C. van de Leemput and H. van Kempen, Rep. Prog. Phys. **55**, 1165 (1992).
[3] *Scanning Tunneling Microscopy I, Springer Series in Surface Sciences* **20**, H.-J. Güntherodt and R. Wiesendanger (Eds.), Springer-Verlag, Berlin (1992).
[4] *Scanning Tunneling Microscopy II, Springer Series in Surface Sciences* **28**, R. Wiesendanger and H.-J. Güntherodt (Eds.), Springer-Verlag, Berlin (1992).
[5] *Scanning Tunneling Microscopy III, Springer Series in Surface Sciences* **29**, R. Wiesendanger and H.-J. Güntherodt (Eds.), Springer-Verlag, Berlin (1993).
[6] J. G. Simmons, J. Appl. Phys. **34**, 1793 (1963).
[7] J. K. Gimzewski and R. Möller, Phys. Rev. B **36**, 1284 (1987);

J. K. Gimzewski, R. Möller, D. W. Pohl, and R. R. Schlittler, Surf. Sci. **189/190**, 15 (1987).

[8] N. D. Lang, Phys. Rev. B **36**, 8173 (1987).

[9] J. Ferrer, A. Martín-Rodero, and F. Flores, Phys. Rev. B **38**, 10113 (1988).

[10] U. Dürig, O. Züger, and D. W. Pohl, Phys. Rev. Lett. **65**, 349 (1990).

[11] S. Ciraci and E. Tekman, Phys. Rev. B **40**, 11969 (1989).

[12] J. M. Krans, C. J. Muller, I. K. Yanson, Th. C. M. Govaert, R. Hesper, and J. M. van Ruitenbeek, Phys. Rev. B **48**, 14721 (1993).

[13] Th. Laloyaux, I. Derycke, J.-P. Vigneron, Ph. Lambin, and A. A. Lucas, Phys. Rev. B **47**, 7508 (1993).

[14] S. Ciraci, E. Tekman, A. Baratoff, and I. P. Batra, Phys. Rev. B **46**, 10411 (1992).

[15] J. Voets, R. J. P. Keijsers, O. I. Shklyarevskii, and H. van Kempen, Phys. Rev. B **53**, 1072 (1996).

[16] C. J. Muller, J. M. van Ruitenbeek, and L. J. de Jongh, Physica C **191**, 485 (1992).

[17] W. C. Young, *Roark's Formulas for Stress and Strain*, McGraw-Hill, New York (1989), ch. 7.

LOW-DIMENSIONAL AND DISORDERED SYSTEMS

On dynamic properties of a two-dimensional degenerate electron gas

H. Buhmann and L. W. Molenkamp

II. Physikalisches Institut RWTH Aachen, 52056 Aachen, Germany[*)]

R. N. Gurzhi, A. N. Kalinenko, A. I. Kopeliovich, and A. V. Yanovsky

B. Verkin Institute for Low Temperature Physics and Engineering, National Academy of Sciences of the Ukraine, 310164 Kharkov, Ukraine[**)]

A detailed theory of electron–electron scattering in two-dimensional degenerate systems in heterostructures is constructed as a result of analysis and numerical computations. The conditions are formulated and the values of characteristic parameters are obtained for which specific two-dimensional effects predicted earlier from theoretical considerations can be observed. New properties of scattering indicatrix, viz., a beam of electrons flying almost antiparallel to the primary beam and a very narrow beam of holes flying in the forward direction, are found. © *1998 American Institute of Physics.* [S1063-777X(98)00810-X]

1. INTRODUCTION

It was shown earlier by us that the momentum relaxation processes in perfect two-dimensional systems at low temperatures differ qualitatively from those in a conventional three-dimensional metal. This is due to the fact that the constraints imposed by a decrease in the dimensionality of space alter significantly the dynamic properties of a degenerate gas of electrons colliding with one another during a transition from three to two dimensions. Since we are speaking of real (and not virtual) processes occurring in a small neighborhood of the Fermi surface, a transition from two dimensions to one dimension takes place in the momentum space.

It follows from the energy and momentum conservation laws (as well as Pauli's exclusion principle) that collisions between electrons result in scattering at a small angle $\varphi \propto T/\varepsilon_F$ under the condition that the sum of momenta of the initial states is not too small. The collisions between electrons with nearly antiparallel momenta $\mathbf{p}_1$ and $\mathbf{p}_2$: $p_F^{-1}|\mathbf{p}_1+\mathbf{p}_2| \lesssim T/\varepsilon_F$ are an exception: in this case, the scattering angle may assume any value $\varphi \sim 1$. (Here, T is the temperature, p_F and ε_F are the Fermi momentum and energy.) Significantly, the probabilities of both types of processes are nearly identical in the case of two dimensions. Processes of the second type are quite effective in the case of relaxation of even-momentum electron distribution, and the corresponding relaxation time $\tau_{ee} \sim (\varepsilon_F/T)^2$ is of the same order of magnitude as in a three-dimensional metal. Both types of collisions are ineffective for relaxation of odd distributions (in particular, of the current states). For collisions of the second type, this is explained by the fact that the rotation of a pair of electrons with strictly antiparallel momenta $(\mathbf{p}_1+\mathbf{p}_2=0)$ through an arbitrary angle φ does not have any effect on odd distribution.[1–3]

The regularities described above are of quite general nature as they are associated only with the dimensionality of the system and the existence of Fermi degeneracy in it. The main purpose of this research is to obtain a detailed picture of electron–electron scattering in the two-dimensional case for different values of the degeneracy parameter $T/\varepsilon_F \ll 1$. In the general case, the characteristic energy of nonequilibrium electrons should be taken in this inequality instead of T, counted from the Fermi level.

2. COLLISION INTEGRAL. RESPONSE FUNCTION

Let f be the nonequilibrium part of the electron distribution. The integral of electron–electron collisions, linearized in f, can be presented in the form

$$\hat{I}f = -\nu f_{\mathbf{p}} + \int d^2\mathbf{p}' \, \nu_{\mathbf{pp}'} f_{\mathbf{p}'} \equiv -\nu f + \hat{K}f. \tag{1}$$

Here,

$$\nu = \nu(\mathbf{p}) \equiv \int d^2\mathbf{p}' \, \nu_{\mathbf{p}'\mathbf{p}}, \tag{2}$$

$$\begin{aligned}
\nu_{\mathbf{pp}'} = \int d^2\mathbf{p}_1 d^2\mathbf{p}_2 \Bigg\{ &2 W_{\mathbf{pp}'\mathbf{p}_2} \frac{n(\varepsilon)}{n(\varepsilon')} n(\varepsilon_1)[1-n(\varepsilon_2)] \\
&\times \delta(\mathbf{p}+\mathbf{p}_1-\mathbf{p}'-\mathbf{p}_2)\delta(\varepsilon+\varepsilon_1-\varepsilon'-\varepsilon_2) \\
&- W_{\mathbf{pp}'\mathbf{p}_1\mathbf{p}_2} \frac{1-n(\varepsilon)}{n(\varepsilon')} n(\varepsilon_1)n(\varepsilon_2) \\
&\times \delta(\mathbf{p}+\mathbf{p}'-\mathbf{p}_1-\mathbf{p}_2)\delta(\varepsilon+\varepsilon'-\varepsilon_1-\varepsilon_2) \Bigg\}.
\end{aligned}$$

The quantity $W_{\mathbf{pp}'\mathbf{p}_1\mathbf{p}_2}$ is proportional to the square of the matrix element of interaction, $\varepsilon \equiv \varepsilon_{\mathbf{p}}$; $\varepsilon' \equiv \varepsilon_{\mathbf{p}'}$; $\varepsilon_1 \equiv \varepsilon_{\mathbf{p}_1}$;

$\varepsilon_2 \equiv \varepsilon_{\mathbf{p}_2}$; $\varepsilon_{\mathbf{p}}$ is the energy of an electron with momentum $\mathbf{p}$, and $n(\varepsilon)$ is the equilibrium Fermi distribution.

Note that the kernel $\nu_{\mathbf{pp}_0}$ of the operator $\hat{K}$ has the meaning of a response function: it describes the change in the number of nonequilibrium quasiparticles in the state $\mathbf{p}$ due to the presence of a nonequilibrium electron in the state $\mathbf{p}_0$ (in formula (1), $f_{\mathbf{p}'}$ should be replaced by $\delta(\mathbf{p}' - \mathbf{p}_0)$). The response function (as well as the effect of the action $\tilde{K}$ on any function) consists of two parts, viz., the "hole" (negative) part describing the emergence of a nonequilibrium hole in the state $\mathbf{p}$, and the "electron" (positive definite) part:

$$\nu_{\mathbf{pp}_0} = -\nu^-_{\mathbf{pp}_0} + \nu^+_{\mathbf{pp}_0}, \quad \nu^-, \nu^+ > 0. \tag{3}$$

For the sake of simplicity, we assume that $\varepsilon = \mathbf{p}^2/2m$ (which is the exact energy–momentum relation for GaAs/AlGaAs-based heterostructures) and disregard the relatively weak dependence of the quantity W on its variables. (Numerical calculations, which we shall not present here, show that the result does not change qualitatively if we use a more realistic model for W.) In this case, we obtain from (2) ($\varepsilon_0 \equiv \varepsilon_{\mathbf{p}_0}$)

$$\nu^-_{\mathbf{pp}_0} = \frac{n(\varepsilon)}{1-n(\varepsilon_0)}\, W \int d\varepsilon_2 [\varepsilon\varepsilon_0 \sin^2 \varphi - (\varepsilon - \varepsilon_0)$$
$$\times (\varepsilon_2 - \varepsilon_0)]^{-1/2}[1-n(\varepsilon_2)][1-n(\varepsilon_0 + \varepsilon - \varepsilon_2)]$$
$$\times \Theta(\varepsilon + \varepsilon_0 - \varepsilon_2)\Theta[\varepsilon\varepsilon_0 \sin^2 \varphi - (\varepsilon - \varepsilon_0)(\varepsilon_2 - \varepsilon_0)], \tag{4}$$

$$\nu^+_{\mathbf{pp}_0} = \frac{1-n(\varepsilon)}{1-n(\varepsilon_0)}\, 2W \int d\varepsilon_2 [\varepsilon\varepsilon_0 \sin^2 \varphi - (\varepsilon_0 + \varepsilon$$
$$- 2\sqrt{\varepsilon\varepsilon_0} \cos\varphi)(\varepsilon_2 - \varepsilon)]^{-1/2} n(\varepsilon_2)[1-n(\varepsilon_0 + \varepsilon_2$$
$$- \varepsilon)]\Theta(\varepsilon_0 + \varepsilon_2 - \varepsilon)\Theta[\varepsilon\varepsilon_0 \sin^2 \varphi - (\varepsilon_0 + \varepsilon$$
$$- 2\sqrt{\varepsilon\varepsilon_0} \cos\varphi)(\varepsilon_2 - \varepsilon)]. \tag{5}$$

Here, φ is the angle between $\mathbf{p}$ and $\mathbf{p}_0$ ("scattering angle"). The "electron" part of $\nu_{\mathbf{pp}_0}$ is presented in terms of the special functions $\text{Li}_{1/2}$ (polylogarithmic function to the base $1/2$):

$$\nu^+_{\mathbf{pp}_0} = 2W \frac{1-n(\varepsilon)}{1-n(\varepsilon_0)} \left[\exp\left(\frac{\varepsilon_0 - \varepsilon}{T}\right) - 1\right]^{-1}$$
$$\times \left\{ \text{Li}_{1/2}\left[-\exp\left(-\frac{\varepsilon - \Delta - \varepsilon_F}{T}\right)\right]\right.$$
$$\left. - \text{Li}_{1/2}\left[-\exp\left(-\frac{\varepsilon_0 - \Delta - \varepsilon_F}{T}\right)\right]\right\}, \tag{6}$$

where

$$\Delta = \frac{2m\varepsilon\varepsilon_0 \sin^2 \varphi}{|\mathbf{p}_0 - \mathbf{p}|^2}. \tag{7}$$

It can be shown that $\nu_{\mathbf{pp}_0}$ is a sharp function of the angle φ in the case when $T, \varepsilon_0 - \varepsilon_F \ll \varepsilon_F$. It follows from formulas (4)–(7) that, in spite of the smallness of T/ε_F and ϵ_0, the nonanalytic dependence of $\nu_{\mathbf{pp}_0}$ on these parameters makes it

impossible to obtain a single asymptotic form for the response function in the entire range of the parameters ε and φ. However, in a wide interval of angles φ, $\pi - \varphi \gg \sqrt{T/\varepsilon_F}$, $\sqrt{\epsilon_0}$, $\sqrt{\epsilon}$, where $\varepsilon = (\varepsilon - \varepsilon_F)/\varepsilon_F$, $\epsilon_0 = (\varepsilon_0 - \varepsilon_F)/\varepsilon_F$, we can easily obtain an approximate expression:

$$\nu_{\mathbf{pp}_0} \simeq \frac{W}{p_F^3 \sin\varphi} \left\{ 2(\varepsilon_0 - \varepsilon)[1-n(\varepsilon)]\left[\exp\left(\frac{\varepsilon_0 - \varepsilon}{T}\right) - 1\right]^{-1}\right.$$
$$\left. - (\varepsilon_0 + \varepsilon - 2\varepsilon_F)n(\varepsilon)\left[\exp\left(\frac{\varepsilon_0 + \varepsilon - 2\varepsilon_F}{T}\right) - 1\right]^{-1}\right\}. \tag{8}$$

Thus, in the main approximation, the distribution of scattered electrons is found to be an even function of $\mathbf{p}$, i.e., invariant to the substitution $\varphi \to \pi - \varphi$ (by definition, the angle φ varies in the interval $[0, \pi]$). Hence, in accordance with the requirement of the momentum conservation for colliding particles, the odd component of $\nu_{\mathbf{pp}_0}$ is concentrated in the interval of angles φ, $\pi - \varphi \lesssim \sqrt{T/\varepsilon_F}$, $\sqrt{\epsilon_0}$. This conclusion is confirmed by numerical computations.

3. HIGH-ENERGY APPROXIMATION

For $\varepsilon_0 - \varepsilon_F \gg T$, the Fermi functions in the expression for $\nu_{\mathbf{pp}_0}$ can be replaced by appropriate step-functions. In this case, the expression for the response function can be presented in an explicit form:

$$\nu^-_{\mathbf{pp}_0} = W\Theta(\varepsilon_0 + \varepsilon - 2\varepsilon_F)\Theta(\sqrt{(\varepsilon_0 - \varepsilon)^2 + 4\varepsilon\varepsilon_0 \sin^2 \varphi}$$
$$- \varepsilon_0 - \varepsilon + 2\varepsilon_F)\arcsin \frac{\varepsilon_0 + \varepsilon - 2\varepsilon_F}{[(\varepsilon_0 - \varepsilon)^2 + 4\varepsilon_0\varepsilon \sin^2 \varphi]^{1/2}}, \tag{9}$$

$$\nu^+_{\mathbf{pp}_0} = 4W\Theta(\varepsilon - \varepsilon_F) \frac{1}{|\mathbf{p}_0 - \mathbf{p}|} \left\{\Theta(\varepsilon_F + \Delta - \varepsilon)\sqrt{\varepsilon_F + \Delta - \varepsilon}\right.$$
$$\left. - \Theta(\varepsilon_F + \Delta - \varepsilon_0)\sqrt{\varepsilon_F + \Delta - \varepsilon_0}\right\}. \tag{10}$$

Figure 1 shows the dependence of the function $\nu_{\mathbf{pp}_0}$ on the energy ε and angle φ, calculated by using formulas (9) and (10), for different values of $\epsilon_0 = 0.1$ (Fig. 1a) and $\epsilon_0 = 0.32$ (Fig. 1b). A comparison of the figures shows that as the parameter ϵ_0 increases, the regions of enhanced concentration of holes in the vicinity of $\varphi, \pi - \varphi \approx 0$ become broader.

Integrating $\nu_{\mathbf{pp}_0}$ with respect to energy, we obtain the scattering indicatrix

$$g_0(\varphi) = \nu^{-1}(\epsilon_0)m \int d\varepsilon\, \nu_{\mathbf{pp}_0} \tag{11}$$

with an asymptotic behavior[3]:

$$g_0(\varphi) \propto \sin^{-1}\varphi, \quad \varphi, \pi - \varphi \gg \sqrt{\epsilon_0}. \tag{12}$$

For the normalization $\int d\varphi\, g_0(\varphi) = 1$ used in this case, the quantity $|g_0(\varphi)|d\varphi$ gives the probability of emergence of a nonequilibrium electron in the interval $d\varphi$ for $g_0 > 0$, or a nonequilibrium hole for $g_0 < 0$.
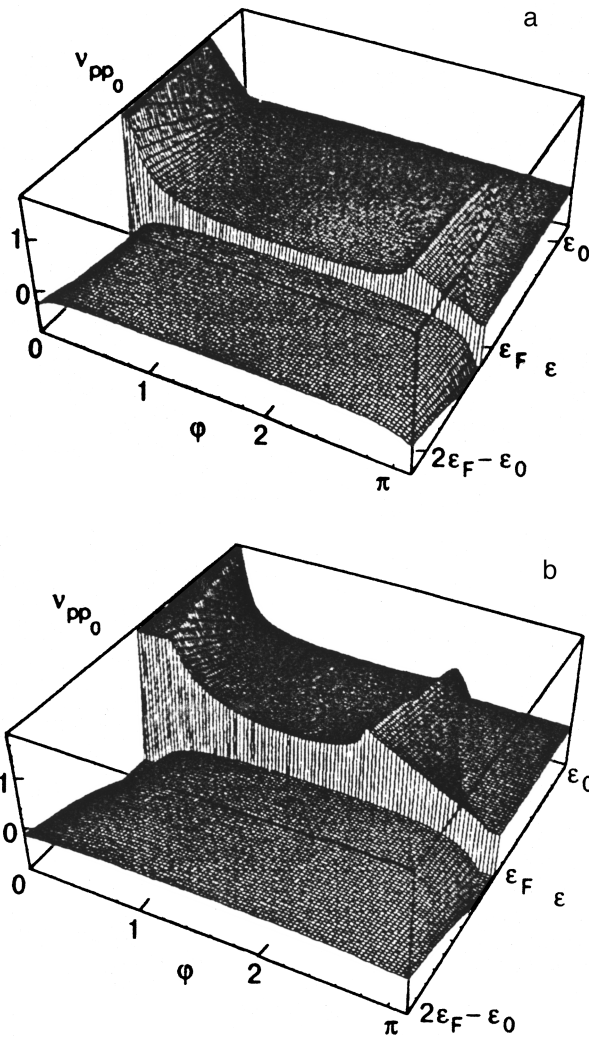
FIG. 1. Dependence of the response function ν_{pp_0} on energy ε and angle φ between **p** and $\mathbf{p}_0$ in the high-energy approximation: $\epsilon_0 = 0.1$ (a); 0.32 (b).

FIG. 2. (a) Scattering indicatrix of high-energy electrons $g_0(\varphi)$ for $\epsilon_0 = 0.01$ (*1*), 0.1 (*2*), 1 (*3*). Curve *4* shows the result obtained by using Callaway's method. The inset shows the small-angle region. A narrow beam of holes can be seen in the figure. (b) Odd component of the scattering indicatrix $g_0(\varphi)$ for $\epsilon_0 = 0.1$ (*1*), 1 (*2*).

The specific features of $2D$ relaxation can be seen clearly from the plots for scattering indicatrix shown in Fig. 2a. Calculations were made by using formulas (9)–(11) for different values of the parameter ϵ_0: 0.01 (curve *1*), 0.1 (curve *2*), and 1 (curve *3*). For the sake of comparison with the $3D$ case, curve *4* shows the dependence obtained by Callaway's method[4] for the case when the odd part of g_0 is simply proportional to $\cos\varphi$, and the even part is a constant:

$$g_0(\varphi) = c_1 \cos\varphi + c_2.$$

Here, the constants c_1 and c_2 are determined from the laws of conservation of momentum and the number of particles during collisions. Callaway's approximation corresponds to the assumption that drift distribution is established in an electron system after several collisions. From the qualitative point of view, this approximation is valid for $3D$ systems. Note that in contrast to the $2D$ case, the angular dependence of the $3D$ scattering indicatrix depends weakly on the parameter ϵ_0. This fact is reflected in Callaway's approximation.

It can be seen from Fig. 2a that two-dimensional effects are manifested significantly even for $\epsilon_0 = 0.1$. In the first
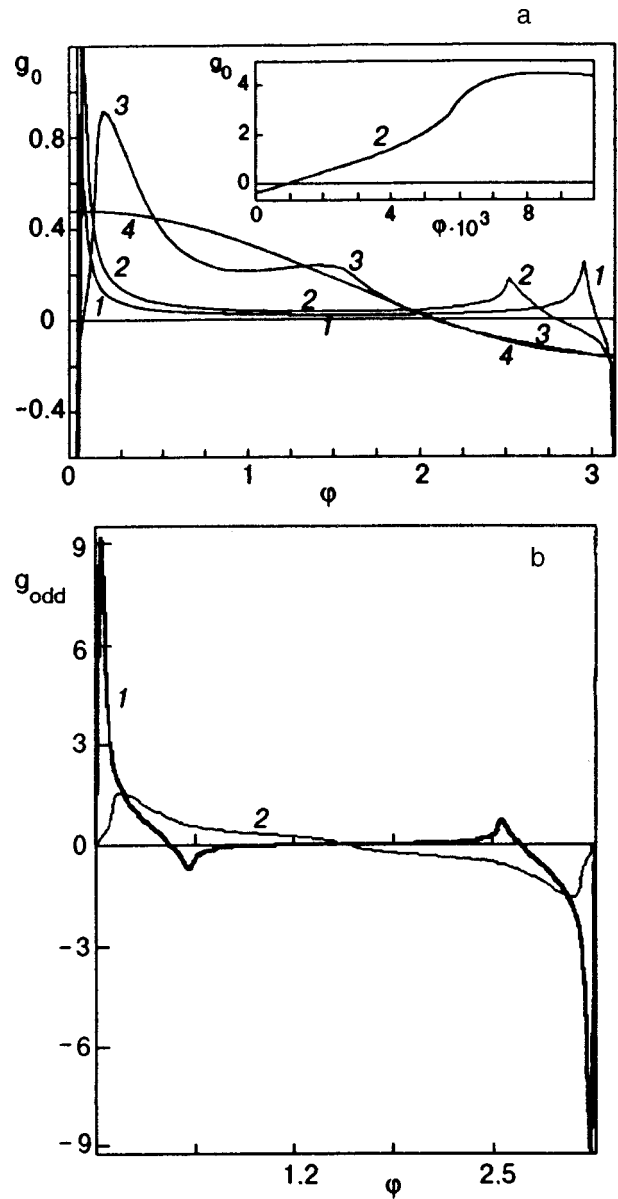
place, these are narrow beams of electrons flying in the forward direction, and of holes flying backwards. The holes flying backwards are concentrated in a narrow interval of angles $\pi - \varphi < 0.32$ (in complete accord with the theoretical estimate[3]: $\pi - \varphi < \sqrt{\epsilon_0} \approx 0.33$).

The weak broadening of the **p**-odd part of the distribution as compared to the even part is specifically also a $2D$ effect. The odd part of the scattering indicatrix is shown in Fig. 2b. For $\epsilon_0 \approx 0.1$, over 90% of the states from the odd part of distribution are concentrated in the interval $\varphi < \sqrt{\epsilon_0} \approx 0.33$. The even part is more smooth, and only 35% of states from this part are concentrated in this interval. Computations show that this difference between the odd and even parts will be enhanced upon a decrease in ϵ_0.
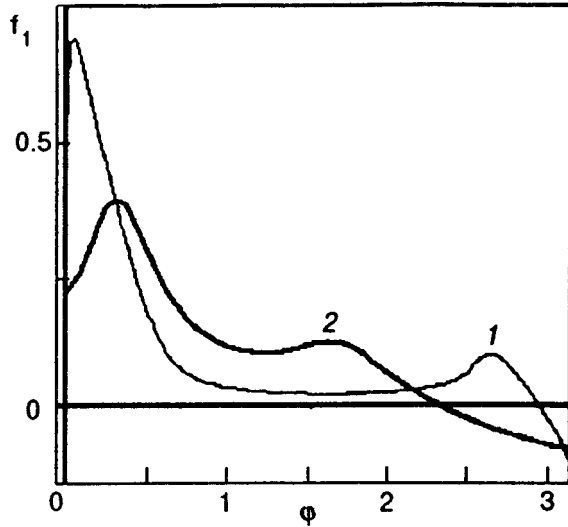
Figure 2 also shows some peculiarities of the scattering

FIG. 3. Dependence of scattered electrons for initial Gaussian distribution, $\sigma=0.3$, $\epsilon_0=0.1$ (*1*), 1 (*2*).

FIG. 4. Scattering indicatrix $g_T(\varphi)$ for thermalized electrons for $T/\varepsilon_F = 0.005$ (*1*), 0.2 (*2*).

indicatrix that have not been observed earlier: a secondary beam of electrons for $\varphi \approx \pi - 2\sqrt{\epsilon_0}$, and a hole valley at the smallest angles $\varphi < 0.1\epsilon_0^{3/2}$. An additional electron peak observed at angles $\varphi \approx \pi - 2\sqrt{\epsilon_0}$ is a purely $2D$ effect since it is associated with rotations of nearly antiparallel pairs with a characteristic angle of departure from antiparallelism $\psi \sim \sqrt{\epsilon_0}$. (According to Ref. 3, $\psi\Delta\varphi \lesssim \epsilon_0$, where $\Delta\varphi$ is the angle of rotation of the pair.) The emergence of ''holes'' at angles $\varphi < 0.1\epsilon_0^{3/2}$ is a consequence of the conservation laws: the electron may give away its surplus energy to equilibrium partners only upon scattering at a finite angle. This effect is weakened for $3D$ systems in parameter $\epsilon_0 \ll 1$.

Figure 3 shows the angular dependence of the distribution f_1 of scattered electrons for an initial Gaussian distribution f_0:

$$f_1(\varphi) = \nu^{-1}(\epsilon_0)m\int d\varepsilon \hat{K}f_0,$$

$$f_0(\mathbf{p}) \propto \delta(\varepsilon_{\mathbf{p}} - \varepsilon_{\mathbf{p}_0})\exp(-\varphi^2/\sigma^2).$$

The conventionally used value $\sigma \simeq 0.3$ is characteristic for experiments with beams injected into a two-dimensional electron gas.[5,6]

Calculations show that the peculiarities of two-dimensional electron–electron relaxation predicted in Ref. 3 are manifested completely right up to excitation energies $0.2\varepsilon_F$. Considerable differences from the $3D$ case are observed even for excitation energies of the order of ε_F.

4. RELAXATION OF THERMALIZED DISTRIBUTIONS

Let us consider the evolution of equilibrium (thermalized) distributions in energy. In this case, the relaxation occurs only in the angular variable. The nonequilibrium part of the distribution function has the form

$$f = \left(-\frac{\partial n}{\partial \varepsilon}\right)\chi(\varphi),$$

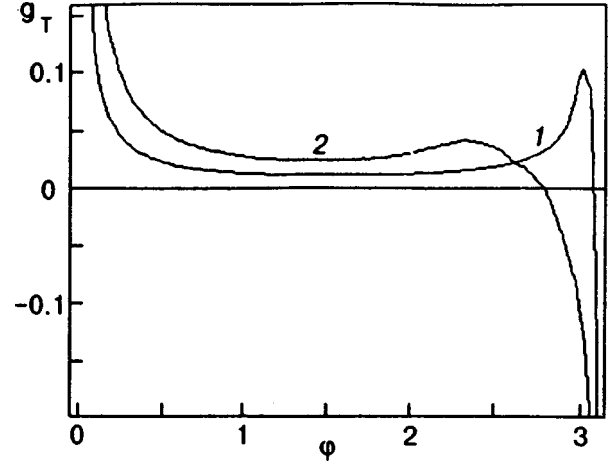while the scattering indicatrix is defined as

$$g_T(\varphi) = m\nu^{-1}(T)\int d\varepsilon \hat{K}f_0, \quad f_0 = \left(-\frac{\partial n}{\partial \varepsilon}\right)\delta(\varphi). \quad (13)$$

Analytically, we can only obtain the asymptotic form

$$g_T(\varphi) \simeq \frac{\pi^2 m W \nu^{-1}(T)}{3}\left(\frac{T}{\varepsilon_F}\right)^2 \sin^{-1}\varphi,$$

$$\varphi, \pi - \varphi \gg \sqrt{T/\varepsilon_F}. \quad (14)$$

Figure 4 shows the curves for the function $g_T(\varphi)$ constructed by using formulas (3), (4) and (13). It can be seen that the main properties of the angular relaxation of thermalized distributions qualitatively repeat the properties of the high-energy distributions. (According to qualitative considerations,[2,3] the best agreement is obtained for $T/\varepsilon_F \sim \epsilon_0/3$.) However, there is no hole valley for the smallest scattering angles. The number of holes increases upon a decrease in T. This is hard to observe in Fig. 4 (curve *1*) since holes are concentrated in an extremely narrow interval of angles $\pi - \varphi < 0.1$. The number of holes may be determined from the requirement of conservation of the momentum component parallel to the beam:

$$\int d\varphi(1 - \cos\varphi)g_T(\varphi) = 0.$$

We also considered the general case of finite temperatures and an arbitrary initial electron energy ε_0. A transition from the high-energy limit to the temperature limit occurs at $T \sim (\varepsilon_0 - \varepsilon_F)/3$.

5. ONE-COLLISION APPROXIMATION

The results obtained above describe directly the evolution of electron distributions (beams) in the momentum space during time periods that are small in comparison with the characteristic time τ_{ee} of electron–electron collisions. In the one-collision approximation, the solution of the kinetic equation

$$\frac{\partial f}{\partial t} = \hat{I}f, \quad f(t=0,\mathbf{p}) = f_0(\mathbf{p}), \quad t \ll \nu^{-1} \quad (15)$$

has the form

$$f = \exp(-t\hat{I})f_0 \approx (1 - t\nu)f_0 + t\hat{K}f_0. \qquad (16)$$

Note that, for high-energy beams with a characteristic energy $(\varepsilon_0 - \varepsilon_F) \gg T$, the probability of a secondary collision is about an order of magnitude higher than the primary collision probability.[2,3] This is due to the fact that the energy of the initial electron is redistributed between three partners: $\bar{\epsilon} \simeq 3^{-1}\epsilon_0$, $\nu(\bar{\epsilon}) \simeq 3^{-2}\nu(\epsilon_0)$ [here $\bar{\epsilon} = (\bar{\varepsilon} - \varepsilon_F)/\varepsilon_F$, $\bar{\varepsilon}$ is the characteristic energy of scattered electrons]. This allows us to consider times $t > \nu^{-1}(\epsilon_0)$. From Eq. (16), we obtain

$$f = f_0 - t(\nu - \hat{K})f_0 + \frac{t^2}{2!}(\nu - \hat{K})^2 f_0 - \dots \ . \qquad (17)$$

Considering that

$$\hat{K}\nu f_0 \sim \nu(\epsilon_0)\hat{K}f_0 \gg \nu\hat{K}f_0 \sim \nu(\bar{\epsilon})\hat{K}f_0, \qquad (18)$$

we obtain in the main approximation in $t\nu(\bar{\epsilon}) \ll 1$

$$f \simeq e^{-t\nu(\epsilon_0)}f_0 + (1 - e^{-t\nu(\epsilon_0)})\nu^{-1}(\epsilon_0)\hat{K}f_0. \qquad (19)$$

Obviously, for larger values of time when multiple collisions are significant, the role of two-dimensional effects can only be enhanced. During a few collisions, the even part of the initial distribution f_0 becomes isotropic while the relaxation of the odd part will occur during transport times that are characteristic of small-angle processes.[2,3]

The one-collision approximation can also be used for considering problems about the variation of profile of a narrow beam as it departs from the injector to distances much smaller than $l_{ee} = v_F\tau_{ee}$. For a detailed comparison with the experiment, however, we must consider a number of circumstances that are beyond the scope of the present work (in particular, the reflection of electrons and holes at the boundaries).[7] The results of preliminary calculations do not contradict the experimental results.[5,6]

6. CONCLUSION

The main specific features of relaxation of electron distributions in a two-dimensional degenerate gas of electrons colliding with one another can be summarized as follows.

(1) A weak broadening of the antisymmetric part of the beam; emission of narrow beams of electrons flying almost parallel to the initial beam, and of holes flying in the opposite direction. These effects are manifested for $\epsilon_0 \lesssim 0.2$ for the case of high energies, or for $T/\epsilon_0 \lesssim 0.1$ for thermalized distributions. However, the effects remain noticeable even for $\epsilon_0 \sim T/\varepsilon_F \sim 1$.

(2) A ''secondary beam'' of electrons at angles close to $\pi - 2\sqrt{\epsilon_0}$. This effect can be observed either in quite high-energy beams for values of parameters $3T/\varepsilon_F < \epsilon_0 < 0.2$, or for thermalized distributions at very low temperatures $T/\varepsilon_F < 0.1$.

(3) A beam of holes flying in the forward direction at the smallest angles ($\varphi < 0.1\epsilon_0^{3/2}$). This effect is observed only in high-energy beams for $\epsilon_0 > 3T/\varepsilon_F$.

*)E-mail: buhmann@physik.rwth-aachen.de;
  molenkmp@physik.rwth-aachen.de
**)E-mail: gurzhi@ilt.kharkov.ua

[1] R. N. Gurzhi, A. N. Kalinenko, and A. I. Kopeliovich, Phys. Rev. Lett. **74**, 3872 (1995).
[2] R. N. Gurzhi, A. N. Kalinenko, and A. I. Kopeliovich, Phys. Rev. B **52**, 4744 (1996).
[3] R. N. Gurzhi, A. N. Kalinenko, and A. I. Kopeliovich, Fiz. Nizk. Temp. **23**, 58 (1997) [Low Temp. Phys. **23**, 44 (1997)].
[4] J. Callaway, Phys. Rev. **113**, 1046 (1959).
[5] L. W. Molenkamp, M. J. P. Brugmans, H. van Houten, and C. T. Foxon, Semicond. Sci. Technol. **7**, B228 (1992).
[6] Th. Shäpers, M. Krüger, J. Appenzeller *et al.*, Appl. Phys. Lett. **66**, 3603 (1995).
[7] A. S. D. Heindrichs, H. Buhmann, S. F. Godijn, and L. W. Molenkamp, Phys. Rev. B **57**, 3961 (1998).

Translated by R. S. Wadhwa

PHYSICAL PROPERTIES OF CRYOCRYSTALS

Electron-impact desorption of metastable particles from CO films

H. Shi, P. Cloutier, and L. Sanche

Groupe du Conseil de Recherches Medicales en Science des Radiations Faculté de Médecine, Université de Sherbrooke, Sherbrooke, QC, Canada J1H 5N4*[)]

The impact of monochromatic low-energy electrons (4–52 eV) is found to induce desorption of metastable particles (MP) from multilayer films formed by condensing CO gas on a Pt(111) substrate held at 20 K. The results are compared with metastable production from gaseous CO. Metastable CO (CO*) is identified as the major desorbed species, its desorption is discussed in terms of intramolecular to molecule-surface vibrational energy transfer. Primary electronic excitation proceeds via the states, $a'^3\Sigma^+$, $d^3\Delta$, $e^3\Sigma^-$, $I^1\Sigma^-$, and $D^1\Delta$ which contribute to MP desorption directly or by first decaying in high vibrational levels of the $a^3\Pi$ configuration. The energy threshold of 8.0 eV for CO* desorption indicates that CO in low vibrational levels of the $a^3\Pi$ state does not desorb. Electronic excitation occurs either near the surface of the CO film or in the bulk. In the latter case, excitonic motion to the surface can be followed by CO* desorption. © *1998 American Institute of Physics.* [S1063-777X(98)00910-4]

1. INTRODUCTION

Desorption from surfaces induced by electronic transitions (i.e., DIET) is a complex process which proceeds through a variety of steps including primary excitation, evolution of electronic excitation (propagation, localization, and on-site evolution, etc.) and coupling of the electronic excitation to nuclear motion.[1] While rather detailed knowledge about DIET from rare gas solids has been obtained,[1] DIET of neutrals from molecular solids is not so well documented due to the additional channels involving coupling of rovibrational internal energy to the translational energy of the desorbing particle.

It is known that molecules are commonly produced and desorbed by electronic excitation on grains in interstellar media as well as on comet.[2] CO is a common molecule in the interstellar medium and a significant component in stellar and planetary atmospheres and comets.[3] CO is chosen here in our effort to understand DIET of cryogenic molecular solids. The selective detection of metastable particles (MP) provides a possibility for isolating particular processes. We report high-resolution excitation functions and time-of-flight (TOF) distributions of MP desorbed from low-temperature CO films by electron impact, with comparison to metastable production of gaseous CO, in order to determine the initial electronic excitation, the desorption species and their kinetic energy. It is suggested that several vibrational excited CO* states contribute to the measured MP signal through intramolecular to molecule-surface vibrational energy transfer.

2. EXPERIMENT

The experiment was performed in an ultra-high-vacuum system reaching a base pressure of -10^{-10} Torr. The apparatus has been described in detail previously.[4] A well-collimated low-energy (0–52 eV, $\Delta E = 60$ meV) electron beam impinges on a Pt(111) single-crystal at 18° with respect to the surface normal; the desorbed charged particles are repelled by concentric grids, whereas UV photons and desorbed MP passing through the grids are measured with a large area micro-channel plate array superimposed on a position-sensitive anode. The electronic energy threshold for the MP detection is estimated to lie slightly below 6 eV, from the fact that N_2^* in the $A^3\Sigma_u^+$ and CO* in the a $a^3\Pi$ states can be detected by the micro-channel plates.[4,5] The energy of the vacuum level is calibrated ± 0.3 eV by measuring the onset of the target current as the voltage between the electron source and the target is slowly increased. The crystal, which is mounted on the tip of a closed-cycle helium cryostat, can be cooled to 20 K and cleaned by electrical heating and Ar bombardment. The target films are grown on the Pt(111) surface by dosing CO gas with a purity of 99.99%. The CO thickness is determined with an uncertainty of $\pm 50\%$ and a reproductivity of $\pm 10\%$.[4]

TOF measurements are performed by switching on the electron beam on for 10 μs and subsequently recording the arrival time of those particles which trigger the micro-channel plates. Emission of UV photons produces a peak at $t=0$ followed by the arrival of the MP. The path length (d) between the target and the detector is 5.2 $\pm$ 0.1 cm. This parameter is related to the kinetic energy $E(t)$ of the metastable particles by the relation

$$E(t) = \frac{M}{2}\left(\frac{d}{t}\right)^2 \tag{1}$$

TABLE I. Lifetimes of some CO excited states in the gas phase.

CO state	$a^3\Pi$	$a'^3\Sigma^+$	$d^3\Delta$	$e^3\Sigma^-$	$b^3\Sigma^+$	$I^1\Sigma^-$ and $D^1\Delta$
Life-time	1–60 ms[a]	4–10 μs[b]	3–7 μs[b]	3–8 μs[b]	60 ns[c]	80 or 97 μs[d] up to 1 s[e]

[a]From Refs. 8 and 9;
[b]from Ref. 10;
[c]from Ref. 11;
[d]from Refs. 12 and 13;
[e]from Ref. 14.

where M is the mass of the metastable-particle (28 amu for CO) and t is the time of flight. From this relation, we find the resolution in translational energy

$$\Delta E(t) = \frac{Md}{t^2}\left(\Delta d + \frac{d}{t}\Delta t\right). \qquad (2)$$

3. PREVIOUS WORK ON METASTABLE PRODUCTION FROM CO

Our present knowledge on metastable production from CO by electron impact has been obtained essentially from gas-phase experiments. A summary of these studies is given here to facilitate the interpretation and discussion of our results in the next section. Our approach can be rationalized by the general similarities between the gas phase and the solid.[6,7] Electron impact excitation of CO in CO films shows that the band positions are shifted to the red by only a few tenth meV, and the intensity distributions in the progressions are well represented by the gas phase Franck-Condon factors.[7] This is also true of CO excitation in light rare gas (Ne, Ar) matrices.[6] Lifetimes of excited CO states are shortened in Ne matrices due to nonradiative relaxation,[6] but they are not far from the radiative lifetimes in the gas phase.

Gas phase lifetimes of some CO excited states are listed in Table I. The lowest electronic excited state ($a^3\Pi$) has a lifetime of 1 to 60 ms.[8,9] This state has been found to provide the dominant contribution to the total cross section for production of metastable CO by electron impact.[15] The $X^1\Sigma^+ \to a^3\Pi$ transition is a spin-forbidden transition and the $a^3\Pi$ state is excited by an electron exchange process or/and cascading from higher excited states. $a^3\Pi$ production has a threshold at about 6 eV, goes over a maximum located at 9 to 10 eV, and then decreases continuously with electron energy.[8,15–17] By direct observation of the Cameron Band system, Ajello reported that the maximum electron-impact cross section for $a^3\Pi$ at about 11 eV has a value of 1.1×10^{-16} cm^2.[16] The value of the peak cross section was re-analyzed and raised to 1.5×10^{-16} cm^2.[17] Excitation of the $a'^3\Sigma^+$ and $d^3\Delta$ states, with lifetimes of several μs,[10] as well as the $b^3\Sigma^+$ state can contribute to the metastable excitation function via the $a^3\Pi$ state;[15] i.e., through $a'^3\Sigma^+ \to a^3\Pi$, Asundi bands, $d^3\Delta \to a^3\Pi$ triplet bands and $b^3\Sigma^+ \to a^3\Pi$, the third positive band.

A higher metastable state lying around 10 eV has been observed by several investigators.[8,12,13,18–20] Olmsted *et al.*,[18] using a silver-magnesium alloy surface detector, observed a strongly rising cross section with an onset at 10.5 eV and estimated the lifetime of this metastable states to be of the order of 100 μs. They proposed that this might be the $b^3\Sigma^+$ state. Using Penning-ionization detection, Cermak[20] established the existence of two metastable states, one with an energy in the range 9.2–10.2 eV and the other with an energy $\geq$10.2 eV. Borst and Zipf[8] derived the excitation cross section of the higher lying state by subtracting from the total excitation cross section the cross section of the $a^3\Pi$ state, observed by Ajello,[16] giving a threshold at 10.4 eV. They estimated the lifetime to be 150 μs, and precluded the $b^3\Sigma^+$ state, which has a lifetime of 60 ns.[11] Later, Wells *et al.*[12] located the threshold at 9.5 eV and determined the state's lifetime to be 97 μs at 15 eV. They also deduced an electron impact cross section of 3×10^{-18} cm^2 at 15 eV and proposed the $D^1\Delta$ and $I^1\Sigma^-$ states as possible metastable states.

Mason and Newell[13] isolated the higher lying metastable state from the influence of the $a^3\Pi$ state by using a channel electron multiplier having a work function of about 8 eV. The threshold excitation energy was determined to be 9.45 eV and the lifetime was deduced to be 80 μs for incident energies between threshold and 35 eV which slightly decreases to 70 μs at electron energies above 40 eV. Maximum cross section was evaluated to be 3×10^{-18} cm^2 at 16 eV. They assigned the MP production to direct excitation of the $I^1\Sigma^-$ state.

Electron impact on CO can also result in the formation of metastable carbon and oxygen atoms from dissociative excitation. Wells *et al.*[21] observed metastable fragments composed of long-lived high-Rydberg carbon and oxygen atoms and O($^5S^0$) atoms with kinetic energies ranging from 0 to 25 eV, for impact energies in the range of 0 to 300 eV. Eight discernible TOF peaks were observed. The lowest appearance potential was found at 20 eV. An electron-impact cross section of 2×10^{-18} cm^2 at 190 eV was deduced for the production of metastable fragments assuming that O*, C*, and O($^5S^0$) have equal cross sections. Barnett *et al.*[22] found only one peak in kinetic energy distributions for the metastable oxygen fragments from carbon monoxide. The peak kinetic energy increases from 3.75 at 40 eV to 4.69 at 60 eV. LeClair *et al.*[23] detected O(^1S) production with a threshold at 16 eV and a maximum cross section of 5×10^{-19} cm^2 at 100 eV.

Becker *et al.*[24] investigated Cameron bands luminescence from CO-doped solid Ar using synchrotron radiation and thermally stimulated luminescence. They observed weak lines at 8 eV in the excitation spectrum which corresponds to direct photoexcitation of the matrix isolated CO by spin-allowed singlet transitions $X^1\Sigma^+ \to A^1\Pi$. Electronic excitation of CO by energy transfer from excitons of the matrix was seen between 12–14 eV. They attributed the strong increase in luminescence just above 21 eV as due to CO*($a^3\Pi$) production by inelastic scattering of low-energy photoelectrons. In the same system, Bahrdt *et al.*[25] found a CO metastable state at about 11 eV with a lifetime of about 15 ms. It was assigned to a CO quintet state populated nonradiatively after excitation of a Rydberg state.

Thresholds for electron stimulated desorption (ESD) of neutral (ground-state+metastable) molecules from several molecular solid films, including solid CO, were reported by

Rakhovskaia *et al.*[26] Desorption thresholds appeared at distinct electron energies: for CO it was about 6 eV and assigned to excitation of the $a^3\Pi$ state. ESD signals below the electronic excitation threshold were smaller by a factor of 250. The desorption mechanism is believed to be conversion of electronic to vibrational and finally to translational energy via radiationless decay. More recently, Scheuer *et al.*[27] and Wurm *et al.*[28] investigated the correlation of internal excitations and substrate-adsorbate coupling for CO molecules desorbed from metallic and Xe surfaces by 150 eV electron impact. They attributed the strong yield of desorbed ground state CO in high vibrational states to quenching, by the metal substrate, of CO* molecules which are dissociative with respect to both the C-O bond and the molecule-surface bond.

Desorption of ground-state neutrals from solid CO also has also been investigated by excitation with energetic ions;[29,30] the yield was found to have a quadratic dependence on the electronic stopping power of the incident particles. Chrisey *et al.*[30] concluded that this dependence is intrinsic to the electronic energy conversion process in CO, i.e., intrinsic to the energy transfer process which sets molecules in motion. However, they did not identify the molecular state involved.

Low energy electron stimulated MP desorption has been investigated in our laboratory for various condensed films.[4,31–33] In the case of CO, only the yield function of MP desorption for a 50 monolayer (ML) film has been reported between 5 and 19 eV.[32] In this paper, we report the results of experiments performed on the thickness dependence of the MP yield within the 4–52 eV electron energy range, and those obtained from the TOF distributions recorded at different impact energies within that range.

4. RESULTS

The metastable yield functions of CO films are shown in Fig. 1 for various CO thicknesses. The curves are similar in shape for film thicknesses larger than 2 ML. For all CO thicknesses, there is a common MP desorption threshold at 8.0 eV, and the yield increases continuously with electron energy, exhibiting a broad peak at about 16 eV. These results are in agreement with those previously reported for 5–19 eV electrons impinging on a 50-ML CO film.[32]

TOF distributions of desorbed MP were measured with different incident electron energy within the 10 to 50 eV range. Apart from the small but sharp peak at $t=0$ due to UV photon emission, each distribution exhibits a single TOF peak; the line shape of all distribution curves are very similar to each other. In Fig. 2, TOF results are shown for a 50-ML CO film for incident energies of 11, 15 and 50 eV, while the integrated peak area is plotted in the insert as a function of electron energy. The later reproduces very well the shape of the metastable yield functions recorded for thicknesses larger than 2 ML shown in Fig. 1. The MP distribution peak at about $45\pm5\ \mu$s corresponds to a kinetic energy of 195 ±50 meV for CO*. With increasing electron energy, there is a slight shift in the rising slope of TOF distributions which indicates that higher energy MP are being fed into the distribution with increasing electron energy. The yield of CO* as
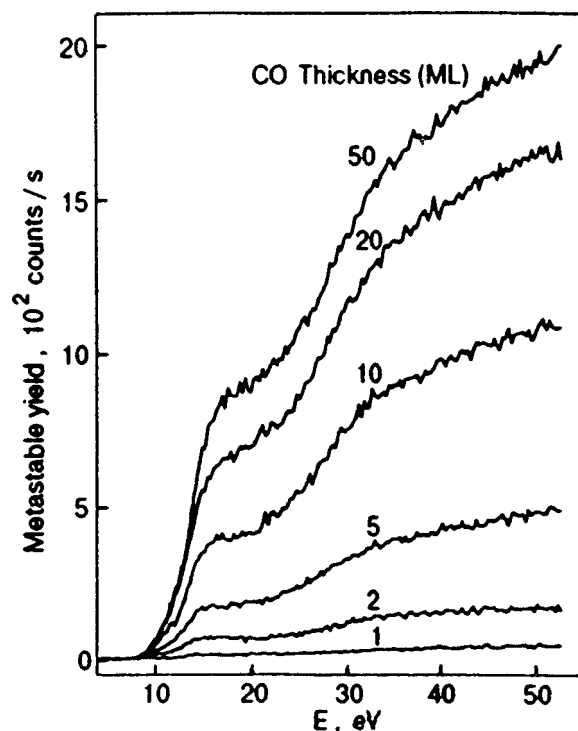

FIG. 1. Metastable carbon monoxide (CO*) desorption yields induced by 4–52 eV electrons impinging on CO films of different thicknesses indicated in monolayers (ML).

a function of film thickness is shown in Fig. 3 for incident electron energies of 26 and 46 eV.

5. DISCUSSION

Below the electron energy of 20 eV, any detected MP signal should arise from metastable carbon monoxide (CO*). Although LeClair *et al.*[23] detected an onset for the production of $O(^1S)$ at 16 eV, the internal energy of this state of 4.17 eV is too low to trigger our MP detector. The $O(^5S^0)$ state possesses an excitation energy of 9.14 eV and a
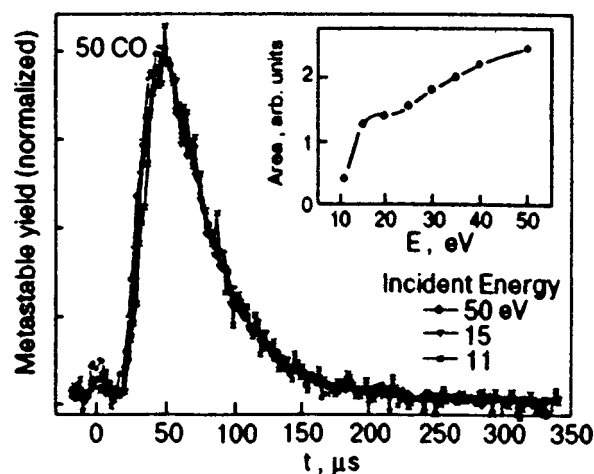

FIG. 2. Normalized time of flight (TOF) distributions of CO* desorbed by the impact of 11-, 15-, and 50-eV electrons on a 50-ML CO film. The integrated TOF peak area are shown in the insert as a function of incident electron energy.
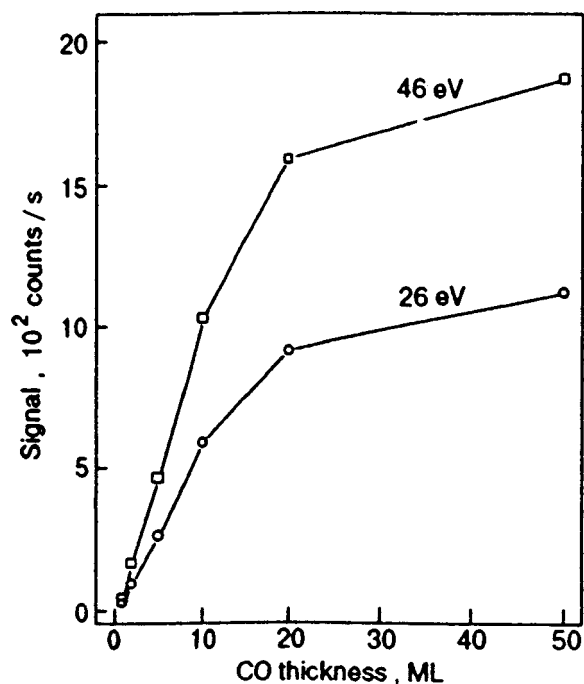
FIG. 3. CO* signal intensity as a function of CO thickness, deduced from Fig. 1.

lifetime of 180 μs, but it is not produced below 20 eV.[21] The threshold energy of 8 eV shown in Fig. 1 is higher than that of 6 eV for the metastable ($a^3\Pi$) production for gaseous CO.[8,15] It indicates that no significant quantities of CO in the $a^3\Pi$ state desorb from a CO film for impact energies between 6–8 eV. Thus, the threshold corresponding to $a^3\Pi$ excitation reported by Rakhovskaia *et al.*[26] in the neutral CO desorption yield from solid CO must arise essentially from CO molecules in their groundstate.

At low electron-impact energies, the desorption process must be simple since ionization, desorption of dissociation fragments, and desorption via collision cascade can be excluded. There are only three possibilities for the desorption of excited molecules from a molecular solid at low energies. In one case, the excited molecule at the surface has an energy higher than in the gas phase. Motion along a repulsive molecule-surface potential-energy curve can lead to acceleration and desorption of the excited molecule. This is called the cavity expulsion mechanism. In crystals with a positive electron affinity, the excited particle is not expelled owing to the attractive interaction of the excited-orbit electron cloud with the neighboring atoms. Solid CO has a positive electron affinity[34] which rules out MP desorption through cavity expulsion.[35] Another possibility is local repulsive CO*-CO interaction near the film surface which could lead to CO* ejection in vacuum (dimeric ejection). This is impossible at low energies for CO because all of the valence CO excited states lie at lower energies in condensed CO than in gaseous CO.[7] The only possibility left is desorption via intramolecular to molecule-surface vibrational energy transfer. Direct excitation to the $a^3\Pi$ state only produces low intramolecular vibrational quanta ($\nu=0-4$)[7] which may not allow sufficient energy transfer to the molecule-surface bond during the

lifetime of the state to induce desorption.[36] This may explains the lack of CO* desorption in the 6–8 eV range.

For a given electronic transition, the vibrational population of the CO molecules is determined by the Franck-Condon factors. From potential-energy diagrams of CO and known molecular constants,[37] excitation to the $a'^3\Sigma^+$, $d^3\Delta$, $e^3\Sigma^-$, $I^1\Sigma^-$, and $D^1\Delta$ states is expected to be in high vibrational levels. Rosenkranz and Kirby[14] calculated the Franck–Condon overlaps which peak at $\nu=14$ and 15 for the I and D states, respectively. For the $a'^3\Sigma^+$ state, vibrational levels $\nu=7-24$ lie within the Franck–Condon region, the $\nu=8$ level corresponds to our threshold of 8 eV for metastable CO desorption observed in the present experiment. According to the near-threshold excitation spectrum of CO multilayers,[7] the $a'^3\Sigma^+$ state is the only one produced with a non-negligible amplitude by 8–10-eV electrons. We therefore ascribe the MP yield in the range 8–10 eV to initial excitation to that state. Above 10 eV, the $d^3\Delta$, $e^3\Sigma^-$, $I^1\Sigma^-$, and $D^1\Delta$ states can also be excited by electron impact and therefore they are expected to be involved in MP desorption.

The CO* molecules may desorb directly in these states or first decay into high vibrational levels of the $a^3\Pi$ configuration, depending on the rate of energy transferred from intramolecular vibration to the molecule-surface bond. This energy transfer is thus strongly dependent on the lifetime of the initial excited state,[38,39] but also on the amount of librational motion and vibrational energy of the excited molecule[36] and the surface temperature. CO with its high vibrational frequencies and small rotational constants has long vibrational relaxation times in the ground state, ranging from milliseconds to seconds depending on environment and other parameters.[40] Since the nonradiative contribution to the relaxation process is multiphonon,[41] we may expect energy transfer to molecular-surface bond to have similar time scales. However, in the excited states, the higher vibrational energy content and the stronger molecule-surface bond may lead to shorter times for such a transfer. In fact, recent three-dimensional quantum calculations on CO physisorbed on a NaCl(100) rigid surfaces[36] show that significant desorption of the molecule can occur within picosecond times for initial librational quanta as small as 2, provided translational motion due to temperature is taken into account. Unfortunately, no such calculation exists for the case of CO on CO at cryogenic temperatures which would allow to determine if the lifetimes given in Table are sufficient for desorption of CO* before decay to the $a^3\Pi$ state, when all the factors previously mentioned are taken into account. Although it is well established that CO desorption can occur as the result of energy transfer from intramolecular to molecule surface desorption modes, we cannot with present experimental and theoretical evidence determine the state of desorption of CO*. We therefore limit our discussion to the configurations which are initially excited by electron impact. In any case, CO* is likely to reach our detector in the $a^3\Pi$ configuration. The other triplet states, having lifetimes of several μs,[10] can be radiatively de-excited into the low-lying $a^3\Pi$ state during the TOF. The lifetimes for $I^1\Sigma^-$ and $D^1\Delta$ states were measured to be 80 or 97 μs, respectively,[12,13] but the lifetimes of the low-lying vibrational levels of these states are very long

(up to 1 s) due to the small transition energies to the $A^1\Pi$ state.[14] Since the desorption by vibrational energy transfer lowers the vibrational levels of desorbed CO*, it may be possible that the desorbed metastables in I and D states live sufficiently long (presumably several hundred μs) to arrive at the detector.

Using the R-matrix method, Morgan and Tennyson[42] have calculated electron-impact excitation cross sections for the lowest seven electronically excited states of CO in the energy range 6–18 eV. A sharp electron resonance feature ($^2\Pi$) is found at 10.4 eV for the $a'^3\Sigma^+$ configuration, and the $d^3\Delta$ results show a shoulder at about 11 eV due to a $^2\Phi$ resonance.[42] For energy above 12 eV, the cross sections for the $a'^3\Sigma^+$, $d^3\Delta$, and $e^3\Sigma^-$ states are of the same order of magnitude while for the $I^1\Sigma^-$ and $D^1\Delta$ states, they are about 5 times smaller. Interestingly, they have compared the excitation of the higher metastables $I^1\Sigma^-$ and $D^1\Delta$ states with the measurement of Mason and Newell[13] and found roughly the same shape, with a maximum located near 16 eV. Cross sections for the excitation of all metastables, i.e., the a, a', d, e, I, and D states, exhibits a maximum at 9 eV due to the major contribution from the $a^3\Pi$ state and a second maximum at about 15.5 eV.[42] The first maximum is not expected to be observed in our experiments since it is dominated by direct excitation of the $a^3\Pi$ state which does not directly contribute to MP desorption from CO films. However, considering that the near-threshold electron-impact excitation spectrum of CO is similar in both phases,[7] we expect the energy dependence sum of the calculated cross sections of the $a'^3\Sigma^+$, $d^3\Delta$, $e^3\Sigma^-$, $I^1\Sigma^-$, and $D^1\Delta$ states to have roughly the same shape (except the resonance features for the $a'^3\Sigma^+$ and $d^3\Delta$ states) as that of the MP yield function for CO films below 20 eV. We therefore ascribe the broad peak at 16 eV in Fig. 1 to contributions from initial excitation of these states. Above 16 eV, MP yield from a CO film increases further while it decreases for gaseous CO. This difference for solid and gas phase excitation possibly arises from multiple inelastic scattering of electrons in solids.

There is a slight shift in the TOF distributions in Fig. 2 with increasing electron energy. This is not expected from a CO* signal originating from a single electronically excited state. Thus, the MP signal is believed to arise from an admixture of CO* configurations whose relative contribution changes slightly with electron energy, assuming that the MP yield at 50 eV is still dominated by molecular desorption. This is in agreement with our discussion that the states $a'^3\Sigma^+$, $d^3\Delta$, $e^3\Sigma^-$, $I^1\Sigma^-$, and $D^1\Delta$ are all possibly involved.

Above 20 eV, metastable carbon and oxygen atoms are observed in CO excitation in the gas phase.[21–23] If produced in highly excited states (e.g., oxygen in the $^5S^0$ state) these fragments could be detected in our experiments. Since they are created with eV's of kinetic energy they are expected to produce a signal between 8–15 μs (4–1 eV) in the TOF distributions, a time domain where the magnitude of the MP yield is minimal. Hence, we suggest that highly excited atoms do not contribute significantly to the MP yields from condensed CO (i.e., the MP signal, produced by incident energy up to 50 eV, is essentially due to CO* desorption). In

the gas phase, however, the cross section for the production of atomic MP is of the order of 10^{-18} cm^2, which is comparable to that of the production of CO* in I and D states.[12,13,21–23] The fact that we do not observe noticeable atomic MP desorption may be caused by preferential deexcitation of highly excited C and/or O atoms in the bulk and near the surface or deexcitation of dissociative states to bound states before complete separation of the C and O atoms, as suggested by Scheuer *et al.*[27] Deexcitation of metastable atoms can occur by recombination, by excitation energy transfer between the atomic MP and the CO molecules as well as other radiationless decay and radiative transitions. Some of these processes may involve kinetic energy that induce collision cascade sputtering of neutral (ground-state) CO or desorption of ground state carbon and oxygen atoms, which we cannot detect.

On the other hand, molecular CO* produced in the bulk is expected to contribute to the MP desorption by exciton motion. Analysis of the data in Fig. 1 indicates that, within the 10–52 eV range, the MP signal increases more or less linearly with CO thickness between 2 and 10 ML; above 10 ML, the rate of increase reduces with a tendency toward saturation above 20 ML. This behavior is shown in Fig. 3 for incident energies of 26 and 46 eV.

Using the mathematical expression developed to explain the dynamics of MP desorption from N$_2$ films,[33] we obtain for a given incident electron energy the following expression for the CO* yield (Y_d) of a film of thickness T (expressed in ML):

$$Y_d \propto P_d \sum_{L=1}^{T} \{P_{CO*}[M, I_e(L)]f(L)\}, \qquad (3)$$

where P_d is the desorption probability of CO* at the surface during a given time interval; P_{CO*} is the probability to form CO*, which is a function of the electronic excitation matrix elements M and electron beam intensity I_e at a distance L from the surface; $f(L)$ is the exciton-motion function which reflects the probability of an exciton to move to the surface. Comparing the results of Fig. 3 to Eq. (3), we see that Y_d increases with T, indicating a contribution to the MP yield from CO excitation in the bulk. $f(L)$ is necessarily non-zero for CO thicknesses up to 50 ML. Furthermore, these results can be interpreted as due to a CO* yield directly proportional to the summation of CO layers in Eq. (3), with P_{CO*} and $f(L)$ being independent of thickness in the range $2 \leq T \leq 10$ ML. The slower increase above 10 ML is probably the results of electron-beam attenuation, which reduces P_{CO*}, and/or a reduction of $f(L)$.

6. CONCLUSION

Low-energy electron stimulated desorption of metastable particles from CO multilayer films exhibits a threshold at 8 eV which suggests direct excitation of the $a'^3\Sigma^+$ state followed by desorption in either the a' or $a^3\Pi$ state via intramolecular to molecular-surface vibrational energy transfer. Similarly, the states $d^3\Delta$, $e^3\Sigma^-$, $I^1\Sigma^-$, and $D^1\Delta$, are believed to be the first excited and contribute to the MP signal by the same energy-transfer mechanism. In this case,

desorption may also be preceded by decay into high vibrational levels of the $a^3\Pi$ state. Excitation of CO^* in the bulk also results in MP desorption through exciton motion. Desorption of metastable atoms in highly excited states is negligible in the electron energy range 0–52 eV. Finally, we note that, besides their interest to DIET processes, investigations such as the present one, may also be of value in the interpretation of luminescence data generated by photons[43] or charged particles[44] of sufficient energy to produce low-energy electrons.

*)E-mail: lsanche@courrier.usherb.ca

[1] P. Feulner and D. Menzel, in *Laser Spectroscopy and Photochemistry on Metal Surfaces*, H.-L. Dai and W. Ho (Eds.), World Scientific, Singapore (1995).

[2] R. E. Johnson, in *Desorption Induced by Electronic Transitions*, DIET III, R. H. Stulen and M. L. Knotek (eds.), Springer, Berlin (1988), p. 47; R. E. Johnson, *Energetic Charged-Particle Interactions with Atmosphere and Surfaces*, Springer, Berlin (1990), p. 1.

[3] E. F. van Dishoeck and J. H. Black, Astrophys. J. **334**, 771 (1988); D. L. Cooper and K. Kirby, J. Chem. Phys. **87**, 424 (1987).

[4] G. Leclerc, A. D. Bass, A. Mann, and L. Sanche, Phys. Rev. B **46**, 4865 (1992).

[5] R. T. Jongma, T. Rasing, and G. Meijer, J. Chem. Phys. **102**, 1925 (1995).

[6] J. Bahrdt, P. Gürtler, and N. Schwentner, J. Chem. Phys. **86**, 6108 (1987); J. Bahrdt and N. Schwentner, *ibid.* **88**, 2869 (1988).

[7] R. M. Marsolais, M. Michaud, and L. Sanche, Phys. Rev. A **A35**, 607 (1987).

[8] W. L. Borst and E. C. Zipf, Phys. Rev. A **3**, 979 (1971).

[9] C. E. Johnson and R. S. van Dyck, Jr., J. Chem. Phys. **56**, 1506 (1972).

[10] H. A. van Sprang, G. R. Möhlmann, and F. J. de Heer, Chem. Phys. **24**, 429 (1977); S. Shadfar, S. R. Lorentz, W. C. Paske, and D. E. Golden, J. Chem. Phys. **76**, 5838 (1982); W. C. Paske, A. W. Garrett, S. Shadfar, D. E. Golden, and J. R. Twist, *ibid.* **76**, 3002 (1982).

[11] R. Anderson, *Atomic Data* **3**, 227 (1971); A. J. Smith, R. E. Imhof, and F. H. Read, J. Phys. B **6**, 1333 (1973).

[12] W. C. Wells, W. L. Borst, and E. C. Zipf, Phys. Rev. A **8**, 2463 (1973).

[13] N. J. Mason and W. R. Newell, J. Phys. B **21**, 1293 (1988).

[14] M. E. Rosenkranz and K. Kirby, J. Chem. Phys. **90**, 6528 (1989).

[15] D. S. Newman, M. Zubek, and G. C. King, J. Phys. B **16**, 2247 (1983).

[16] J. M. Ajello, J. Chem. Phys. **55**, 3158 (1971).

[17] P. W. Erdman and E. C. Zipf, Planet. Space Sci. **31**, 317 (1983); J. M. Furlong and W. R. Newell, J. Phys. B **29**, 331 (1996).

[18] J. Olmsted III, A. S. Newton, and K. Street, Jr., J. Chem. Phys. **42**, 2321 (1965).

[19] J. N. H. Brunt, G. C. King, and F. H. Read, J. Phys. B **11**, 173 (1978).

[20] V. Cermak, J. Chem. Phys. **44**, 1318 (1966).

[21] W. C. Wells, W. L. Borst, and E. C. Zipf, Phys. Rev. A **17**, 1357 (1978).

[22] S. M. Barnett, N. J. Mason, and Mason Newell, J. Phys. B **25**, 1307 (1992).

[23] L. R. LeClair, M. D. Brown, and J. W. McConkey, Chem. Phys. **189**, 769 (1994).

[24] J. Becker, O. N. Grigorashchenko, A. N. Ogurtsov, M. Runne, E. V. Savchenko, and G. Zimmerer, J. Phys. D **31**, 749 (1998).

[25] J. Bahrdt and N. Schwentner, Chem. Phys. **127**, 263 (1988); J. Bahrdt, H. Nahme, and N. Schwentner, *ibid.* **144**, 273 (1990).

[26] O. Rakhovskaia, P. Wiethoff, and P. Feulner, Nucl. Instrum. Methods Phys. Res. B **101**, 169 (1995).

[27] M. Scheuer, D. Menzel, and P. Feulner, Surf. Sci. **390**, 23 (1997).

[28] S. Wurm, P. Feulner, and D. Menzel, Phys. Rev. Lett. **74**, 2591 (1995).

[29] W. L. Brown, W. M. Augustyniak, K. J. Marcantonio, E. H. Simmons, J. W. Boring, R. E. Johnson, and C. T. Reimann, Nucl. Instrum. Methods Phys. Res. B **1**, 307 (1984); J. Schou, O. Ellegaard, P. Borgesen, and H. Sorensen, in *Desorption Induced by Electronic Transitions*, DIET II, W. Brenig and D. Menzel (Eds.), Springer, Berlin (1985), p. 170.

[30] D. B. Chrisey, W. L. Brown, and J. W. Boring, Surf. Sci. **225**, 130 (1990).

[31] G. Leclerc, A. D. Bass, M. Michaud, and L. Sanche, J. Electron Spectrosc. Relat. Phenom. **52**, 725 (1990); A. Mann, G. Leclerc, and L. Sanche, Phys. Rev. B **46**, 9683 (1992); A. Mann, P. Cloutier, D. Liu, and L. Sanche, *ibid.* **51**, 7200 (1995).

[32] H. Shi, P. Cloutier, and L. Sanche, Phys. Rev. B **52**, 5385 (1995).

[33] H. Shi, P. Cloutier, J. Gamache, and L. Sanche, Phys. Rev. B **53**, 13 830 (1995).

[34] G. Bader, G. Perluzzo, L. G. Caron, and L. Sanche, Phys. Rev. B **30**, 78 (1984).

[35] F. Coletti, J. M. Debever, and G. Zimmerer, J. Phys. (France) Lett. **45**, 467 (1984).

[36] F. Dzegilenko, E. Herbst, and T. Uzer, J. Chem. Phys. **102**, 2593 (1995) and citations therein; E. Galloway and E. Herbst, Astron. Astrophys. **287**, 633 (1994).

[37] K. P. Huber and G. Herzberg, *Constants of Diatomic Molecules*, Van Nostrand Reinhold, New York (1979); S. G. Tilford and J. D. Simmons, J. Phys. Chem. Ref. Data Suppl. **1**, 147 (1972).

[38] H. J. Kreuzer and D. N. Lowy, Chem. Phys. Lett. **78**, 50 (1981); Z. W. Gortel, H. J. Kreuzer, P. Piercy, and R. Teshima, Phys. Rev. B **27**, 5066 (1983); Phys. Rev. B **28**, 2119 (1983); H. J. Kreuzer and Z. W. Gortel, *ibid.* **29**, 6926 (1984).

[39] B. Fain and S. H. Lin, Chem. Phys. Lett. **114**, 497 (1985); B. Fain, *ibid.* **118**, 283 (1985).

[40] H. Dubost, in *Inert Gases*, M. Klein (Ed.), Springer, Berlin (1984).

[41] S. A. Egorov and J. L. Skinner, J. Chem. Phys. **106**, 1034 (1997) and citations therein.

[42] L. A. Morgan and J. Tennyson, J. Phys. B **26**, 2429 (1993).

[43] A. N. Ogurtsov, E. V. Savchenko, J. Becker, M. Runne, and G. Zimmerer, Fiz. Nizk. Temp. **23**, 1131 (1997) [Low Temp. Phys. **23**, 851 (1997)].

[44] See for example, E. V. Savchenko, A. N. Ogurtsov, O. N. Grigorashchenko, and S. A. Gubin, Chem. Phys. **189**, 415 (1994).

LATTICE DYNAMICS

Surface and quasi-surface phonons and transformation waves in a hexagonal crystal

A. M. Kosevich and S. E. Savotchenko

B. Verkin Institute for Low Temperature Physics and Engineering, National Academy of Sciences of the Ukraine, 310164 Kharkov, Ukraine[*)]

D. V. Matsokin

Kharkov State University, 310077 Kharkov, Ukraine

A simple model of the dynamics of a layered crystal having a hexagonal lattice with weak interaction of atoms in neighboring basal planes is formulated. Vibrations propagating in the basal plane with displacement vectors lying in the same plane are investigated. Energy–momentum relations are obtained for low-frequency (Rayleigh type) as well as high-frequency (gap-mode) vibrations localized at the free surface. The region of existence of quasi-surface phonons, whose boundaries are determined to a considerable extent by the shape of constant-frequency surfaces for two branches of bulk vibrations is determined. It is shown that peculiarities in the interaction of elastic waves with the crystal surface appear in the bulk spectrum at certain frequencies. The dispersion curves for surface vibrations separated from the continuous spectrum have a continuation in this spectrum in the form of dependences corresponding to transformation of a transverse wave into a longitudinal one. The effect of a surface monolayer of impurity atom on localized and pseudolocalized vibrations is investigated. © *1998 American Institute of Physics.* [S1063-777X(98)01010-X]

INTRODUCTION

Many applications of multilayered crystal systems formed on the basal of resonant properties require information on peculiarities in the vibrational spectrum associated with planar defects. The simplest $2D$ defect in a crystal is its surface with alien atoms absorbed on it. It is well known that localized waves of the Rayleigh type, whose penetration depth into the bulk of the crystal is usually small, can emerge near the crystal surface. The position of possible frequencies of localized waves is determined to a considerable extent by the spectrum of bulk vibrations of the crystal.

Surface waves in continuous media (in the long-wave approximation) and in the crystal lattice were studied by many authors. We shall mention here only the publications[1–8] close in content to the present paper.

This research aims at a detailed analysis of the spectrum of surface and pseudosurface waves emerging in an aniso-tropic crystal near the surface as well as various types of transformation waves with peculiar frequency dependences in the spectrum of bulk vibrations. The term pseudosurface is applied to two-partial elastic vibrations near the surface with basically different behavior of the two components (parts). One of them (pseudolongitudinal part) is localized near the surface, while the other (pseudotransverse part) has the form of a standing wave existing in the entire half-space. The interest in such vibrations grew when it was found that they determine the resonant properties of scattering of a trans-verse wave by the planar defect. The ''transformation of

waves'' includes conditionally the scattering of elastic waves at the crystal surface, during which an incident transverse wave, for example, is reflected in the form of a purely lon-gitudinal wave. Another example is a process in which an incident transverse (longitudinal) wave is reflected in the form of a purely transverse (longitudinal) wave. Since elastic vibrational modes which are independence in the bulk are interrelated at the surface in the case of standard scattering processes, the above-mentioned ''transformation'' can occur only under special conditions connecting frequency with the wave vector of the wave.

We consider a crystal with a simple hexagonal lattice in which the interactions of atoms in the basal plane xz and along the sixth-order symmetry axis y are different, the atomic interaction in the xz plane being assumed to be con-siderably stronger than the interaction between atoms in neighboring basal planes. We shall describe vibrations polar-ized in the basal plane by using a model in which the strong interaction between only the nearest neighbors in the xz plane is taken into account, while the interaction between atoms in neighboring basal planes is not manifested if a plane wave propagates in a direction perpendicular to the sixth-order axis.

Thus, the model of an anisotropic crystal applied in an analysis of vibrations polarized in a basal plane and propa-gating in the same plane can be reduced to the model of a two-dimensional hexagonal lattice with central interaction between nearest neighbors. The surface bounding the crystal
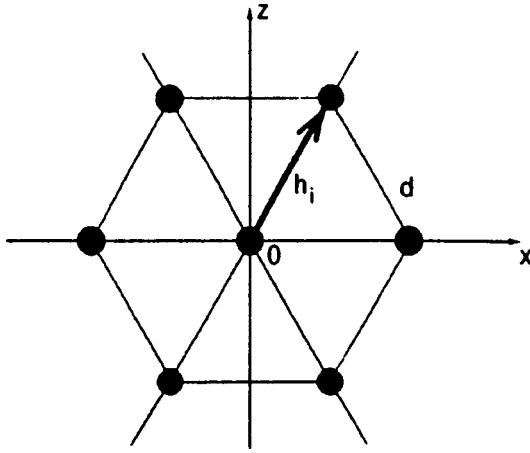
FIG. 1. Choice of nearest neighbors in the basal plane of a hexagonal crystal.

contains a sixth-order axis and is perpendicular to the basal plane.

The analysis includes the effect of a monolayer of atoms absorbed at the surface on the spectrum of surface and resonant vibration of the crystal.

1. EQUATIONS OF MOTION AND ENERGY–MOMENTUM RELATION FOR BULK VIBRATIONS

We consider a two-dimensional hexagonal lattice with atomic spacing d (Fig. 1). Each site in such a lattice contains a sixth-order symmetry axis. The positions of atoms are characterized by the coordinates x and z, the x-axis being directed towards the nearest neighbor. The interaction between all nearest atoms is the same and is characterized by the force constant α. We choose an atom located at the origin $(0,0)$ whose six nearest neighbors have the following coordinates (we assume for simplicity that $d=1$):

$$\mathbf{h}_1=(1,0), \quad \mathbf{h}_2=\left(\frac{1}{2},\frac{\sqrt{3}}{2}\right), \quad \mathbf{h}_3=\left(-\frac{1}{2},\frac{\sqrt{3}}{2}\right),$$

$$\mathbf{h}_4=(-1,0), \quad \mathbf{h}_5=\left(-\frac{1}{2},-\frac{\sqrt{3}}{2}\right), \quad \mathbf{h}_6=\left(\frac{1}{2},-\frac{\sqrt{3}}{2}\right).$$

In this case, the potential energy of interaction between the chosen atom and its nearest neighbors can be written in the form

$$U=\frac{\alpha}{2}\sum_{\mathbf{n}}[\delta l(\mathbf{n})]^2, \tag{1}$$

where the elongation is

$$\delta l(x,z)=\sqrt{[x+\Delta u_x(x,z)]^2+[z+\Delta u_z(x,z)]^2}-1;$$

the increment $\Delta u_i(x,z)=u_i(x,z)-u_i(0,0)$, and the summation is carried out over all the nearest neighbors. With the potential energy in the form (1), we can easily write the equation of motion for harmonic vibrations of atoms:

$$\left\{\frac{m}{\alpha}\frac{\partial^2 u_x}{\partial t^2}=-3u_x(0,0)+\frac{1}{4}[u_x(\mathbf{h}_2)+u_x(\mathbf{h}_3)+u_x(\mathbf{h}_6)\right.$$

$$+u_x(\mathbf{h}_5)]+\frac{\sqrt{3}}{4}[u_z(\mathbf{h}_2)+u_z(\mathbf{h}_6)-u_z(\mathbf{h}_5)$$

$$-u_z(\mathbf{h}_3)]+u_x(\mathbf{h}_1)+u_x(\mathbf{h}_4),$$

$$\frac{m}{\alpha}\frac{\partial^2 u_z}{\partial t^2}=-3u_z(0,0)+\frac{3}{4}[u_z(\mathbf{h}_2)+u_z(\mathbf{h}_3)+u_z(\mathbf{h}_6)$$

$$+u_z(\mathbf{h}_5)]+\frac{\sqrt{3}}{4}[u_x(\mathbf{h}_2)+u_x(\mathbf{h}_6)$$

$$\left.-u_x(\mathbf{h}_3)-u_x(\mathbf{h}_5)].\right. \tag{2}$$

We begin with an analysis of intrinsic bulk vibrations of a perfect lattice. We choose the displacement of interest in the form

$$\mathbf{u}(x,z)=\mathbf{u}_0 e^{i(kx+qz-\omega t)}. \tag{3}$$

Substituting (3) into the equations of motion (2), we obtain a system of homogeneous algebraic equations in components of the vector $\mathbf{u}_0$ (the subscript "0" will be omitted in order to simplify notation):

$$\left\{u_x\left(\lambda-5+4\cos^2\frac{k}{2}+\cos\frac{k}{2}\cos\frac{\sqrt{3}q}{2}\right)\right.$$

$$-u_z\sqrt{3}\sin\frac{k}{2}\sin\frac{\sqrt{3}q}{2}=0,$$

$$u_x\sqrt{3}\sin\frac{k}{2}\sin\frac{\sqrt{3}q}{2}-u_z\left(\lambda-3+3\cos\frac{k}{2}\cos\frac{\sqrt{3}q}{2}\right)=0, \tag{4}$$

where $\lambda=m\omega^2/\alpha$. Relations (4) lead to the characteristic equation

$$(\lambda-5+4a^2+ab)(\lambda-3+3ab)=3(1-a^2)(1-b^2), \tag{5}$$

where $a\equiv\cos(k/2)$, $b\equiv\cos(\sqrt{3}q/2)$. Equation (5) quadratic in λ defines two independent branches of bulk vibrations, which will be henceforth referred to a the pseudolongitudinal (upper branch l) and pseudotransverse (lower branch t) branches.

The continuous spectrum of bulk vibrations consists of two partially overlapping branches, whose energy–momentum relations can be found from the characteristic equation (5):

$$\lambda_{l,t}(k,q)=2[2-a(a+b)]\pm\sqrt{D},$$

$$D=4[2-a(a+b)]^2-3[4-3a^2+b^2-2ab(3-2a^2)], \tag{6}$$

where the plus and minus signs correspond to the l-branch and t-branch, respectively.

It is convenient to choose the principal Brillouin zone for the hexagonal lattice under investigation as follows: $-(2\pi/\sqrt{3})<q<(2\pi/\sqrt{3})$, $-2\pi<k<2\pi$. The frequency spectra of bulk harmonic vibrations (6) as functions of the wave vector k in the limits $0<k<\pi$ and $0<q<2\pi/\sqrt{3}$ are shown in Fig. 2 (hatched regions). Curve *1* is the lower boundary of the continuous spectrum, which is the envelope
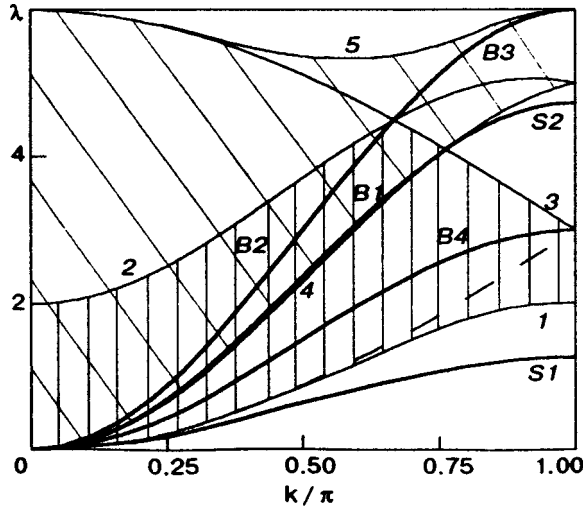
FIG. 2. Frequency spectra of bulk vibrations (hatched regions), of surface waves *S1* and *S2*, and of transformation waves *B1*, *B2*, *B3* and *B4* as functions of the wave vector *k*. The vertical hatching corresponds to pseudotransverse branch, while the slanted hatching corresponds to the pseudolongitudinal branch.

of the curves $\lambda = \lambda(k,q)$ corresponding to minimum values of λ for each k. Curves *2* and *3* denote the upper boundary of the pseudotransverse branch corresponding to $q = 2\pi/\sqrt{3}$. Curve *4* marks the lower boundary of the pseudolongitudinal branch, while curve *5* is the upper boundary of the pseudolongitudinal branch, which is also an envelope corresponding to the maximum values of λ for each k.

The continuous spectrum of bulk vibrations has a high-frequency gap adjoining the Brillouin zone boundary and formed by the intersection of the lower boundary curve for the pseudolongitudinal branch and the upper boundary curve for the pseudotransverse branch at the point $\lambda_0(k_0) = 3(1 + \sqrt{3})/2$ for $k_0 = 2 \arccos[(\sqrt{3}-1)/2]$.

Since each site of the hexagonal lattice lies on the sixth-order symmetry axis, all equations of motion, and hence the energy–momentum relations in the range of small values of wave numbers (long-wave approximation) must be transformed into the equations of the theory of elasticity for an isotropic solid. Indeed, expanding expression (6) for $k \ll 1$, we can obtain long-wave energy–momentum relations for bulk vibrations, which readily lead to the velocity $c = \omega/k$ of transverse and longitudinal acoustic waves propagating in the bulk of the crystal:

$$c_t^2 = \frac{3\alpha}{8m}, \quad c_l^2 = \frac{9\alpha}{8m}. \tag{7}$$

Thus, the relation between the longitudinal and transverse velocities of sound in the model under consideration is $c_l = \sqrt{3}c_t$. In other words, the vibrations of the hexagonal crystal under consideration are equivalent to vibrations of an isotropic solid with the Lamé coefficients $\lambda = \mu = 3\alpha/8$, which corresponds to the Poisson coefficient $\sigma = \lambda/[2(\lambda + \mu)] = 1/4$.

2. EFFECT OF FREE SURFACE ON THE CONTINUOUS FREQUENCY SPECTRUM OF BULK VIBRATIONS OF CRYSTAL

Let us suppose that a crystal fills the half-space $z \geq 0$. In this case, we simulate the free surface by the break in the interaction between atoms of the boundary layer $z = 0$ and the nearest layer with $z < 0$. The equations of motion for atoms in the boundary layer which play the role of the boundary conditions to the bulk equations (2) in the problem under consideration have the form

$$\begin{cases} \frac{m}{\alpha} \frac{\partial^2 u_x}{\partial t^2} = -\frac{3}{2} u_x(0,0) + u_x(\mathbf{h}_1) + u_x(\mathbf{h}_4) + \frac{1}{4} [u_x(\mathbf{h}_2) \\ \qquad + u_x(\mathbf{h}_3)] + \frac{\sqrt{3}}{4} [u_z(\mathbf{h}_2) - u_z(\mathbf{h}_3)], \end{cases}$$

$$\frac{m}{\alpha} \frac{\partial^2 u_z}{\partial t^2} = -\frac{3}{2} u_z(0,0) + \frac{3}{4} [u_z(\mathbf{h}_2) + u_z(\mathbf{h}_3)]$$

$$\qquad + \frac{\sqrt{3}}{4} [u_x(\mathbf{h}_2) - u_x(\mathbf{h}_3)]. \tag{8}$$

Since two waves can propagate in the crystal lattice along the *x*-axis, the displacement vector can be written in the form

$$u_x(x,z) = (u_t e^{iq_t z} + u_l e^{iq_l z}) e^{i(kx - \omega t)},$$

$$u_x(x,z) = (\Gamma_{t_t} u_t e^{iq_t z} + \Gamma_l u_l e^{iq_l z}) e^{i(kx - \omega t)}, \tag{9}$$

where the eigenvectors of the bulk equations (4) are given by

$$\Gamma_\mu = \frac{u_{z\mu}}{u_{x\mu}} = \frac{\lambda - 5 + 4a^2 + ab_\mu}{\sqrt{3(1-a^2)(1-b_\mu^2)}} = \frac{\sqrt{3(1-a^2)(1-b_\mu^2)}}{\lambda - 3 + 3ab_\mu}, \tag{10}$$

$\mu = l, t$, and the roots of the characteristic equation (5) for the corresponding vibrational branches are

$$b_\mu = \frac{1}{3} \{a[9 - 2(\lambda + 3a^2)] \pm \sqrt{d}\}, \tag{11}$$

$$d = a^2[9 - 2(\lambda + 3a^2)]^2 - 3[\lambda^2 + 4\lambda(a^2 - 2) + 3(4 - 3a^2)].$$

Substituting the expressions for the components of the displacement vector (9) into the boundary equations (8), we obtain the system of homogeneous algebraic equations in the vibrational amplitudes in the surface wave:

$$\sum_{\mu = l,t} u_{\mathbf{u}} C_{j\mu} = 0, \quad (j = 1,2), \tag{12}$$

where the matrix elements $C_{j\mu}$ ($\mu = l,t$) have the form

$$C_{1\mu} = \frac{9}{2} - \lambda - 4a^2 - \frac{1}{2} [a + i\Gamma_\mu \sqrt{3(1-a^2)}](b_\mu + \sqrt{b_\mu^2 - 1}), \tag{13}$$

$$C_{2\mu} = \left\{ \frac{3}{2} \left[a(b_\mu + \sqrt{b_\mu^2 - 1}) - 1 \right] + \lambda \right\} \Gamma_\mu$$
$$- i \frac{1}{2} \sqrt{3(1-a^2)}(b_\mu + \sqrt{b_\mu^2 - 1}).$$

The conditions of solvability of the system of equations (12) lead to the following equation for finding possible values of λ:

$$C_{1t}C_{2l} - C_{1l}C_{2t} = 0. \tag{14}$$

In the long-wave limit, the dispersion equation (14) is transformed into the well-known equation for the phase velocity $(c = \omega/k)$ of a Rayleigh wave in the isotropic half-space[2]:

$$4\kappa_t\kappa_l = \left(2 - \frac{c^2}{c_t^2} \right)^2 k^2, \tag{15}$$

where $\kappa_\mu = k\sqrt{1 - c^2/c_\mu^2}$, $\mu = l,t$. The parameters κ_l and κ_t characterize the rates of decrease of the longitudinal and transverse mode respectively: $u_\mu(x,z) = u_\mu^0 \exp(-\kappa_\mu z)e^{ikx}$. Equation (15) defines the phase velocity of an ordinary Rayleigh wave localized at the free surface of an isotropic solid and having a velocity c_R whose square is given by

$$c_R^2 = c_t^2 2 \left(1 - \frac{1}{\sqrt{3}} \right).$$

A similar result was obtained for a two-dimensional square lattice in Ref. 12. The phase velocity of a surface wave with arbitrary k cannot be written in explicit form. For any value of k, however, the energy–momentum relation for this surface wave can be obtained by numerical methods. The curve corresponding to this relation is shown in Fig. 2 (curve *S1*).

It is well known that the type of spatial decrease of a localized wave is determined by the shape of the cross section of the constant-frequency surface.[11] If the constant-frequency sections are convex relative to the direction of propagation, the vibrations decrease monotonically towards the bulk of the crystal, while in the case of nonconvex cross sections the surface waves can only be ''generalized.'' Displacements in a generalized surface wave, which decrease towards the bulk, oscillate with a certain characteristic wavelength determined by the shape of the nonconvex constant-frequency surface.

For $k < \pi/2$, the wave *S1* decreases monotonically, while in the interval $\pi/2 < k < \pi$ the decrease of vibrations in *S1* oscillates since the wave numbers q_μ have both real and imaginary components, and the wave becomes a generalized Rayleigh wave.

The limiting value of frequency of surface vibrations for this low-frequency wave at the boundary of the Brillouin zone ($k = \pi$) is given by $\lambda_s^{(low)}(\pi) = 3 - \sqrt{3}$.

Apart from the wave of the Rayleigh type, a localized high-frequency gap wave *S2* also exists in the range of wave numbers close to the Brillouin zone boundary (Fig. 2). The wave *S2* is an ordinary surface wave attenuating monotonically from layer to layer. It was found that curve *S2* originates at the point $\lambda_0(k_0) = 3(1 + \sqrt{3})/2$ for $k_0 = 2 \arccos[(\sqrt{3} - 1)/2]$ of the continuous spectrum (the point of intersection

of the lower boundary of the pseudolongitudinal and the upper boundary of the pseudotransverse branches of bulk vibrations) and terminates at the Brillouin zone boundary, where $\lambda_2^{(gap)}(\pi) = 3 + \sqrt{3}$.

In addition to the roots corresponding to real-valued κ_μ (i.e., waves decreasing exponentially towards the bulk of the crystal), Eq. (15) has roots in the region of continuous spectrum ($c > c_l$), corresponding to imaginary κ_μ. These roots correspond to $\kappa_\mu = iq_\mu$ under the necessary condition $q_t q_l < 0$ (q_t and q_l must have opposite signs). Such solutions correspond, for example, to a process in which a pseudotransverse wave $\exp(iq_t z)e^{-i\omega t}$ is incident on the surface, while the pseudolongitudinal wave $\exp(iq_l z)e^{(-i\omega t)}$ is reflected from it, or vice versa. Such a transformation of a wave into the one with the different polarization is known in the theory of elasticity as the wave transformation during reflection at the surface,[8] and the corresponding dispersion equation (15) in this case can be naturally referred to as the transformation equation. Equation (15) has two solutions corresponding to the velocity of propagation of waves being transformed at the free surface towards the bulk of the crystal:

$$c_1^2 = c_t^2 2 \left(1 + \frac{1}{\sqrt{3}} \right), \quad c_2^2 = 4c_t^2. \tag{16}$$

This corresponds to velocity values for transformation waves in an isotropic half-space with a Poisson coefficient $\sigma = 1/4$.[8]

A wave propagating with the velocity c_1 is incident on the crystal surface at an angle $\theta_{1t} = \arctan(1 + 2/\sqrt{3})^{1/2}$ (the angle of incidence is defined as $\tan\theta = q_\mu/k$, $\mu = l,t$) and is reflected at an angle $\theta_{1t} = \arctan[1/3(2/\sqrt{3} - 1)]^{1/2}$. A wave propagating at a velocity c_2 is incident on the surface at an angle $\theta_{2t} = \pi/3$ and is reflected at an angle $\theta_{2l} = \pi/6$.

Naturally, the coefficient of reflection of a transverse (or longitudinal) wave at the surface vanishes at the values of preferred frequencies $\omega_1 = c_1 k$ and $\omega_2 = c_2 k$. It should be noted that the obtained results do not depend on the type of the wave (transverse or longitudinal) incident on the surface and reflected from it.

An analysis of the bulk energy–momentum relation (6) shows that both branches contain regions in which constant-frequency curves in the kq plane are convex (Fig. 3a) as well as regions of a nonconvex shape, in which a given value of the wave vector k corresponds to more than two wave numbers q corresponding to a certain vibrational branch (Fig. 3b). Consequently a transformation of waves involving a change $t \leftrightarrow l$ can take place in regions of the type *T1*, while in regions of the type *T2* waves are transformed without changing the branch: $q_l^{(1)} \leftrightarrow q_l^{(2)}$.

Figure 2 shows wave transformation curves for an arbitrary value of the wave vector k (curves *B1* and *B2*). It was found that curve *B1* arrives at the same point $\lambda_0(k_0)$ of the continuous spectrum at which the curve *S2* of the surface wave originates (the point of intersection of the lower boundary of the pseudolongitudinal and the upper boundary of pseudotransverse branches of bulk vibrations).
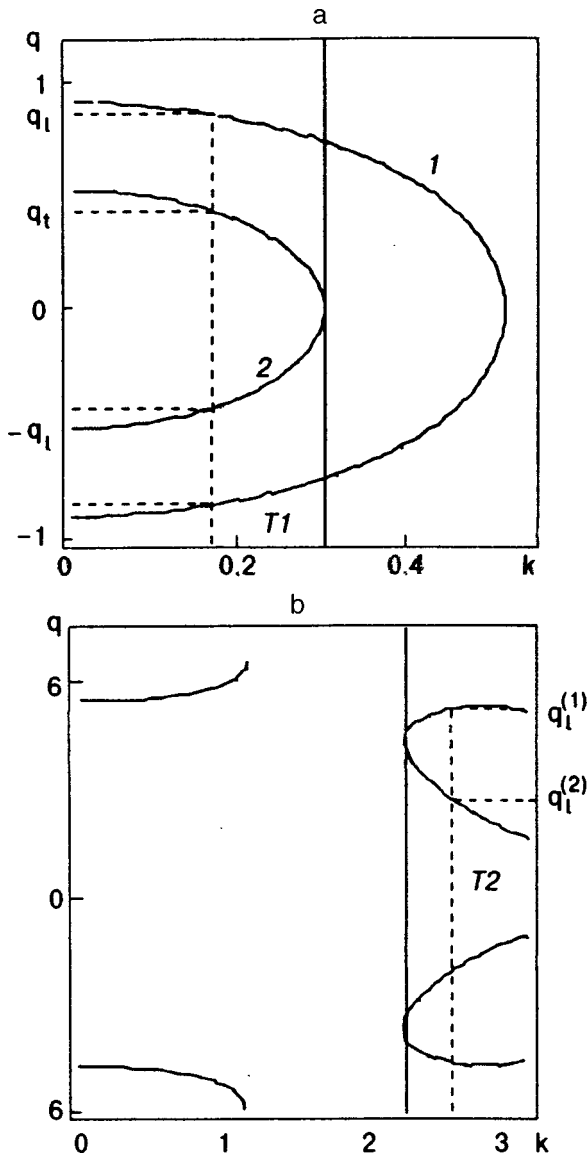
FIG. 3. Cross-section of constant-frequency surfaces by the kq plane: (a)-low-frequency region ($\lambda = 0.1$). Curve *1* corresponds to the pseudotransverse branch, while curve *2* corresponds to the pseudolongitudinal branch; (b)-high-frequency region ($\lambda = 5.5$) in which only pseudolongitudinal oscillations exist.

The energy–momentum relation for another special wave (curve *B2* in Fig. 2) (in the long-wave approximation $\omega = 2c_t k$) also belongs to the range of t- and l-branches of the continuous spectrum; as the wave number increases, it approaches the upper boundary of the pseudotransverse mode at the point $\omega_2^2 = 9\alpha/(2m)$ for $k = 2\pi/3$.

Starting from $k > 2\pi/3$, curve *B2* goes over to the range of only pseudolongitudinal bulk vibrations, in which another type of transformation takes place. In this region of continuous spectrum, cross sections of constant-frequency surfaces of bulk modes by the kq plane become nonconvex relative to the direction of propagation of the wave, and each wave number k at a fixed frequency corresponds to two pairs of wave numbers $\pm q^{(1)}$ and $\pm q^{(2)}$, describing the pseudolongitudinal branch (Fig. 3b). A bulk wave undergoes inelastic scattering at the free surface of the crystal without a change

in the polarization, but with a change in q. It was found that only a process of the type $q^{(1)} \leftrightarrow q^{(2)}$ is possible in this case (Fig. 3b).

Special bulk states formed along the curves *B1*, *B2*, and *B3* due to the presence of the surface are characterized by the vanishing of the corresponding reflection coefficients at their frequencies, i.e., peculiarities of this type are manifested during scattering of bulk waves at the crystal surface.

3. QUASISURFACE PHONONS IN A SEMI-INFINITE CRYSTAL AND ELASTIC VIBRATIONS NEAR A PLANAR DEFECT

The surface of a crystal can be responsible for the emergence of a different type of vibrations whose frequencies also belong to the continuous spectrum, but in the region in which only bulk pseudotransverse waves exist. Such vibrations are called pseudolocal (or quasisurface) phonons.[9,10] Waves of this type are two-partial waves and consist of an incident and a specularly reflected t-waves (one component) and the l-mode localized due to the presence of the surface (the other component):

$$u_x(x,z) = [u_t \cos(q_t z - \varphi) + u_l e^{-\kappa_l z}] e^{ik(x-ct)},$$

$$u_z(x,z) = [iu_t \Gamma_t \sin(q_t z - \varphi) + u_l \Gamma_l e^{-\kappa_l z}] e^{ik(x-ct)}, \quad (17)$$

where Γ_t and Γ_l are defined by formulas (10) as before, but now $b_t \equiv \cos(\sqrt{3}q_t/2)$, and $b_l \equiv \cosh(\sqrt{3}\kappa_l/2)$, and hence Γ_l are purely imaginary quantities. The phase φ of the wave characterizes the continuous change in frequency within the spectrum of pseudolocal vibrations.

Pseudolocalized vibrations can exist in the region of continuous spectrum below the lower boundary of the pseudolongitudinal branch $\lambda_{l\,\min}(k) = 1 - \cos(k/2) + 4\sin^2(k/2)$ (curve *4* in Fig. 2) and above the frequencies $\lambda_{t\,\min}(k) = 3(1 - \cos(k/2))$ of bulk vibrations corresponding to $q = 0$ (dashed curve in Fig. 2). For $k < \pi/2$, the latter curve is the lower boundary of the pseudotransverse branch. This is the region of continuous spectrum (similar to *T1* in Fig. 3a) in which cross sections of constant-frequency surfaces of bulk modes by the kq plane remain convex in the direction of propagation of the wave, each wave number k corresponding to a pair of wave numbers $\pm q_t$ at a fixed frequency.

The energy–momentum relation calculated for a pseudotransverse wave propagating near the surface is shown in Fig. 2 for all values of the wave number k within the Brillouin zone (curve *B4*).

Since long-wave oscillations polarized in the basal plane of a layered hexagonal crystal are equivalent to vibrations of an isotropic medium, the frequency dependence of pseudolocal oscillations in this limit is transformed into the energy–momentum relation described in Refs. 9 and 10. The phase velocities $c(\varphi)$ of such waves lie between the velocities (7) of transverse and longitudinal acoustic waves ($c_t < c(\varphi) < c_l$), and the dependence $c = c(\varphi)$ is defined by the relation

$$\tan \varphi = 4 \frac{[(c^2/c_t^2 - 1)(1 - c^2/c_l^2)]^{1/2}}{(c^2/c_t^2 - 2)^2}. \quad (18)$$
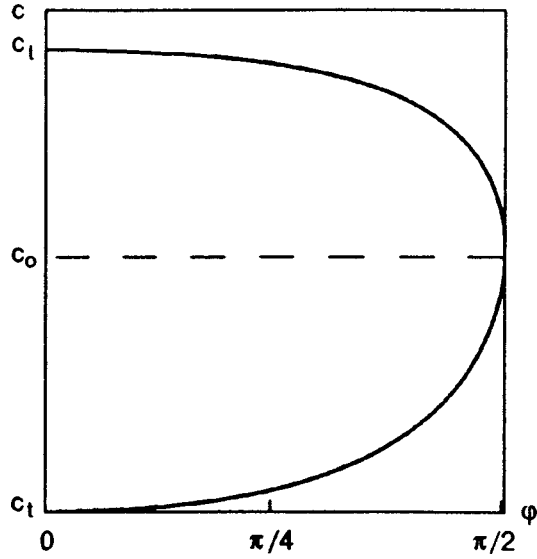
FIG. 4. Phase dependence of the pseudolocalized wave velocity.

An analysis of this relation shows that the crystal can confine simultaneously two pseudolocalized waves for the same value of phase. As $\varphi \to 0$, the velocity of the pseudolocal wave tends to the limiting velocities c_t and c_l of bulk waves (Fig. 4). For $\varphi = \pi/2$, only a wave with the velocity $c_0 = \sqrt{2} c_t$ corresponding to the velocity of a transverse wave

undergoing specular reflection at an angle $\theta = \pi/4$ at the free surface can propagate (the process of wave transformation into itself).

The possibility to a transition to an isotropic medium for $kd \ll 1$ suggests the possibility of a long-wave description of peculiarities of localized and pseudolocalized vibrations at a planar defect of a more general type in the bulk of the crystal.

Let us suppose that the plane $z=0$ lies in the bulk of the crystal and coincides with the surface of a certain stacking fault. We assume that the interaction of atoms in the layer with $z=0$ with atoms belonging to a higher-lying layer is characterized by the parameter α as before, while the interaction with atoms in a lower-lying layer $z = -\sqrt{3}d/2$ is characterized by the parameter β of force interaction, which differs from α. Similarly, the interaction of atoms in the layer $z = -\sqrt{3}d/2$ with atoms from a lower-lying layer is described by the parameter α (while describing a free surface, we assumed that $\beta = 0$). We can easily obtain the boundary conditions for dynamic equations for vibrations presuming the limiting transition $kd \ll 1$. We write the equations of motion for atoms lying in two layers on both sides of the defect. In the layer $z=0$, we denote by the vector $\mathbf{h}_0^+ = d(0,0)$ the coordinates of an isolated atom and by the vector $\mathbf{h}_0^- = (d/2) \times (1, -\sqrt{3})$ the coordinates of an isolated atom in a lower-lying atom. In this case, we have

$$
\begin{cases}
m \, \dfrac{\partial^2 u_x(\mathbf{h}_0^{\pm})}{\partial t^2} = -\dfrac{1}{2}\,(5\alpha + \beta) u_x(\mathbf{h}_0^{\pm}) + \alpha [u_x(\mathbf{h}_0^{\pm} + \mathbf{h}_1) + u_x(\mathbf{h}_0^{\pm} + \mathbf{h}_4)] \\[2mm]
\qquad + \dfrac{\alpha}{4}\,[u_x(\mathbf{h}_0^{\pm} \pm \mathbf{h}_2) + u_x(\mathbf{h}_0^{\pm} + \mathbf{h}_3)] \pm \dfrac{\sqrt{3}}{4}\,\alpha [u_z(\mathbf{h}_0^{\pm} \pm \mathbf{h}_2) - u_z(\mathbf{h}_0^{\pm} \pm \mathbf{h}_3)] \\[2mm]
\qquad + \dfrac{\beta}{4}\left[u_x(\mathbf{h}_0^{\pm} \pm \mathbf{h}_5) + u_x(\mathbf{h}_0^{\pm} \pm \mathbf{h}_6) \pm \dfrac{\sqrt{3}}{4}\,\beta [u_z(\mathbf{h}_0^{\pm} \pm \mathbf{h}_6) - u_z(\mathbf{h}_0^{\pm} \pm \mathbf{h}_5)\right] ; \\[2mm]
m \, \dfrac{\partial^2 u_z(\mathbf{h}_0^{\pm})}{\partial t^2} = -\dfrac{3}{2}\,(\alpha + \beta) u_z(\mathbf{h}_0^{\pm}) + \dfrac{3}{4}\,\alpha [u_z(\mathbf{h}_0^{\pm} \pm \mathbf{h}_2) + u_z(\mathbf{h}_0^{\pm} \pm \mathbf{h}_3)] \\[2mm]
\qquad \pm \dfrac{\sqrt{3}}{4}\,\alpha [u_x(\mathbf{h}_0^{\pm} \pm \mathbf{h}_2) - u_x(\mathbf{h}_0^{\pm} \pm \mathbf{h}_3)] + \dfrac{3}{4}\,\beta [u_z(\mathbf{h}_0^{\pm} \pm \mathbf{h}_5) + u_z(\mathbf{h}_0^{\pm} \pm \mathbf{h}_6)] \pm \dfrac{\sqrt{3}}{4}\,\beta [u_x(\mathbf{h}_0^{\pm} \pm \mathbf{h}_6) - u_x(\mathbf{h}_0^{\pm} \pm \mathbf{h}_5)],
\end{cases}
$$

$$(19)$$

where the plus sign corresponds to the equations of motion for an atom from the upper bank of the defect and the minus sign to the same for the lower bank.

We expand the displacements $u_i(x,z)$ in (19) into a power series in h_i ($i = 1,2,3,4,5,6$) for the chosen lattice sites $\mathbf{h}_0^+$ and $\mathbf{h}_0^-$, confining ourselves only to the first terms. In this case, we can easily go over to the long-wave boundary conditions for the equations of elastic fields at a planar defect:

$$
\sigma_{iz}^+ - \sigma_{iz}^- = \frac{3}{8}\,\beta\,\frac{\partial}{\partial x}\,(u_z^- - u_z^+), \quad (i = x, z),
$$

$$
\sigma_{xz}^+ + \sigma_{xz}^- = \frac{\sqrt{3}}{2}\,\frac{\beta}{d}\,\frac{\partial}{\partial x}\,(u_x^+ - u_x^-) + \frac{3}{8}\,\beta\,\frac{\partial}{\partial x}\,(u_z^+ + u_z^-),
$$

$$
\sigma_{zz}^+ + \sigma_{zz}^- = \frac{3\sqrt{3}}{2}\,\frac{\beta}{d}\,\frac{\partial}{\partial x}\,(u_z^+ - u_z^-) + \frac{3}{8}\,\beta\,\frac{\partial}{\partial x}\,(u_x^+ + u_x^-),
$$

$$(20)$$

where u_i^+ are displacements in the upper half-space (for $z=0$) and u_i^- the displacements in the lower half-space (for $z = -\sqrt{3}d/2$). Hooke's law for the model under investigation has the form

$$\sigma_{xz}=\mu\left(\frac{\partial u_x}{\partial z}+\frac{\partial u_z}{\partial x}\right),\quad \sigma_{zz}=\lambda\,\frac{\partial u_x}{\partial x}+(\lambda+2\mu)\,\frac{\partial u_z}{\partial x},$$

and the corresponding elastic moduli are $\lambda=\mu=3\alpha/8$. The boundary conditions (20) obtained from the equations of lattice dynamics coincide except for the notation of elastic moduli with the phenomenological boundary conditions derived in Ref. 10 from the equations in the theory of elasticity. It was proved[10] that pseudolocalized vibrations exist in a crystal with a planar defect in addition to localized vibrations. Elastic fields of such vibrations in the upper half-space $u_i^+(x,z)$ have the form (17). The form of solutions in the lower half-space $u_i^-(x,z)$ is determined by their symmetry. It was found that vibrations can be classified as symmetric, for which $u_{x\mu}^-(x,z)=-u_{x\mu}^+(x,-z)$, $u_{z\mu}^-(x,z)=u_{z\mu}^+(x,-z)$, and antisymmetric, for which $u_{x\mu}^-(x,z)=u_{x\mu}^+(x,-z)$, $u_{z\mu}^-(x,z)=-u_{z\mu}^+(x,-z)$. The results obtained in Ref. 10 can be extended except for notation to the case of long-wave vibrations of the given model of a discrete lattice.

The spectra of long-wave vibrations of a crystal with a planar defect in the form of an intercalated basal plane of isotope atoms with a coupling between adjacent layers differing from that in the unperturbed matrix were studied by Ivanov and Skripnik[13] who carried out similar investigations. The results obtained by us differ from those in Ref. 13 in a different arrangement of the defect plane (which was parallel to the basal plane of the crystal) and in the theoretical approach. Nevertheless, the conclusions concerning the conditions of formation of symmetric and antisymmetric local states as well as the dispersion curves of resonant modes in the continuous spectrum as a continuation of the frequency curves for local vibrations are qualitatively similar.

4. MONOLAYER OF ALIEN ATOMS ABSORBED AT THE CRYSTAL SURFACE

An analysis of the spectra of vibrations localized at the free surface shows that their frequencies can appear in gaps under the continuous spectrum also. It is well known that, in the case of a ''loaded'' surface, the frequencies of local vibrations can also appear above the spectrum of bulk vibrations. Such energy–momentum relations were obtained by Allen *et al.*[3] for an fcc crystal with a monolayer of atoms adsorbed at the surface, their atomic mass differing from that for internal layers. Kaplan[4] studied the effect of an adsorbed monolayer on the frequency spectrum of localized vibrations in a two-dimensional square lattice in the long-wave limit and for values of k corresponding to the corresponding boundary of the Brillouin zone.

Let us analyze the influence of a planar defect in the model of an anisotropic layered crystal under investigations, in which the atoms from the surface layer have a mass M differing from the atomic mass m for internal layers. In this case, the equations of motion for the boundary layer $z=0$ are obtained from (8) by the substitution $m\rightarrow M$. Substituting the solutions of the form (9), relation (10), and the roots of the characteristic equation (11) into these equations, we obtain a system of the form (12), in which the coefficients are given by
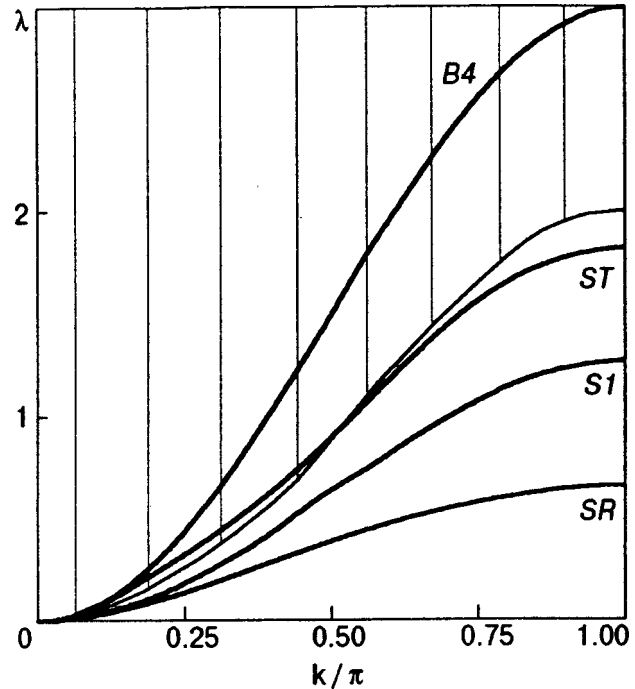

FIG. 5. Energy–momentum relations for a localized low-frequency Rayleigh-type wave *SR* and the transverse mode *ST* in the presence of a monolayer of heavy atoms ($M=2m$) on the surface. *S1* and *B4* are a wave of the Rayleigh type and a transformation wave, respectively, in the case of a defect-free surface. The hatched region corresponds to the continuous spectrum of frequencies of bulk vibrations.

$$C_{1\mu}=\frac{9}{2}-\eta\lambda-4a^2-\frac{1}{2}\left[a+i\Gamma_\mu\sqrt{3(1-a^2)}\right]$$
$$\times(b_\mu+\sqrt{b_\mu^2-1}),$$
$$C_{2\mu}=\left\{\frac{3}{2}\left[a(b_\mu+\sqrt{b_\mu^2-1})-1\right]+\eta\lambda\right\}\Gamma_\mu$$
$$-i\frac{1}{2}\sqrt{3(1-a^2)}(b_\mu+\sqrt{b_\mu^2-1}),$$

(21)

where $\eta=M/m$. The frequencies of different types of vibrations can be obtained numerically from the dispersion equation (14) with coefficients (21).

Figure 5 presents energy–momentum relations for vibrations in the presence of a heavy impurity with $M=2m$. It can be seen that the frequency of a surface wave *SR* of the Rayleigh type is lower than the frequency of the Rayleigh-type wave *S1* at the surface for $M>m$. It was found that additional localized transverse vibrations *ST* can also emerge. The frequencies of waves of this type split from the lower boundary of the continuous spectrum for $M>3m/2$. For values of atomic mass of the surface layer $M=3m/2$, the frequency of the *ST* wave coincides with the frequency of the lower boundary of the pseudotransverse branch at the Brillouin zone boundary $\lambda_{ST}(\pi)=\lambda_{t\,\min}(\pi)=2$. Vibrations of this type are localized in the surface layers for values of the wave number k from the interval $k^*(\eta)<k<\pi$. For $k<k^*$, the frequencies of the *ST* wave fall in the continuous spectrum and are continued in it in the form of an isolated
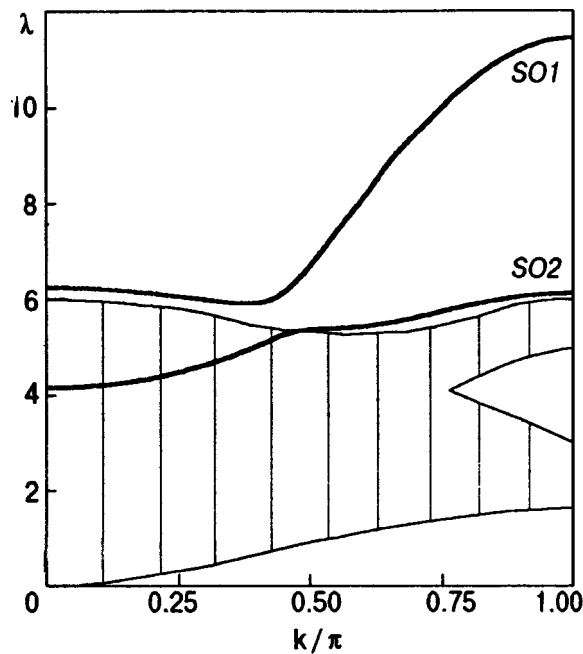
FIG. 6. High-frequency surface waves *SO1* and *SO2* in the presence of a light impurity ($M = 0.4\ m$) at the crystal surface. The hatched region corresponds to the continuous spectrum of frequencies of bulk vibrations.

line corresponding to frequencies of a transverse wave undergoing specular reflection at the surface (in the case of a free surface, this is a wave of the *B4* type).

An analysis of the dispersion equation shows that the mass defect M/m in the long-wave spectral region leads to weak dispersion of the velocity of the wave.

Low-frequency waves *SR* of the Rayleigh type can also exist in the presence of a light impurity, when the mass of surface-layer atoms is smaller than the mass of atoms from inner layers of the crystal: $M < m$. The frequencies of a wave of the *SR* type become higher than the frequencies of the surface wave $S1$ localized at the free surface with decreasing ratio M/m, and the frequency of the *SR* wave for $M = m/2$ at the boundary of the Brillouin zone coincides with the frequency of the lower boundary of the continuous spectrum. As the mass decreases further, the point at which this wave touches the continuous spectrum moves towards lower values of k.

The presence of a light impurity leads to the emergence of localized vibrations whose frequencies lie above the continuous spectrum (Fig. 6). Such high-frequency surface vibrations exist in the range of wave numbers k close to the boundary of the Brillouin zone. The first surface wave *SO1* appears for any $M < m$. Such a splitting for a small perturbation in the parameter $|m - M|/m \ll 1$ is associated with the fact that an isolated frequency curve for the transformation wave *B3* for $M = m$ (free surface) arrives at the upper edge of the pseudolongitudinal branch at the point $\lambda_{l\ max}(\pi) = 6$. When the difference between the mass of atoms from the surface layer and the mass of atoms from inner layers is infinitely small, the frequencies of waves of the *B3* type leave the continuous spectrum, and vibrations are localized in the surface layers.
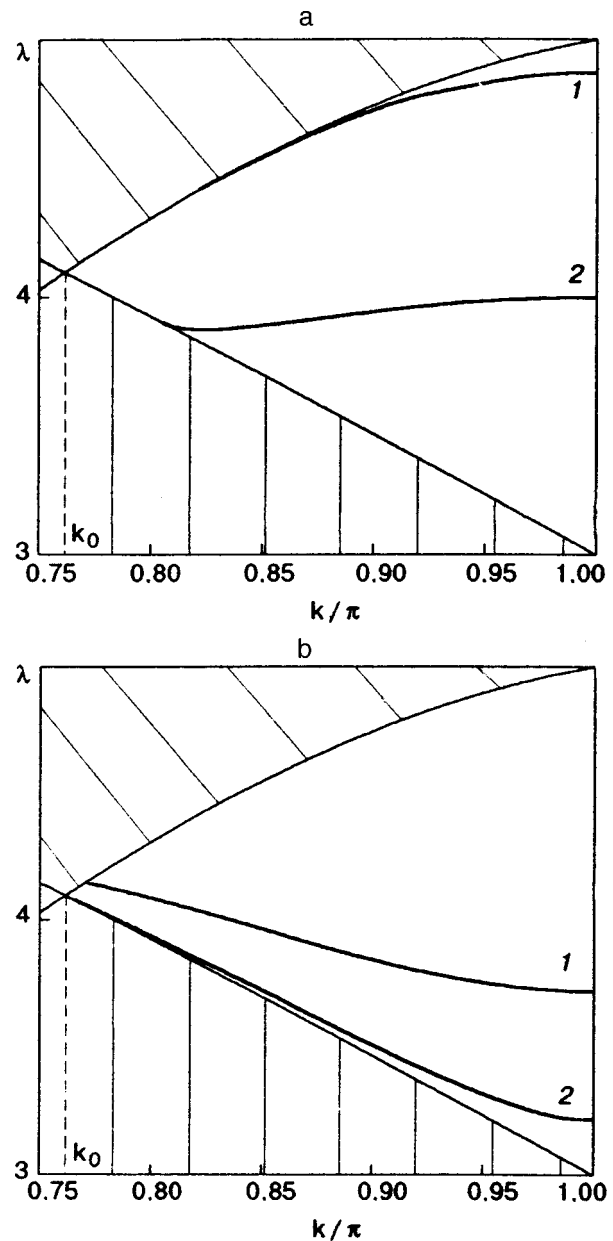

FIG. 7. Gap surface waves of the *SG* type (heavy impurity) with $M = 0.96m$ (curve *1*) and $M = 1.25m$ (curve *2*) (a); and of the *SI* type (light impurity) with $M = 0.3m$ (curve *1*) and $M = 0.4m$ (curve *2*) (b).

For $M < m/2$, the second high-frequency surface wave *SO2*, whose frequency decreases with k is formed and arrives at the continuous spectrum for a certain value of k_1^* $= k_1^*(\eta)$, at which it is continued in the form of a pseudo-surface wave reflected specularly by the surface. Figure 6 shows the dispersion curves obtained numerically for the *SO1* and *SO2* waves in the case of a light impurity for the value $M = 0.4\ m$.

In the gap of the continuous spectrum, surface waves can exist in the case of a light as well as a heavy impurity. For $M > 9m/10$, a wave *SG* is formed (Fig. 7a), and the frequencies of the *SG* wave decrease with increasing η. For $\eta = 1$, the energy–momentum relation for such a wave is transformed to the energy–momentum relation of *S2* waves localized near the free surface.

In the case of a light impurity in the gap for $M < m/2$, a gap wave *SI* of another type is formed (Fig. 7b). This wave splits from the upper boundary of the *t*-branch of the continuous spectrum of bulk vibrations (lower edge of the gap).

It should be noted in conclusion that the presence of the surface leads to the emergence of new types of waves propagating in the crystal. Local frequencies entering the continuous spectrum are continued in the form of selected energy–momentum relations for bulk vibrations corresponding to transformation waves of various types. Pseudolocal vibrations in the form of local vibrations coupled through the boundary and split from the upper bulk branch *l* can also be formed near the surface along with waves of the lower bulk branch *t*. The difference between the masses of atoms from the surface layer and from the inner layers of the crystal leads to the emergence of high-frequency surface waves above the continuous spectrum for $M < m$ and to the emergence of the second local mode in this region for $M < m/2$. Low-frequency vibrations of the Rayleigh type exist for any $M > m/2$, and the second localized low-frequency mode is also formed for $M > 3m/2$. It is also important that dynamic equations of crystal lattice with a planar defect lead to phenomenological boundary conditions in the theory of elasticity for limiting transition $kd \ll 1$.

[1] A. M. Kosevich and A. V. Tutov, Phys. Lett. (in press).
[2] L. D. Landau and E. M. Lifshitz, *Theoretical Physics*, vol. 7. *Theory of Elasticity*, Pergamon Press, Oxford, 1986.
[3] R. E. Allen and G. P. Alldredge and F. W. de Wette, Phys. Rev. B **4**, 1661 (1971).
[4] H. Kaplan, Phys. Rev. **125**, 1271 (1962).
[5] A. M. Kosevich, D. V. Matsokin, and S. E. Savotchenko, Fiz. Nizk. Temp. **23**, 92 (1997) [Low Temp. Phys. **23**, 69 (1997)].
[6] J. Black, A. Franchini, V. Bortolani, and R. Wallis, Phys. Rev. B **36**, 2996 (1987).
[7] G. Braco, R. Tatarek, F. Tommasini *et al.*, Phys. Rev. B **36**, 2928 (1987).
[8] I. A. Viktorov, *Surface Waves in Solids* [in Russian], Nauka, Moscow (1981).
[9] A. M. Kosevich and A. V. Tutov, Fiz. Nizk. Temp. **19**, 1273 (1993) [Low Temp. Phys. **19**, 905 (1993)].
[10] A. M. Kosevich and A. V. Tutov, Phys. Lett. A **213**, 265 (1996)
[11] A. M. Kosevich, Yu. A. Kosevich, and E. S. Syrkin, Zh. Éksp. Teor. Fiz. **88**, 1089 (1985) [Sov. Phys. JETP **61**, 639 (1985)].
[12] H. A. Dieterman and A. Metrikine, *Wave Motion* (in press).
[13] M. A. Ivanov and Yu. V. Skripnik, Fiz. Nizk. Temp. **23**, 208 (1997) [Low Temp. Phys. **23**, 153 (1997)].

Translated by R. S. Wadhwa

BRIEF COMMUNICATIONS

Attenuation of low-frequency acoustic energy in Bi-based superconductors

G. G. Sergeeva

National Science Center ''Kharkov Physicotechnical Institute,'' 310108 Kharkov, Ukraine
(Submitted March 2, 1998; revised May 11, 1998)
Fiz. Nizk. Temp. **24**, 1003–1006 (October 1998)

The attenuation of low-frequency acoustic energy in stripes of the low-temperature tetragonal phase of Bi-2212 ceramics is studied taking into account the $d_{x^2-y^2}$-symmetry of the superconducting order parameter (SOP) and the dynamic analog of phase separation. The contribution to the energy density of the strain–order parameter coupling leads to a finite value of attenuation in superconductors with a peculiar SOP. The frequency and temperature dependences of attenuation are analyzed and compared with the available experimental results. It is shown that these data are an indirect evidence of the SOP symmetry: the $d_{x^2-y^2}$-symmetry for the Bi-2212 phase and the s-symmetry for the Bi–2223 phase. The existence of an ordered low-temperature state responsible for the low-frequency attenuation peak and other anomalies in the properties of Bi-based ceramics in the temperature range 20–40 K is proposed. © *1998 American Institute of Physics.* [S1063-777X(98)01110-4]

INTRODUCTION

Peculiarities in the attenuation of acoustic energy in HTSC have been studied by many authors.[1–6] The results obtained in Refs. 3, 4 proved that the temperature dependence of the attenuation coefficient $\delta(T)$ in Bi-based superconductors in general does not contradict the assumption on the pairing of charge carriers in the BCS theory. However, some aspects such as the nonexponential dependence $\delta(T)$ in the superconducting state, the existence of one or two peaks on this dependence,[3–6] and the absence of a noticeable frequency dependence $\delta(\omega)$ (a change in frequency from 0.8 Hz[3,4] to a few kilohertz[5,6] leads to an insignificant change in δ; Fig. 1) remain unclear. It was noted in Ref. 4 that in order to determine the attenuation δ of sound at frequency 0.8 Hz, the diffusive displacement of points of fixation of a moving dislocation and the separation of dislocations[7] must be taken into consideration.

At the present time, the following two important peculiarities of the superconducting state in Bi-2212 can be regarded as established reliably. One of these peculiarities is a dynamic analog of ''phase separation'' into stripe phases in CuO planes (ab) (the stripes of low-temperature tetragonal (LTT) insulating phase and those of low-temperature orthorhombic (LTO) conducting phase with widths $W=2a$ and $L=2.65a$, respectively, where a is twice the distance between oxygen positions in this plane). These stripes were discovered in Bi-2212 in experiments on long-range fine structure of x-ray absorption (EXAFS).[8] The other important peculiarity of this compound, i.e., the $d_{x^2-y^2}$-symmetry of the superconducting order parameter η, was established quite recently.[9] Taking these peculiarities of the superconducting state of Bi-2212 into account, we shall analyze here the temperature and frequency dependences of the low-frequency

acoustic attenuation coefficient and compare the results with the experimental data obtained in Refs. 3–6.

ACOUSTIC ENERGY ATTENUATION IN STRIPES OF THE LTT PHASE

Let us consider the attenuation of low-frequency acoustic energy in stripes of the LTT phase in a Bi-2212 sample. In analogy with the procedure used in Ref. 10 for planar defects, these stripes can be regarded as elastic membranes. The wavelength of a low-frequency acoustic wave is much larger than the width W of the LTT phase stripe, and hence the strains induced by the acoustic wave can be regarded as practically uniform for a large number of stripes. The acoustic attenuation coefficient can be calculated from the equation of motion for the strain tensor ε and the stress tensor σ:

$$\frac{\partial^2 \sigma_{ij}}{\partial x_j^2} = \rho \, \frac{\partial^2 \varepsilon_{ij}}{\partial t^2}, \tag{1}$$

$$\sigma_{ij} = \frac{\partial f}{\partial \varepsilon_{ij}}, \tag{2}$$

where ρ is the sample density and f the energy density taking into account the coupling between uniform strain and the superconducting order parameter (SOP) η,[11]

$$f = \frac{1}{2} \sum_{\gamma} B(\gamma)\varepsilon^2(\gamma) + \frac{1}{alW} \sum_{\gamma} \Delta V(\gamma, \eta)\varepsilon(\gamma)$$

$$\times \int \zeta dS + \frac{\epsilon_0}{2alW} \int (\nabla_{x,y}\xi)^2 dS. \tag{3}$$

Here ϵ_0 is the energy of formation of an LTT phase stripe of length l equal to the sample length along the b-axis, ζ are small deviations of the stripe of the LTT phase in the (ab)
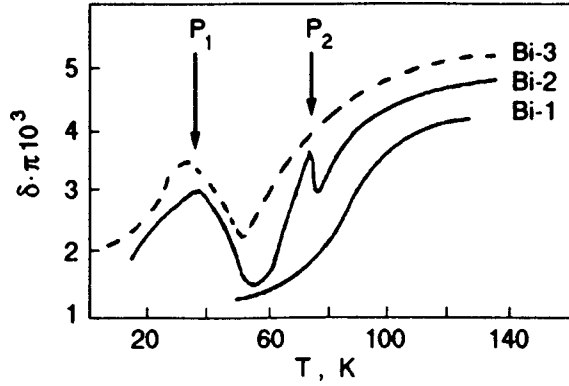
FIG. 1. Temperature dependence of attenuation of low-frequency sound in three different Bi-based samples: Bi-2223 (curves *1* and *3* from Refs. 6, 3) and 90% Bi-2223–10% Bi-2212 (curve *2* from Ref. 4). The positions of the low-temperature peak P_1 and the peak P_2 are marked by arrows.

plane, $B(\gamma)$ are elastic constants, $\Delta V(\gamma, \eta)$ is the difference in forms quadratic in η (with all the basis functions of irreducible representations γ of the point groups corresponding to the crystal symmetry) for the nearest superconducting stripes whose order parameter is coupled with the strains $\varepsilon(\gamma)$. The attenuation of sound is finite if $\Delta V(\gamma, \eta) \neq 0$. For superconductors with the s-wave symmetry of the SOP, this quantity is equal to zero,[12] and the coupling of uniform strain with SOP does not lead to acoustic energy attenuation.

For a longitudinal acoustic wave propagating along the z-axis, we have

$$\sigma = \sigma_{zz}, \quad \varepsilon = \varepsilon_{zz}.$$

For attenuating motion with a drag coefficient Γ for which the kinetic energy of a stripe can be neglected, the equation of motion for displacements ζ from the equilibrium position has the form

$$\Gamma \frac{\partial \zeta(x,y,t)}{\partial t} = -\frac{\partial f}{\partial \zeta}. \tag{4}$$

Supplementing the system of equations (1), and (2) with the equation of motion (4) and writing the solution in the form

$$\sigma(z,t) = \sigma_0 \exp[-\delta(\omega)z + i\omega(t - z/v)], \tag{5}$$

for a mode with the lowest frequency

$$\omega_1 = \frac{\pi^2 \epsilon_0}{\Gamma l W}$$

we obtain

$$\delta(\omega) = \frac{4\omega^2}{\pi^2 a \rho \Gamma v_0^3 (\omega^2 + \omega_1^2)} \sum_\gamma |\Delta V(\gamma, \eta)|^2, \tag{6}$$

where v_0 is the velocity of sound.

While estimating the temperature dependence $\delta(T)$, we can assume that only the order parameter $\eta \propto (T - T_c)^{1/2}$ (T_c is the superconducting transition temperature) and the surface energy ϵ_0 are functions of temperature. The $\epsilon_0(T)$ dependence can be determined by multiplying the volume en-

ergy, which is proportional to $|\eta|^4$, by the coherence length[12] $\sim |\eta|^{-1}$:

$$\epsilon_0 \sim |\eta|^3 \sim (T - T_c)^{3/2}.$$

Equation (6) for $\delta(T)$ can be used to determine a temperature dependence similar to that obtained by Sigrist and Ueda[12] for attenuation of ultrasound by domain walls in an anisotropic superconductor with a multicomponent order parameter:

$$\delta(T) \sim \frac{\omega^2 \eta^4}{\omega^2 + \hat{\omega}^2 \epsilon_0^2} \sim \frac{\omega^2 |T - T_c|^2}{\omega^2 + \hat{\omega}^2 |T - T_c|^3}. \tag{7}$$

Here $\hat{\omega}$ is the temperature-independent coefficient in the expression for ω_1. Equation (7) shows that the $\delta(T)$ dependence in the superconducting state has a peak at $T < T_c$, and attenuation decreases with temperature in proportion to $|T - T_c|^{-1}$. The frequency dependence $\delta(\omega)$ is determined by the relation between the terms in the denominator of (7): attenuation does not depend on frequency for $\omega \sim \hat{\omega}$.

DISCUSSION OF EXPERIMENTAL RESULTS

Unfortunately, we are not aware of any results on low-frequency acoustic energy absorption in Bi-2212 type superconductors for which charge ordering as well as the $d_{x^2-y^2}$-symmetry of the SOP have been established. We shall compare the results obtained above with the results of measurements of the attenuation coefficient for low-frequency sound in $Bi_2Sr_2Ca_2Cu_3O_x$ (Bi-2223) superconductors, pure samples (Bi-1 and Bi-3) and those containing an impurity of the 2212 phase (Bi-2 sample). Figure 1 shows the $\delta(T)$ dependence for these samples:

Bi-1: $T_c = 104$ K, $\Delta T_c \simeq 2.9$ K,[6]
Bi-3: $T_c = 106$ K, $\Delta T_c \simeq 3$ K,[3]
Bi-2: 90% 2223 phase and 10% 2212 phase,
$T_c = 106$ K, $\Delta T_c \simeq 3.5$ K[4]
(ΔT_c is the superconducting transition width).

In the measurements of $\delta(T)$, the frequency was 0.8 Hz for Bi-2 and Bi-3 samples and 0.81 kHz for Bi-1 sample, It can be seen from Fig. 1 that the shape of the $\delta(T)$ curve is almost independent of frequency and the method of sample preparation: the attenuation does not differ by more than 14–20%. The samples Bi-3 and Bi-2 exhibit a low-temperature peak P_1 at $T \simeq 30$ K, while the two-phase sample Bi-2 has a second peak P_2 in the region 69–75 K below the transition temperature $T_{2c} = 86$ K for the 2212 phase. It was proposed in Refs. 3, 4 that both peaks are associated with the depairing effect at dislocation velocities higher than the critical value. In the absence of the results of measurements of the velocity of dislocations moving in HTSC, we can assume that the peak P_2 is associated with the attenuation (7) of sound in the stripes of the LTT phase in Bi-2212 at $T < T_{2c}$ considered above.

To our knowledge, there are no data on phase separation and a peculiar symmetry of the SOP for Bi-2223. The absence of a peak similar to P_2 near the superconducting transition temperature T_c of the 2223 phase in Bi-1 and Bi-3 samples is in accord with the s-wave symmetry of the SOP of this phase: the existence of fluctuation stripes of the LTT

phase at $T > T_{2c}$ for an s-wave type superconductor does not lead to such an effect.[12] Additional studies are required in order to determine the origin of the low-temperature peak P_1 whose height increases by two orders of magnitude in a magnetic field of 950 Oe.[13] The coincidence of low-temperature anomalies in mechanical,[3–6] magnetomechanical,[13] and magnetic measurements (discontinuity of the melting curve for the flux line lattice[14] and a sharp jump in the temperature dependence of the remanent magnetization[15]) for Bi-based superconductors is not accidental. It can be assumed that a low-temperature ordered state exists with $T_{c0} \simeq 35$ K and the order parameter differing from the SOP of the main phase. This can be either a superconducting state with a different symmetry of the SOP, or an antiferromagnetically ordered state of the stripes of the LTT phase. It was proved in Ref. 12 that the coexistence of a superconducting phase and another ordered state leads to a peak on the $\delta(T)$ curve at $T < T_{c0}$.

Thus, the comparison of the experimental results with the theoretical dependence $\delta(T)$ (7) leads to the conclusion that the results of measurements of attenuation of low-frequency acoustic energy can be used as an indirect evidence of the symmetry of the SOP.

[1] V. P. Soldatov, V. D. Natsik, and N. F. Chaĭkovskaya, Fiz. Tverd. Tela (Leningrad) **33**, 1777 (1991) [Sov. Phys. Solid State **33**, 999 (1991)].

[2] V. S. Boĭko, V. M. Gorbatenko, L. F. Krivenko *et al.*, Fiz. Nizk. Temp. **15**, 988 (1989) [Sov. J. Low Temp. Phys. **15**, 547 (1989)].

[3] B. G. Lazarev, Ya. D. Starodubov, M. B. Lazareva *et al.*, Physica C **C235–240**, 1213 (1994); Fiz. Nizk. Temp. **20**, 840 (1994) [Low Temp. Phys. **20**, 660 (1994)].

[4] B. G. Lazarev, Ya. D. Starodubov, G. G. Sergeeva *et al.*, Fiz. Nizk. Temp. **22**, 819 (1996) [Low Temp. Phys. **22**, 629 (1996)].

[5] Y. N. Huang, Y. N. Wang, and Z. X. Zhao, Phys. Rev. B **49**, 1320 (1994).

[6] Y. N. Huang, X. Li, Q. M. Zhang *et al.*, Physica C **C282–287**, 1523 (1997).

[7] R. A. Vardanyan and Yu. O. Osip'yan, Zh. Éksp. Teor. Fiz. **94**, 291 (1988) [Sov. Phys. JETP **67**, 1682 (1988)].

[8] A. Bianconi and M. Missori, J. Phys. **4**, 361 (1994).

[9] T. M. Rice, Physica C **C282–287**, p. **I**, xix (1997).

[10] R. Truell and C. Elbaum, in *Handbuch der Physik*, vol. XI (ed. by S. Flugge), Springer, Berlin (1962), p. 153.

[11] M. Ozaki, Prog. Theor. Phys. **76**, 1008 (1986).

[12] M. Sigrist and K. Ueda, Rev. Mod. Phys. **63**, 239 (1991).

[13] G. d'Anna, Phys. Status Solidi A **125**, 589 (1991).

[14] B. Khaykovich, E. Zeldov, D. Majer *et al.*, Phys. Rev. Lett. **76**, 2555 (1996).

[15] C. D. Dewheerst and R. A. Doyle, Phys. Rev. B **56**, 10 032 (1997).

Translated by R. S. Wadhwa

Magnetic transformations in reentrant region of the *x−T* diagram of Li$_{0.5}$Fe$_{2.5−x}$Ga$_x$O$_4$ spin-glass system

N. N. Efimova and S. R. Kufterina

Kharkov State University, 310077 Kharkov, Ukraine

A. G. Anders, S. V. Startsev, A. M. Gurevich, and V. N. Eropkin

B. Verkin Institute for Low Temperature Physics and Engineering, National Academy of Sciences of the Ukraine, 310164 Kharkov, Ukraine*
(Submitted May 6, 1998)

Reentrant spinels Li$_{0.5}$Fe$_{2.5−x}$Ga$_x$O$_4$ with $x=0.9$ and 1.2 display peaks on the temperature dependences of heat capacity C at $T_1=13.4$ K ($x=0.9$) and 14.2 K ($x=1.2$) respectively, which are typical of a first-order phase transition. This transition is identified with the transformation of the collinear ferrimagnetic structure into a noncollinear structure preceding on the temperature scale the state of ferrimagnetic spin glass existing in the temperature range 0 K$\leqslant T\leqslant T_f$, where transition temperatures T_f are 9 K ($x=0.9$) and 12 K ($x=1.2$). © *1998 American Institute of Physics.* [S1063-777X(98)01210-9]

We report here on the results of investigation of temperature dependences of heat capacity C for reentrant ferrimagnets Li$_{0.5}$Fe$_{2.5−x}$Ga$_x$O$_4$ with $x=0.9$ and 1.2, which were carried out to study a sequence of magnetic transformations occurring in this concentration range upon a change in temperature. The objects of investigations are Heisenberg magnets with a short-range exchange. Studies of the evolution of magnetic states of these materials upon an increase in the extent of dilution x as well as upon cooling (with $x=$ const) continue to attract the attraction of researchers. The problem is that the exchange mechanism of formation of disordered states of the spin glass (SG) type in such systems remains disputable since the results of computer simulation (the absence of a spin-glass transition at $T_f>0$ K)[2,3] contradict the available experimental data,[1,4,5] and a consistent theory has not been developed so far. On the other hand, the experimental $x−T−H$ phase diagrams for Heisenberg systems with a short-range exchange match on the whole with the general canonical type typical of classical spin-glass systems of the type of Cu–Mn, Au–Fe, etc.[1,4,5] This allows us to use (with certain reservations) the mean-field theory with an infinitely large interaction range for an analysis of spin-glass systems with a short-range interaction also.

Gabay and Toulouse[6] proved by using the mean-field approach that the $x−T$ diagram for Heisenberg systems contains a reentrant region in which the magnetic states are transformed upon cooling according to the following sequence: PM→FM→M$_1$→M$_2$, where PM and FM are para- and ferromagnetic states, respectively, and M$_1$ and M$_2$ are noncollinear states with preserved long-range order. In analogy with the transition PM→SG (''pure'' spin glass), the transition M$_1$→M$_2$ is manifested in the form of spontaneous breaking of the replica symmetry at temperature T_f. In all cases, T_f is detected experimentally from the clearly manifested SG properties, e.g., the existence of long-lived logarithmic relaxation of nonequilibrium magnetization σ_{ZFC} at

$T\leqslant T_f$.[1,4,5] For this reason, M$_2$ is usually identified with the state of ferromagnetic spin glass (FSG), in which two types of magnetic order (i.e., ferromagnetic and spin-glass ordering) coexist at $T<T_f$.[1,4,7] The form of the transformation M$_1$→M$_2$ and the very fact of its existence were subjects of numerous experimental investigations which, however, failed to clarify the situation completely.[1,4,7]

It should be noted that in the previous investigations of the transformation M$_1$→M$_2$, main attention was paid, as a rule, to the ''spin-glass'' aspect of the problem. Analyzing experimental data (including those obtained for Li–Ga spinels),[5,8] we proposed that the formation of long-range correlations between transverse spin components in the M$_1$ phase considered by Gabay and Toulouse[6] is associated with the formation of an ordered noncollinear FM structure (ferrimagnetic FM* structure in the case of Li–Ga spinels) rather than with the formation of a certain spin-glass state other than M$_2$. In such a case, FM→M$_1$ or FM*→M$_1$ transitions must exhibit features of a thermodynamic phase transition.[9] The results of verification of this proposition will be considered below.

An analysis of temperature dependences of the heat capacity C for Li$_{0.5}$Fe$_{2.5−x}$Ga$_x$O$_4$ samples with $x=0.9$ and 1.2 in the temperature range 12–16 K was carried out by using the same technique as the one used earlier for the temperature interval 2–20 K.[8] The obtained results are presented in Fig. 1.

It was found earlier[10] that the phonon contribution to the heat capacity of Li–Ga spinels can be assumed to be equal to the heat capacity of the isostructural nonmagnetic lithium gallate Li$_{0.5}$Ga$_{2.5}$O$_4$. At $T=15$ K, its magnitude does not exceed 2.5%, and the $C(T)$ dependence has no singularities and obeys the T^3 law.[8,10] On the other hand, magnetic spinels exhibit clearly manifested narrow symmetric peaks at $T=13.4$ K ($x=0.9$) and 14.2 K ($x=1.2$). In addition, according to preliminary results, the heat capacity $C(T)$ exhibits a
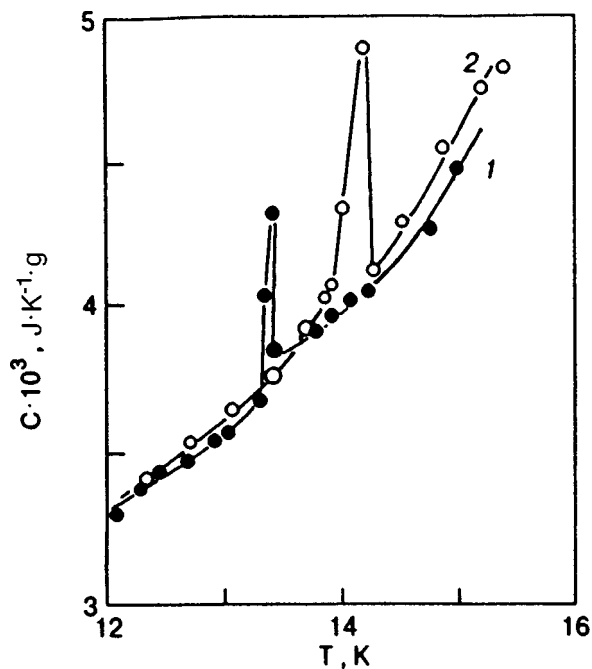
FIG. 1. Temperature dependences $C(T)$ of heat capacity in dilute spinels $Li_{0.5}Fe_{2.5-x}Ga_xO_4$ with $x=0.9$ (curve *1*) and 1.2 (curve *2*).

hysteresis in the vicinity of these temperatures. All these facts allow us to attribute the observed phase transition to first-order phase transitions (PT1).[11] It is important to note that in both cases the values of temperatures corresponding to the peak on the $C(T)$ curve and denoted henceforth by $T_1(x)$ are higher than the values of T_f which are ~ 9 K for $x=0.9$ and ~ 12 K for $x=1.2$.[5,12] It was reported in Ref. 8 that the magnetic contribution to heat capacity below T_f changes linearly with temperature ($C_m \propto T$), which is regarded as an indication of disordered states of the FSG ad SG types.[1,3,7,10] Thus, according to our results, the FSG state in Li–Ga spinels with $x=0.9$ and 1.2 is preceded on the temperature scale by a noncollinear ordered state.

Taking into account the results of previous investigations,[5,8,12] we can present the following sequence of magnetic transformations induced by cooling in the reentrant region of the $x-T$ diagram of the $Li_{0.5}Fe_{2.5-x}Ga_xO_4$ system for the concentration range under investigation ($0.9 \leqslant x \leqslant 1.2$): Pm $\rightarrow$ collinear ferrimagnetic (FM*) structure $\rightarrow$ locally noncollinear FM* structure $\rightarrow$ noncollinear ordered FM* structure $\rightarrow$ FSG. This sequence of transformations contains two peculiar thermodynamic PT: a second-order transition at T_c (PM $\rightarrow$ FM*) and a first-order transition at T_1 between the collinear and noncollinear FM* structures identified on the macroscopic scale. The transition to the FSG state at $T=T_f$ is detected, as usual, from the emergence of spin-glass properties and from the peak on the temperature dependence of the imaginary component $\chi''(T)$ of the magnetic susceptibility.[5,12]

The results of the present communication can be compared with the results of computer simulation in which low concentrations of nonmagnetic ions are usually considered.[1–3] In most cases, computer experiments for Heisenberg systems with short-range interaction lead to only

two types of states, namely, the collinear FM state at $T \leqslant T_c$ and the locally noncollinear FM state (the FM structure collinear in the macroscopic sense with imperfections in the form of local noncollinearity regions) upon a further cooling down to $T=0$ K.[2,3] We can assume that the existence of a PT1 observed by us at $T_f < T_1 < T_c$, like a transition to the SG state at $T_f > 0$ K,[13] cannot exist in isotropic Heisenberg systems with short-range exchange. However, real objects are virtually always anisotropic, which affects to a certain extent the formation of noncollinear spin structures of various types.[14–16] For example, according to the results of neutron-diffraction experiments and symmetry analysis, Li–Ga spinels in the concentration range under investigation can contain a noncollinear ordered ferrimagnetic structure of the umbrella type.[17] However, the structures of this type are formed only in anisotropic materials.[16]

Thus, the results of analysis of heat capacity $C(T)$ in dilute spinels $Li_{0.5}Fe_{2.5-x}Ga_xO_4$ with $x=0.9$ and 1.2, indicating the existence of a first-order phase transition of the order–order type at $T_1(x)$ [$T_f(x) < T_1 < T_c(x)$], supplement considerably the prevailing concepts of temperature evolution of magnetic states in the reentrant region of the $x-T$ diagrams of real spin-glass Heisenberg systems with a short-range exchange. According to these results, the phase diagram of such systems must contain an additional curve $T_1(x)$. A continuation of these investigations together with the results obtained by us and those obtained in Ref. 18 will allow us to determine exactly the position of the $T_1(x)$ curve on the $x-T$ diagram for Li–Ga spinels.

*E-mail: aanders@ilt.kharkov.ua

[1] K. Binder and A. P. Yuong, Rev. Mod. Phys. **58**, 801 (1986).
[2] W. M. Saslow and G. Parker, Phys. Rev. Lett. **56**, 1074 (1985).
[3] J. R. Thomson, Hong Guo, D. H. Ryan *et al.* Phys. Rev. B **45**, 3129 (1992).
[4] C. Y. Huang, J. Magn. Magn. Mater. **51**, 1 (1985).
[5] N. N. Efimova, Yu. A. Popkov, and N. V. Tkachenko, Zh. Éksp. Teor. Fiz. **90**, 1413 (1986) [Sov. Phys. JETP **63**, 827 (1986)]; Fiz. Nizk. Temp. **15**, 1055 (1989) [Sov. J. Low Temp. Phys. **15**, 584 (1989)]; Fiz. Nizk. Temp. **16**, 1565 (1990) [Sov. J. Low Temp. Phys. **16**, 881 (1990)].
[6] M. Gabay and G. Toulouse, Phys. Rev. Lett. **47**, 201 (1981).
[7] I. Ya. Korenblit and E. F. Shender, Usp. Fiz. Nauk **157**, 267 (1989) [Sov. Phys. Usp. **32**, 139 (1989)].
[8] N. N. Efimova, S. R. Kufterina, A. G. Anders *et al.*, Fiz. Nizk. Temp. **24**, 337 (1998) [Low Temp. Phys. **24**, 255 (1998)].
[9] K. P. Belov, *Ferrites in Strong Magnetic Fields* [in Russian], Nauka, Moscow (1972).
[10] N. N. Efimova, V. A. Pervakov, V. I. Ovcharenko, and N. Yu. Tyutryumova, Fiz. Tverd. Tela **35**, 2838 (1993) [Phys. Solid State **35**, 1405 (1993)].
[11] R. White and T. Geballe, *Long Range Order in Solids*, Academic Press, New York (1979).
[12] N. N. Efimova, Yu. A. Popkov, S. R. Kufterina *et al.*, Fiz. Nizk. Temp. **20**, 546 (1994) [Low Temp. Phys. **20**, 431 (1994)].
[13] B. W. Morris, S. G. Colborne, M. A. Moore *et al.*, J. Phys. C **19**, 1157 (1986).
[14] S. V. Vonsovskii, *Magnetism,* Wiley, NY, 1974.
[15] M. F. Bertaut, Compt. Rend. **250**, 85 (1960); *ibid* **252**, 76, 252 (1961).
[16] B. Boucher, R. Buhl, and M. Perrin, Phys. Chem. Solids **31**, 2251 (1970).
[17] V. I. Maltzev, Phys. Status Solidi B **128**, 193 (1985).
[18] N. N. Efimova, Pis'ma Zh. Éksp. Teor. Fiz. **67**, 329 (1998) [JETP Lett. **67**, 346 (1998)].

Translated by R. S. Wadhwa

Influence of dynamic magnetoelectric interaction on surface polaritons in ferroelectrics

I. E. Chupis and D. A. Mamaluy

B. Verkin Institute for Low Temperature Physics and Engineering, National Academy of Sciences of the Ukraine, 310164 Kharkov, Ukraine[*)]

The existence of additional transverse electric (TE) and magnetic (TM) surface polaritons formed as a result of high-frequency magnetoelectric interaction in a ferroelectric is predicted. The spectrum of the new type of surface polaritons is analyzed for transverse orientation of the electric polarization relative to the crystal surface. These polaritons are different in ferroelectric domains with opposite directions of spontaneous electric polarization. Thus, TE surface polaritons exist only in domains with electric polarization directed into the medium. Besides, magnetoelectric interaction induces effects like birefringence and anomalous dispersion of TM polaritons. Moreover, it is found that TM polaritons can exist in those types of ferroelectrics in which their existence was forbidden earlier. The same effects must also exist not only in ferroelectrics, but also in ordinary dielectrics in a constant electric field at right angles to the crystal surface. The above-mentioned asymmetry of the effects, including their switching on/off, must be observed upon a change in the direction of the applied electric field. © *1998 American Institute of Physics.* [S1063-777X(98)01310-3]

The interest of researchers in ferroelectric crystals has grown considerably in recent years following the discovery of new aspects of their technical applications. Since thin-film structures are used frequently in devices, it is important to study phenomena occurring at the surface of a ferroelectric, e.g., surface waves.

The theoretical studies of the influence of magnetoelectric (ME) interaction on surface waves in crystals were carried out recently in antiferromagnets with a linear ME effect.[1] Although such an effect is not observed in ferroelectrics, it was shown by us earlier[2] that a varying electromagnetic field induces in a ferroelectric a high-frequency linear ME susceptibility proportional to the frequency and magnitude of the spontaneous electric polarization. This linear high-frequency effect is of dynamic origin (see below) and is not subjected to any constraints concerning the symmetry of the crystal.

In this work, we analyze the influence of dynamic ME interaction on surface polaritons in a ferroelectric. It is shown that TE and TM surface excitations can exist under conditions in which their existence was forbidden earlier. New effects like birefringence, anomalous dispersion and the existence of forbidden spectral regions are predicted. The domain structure is reflected for the first time in the properties of surface waves.

For the sake of definiteness (although this is not significant in the following analysis), we consider a uniaxial ferroelectric (Z is the easy axis) occupying the halfspace $z > 0$. Using the phenomenological description of a ferroelectric in terms of the densities of electric polarization $\mathbf{P}(\mathbf{r})$ and momentum $\mathbf{\Pi}(\mathbf{r})$, we can represent the Hamiltonian of the system in a varying electromagnetic field $\mathbf{e}$, $\mathbf{h}$, disregarding the spatial dispersion ($a_c k \ll 1$, a_c being the lattice constant), in the form

$$\hat{H} = \int \left(-\frac{c_1}{2}\,\hat{P}_z^2 + \frac{c_2}{2}\,(\hat{P}_x^2 + \hat{P}_y^2) + \frac{\delta}{4}\,\hat{P}_z^4 - \mathbf{e}\cdot\mathbf{P} + \frac{\hat{\Pi}^2}{2\rho} \right.$$
$$\left. + \xi\hat{\mathbf{P}}\cdot[\hat{\mathbf{\Pi}}\cdot\mathbf{h}] \right) dV. \tag{1}$$

Here the first three terms are the potential ferroelectric energy operators, $\hat{\Pi}^2/2\rho$ the kinetic ferroelectric energy operator, and ρ the density of the medium. The last term corresponds to the energy of electric polarization in the electric field $\mathbf{E}$ produced by the motion of ions (electrons) with a velocity $\mathbf{v}$ under the action of a magnetic field $\mathbf{h}$, $\mathbf{E} = (1/c) \times [\mathbf{h}\cdot\mathbf{V}]$. Since $\mathbf{v} = V_c\mathbf{\Pi}/m$ (V_c is the unit cell volume and m the particle mass), the constant $\xi = V_c(mc)^{-1}$ (c is the velocity of light). In contrast to the ME energies considered earlier (see, for example, Ref. 3 as well as Ref. 1), which are potential energies and hence depend on the symmetry of the system, the ME energy in formula (1) is of dynamic origin. This is a scalar which appears in the expression for the energy of a ferroelectric of any symmetry.

The linear response of the system to an electromagnetic field $(\mathbf{e}, \mathbf{h})$ can be described in terms of the electric (χ^e) and magnetoelectric (χ^{me}) susceptibilities whose Fourier components are defined by the relations

$$P_i = \chi^e_{ik} e_k + \chi^{em}_{ik} h_k.$$

Disregarding the attenuation for the Hamiltonian (1) in the ferroelectric state, we can represent the nonzero components of susceptibility in the form[2]

$$\chi^e_{xx} = \chi^e_{yy} = \frac{\bar{\omega}_0^2}{\omega_0^2 - \omega^2}, \quad \chi^e_{zz} = \frac{\bar{\omega}_0^2}{\omega_e^2 - \omega^2},$$

$$\chi_{xy}^{em}=(\chi_{yx}^{me})^*=\frac{i\omega g P_0}{\omega^2-\bar\omega_0^2}, \quad \bar\omega_0^2=\frac{z^2}{\rho V_c^2},$$

$$\omega_0^2=\bar\omega_0^2 c_2, \quad \omega_e^2=\bar\omega_0^2 2c_1, \quad g=\frac{z}{mc}, \quad P_0^2=\frac{c_1}{\delta}. \qquad (2)$$

In these formulas, z is the magnitude of the charge of an ion (or electron, if the incident electromagnetic field has high frequencies which effectively excite the electronic part of the electric polarization), g is the gyromagnetic ratio for the ion (or the electron), $P_0=P_{0z}$ is the equilibrium value of the electric polarization which is assumed to be directed along the Z-axis, and the constants c_1, c_2 and δ are assumed to be positive.

The electric (**d**) and magnetic (**b**) inductions of the medium are connected with the electric and magnetic fields through the relations

$$d_i=\varepsilon_{ik}e_k+\gamma_{ik}h_k, \quad b_i=\mu_{ik}h_k+\gamma_{ki}^*e_k,$$

where

$$\varepsilon_{xx}=\varepsilon_{yy}=\varepsilon_1=1+4\pi\chi_{xx}^e, \quad \varepsilon_{zz}=\varepsilon_2=1+4\pi\chi_{zz}^e,$$

$$\mu_{ik}=\delta_{ik}, \quad \gamma_{xy}=\gamma_{yx}^*=-i\gamma, \quad \gamma=4\pi i\chi_{xy}^{em} \qquad (3)$$

in the case considered by us.

A distinguishing feature of the case considered by us here is the existence of the nondiagonal component χ_{xy}^{em} of the ME susceptibility, which indicates the ME effect of induction of transverse (with respect to spontaneous polarization) components p_x and p_y of electric polarization by the varying magnetic field of the incident wave. This effect emerges only in a varying field ($\chi_{xy}^{em}\propto\omega$) and in the presence of spontaneous polarization ($\chi^{em}\propto P_0$). Note that if the existence of a varying field is a necessary condition, the electric field may play the role of the spontaneous polarization. Hence all the effects considered below will also be observed in normal dielectrics in a constant electric field E_0. In this case, P_0 should be replaced by E_0 in the final expressions.

In order to obtain the energy-momentum relations for the surface polaritons, we must solve Maxwell's equations taking into account formula (3) and the boundary conditions for the continuity of the tangential components of the electric and magnetic fields as well as the normal components of the electric and magnetic inductions at the interface ($z=0$) between vacuum ($z<0$) and a ferroelectric ($z>0$).

The solution is sought in the form of a wave traveling along the X-axis:

$$\mathbf{e},\mathbf{h}\propto\begin{cases}\exp(-i\omega t+ikx+\tilde k_0 z), & z<0, \ \tilde k_0>0,\\ \exp(-i\omega t+ikx-k_0 z), & z>0, \ k_0>0.\end{cases} \qquad (4)$$

In the geometry chosen by us, polaritons of TE and TM types propagate along the surface. Maxwell's equations (3) and (4) lead to the following expressions for the quantities $\tilde k_0$ and k_0 which are reciprocals of the penetrations depths of the waves in vacuum and in the ferroelectric, respectively:

$$\tilde k_0^2=k^2-\frac{\omega^2}{c^2} \quad (\text{TE,TM}),$$

$$k_0^2=k^2-\frac{\omega^2}{c^2}(\varepsilon_1-\gamma^2) \quad (\text{TE}), \qquad (5)$$

$$k_0^2=\frac{\varepsilon_1}{\varepsilon_2}k^2-\frac{\omega^2}{c^2}(\varepsilon_1-\gamma^2) \quad (\text{TM}).$$

It will be expedient to carry out the subsequent analysis separately for TE and TM types of waves.

1. TRANSVERSE ELECTRIC POLARITONS

The nonzero components of the fields for a TE wave are e_y, h_x, and h_z. The boundary conditions lead to the equality

$$\tilde k_0=\gamma\frac{\omega}{c}-k_0. \qquad (6)$$

It can be seen from this relation that $k_0=\tilde k_0=0$ for $\gamma=0$. In other words, the surface polaritons do not exist at all in the geometry considered here unless the dynamic ME interaction is taken into consideration. Formula (6) and other relations between the variables lead to the conditions

$$\omega\gamma>0, \quad 0<k_0<\gamma\frac{\omega}{c}, \quad \omega^2<c^2 k^2,$$

$$c^2 k^2>\omega^2(\varepsilon_1-\gamma^2), \quad 1+2\gamma^2>\varepsilon_1>1. \qquad (7)$$

For example, the condition $\omega\gamma>0$ follows from (6) by considering that k_0 and $\tilde k_0$ are positive. The quantity γ [see formulas (2) and (3)] depends on frequency through the relation

$$\gamma=\frac{4\pi\omega g P_0}{\omega_0^2-\omega^2}. \qquad (8)$$

Conditions $\omega\gamma>0$ and $\varepsilon_1>1$ [see formulas (2) and (3)] lead to the necessary condition $P_0>0$, i.e., the surface polaritons exist only in domains in which the electric polarization is directed into the bulk of the ferroelectric. This is due to the following reason: Eq. (6) is the boundary condition for the field h_x. For $\gamma=0$, h_x has opposite signs in vacuum and in a ferroelectric, the continuity condition is not observed, and TE waves do not exist. The dynamic ME effect $\gamma\neq 0$ indicates that the excitation of electric polarization p_y in a direction perpendicular to the spontaneous polarization P_0 induces an additional field $h_x\propto\gamma\omega\propto P_0\omega^2$ in the ferroelectric. If the sign of this induced field is the same as in vacuum, condition (6) is satisfied and TE polaritons can emerge in the system. Otherwise (in a domain with $P_0<0$), the induced field does not help in the fulfillment of the boundary conditions. In essence, the ME energy in formula (1), which connects $P_0=P_z$, $\mathbf{\Pi}_{x(y)}\propto\mathbf{p}_{x(y)}$ and $\mathbf{h}_{y(x)}$, describes the high-frequency analog of the Hall effect.

An analysis of conditions (7) taking into account the frequency dependences of γ and ε_1 shows that the TE waves exist in the interval

$$\omega_L<\omega<\omega_0, \quad \omega_L=\omega_0\bar\omega_0(\bar\omega_0^2+8\pi\omega_g^2)^{-1/2}, \qquad (9)$$

where we have introduced the notation $\omega_g = gP_0$. The energy-momentum relation $\omega(\mathbf{k}) = \omega(-\mathbf{k})$ and the quantities $\tilde{k}_0$, k_0, which are reciprocals of penetration depths, are defined as follows:

$$\omega = \left(c^2 k^2 - \frac{\bar{\omega}_0^4}{4\omega_g^2} \right)^{1/2}, \quad \tilde{k}_0 = \frac{\bar{\omega}_0^2}{2c\omega_g},$$

$$k_0 = \frac{\bar{\omega}_0^2 \omega_0^2 (\omega^2 - \omega_L^2)}{2c\omega_g \omega_L^2 (\omega_0^2 - \omega^2)}. \tag{10}$$

It can be seen from formulas (9) and (10) that the TE polaritons are virtual, i.e. exist only if the delay is taken into consideration. Their penetration depth $\tilde{k}_0^{-1}$ in vacuum is constant, while the penetration depth k_0^{-1} in a ferroelectric depends on the frequency [see (10)]: $k_0^{-1} = \infty$ for $\omega = \omega_L$ and $k_0^{-1} = 0$ for $\omega = \omega_0$, i.e., the wave does not penetrate the ferroelectric.

The frequency interval (9) in which TE type surface polaritons exist depends on the gyromagnetic ratio g which is inversely proportional to the particle mass [see Eqs. (2)]. At frequencies $\omega \sim 10^{15}$ rad·s^{-1}, when the electrons are predominately polarized, the value of $g \sim 10^7$ cm/g$^{1/2}$. Assuming that $P_0 \sim 10^4 - 10^5$ CGSE units, we obtain $\omega_g \sim 10^{11} - 10^{12}$ rad·s^{-1}. At IR frequencies $\omega \sim 10^{13}$ rad·s^{-1}, the ionic gyromagnetic ratio $g \sim 10^3$ cm/g$^{1/2}$. Hence $\omega_g \sim 10^7 - 10^8$ rad·s^{-1}. In any case, the ratio $\omega_g / \omega_0 \ll 1$ in formulas (9) and (10), so that the interval (9) is narrow: $\Delta\omega = \omega_0 - \omega_L \approx 4\pi\omega_0 \omega_g^2 / \bar{\omega}_0^2$.

2. TRANSVERSE MAGNETIC POLARITONS

The nonzero components of the fields for a TM wave are e_x, e_z, and h_y. For $z = 0$, the boundary conditions lead to the equality

$$k_0 + \tilde{k}_0 \varepsilon_1 + \gamma \frac{\omega}{c} = 0. \tag{11}$$

For positive values of k_0 and $\tilde{k}_0$, we arrive at the conditions

$$\omega^2 < k^2 c^2, \quad \varepsilon_1 \tilde{k}_0 + \gamma \frac{\omega}{c} < 0,$$

$$\frac{\varepsilon_1}{\varepsilon_2} k^2 - \frac{\omega^2}{c^2} (\varepsilon_1 - \gamma^2) > 0, \tag{12}$$

where $\varepsilon_1 = \varepsilon_1(\omega)$, $\varepsilon_2 = \varepsilon_2(\omega)$, $\gamma = \gamma(\omega)$ according to formulas (2), (3), and (8).

The energy-momentum relation for TM polaritons can be presented in the form

$$\frac{\omega^2}{c^2} = \frac{\varepsilon_1 k^2 - \varepsilon_2 k_0^2}{\varepsilon_1 \varepsilon_2 - \gamma^2 \varepsilon_2}. \tag{13}$$

We shall carry out a detailed analysis of the conditions (11)–(13) for the existence of TM polaritons.

In the absence of dynamic ME interaction (i.e., for $\gamma = 0$), TM polaritons exist in the frequency interval
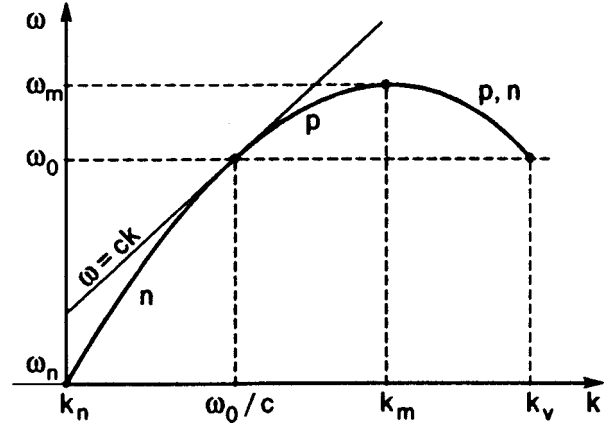

FIG. 1. Energy-momentum relations for surface TM polaritons in A-type ferroelectrics. Letters p and n indicate the segments of the dispersion dependences for p- and n-domains.

$$\omega_0 < \omega < \omega_S, \quad \omega_S^2 = \frac{1}{2} (\Omega_e^2 + \omega_0^2),$$

$$\Omega_e^2 = \omega_e^2 + 4\pi\bar{\omega}_0^2. \tag{14}$$

This leads to the condition $\Omega_e > \Omega_0$. Ferroelectrics whose parameters satisfy this condition will be termed B-type ferroelectrics, while ferroelectrics for which $\Omega_e < \omega_0$ will be termed A-type ferroelectrics. So far, surface TM polaritons were known to exist only in B-type ferroelectrics (see, for example, Ref. 4). The inclusion of dynamic ME interaction makes it possible for TM polaritons to exist in B- as well as A-type ferroelectrics.

The obtained results can be presented in a convenient manner separately for different types of ferroelectrics. These results also depend on the orientation of the electric polarization vector in a domain. We denote the domain with electric polarization $\mathbf{P}_0$ directed into the bulk of the crystal by p, and the domain with opposite direction of $\mathbf{P}_0$ by n.

2.1. A-type ferroelectrics

In n-domains, the surface polaritons exist in the following intervals of frequencies and wave vectors (Fig. 1):

$$k_n \leqslant k \leqslant \frac{\omega_0}{c}, \quad \omega_n \leqslant \omega \leqslant \omega_0,$$

$$k_m \leqslant k \leqslant k_v, \quad \omega_0 \leqslant \omega \leqslant \omega_m,$$

where we have used the notation

$$k_n = \frac{\omega}{c} \left[1 - \beta^2 \left(1 - \frac{3}{2} \frac{\Omega_e^2}{\omega_0^2} \right) \right],$$

$$\omega_n^2 = \omega_0^2 - 3\beta^2 (\omega_0^2 - \Omega_e^2),$$

$$k_m = \frac{\omega}{c} \left[1 + \beta^2 \left(1 - \frac{\Omega_e^2}{2\omega_0^2} \right) \right], \tag{15}$$

$$\omega_m^2 = \omega_0^2 + \beta^2 (\omega_0^2 - \Omega_e^2),$$

$$k_v = \frac{\omega}{c} (1 - 2\beta^2), \quad \beta = |\omega_g| \omega_0 / \bar{\omega}_0^2 \ll 1.$$

In p-domains, TM polaritons are characterized by wave vectors in the interval $[\omega_0/c, k_v]$.

The energy-momentum relations for TM polaritons in Fig. 1 are described by the relation

$$\frac{k^2 c^2}{\omega^2} = 1 + \beta^2 (\chi \pm 1)^2, \tag{16}$$

where

$$\chi = \left[1 + \frac{\omega_0^2 - \omega^2}{\beta^2 (\omega_0^2 - \Omega_e^2)} \right]^{1/2}.$$

The dispersion curve in the interval $[k_n, k_m]$ corresponds to minus sign, while the curve in the interval $[k_m, k_v]$ corresponds to plus sign in formula (16). At the point $k = \omega_0/c$, the straight line $\omega = ck$ touches the dispersion curve, and the equality $d\omega/dk = 0$ is satisfied at the point $k = k_m$.

The quantity k_0, which is reciprocal to the wave penetration depth in a ferroelectric, is defined by the relations

$$k_0 = \begin{cases} -\dfrac{\omega}{c} \, \gamma(2 - \chi), & \omega < \omega_0, \\[2mm] \dfrac{\omega}{c} \, \gamma\chi, & \omega > \omega_0, \end{cases} \tag{17}$$

in the n-domain, and by

$$k_0 = -\frac{\omega}{c} \, \gamma(2 \pm \chi), \tag{18}$$

in the p-domain. The choice of the signs is the same as for Eqs. (16).

It can be seen from Fig. 1 that the TM polaritons in the p-domain are distinguished by the presence of *birefringence*. In this domain, waves with positive and negative dispersion, i.e., with opposite group velocities $d\omega/d\mathbf{k}$, propagate with the same frequency.

The distinguishing feature of TM waves in the n-domain is the existence of forbidden wavelengths in the frequency interval $[\omega_0, \omega_m]$ for the values of wave vectors in the interval $\omega_0/c \leqslant k \leqslant k_m$.

The qualitative behavior of the penetration depth of waves in a ferroelectric (k_0) and in vacuum ($\tilde{k}_0$) is shown in Figs. 2a and 2b.

In the n-domain, the penetration depth in ferroelectrics at the boundaries ω_n and ω_m of the frequency intervals is equal to infinity, i.e., the wave becomes a bulk wave. If, however, $\omega = \omega_0$, waves do not penetrate the crystal ($k_0^{-1} = 0$), and propagate in vacuum ($\tilde{k}_0^{-1} = \infty$).

In the p-domain, the penetration depth in a ferroelectric is equal to zero for $\omega = \omega_0$ and attains its peak for $\omega = \omega_m$.

The surface TM polaritons in an A-type ferroelectric are *virtual*.

2.2. B-type ferroelectrics

TM polaritons exist in these ferroelectrics even without the ME interaction, and the range of their existence is quite wide. This interval is slightly altered when the ME interac-
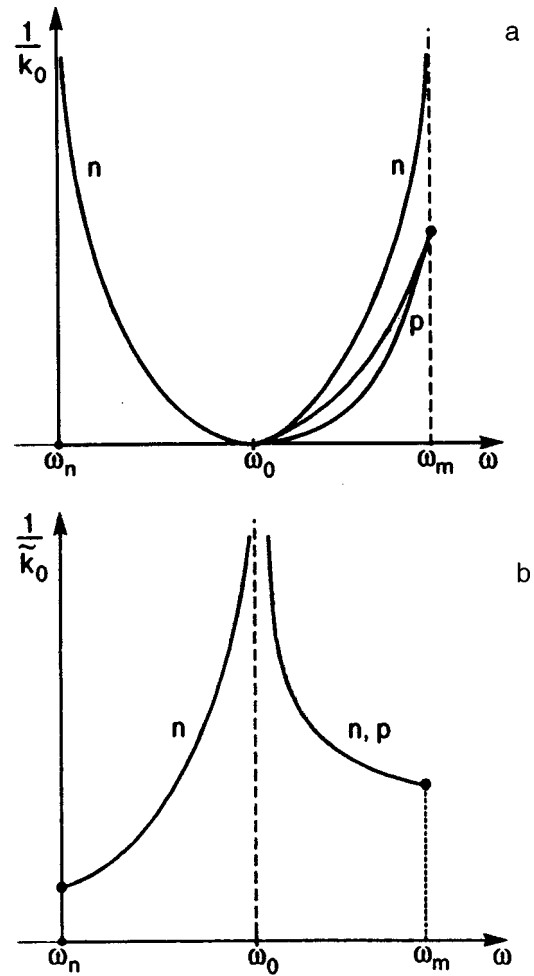
FIG. 2. Penetration depth of TM polaritons in an A-type ferroelectric (a) and in vacuum (b).

tion is taken into account, narrow frequency regions are added to the range of TM polaritons, and a new effect (*birefringence*) is observed.

Figure 3 shows the qualitative form of the dispersion curves for n- and p-domains. Starting from the value
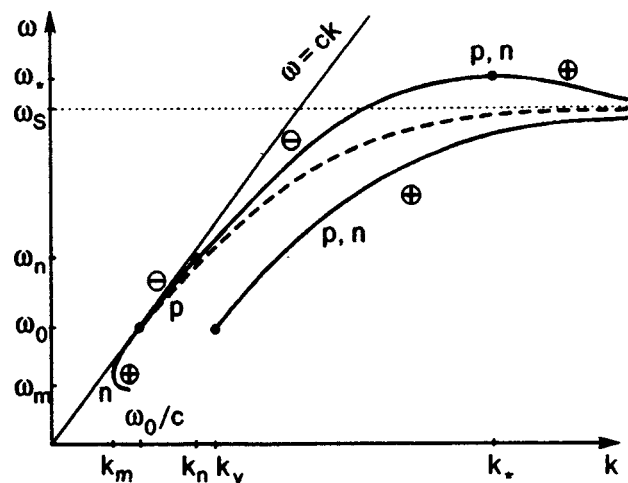
FIG. 3. Energy-momentum relations for TM polaritons in B-type ferroelectrics.

$k = \omega_0/c, \omega = \omega_0$, the dashed curve is the dispersion curve for TM polaritons in the absence of ME interaction. The ME interaction slightly extends the frequency interval downwards for the n-domains, the broadening of the interval being $[\omega_m, \omega_0]$. On the other hand, the frequency interval for both n- and p-domains increases to the value ω_*, where

$$\omega_* = \omega(k_*) = \omega_S \left[1 + \beta^2 \frac{\Omega_e^2 - \omega_S^2}{2\omega_0^2} \right]^{1/2}, \quad k_* = \frac{\bar{\omega}_0^2}{c\omega_g}. \quad (19)$$

The domain-related singularities in the dispersion are manifested only in the vicinity of ω_0.

Apart from the additional frequency interval $[\omega_m, \omega_0]$, the n-domain also has a forbidden band of wave vectors $[\omega_0/c, \min(k_n, k_v)]$. For the p-domain, there are no forbidden values of k in the entire frequency interval $[\omega_0, \omega_*]$. Birefringence appears in the n-domain for waves with $k \geqslant k_n$, while for the p-domain it exists in the entire frequency range.

Except for the interval $[\omega_m, \omega_0]$, the TM polaritons are *real*.

The dispersion curves in Fig. 3 are described by the general relation

$$\frac{k^2 c^2}{\omega^2} = .1 + \frac{1}{E_2^2} (\sqrt{\gamma^2 - E_1 E_2 - E_2^2} \pm \gamma)^2, \quad (20)$$

$$E_1 = \varepsilon_1 - 1, \quad E_2 = \frac{1 - \varepsilon_1 \varepsilon_2}{\varepsilon_2},$$

in which the above-mentioned conditions (12) must be taken into consideration. The choice of signs in formula (20) for various segments of the dependence $\omega(k)$ is indicated in Fig. 3.

The penetration depth of TM waves in a ferroelectric for $\omega \to \omega_0$ tends to zero. In the n-domain (for $\omega > \omega_n$), $k_0^{-1} = \to \infty$ for $\omega \to \omega_n$, i.e., the wave becomes a bulk wave. In both domains, the penetration depth for TM waves in a ferroelectric tends to zero for $k \to \infty$ and $\omega \to \omega_S$.

CONCLUSION

The above analysis shows that a consideration of dynamic magnetoelectric energy in a ferroelectric leads to a number of qualitatively new results.

The existence of a domain structure in a ferroelectric is manifested for the first time in the properties of surface waves: it is found that the surface TE polaritons can also exist in ferroelectrics. An interesting feature of these polaritons is that they can exist only in domains with the electric polarization directed into the bulk of the crystal. This asymmetry may turn out to be useful for studying the domain structure of ferroelectrics.

Magnetoelectric interaction leads to the emergence of TM polaritons in A-type ferroelectrics, in which their existence was forbidden earlier. ME interaction also induces new effects like birefringence of surface TM polaritons and their anomalous dispersion.

Moreover, spectral regions of excitations appear for TM polaritons, their existence being possible only in certain domains. Thus, TM polaritons with wave vectors $[\omega_0/c, k_m]$ cannot appear in the n-domain for A-type ferroelectrics (Fig. 1), while TM polaritons with values of k in the interval $[\omega_0/c, \min(k_n, k_v)]$ cannot appear for B-type ferroelectrics (Fig. 3).

The domain nonreciprocity of TE and TM excitations mentioned above is a spatial analog of the non-reciprocity in time for optical phenomena, which is used quite extensively in modern optical electronics.

In conclusion, it should be remarked that the above-mentioned effects will occur not only in ferroelectrics, but also in normal dielectrics in a constant electric field. In this case, the existence of certain surface excitations could be controlled by changing the direction of the applied electric field.

*)E-mail: mamaluy@ilt.kharkov.ua

[1] V. D. Buchel'nikov and V. G. Shavrov, Zh. Éksp. Teor. Fiz. **109**, 706 (1996) [JETP **82**, 380 (1996)].
[2] I. E. Chupis, Fiz. Nizk. Temp. **23**, 290 (1997) [Low Temp. Phys. **23**, 213 (1997)].
[3] G. A. Smolenskii and I. E. Chupis, Usp. Fiz. Nauk **137**, 415 (1982) [Sov. Phys. Usp. **25**, 475 (1982)].
[4] V. M. Agranovich and D. L. Mills (Eds.), *Surface Polaritons*, North-Holland, Amsterdam (1982).

Translated by R. S. Wadhwa

LETTERS TO THE EDITOR

Magnetic flux locking in two weakly coupled superconducting rings

R. de Bruyn Ouboter

Kamerlingh Onnes Laboratory, Leiden Institute of Physics, Leiden University, P.O. 9506, 2300 RA Leiden, The Netherlands

A. N. Omelyanchuk and E. D. Vol

B. I. Verkin Institute for Low Temperature Physics and Engineering, National Academy of Sciences of Ukraine, 47 Lenin Ave., 310164 Kharkov, Ukraine*

We have analyzed the quantum interference effects in the macroscopic ''superconducting molecule.'' The composite system consists of two massive superconducting rings, each interrupted by a Josephson junction, which are at the same time weakly coupled with one another. The special case of coupling via the Josephson four-terminal junction is considered. The structure of the macroscopic quantum states in an applied magnetic field is calculated. It is shown that, depending on the values of the magnetic fluxes through each ring, the system displays two groups of states, the ''orthostates'' with both induced currents going in the same direction, and the ''parastates'' with the opposite currents and with the total induced flux locked to zero value. The transition to the flux locked state with changing of the total applied flux is sudden and is preserved in a certain interval which is determined by the difference of the fluxes applied through each ring. It makes the system sensitive to small gradients of the external magnetic field. © *1998 American Institute of Physics.* [S1063-777X(98)01410-8]

The system that we studied is shown in Fig. 1 and consists of two bulk superconducting rings, coupled via the 4-terminal Josephson junction.[1,2] The 4-terminal Josephson junction is a system of two microbridges, 1–2 and 3–4, having the common center ''0''. The interference in the cross section ''0'' of macroscopic wave functions Ψ_j of the jth terminal ($j=1,...,4$) leads to nonlinear coupling and consequently to interference between the current states in each ring. The resulting current state of the whole system can be regulated by the difference of the magnetic fluxes applied through the rings, in analogy with the phase difference between two weakly coupled bulk superconductors. The studying of the macroscopic quantum states of such ''superconducting molecule'' is the subject of the present paper.

The free energy U of our system in an applied magnetic field contains the magnetic energy U_m and the Josephson coupling energy U_J. The energy U_m has the form:[3]

$$U_m = \frac{(\Phi_1^e - \Phi_1)^2 L_2}{2(L_1 L_2 - L_{12}^2)} + \frac{(\Phi_2^e - \Phi_2)^2 L_1}{2(L_1 L_2 - L_{12}^2)}$$

$$- \frac{L_{12}}{(L_1 L_2 - L_{12}^2)} (\Phi_1^e - \Phi_1)(\Phi_2^e - \Phi_2), \quad (1)$$

where $\Phi_{1,2}^e$ are the external magnetic fluxes applied to the rings 1, 2 and $\Phi_{1,2}$ are the resulting fluxes embraced by the rings; $L_{1,2}$ and L_{12} are the ring self-inductances and the mutual inductance ($L_{12}^2 < L_1 L_2$). The coupling energy U_J (in

dimensionless units) is expressed in terms of phase φ_j ($j=1,...,4$) of the superconducting order parameter in the jth terminal:[2]

$$U_J = -\kappa^2 \cos^2 \frac{\phi_1}{2} - \cos^2 \frac{\phi_2}{2}$$

$$- 2\kappa \cos \frac{\phi_1}{2} \cos \frac{\phi_2}{2} \cos \chi, \quad (2)$$

if we introduce the phase differences across the weak links in the rings

$$\phi_1 = \varphi_1 - \varphi_2, \quad \phi_2 = \varphi_3 - \varphi_4$$

and the ''total'' phase difference between the rings

$$\chi = \frac{\varphi_1 + \varphi_2}{2} - \frac{\varphi_3 + \varphi_4}{2}.$$

The coupling constant κ in (2) is the ratio of critical currents of the weak links 1–2 and 3–4. In the following for simplicity we will consider the case of identical rings with $L_1 = L_2 = L$ and the symmetrical coupling $\kappa = 1$ ($I_{c,12} = I_{c,34} = I_c$).

The phase differences $\phi_{1,2}$ are related to the magnetic fluxes $\Phi_{1,2}$ by: $\varphi_{1,2} = -2e\Phi_{1,2}/\hbar$. Thus, the total energy in reduced units of the two coupled rings as function of the embraced magnetic fluxes at given values of the applied fluxes is defined as
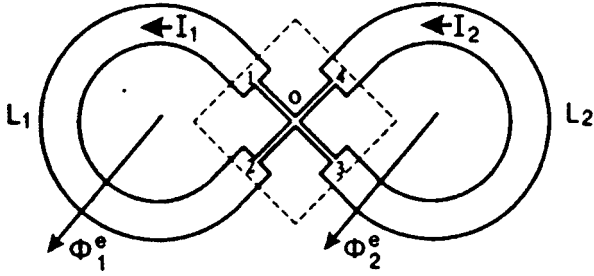
FIG. 1. The two bulk superconducting rings, coupled via the 4-terminal Josephson junction (the region closed by the dashed lines, of which the area is of the order of the coherence length squared).

$$U(\Phi_1,\Phi_2,\chi|\Phi_1^e,\Phi_2^e) = \frac{(\Phi_1^e-\Phi_1)^2}{2\mathscr{L}} + \frac{(\Phi_2^e-\Phi_2)^2}{2\mathscr{L}}$$

$$-\frac{l}{\mathscr{L}}(\Phi_1^e-\Phi_1)(\Phi_2^e-\Phi_2)$$

$$-\cos^2\frac{\Phi_1}{2}-\cos^2\frac{\Phi_2}{2}$$

$$-2\cos\frac{\Phi_1}{2}\cos\frac{\Phi_2}{2}\cos\chi, \quad (3)$$

where $l=L_{12}/L$ is the normalized mutual inductance ($l<1$), $\mathscr{L}=(2eI_c/\hbar)L(1-l^2)$-the dimensionless effective self-inductance; the magnetic fluxes are measured in units $\hbar/2e$. Note the dependence of the potential U on the phase χ. As we shall see, in the stable steady state the phase χ can take only the value 0 or π, which corresponds the existence of two groups of states with different symmetry.

The minima of the potential U (3) with respect to variables Φ_1,Φ_2,χ at given external fluxes Φ_1^e and Φ_2^e determine the stable steady states of our system. The minimization of U with respect to χ gives that the phase χ takes the value 0 or π, depending on the equilibrium values of Φ_1 and Φ_2

$$\cos\chi=\text{sign}\left(\cos\frac{\Phi_1}{2}\cos\frac{\Phi_2}{2}\right). \quad (4)$$

In the steady state $\partial U/\partial\Phi_1=\partial U/\partial\Phi_2=0$, or:

$$\Phi_1^e-l\Phi_2^e=\Phi_1-l\Phi_2+\mathscr{L}\sin\frac{\Phi_1}{2}\left[\cos\frac{\Phi_1}{2}+\cos\chi\cos\frac{\Phi_2}{2}\right], \quad (5)$$

$$\Phi_2^e-l\Phi_1^e=\Phi_2-l\Phi_1+\mathscr{L}\sin\frac{\Phi_2}{2}\left[\cos\frac{\Phi_2}{2}+\cos\chi\cos\frac{\Phi_1}{2}\right], \quad (6)$$

with $\cos\chi$ defined by the condition (4).

The solutions of Eqs. (5) and (6) $\{\Phi_1,\Phi_2\}$ which correspond to the minima of the potential U must satisfy the requirements:

$$\frac{\partial^2 U}{\partial\Phi_1^2}>0, \quad \frac{\partial^2 U}{\partial\Phi_2^2}>0, \quad \frac{\partial^2 U}{\partial\Phi_1^2}\frac{\partial^2 U}{\partial\Phi_2^2}-\left(\frac{\partial^2 U}{\partial\Phi_1\partial\Phi_2}\right)^2>0. \quad (7)$$

It can be shown that the conditions (7) are fulfilled for all values of Φ_1 and Φ_2 if $\mathscr{L}+l<1$. In the following we shall

consider the case when the inductances $\mathscr{L}$ and l are small enough to satisfy this inequality. Thus, all solutions $\{\Phi_1,\Phi_2\}$ of the Eqs. (4), (5) and (6) determine the possible stable or metastable states of the system. The circulating ringcurrents $I_{1,2}$ in state $\{\Phi_1,\Phi_2\}$ are:

$$I_1=-\frac{1}{2}\sin\Phi_1-\sin\frac{\Phi_1}{2}\text{sign}\left(\cos\frac{\Phi_1}{2}\right)\left|\cos\frac{\Phi_2}{2}\right|, \quad (8)$$

$$I_2=-\frac{1}{2}\sin\Phi_2-\sin\frac{\Phi_2}{2}\text{sign}\left(\cos\frac{\Phi_2}{2}\right)\left|\cos\frac{\Phi_1}{2}\right| \quad (9)$$

in units of I_c.

The value of $\cos\chi$ in Eqs. (5) and (6), which equals ± 1, determines two possible ''binding'' of the current states in individual rings. The group of states $\{\Phi_1,\Phi_2,\chi=0\}$ we shall call symmetric, or ''ortho'', states and the group of states $\{\Phi_1,\Phi_2,\chi=\pi\}$—antisymmetric, or ''para''; states. As we shall see, the first one corresponds to the induced ring-currents going in the same direction, and the second one—to the currents going opposite.

We shall study the behavior of our system in an applied magnetic field as the response on the total applied magnetic flux $\Phi^e=\Phi_1^e+\Phi_2^e$ at given difference $\delta^e=\Phi_1^e-\Phi_2^e$ of the fluxes through each ring. The state of the system as whole is determined by the total embraced magnetic flux $\Phi=\Phi_1+\Phi_2$, or by the total orbital magnetic moment M, which is proportional to the sum of the induced ringcurrents, $I=I_1+I_2$. Note, that the positive (negative) sign of I corresponds to the parallel (antiparallel) direction of M with respect to the external magnetic field H. From the (4)–(6) we obtain:

$$\Phi_e=\Phi+\frac{\mathscr{L}}{1-l}\sin\frac{\Phi}{2}\left[\cos\frac{\delta}{2}+\cos\chi\right], \quad (10)$$

$$\delta^e=\delta+\frac{\mathscr{L}}{1+l}\sin\frac{\delta}{2}\left[\cos\frac{\Phi}{2}+\cos\chi\right], \quad (11)$$

$$\cos\chi=\text{sign}\left(\cos\frac{\Phi}{2}+\cos\frac{\delta}{2}\right), \quad (12)$$

where $\delta=\Phi_1-\Phi_2$.

Let us start from the case of small inductances l, $\mathscr{L}\ll 1$. If $\delta^e=0$, from the Eqs. (11) and (12) follows that $\delta=0$ and $\chi=0$. For $\Phi(\Phi^e)$ we have the usual equation $\Phi_e=\Phi+2\mathscr{L}\sin(\Phi/2)$ for the case of decoupled rings,[4] each interrupted by a Josephson junction. At $\delta^e\neq 0$ and consequently $\delta\neq 0$, the solutions with $\chi=\pi$ are possible in the vicinity of $\Phi\approx 2\pi$. In the limit $\mathscr{L}\to 0$ for the total induced magnetic flux $\Phi(\Phi^e,\delta^e)$ we have the expression

$$\Phi=\Phi^e-\mathscr{L}\sin\frac{\Phi^e}{2}\left[\cos\frac{\delta^e}{2}+\text{sign}\left(\cos\frac{\Phi^e}{2}+\cos\frac{\delta^e}{2}\right)\right]. \quad (13)$$

In the case of small $\delta^e\ll 1$ it becomes:

$$\Phi=\begin{cases}\Phi^e-2\mathscr{L}\sin\dfrac{\Phi^e}{2} & \text{if }|\Phi^e-2\pi|>|\delta^e|\\[2mm]\Phi^e & \text{if }|\Phi^e-2\pi|<|\delta^e|.\end{cases} \quad (14)$$

Thus, for given value of δ^e with changing of the total applied flux Φ^e the system switches from the state with χ
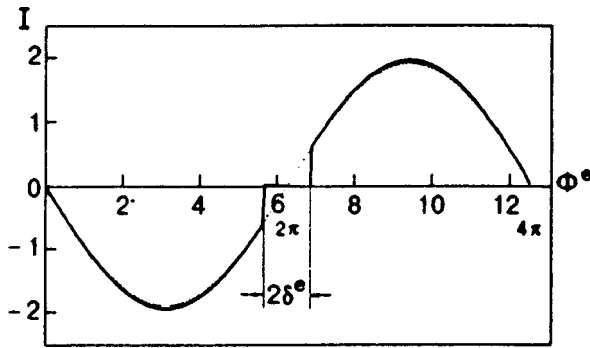
FIG. 2. The total induced current as a function of the total applied flux at given difference of applied fluxes through each ring $\delta^e = 2\pi/10$ (or 1/10 of a flux quantum $h/2e$). $\mathscr{L}=0$. The dashed line is the corresponding dependence in the case of decoupled rings.

$=0$ to the state with $\chi=\pi$. In the interval $2\pi-\delta^e<\Phi^e$ $<2\pi+\delta^e$ the total induced flux $\Phi-\Phi^e$ equals zero for $\delta^e\ll1$. We call such behavior magnetic flux locking. It is emphasized that the transition to the flux locked state is sudden and is preserved in a certain interval of the applied magnetic flux. For the sum of the induced ringcurrents $I=I_1$ $+I_2$, in the limit $\mathscr{L}\to0$ we have

$$I(\Phi^e, \delta^e) = -\sin\frac{\Phi^e}{2}\left[\cos\frac{\delta^e}{2}+\text{sign}\left(\cos\frac{\Phi^e}{2}+\cos\frac{\delta^e}{2}\right)\right].$$
(15)

In the flux locked state the total current I equals to zero in correspondence with (14). Thus the ringcurrents $I_{1,2}$ are going in opposite directions and compensate each other, or the system is in the ''para'' state. The complete compensation takes place for $\delta^e\ll1$, with the corrections to zero value being of the order of $(\delta^e)^2$. In Fig. 2 we plot the dependence of $I(\Phi^e)$ (15) for the flux difference $\delta^e=2\pi/10$, or in dimension units 1/10 of a flux quantum $h/2e$. The dashed line is the sum of the currents in the same, but decoupled, rings with the same applied fluxes $\Phi_1^e=(1/2)(\Phi^e+\delta^e)$ and $\Phi_1^e=(1/2)(\Phi^e-\delta^e)$. The magnetic susceptibility of the system as whole is proportional to $-\partial I/\partial\Phi^e$ and will reflect the behavior of the induced currents.

For finite, but small, values of the inductances, the behavior described above will be qualitatively the same. Only instead of the sharp switches hysteretic regions appear, of which the width is proportional to $\mathscr{L}$. In Fig. 3 the dependence $\Phi(\Phi^e)$ for $\mathscr{L}=0.25$, $l=0$ and $\delta^e=1$ is shown, as follows from the numerical solution of the Eqs. (10)–(12). Naturally, these hysteretic regions will be smeared by thermal fluctuations (see the analysis of the influence of noise on the similar system, the so called 4-terminal SQUID, in Ref. 5).

In conclusion, we have studied the macroscopic quantum states in the system of two weakly coupled superconducting rings. The nonlinear coupling leads to interference between the current states in each ring. It is manifested as the cooperative behavior of the rings in some region of the applied magnetic fluxes, which we call magnetic flux locking. We would like to remark that our macroscopic approach is not restricted by the special kind of the coupling through the
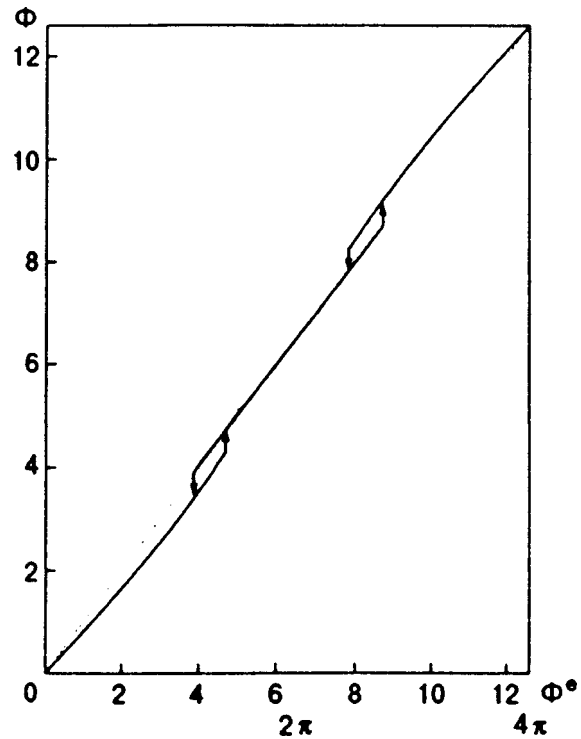

FIG. 3. The dependence of the total magnetic flux Φ on the total external flux Φ^e for $\delta^e=1$, $\mathscr{L}=0.25$, $l=0$. The arrows indicate the jumps of the flux from metastable to stable states. The dashed line is $\Phi=\Phi^e$.

crossed superconducting bridges. In fact, any mesoscopic 4-terminal weak link will produce a coupling similar to the U_J (2). For example, it can be the experimental setup described in Ref. 6, namely the two-dimensional normal layer which is connected with four terminals instead of the two ones as studied in Ref. 7.

[*]E-mail: omelyanchouk@ilt.kharkov.ua

[1]E. D. Vol and A. N. Omelyanchouk, Fiz. Nizk. Temp. **20**, 107 (1994) [Low Temp. Phys. **20**, 87 (1994)].
[2]R. de Bruyn Ouboter, A. N. Omelyanchouk, and E. D. Vol, Physica **B205**, 153 (1995); Physica **B239**, 203 (1997).
[3]L. D. Landau and E. M. Lifshitz, *Electrodynamics of Continuous Media*, Pergamon Press, New York (1963), Ch. 4.
[4]A. Barone and G. Paterno, *Physics and Applications of the Josephson Effect*, Wiley, New York (1982).
[5]R. de Bruyn Ouboter and A. N. Omelyanchouk, to be published in Physica **B**; Los Alamos archive condmat/9805109.
[6]J. P. Heida, B. J. van Wees, T. M. Klapwijk, and G. Borghs, Phys. Rev. **B57**, R5618 (1998).
[7]K. K. Likharev, Radiotekh. Elektron. **20**, 660 (1975); Rev. Mod. Phys. **51**, 101, 146 and 147 (1979).